

Investigation into micro machinability of Mg based
metal matrix composites (MMCs) reinforced with
nanoparticles



Xiangyu Teng

School of Engineering

Newcastle University

A thesis submitted for the degree of

Doctor of philosophy

October 2018

Acknowledgements

First and foremost, I would like to express my sincere appreciation to my supervisor Dr. Dehong Huo, for the continuous support and guidance received throughout my PhD studies. Without his generous support, encouragement and patience the completion of the PhD project would not have been possible. My appreciation also goes to my second supervisor Dr. Eugene Wong based at the Newcastle University of Singapore Campus, for the helpful guidance on the knowledge of composite materials. I must thank him for answering any questions I had and spending time reviewing the manuscripts.

I am also grateful to Dr. Wanqun Chen for his encouragement and help during difficult periods. His valuable suggestions always help me to solve the problems I met and give me insights to think through research problems from different perspectives.

Last, special thanks to my parents Lixin Ma and Bin Teng and my wife Jing Li. Their unconditional love and consistent support have continuously encouraged me throughout this crucial time of my life.

Abstract

As composite materials with combination of low weight and high engineering strength, traditional metal matrix composites (MMCs) with micro-sized reinforcement (micro-MMCs) have been utilized in numerous area such as aerospace, automobile, medical and advanced weapon systems in the past two decades. With the development of composite materials, metal matrix composites reinforced with small volume fraction of nano-sized reinforcements (nano-MMCs) exhibits an equivalent and even better properties than that reinforced with large volume of micro-sized reinforcement and thus receive increasing attention from academia and industries. MMCs components are typically fabricated in near net shape process such as casting. But micro machining processes are indispensable in order to meet the increasing demands on the component with high dimensional accuracy and complex shapes. However, the enhanced mechanical properties of MMCs and tool-like hardness of reinforced particles bring challenges to machining process. The deteriorative machined surface finish and excessive tool wear have been recognised as the main obstacles during machining of MMCs due to their heterogeneous and abrasive nature. In this research, the detailed material removal mechanism of nano-MMCs in terms of micro machinability, micro tool wear and simulated material removal process with finite element analysis (FEA) is investigated.

The systematic experimental studies on micro machining mechanism of magnesium-based MMCs reinforced with nanoparticles (Ti, TiB₂, BN, ZnO) are conducted. The cutting force, burr formation, surface roughness and morphology are characterised to investigate the micro machinability under the effect of various machining parameters, particle volume fraction and matrix/reinforcement materials using design of experiment (DoE) and analysis of variance (ANVOA) methods. The micro structure changes of Mg-MMCs by addition of nanoparticles were taken into account. In addition, surface morphology and the minimum chip thickness is obtained and characterised with the aim of examining the specific cutting energy.

A comprehensive investigation of tool wear mechanisms in the micro milling of Mg-MMCs is conducted. The tool wear is characterised both quantitatively and qualitatively by observing tool wear patterns and analysing the effect of cutting parameters and tool coating on average flank wear, reduction in tool diameter, cutting forces, surface roughness, and burr formation. The main wear mechanisms at different machining conditions are determined. Finally, the tool wear phenomenon observed from experiments is explained by simulating the tool-particles interaction using finite element modelling, and hence new wear mechanisms are proposed for machining nano-MMCs.

The two dimensional micromechanical finite element (FE) models are established to study the material removal mechanism of MMCs reinforced with micro-sized and nanoparticles in micro machining process with consideration of size effect. Two phases, namely particle and matrix are modelled in FE cutting models. Particle fracture properties are involved in micro-sized particles to study the fracture behaviours. The cutting force, tool-particles interaction, particle fracture behaviours, stress/strain distribution, chip formation process and surface morphology are investigated in the FE models. The surface defect generation mechanism is studied in details by developing the additional three dimensional (3D) FE models in machining micro-MMCs. Moreover, the cutting mechanism comparison between machining nano-MMCs and micro-MMCs is conducted to investigate the effect of significant particle size reduction from micro to nano-scale. The model validation is carried out by studying the chip morphology, cutting force, surface morphology obtained from machining experiments and good agreements are found with the simulation results.

Contents

Acknowledgements	i
Abstract.....	iii
List of Figures.....	ix
List of Tables.....	xvi
Nomenclature.....	xvii
Chapter 1 Introduction	1
1.1 Background and motivation.....	1
1.2 Aim and objectives	4
1.3 Scopus of this research	1
Chapter 2 Literature review	2
2.1 Overview of metal matrix composites (MMCs)	2
2.1.1 Background and characteristics of MMCs	2
2.1.2 State-of-the-art of MMCs reinforced with nanoparticles	3
2.1.3 Characterisation of Mg-based MMCs reinforced with nanoparticles	6
2.2 Machining of MMCs	8
2.2.1 Conventional machining.....	8
2.2.2 Non-conventional machining	12
2.2.2.1 Electric discharge machining (EDM)	13
2.2.2.2 Laser beam machining (LBM).....	18
2.2.2.3 Abrasive water jet machining (AWJ)	21
2.3 Tool wear in machining particulate-reinforced MMCs	23
2.4 Overview of the micro machining process	27
2.4.1 General review of the micro machining process	27
2.4.2 Size effect and minimum chip thickness	28
2.4.3 Microstructure effect	31
2.4.4 Tool wear mechanism in micro machining	33
2.5 Finite element modelling on machining of MMCs.....	36
2.5.1 Numerical formulation in FEM of machining process.....	36
2.5.1.1 Lagrangian formulation	37
2.5.1.2 Eulerian formulation	37
2.5.1.3 Arbitrary Lagrangian Eulerian (ALE)	37
2.5.2 Finite element modelling of machining particulate-reinforced MMCs.....	38
2.6 Summary.....	42
Chapter 3 Comprehensive micro-machinability study of Mg based MMCs reinforced with nanoparticles.....	44

3.1	Introduction.....	44
3.2	Experimental setup	45
3.2.1	Machine tool.....	45
	Experiment A&B.....	45
3.2.2	Workpiece materials	45
	Experiment A.....	45
	Experiment B.....	46
3.2.3	Micro end mills.....	46
	Experiment A&B.....	46
3.3.4	Experimental Procedure	47
	Experiment A.....	47
	Experiment B.....	48
3.4	Results and discussions (Experiment A)	49
3.4.1	Surface roughness analysis.....	49
3.4.1.1	Main effect of cutting parameters on surface roughness	51
3.4.1.2	ANOVA analysis	52
3.4.1.3	Regression analysis.....	53
3.4.2	Cutting force analysis	54
3.4.2.1	Main effect of cutting parameters on cutting force.....	54
3.4.2.2	Mechanistic model.....	56
3.4.3	Size effect	57
3.4.3.1	Specific cutting energy	58
3.4.3.2	Machined surface morphology	59
3.5	Results and discussion (Experiment B)	61
3.5.1	Influence of nanoparticles contents and materials on cutting force	61
3.5.2	Influence of nanoparticles contents and materials on surface roughness and morphology	63
3.5.3	Influence of nanoparticles contents and materials on chip formation	66
3.6	Conclusions.....	67
Chapter 4	Modelling of machining micro-sized & nanoparticle reinforced MMCs	70
4.1	Introduction.....	70
4.2	Overview of finite element (FE) method formulation	70
4.2.1	Materials constitutive modelling formulation	70
4.2.2	Fracture criterion	72
4.2.2.1	Constant strain criterion.....	72
4.2.2.2	Johnson-Cook fracture criterion	73

4.2.2.3	Cockcroft-latham fracture criterion	73
4.2.2.4	Fracture criterion coupled with damage evolution step	73
4.2.3	Friction between tool-chip interface	75
4.3	Case i: Cutting mechanism of MMCs reinforced with nanoparticles	76
4.3.1	FE modelling procedures	76
4.3.1.1	Simplification of 2D milling to orthogonal machining process	76
4.3.1.2	Model setup	77
4.3.1.3	Material modelling	78
4.3.1.4	Boundary condition and contact definitions	79
4.3.2	Chip formation process analysis	80
4.3.3	Model validation	86
4.3.4	Effect of uncut chip thickness	88
4.3.4.1	Specific cutting force analysis	88
4.3.4.2	Chip morphology analysis	88
4.4	Case ii: Cutting mechanism of MMCs reinforced with micro-sized particles	90
4.4.1	FE modelling procedure	91
4.4.2	Effect of relative position of particles to cutting path on the cutting mechanism	93
4.5	Case iii: Comparison of cutting mechanism when machining micro and nanoparticles reinforcing SiC/Al MMCs	102
4.5.1	Modelling procedures	102
4.5.2	von-Mises stress distribution in cutting area	106
4.5.3	Chip formation process	110
4.5.4	Tool-particle interaction process	112
4.5.5	Machined surface morphology	116
4.6	Conclusion	117
Chapter 5	Tool wear behaviours in micro milling of nano-Mg/Ti MMCs	120
5.1	Introduction	120
5.2	Experimental setup	120
5.2.1	Workpiece materials	120
5.2.2	Experiments setup	121
5.2.3	Micro endmills and tool wear criteria	122
5.3	Tool wear mechanism analysis	123
5.3.1	Effect of cutting speed	124
5.3.2	Effect of feed per tooth	128
5.3.3	Effect of tool coating	129
5.4	Effect of input parameters on cutting force with tool wear progression	131

5.5	Effect of input parameters on surface roughness and burr formation.....	133
5.6	Conclusions.....	136
Chapter 6	Conclusions and further works.....	138
6.1	Summary and conclusions	138
6.2	Future work.....	140
Reference	142
Appendix	161

List of Figures

Figure 1.1 Macro scale applications of MMCs (Rawal, 2001) (a) B/Al tubular used as mid-fuselage structure of space shuttle orbiter; (b) The P100/6061 Al high-gain antenna wave guides/boom for the Hubble Space Telescope; (c) Cast SiCp/Al multi-inlet fittings for a truss node.	2
Figure 1.2 Micro-scale applications of MMCs: (a) micro machined electrospray atomizers (hole inner diameter 50µm fabricated in RISE lab) (Liu and China, 2011); (b) bio-implant: bone plates.	3
Figure 1.3 Schematic of research methodology	1
Figure 2.1 Effect of volume fraction on tensile properties of Al/MMCs. (Kang and Chan, 2004).....	5
Figure 2.2 TEM images of: (a) pure aluminium; (b) Al/1 Vol.% Al ₂ O ₃ ; (c) Al/4 Vol.% Al ₂ O ₃ . (Kang and Chan, 2004).....	5
Figure 2.3 TEM micrographs of Mg/3 Vol.% SiC nano-MMCs: (a) after mixing; (b) after mixing and milling; (c) schematic diagram of nanoparticle distribution with the grain boundary of the Mg matrix.....	7
Figure 2.4 Microstructure of grain characteristic of: (a) pure magnesium; (b) Mg/0.58 Vol.% Ti; (c) Mg/0.97 Vol.% Ti; (d) Mg/1.98 Vol.% Ti. (Meenashisundaram and Gupta, 2014).....	8
Figure 2.5 (a) Typical wire EDM process of particulate reinforced MMCs; (b) three scenarios based on the relative location of particle to path of wire. (Pramanik, 2014).....	15
Figure 2.6 SEM micrograph of the re-cast layer of aluminium MMCs reinforced with SiC particles (AA2618Al/SiC). (Müller and Monaghan, 1997).....	15
Figure 2.7 Effect of discharge current and pulse-on time on surface roughness when EDM of AA2618Al/SiC, A356Al/SiC and pure A356 Al. (Müller and Monaghan, 2000)	18
Figure 2.8 Effect of current on the material removal rate when machining AlSi7Mg with 20 vol.% SiC at different pulse-on times. (Rozenek, Kozak and Da, 2001)	18
Figure 2.9 Surface morphology obtained from the LBM of (a) aluminium alloy; (b) AA2618/SiC particulate reinforced MMCs. (Müller and Monaghan, 1997)	21
Figure 2.10 Damage to sub-surface layer caused by excessive heating. (Müller and Monaghan, 1997).....	21
Figure 2.11 Saw-tooth-like machined surface profile under the effect of minimum chip thickness. (Weule, Hüntrup and Tritschler, 2001).....	29
Figure 2.12 Extraction of the minimum chip thickness from the surface profile. (Liu, DeVor and Kapoor, 2006).....	31

Figure 2.13 Schematic diagram of micro structure size effect in the micro machining process. (Cheng and Huo, 2013)	32
Figure 2.14 SEM images of severely worn endmill. (Filiz et al., 2007)	35
Figure 2.15 Tool wear criteria: (a) effective tool diameter; (b) cutting edge radius. (Ucun, Aslantas and Bedir, 2013)	35
Figure 2.16 (a) Von Mises stress distribution within matrix material; (b) modelling of particle interface. (Zhu and Kishawy, 2005)	39
Figure 2.17 (a) Three scenarios of tool-particles interaction; (b) Schematic representation for MMCs machining simulation. [131]	40
Figure 2.18 (a) Stress distribution obtained from machining EHM model; (b) sub-surface damage a depth of 40.7 μm	41
Figure 3.1 Configuration and machine tool with Kislter dynamometer.....	45
Figure 3.2 AlTiN coated Tungsten carbide micro end mill used with cutting edge radius	46
Figure 3.3 Main effects of cutting parameters on the surface roughness. (a) Mg/TiB ₂ MMCs; (b) Mg/Ti MMCs.	52
Figure 3.4 Variation of cutting force with three cutting parameters. (a) Mg/TiB ₂ MMCs; (b) Mg/Ti MMCs.....	55
Figure 3.5 The influence of reinforcement material on average cutting force at spindle speed: 40,000rpm, depth of cut: 150 μm	56
Figure 3.6 Comparison of simulated and experimental measured cutting force for machining Mg/TiB ₂ MMCs at depth of cut: 300 μm , spindle speed: 40000rpm; feed per tooth: 3 μm /tooth (a) cutting force in cross feed direction, F _x ; (b) cutting force in feed direction, F _y and at feed per tooth of 4 μm /tooth; (c) cutting force in cross feed direction, F _x ; (d) cutting force in feed direction, F _y	57
Figure 3.7 Specific cutting energy of Mg/TiB ₂ and Mg/Ti MMCs obtained at spindle speed: 40,000rpm, depth of cut: 200 μm	59
Figure 3.8 SEM micrographs of micro machined slots for Mg/TiB ₂ MMCs and Mg/ Ti MMCs, (a) & (e) at feed per tooth of 0.15 μm /tooth; (b) & (f) 0.3 μm /tooth; (c) & (g) 0.5 μm /tooth; (d) & (h) 0.8 μm /tooth and spindle speed: 40,000rpm, depth of cut: 200 μm ; (k) magnified image of (e); (j) magnified image of (h).....	60
Figure 3.9 The effect of different cutting parameters on average cutting forces (a) effect of feedrate (depth of cut: 60 μm ; spindle speed:10,000rpm); (b) effect of spindle speed (feed per tooth: 3 μm /tooth; depth of cut: 60 μm); (c) effect of depth of cut (spindle speed:10,000 rpm; feed per tooth: 3 μm /tooth).....	62

Figure 3.10 The effect of different cutting parameters on surface roughness in machining pure Mg and its nanocomposites (a) effect of feedrate at depth of cut of 60 μm and a spindle speed of 10,000 rpm; (b) effect of spindle speed at feed per tooth of 3 $\mu\text{m}/\text{tooth}$ and depth of cut of 60 μm ; (c) effect of depth of cut at spindle speed of 10,000 rpm and feed per tooth of 3 $\mu\text{m}/\text{tooth}$	64
Figure 3.11 SEM micrographs of machined surface for pure Mg at feed per tooth of 1 $\mu\text{m}/\text{tooth}$, spindle speed of 6,000rpm and depth of cut of 30 μm	65
Figure 3.12 SEM micrographs of machined surface for Mg/2.5 wt.% BN at feed per tooth of 1 $\mu\text{m}/\text{tooth}$, spindle speed of 6,000rpm and depth of cut of 30 μm	65
Figure 3.13 SEM morphology of chips of (a) Mg/2.5wt.% BN; (b) pure Mg; (c) Mg/2.5wt.% ZnO (at feed per tooth of 0.5 μm , depth of cut of 30 μm , spindle speed of 6,000rpm).	67
Figure 4.1 Stress-strain curve of damage evolution process. (‘Abaqus/Explicit V6.14 User manual’, 2016).....	74
Figure 4.2 (a) Schematic diagram of 2D milling process in 180° of tool rotation; (b) Relationship between 2D milling process to orthogonal machining process [17].	77
Figure 4.3 (a) Schematic representation of the established models for micro orthogonal machining of Mg/SiC MMCs; (b) local zooming of mesh element.	78
Figure 4.4 Chip formation process during micro-machining of nano Mg/SiC MMCs	81
Figure 4.5 Effect of addition of nanoparticles on distribution pattern of von Mises stress contour.....	81
Figure 4.6 Distribution of equivalent plastic strain within nano Mg/SiC MMCs.	82
Figure 4.7 Evolution of von Misses stress distribution on the matrix element close to interface of particle.....	84
Figure 4.8 Evolution of von Misses distribution on the particle located immediately below cutting edge with advancement of cutting tool.....	85
Figure 4.9 Distribution of equivalent plastic strain within formed chips.....	85
Figure 4.10 Formation of high stress bands within chips with advancement of cutting tool...	85
Figure 4.11 Comparison between simulated and experimental cutting force at different uncut chip thickness	86
Figure 4.12. Chip morphology comparison between (a) simulation; (b) experiments.....	87
Figure 4.13 Band width comparison between simulation and experiments	87
Figure 4.14 Specific cutting force at different uncut chip thickness	88
Figure 4.15 Chip morphology at uncut chip thickness of (a) 0.1 μm ; (b) 0.2 μm ; (c) 0.5 μm ; (d) 1 μm ; and (e) 2 μm	89

Figure 4.16. Stress and strain distribution within workpiece at material removal process under uncut chip thickness of 0.1 μm	90
Figure 4.17 The variation of shear angle with uncut chip thickness in FE model	90
Figure 4.18 (a)Schematic representation diagram of FE model setup on orthogonal turning of aluminium-based MMCs reinforced with SiC particles; (b) Different relative position of particles to the cutting path.....	92
Figure 4.19 ultraprecision machine tool (Nanoform700, Precitech, USA) with PCD turning insert	92
Figure 4.20 Simulated machined surface topography with particle behaviours under depth of cut of 2 μm	94
Figure 4.21 SEM image of machined surface obtained from turning experiment showing the shallow cavity surrounding the intact particle.	94
Figure 4.22 Simulated machined surface topography with particle behaviours under depth of cut of 4 μm	95
Figure 4.23 von-Mises stress distribution on particle at depth of cut of 4 μm	96
Figure 4.24 Simulated machined surface topography with particle behaviours under depth of cut of 6 μm	97
Figure 4.25 Von-Mises distribution of (a)-(c) completed fractured particle at entrance of cutting; (e)-(g) partially fractured particle at depth of cut of 6 μm	97
Figure 4.26 Simulated machined surface topography with particle behaviours at the depth of cut (a) 8 μm ; (b) 10 μm ; (c) 15 μm	99
Figure 4.27 Von-Mises distribution on particles at depth of cut (a-c) 10 μm ; (d-f) 15 μm	99
Figure 4.28 (a) SEM image of machined surface obtained from turning experiment showing the cavity filled with residual particle fragments; (b) EDS spectra of machined surface.	100
Figure 4.29 Simulated machined surface topography with particle behaviours at the depth of cut (a) 20 μm ; (b) 25 μm	101
Figure 4.30 Von-Mises distribution on particles at depth of cut 25 μm	101
Figure 4.31 SEM image of machined surface obtained from turning experiment showing the cavity caused by complete particle debonding.	102
Figure 4.32 FEA model setup for orthogonal aluminium-based MMCs reinforced with (a) nano-sized SiC particles, (b) micro-sized particles.	103
Figure 4.33 Chip formation when micro machining of Al/SiC MMCs reinforced with nano-sized particles (0.2 μm diameter).	108
Figure 4.34 Chip formation when micro machining of Al/SiC MMCs reinforced with micro-sized particles (10 μm diameter).	108

Figure 4.35 Von Mises stress contour in machining pure Aluminium using the same cutting parameters of nano Al/SiC MMCs machining	109
Figure 4.36 Effect of nano-particles on primary shear zone propagation (a) primary shear zone propagation direction; (b) distorted stress contour caused by prevented stress propagation.	109
Figure 4.37 Distorted plastic strain field in machining nano Al/SiC MMCs	109
Figure 4.38 Distribution of plastic strain filed in machining of micro Al/SiC MMCs	110
Figure 4.39 Fragmented chips formation when micro machining of micro Al/SiC MMCs.	111
Figure 4.40 SEM images of chips obtained from machining Al/SiC MMCs reinforced with Vol.10 % (a) micro-sized particles (Φ :10 μ m); (b) nano-sized particles (Φ :0.2 μ m) under feed per tooth of 4 μ m/tooth, cutting speed of 125.64 m/min and depth of cut of 30 μ m	112
Figure 4.41 Nanoparticles interacting with cutting tool	113
Figure 4.42 Different tool-particle interaction behaviours in machining micro Al/SiC MMCs.	114
Figure 4.43 Simulated cutting forces of micro machining Al/SiC MMCs reinforced with (a) micro-sized particles; (b) nanoparticles.....	115
Figure 4.44 SEM micrographs of main cutting edge wear of micro endmill obtained from machining Al/SiC MMCs reinforced with Vol.10 % (a) micro-sized particles (Φ :10 μ m); (b) nano-sized particles (Φ :0.2 μ m) under feed per tooth of 4 μ m/tooth, cutting speed of 125.64 m/min and depth of cut of 30 μ m.	115
Figure 4.45 Simulated surface morphology from machining (a) micro-MMCs; (b) nano-MMCs.....	116
Figure 4.46 SEM micrographs of machined surface from experimental works (a)&(b) micro-MMCs; (c)&(d) nano-MMCs under the feed per tooth of 4 μ m/tooth, cutting speed of 125.64 m/min and depth of cut of 30 μ m.	117
Figure 5.1 Distribution of nano Ti particles in Mg/Ti MMCs (Meenashisundaram and Gupta, 2014).....	121
Figure 5.2 Dimension of the micro endmill (uncoated & coated).....	122
Figure 5.3 Measurement of (a) flank wear, V_B and (b) effective tool diameter (D_E).....	123
Figure 5.4 Top view of SEM micrograph for (a) worn tool (Tool #1); (b) & (c) new tool (uncoated endmill).....	124
Figure 5.5 Side view of SEM micrograph for (a) worn tool (Tool #1); (b) & (c) new tool (uncoated endmill).....	124
Figure 5.6 SEM micrographs of the tool wear progression under various cutting conditions.	126

Figure 5.7 The effect of cutting speed on the progression of (a) flank wear; (b) reduction in tool diameter at constant feed per tooth of $3\mu\text{m}/\text{tooth}$ and depth of cut of $100\mu\text{m}$	127
Figure 5.8 SEM micrographs and EDS spectra of uncoated endmills after cutting volume of 620 mm^3 from (a)(c) Tool #1 (cutting speed of $31.4\text{m}/\text{min}$); (b)(d) Tool #2 (cutting speed of $62.8\text{m}/\text{min}$) at feed per tooth of $3\mu\text{m}/\text{tooth}$ and depth of cut of $100\mu\text{m}$ (with adhesion effect).	127
Figure 5.9 SEM micrographs and EDS spectra of uncoated endmill after cutting volume of 620 mm^3 from Tool #3 (cutting speed of $125.6\text{ m}/\text{min}$) at feed per tooth of $3\mu\text{m}/\text{tooth}$ and depth of cut of $100\mu\text{m}$ (without adhesion effect).	128
Figure 5.10 The effect of feed per tooth on the progression of (a) flank wear; (b) reduction in tool diameter at constant cutting speed of $62.8\text{ m}/\text{min}$ and depth of cut of $100\mu\text{m}$	129
Figure 5.11 SEM micrographs and EDS spectra of uncoated endmill after cutting volume of 620 mm^3 from Tool #4 (feed per tooth of $0.75\mu\text{m}/\text{tooth}$) at cutting speed of $62.8\text{ m}/\text{min}$ and depth of cut of $100\mu\text{m}$	129
Figure 5.12 The effect of tool coating on the progression of reduction in tool diameter at constant feed per tooth of $3\mu\text{m}/\text{tooth}$, cutting speed of $62.8\text{ m}/\text{min}$ and depth of cut of $100\mu\text{m}$	130
Figure 5.13 SEM micrographs and EDS spectra of coated endmill after cutting volume of 620 mm^3 from Tool#6 at constant feed per tooth of $3\mu\text{m}/\text{tooth}$, cutting speed of $62.8\text{ m}/\text{min}$ and depth of cut of $100\mu\text{m}$	130
Figure 5.14 Variation of average cutting force with progression of tool wear under the effected by (a) cutting speed at feed per tooth of $3\mu\text{m}/\text{tooth}$ and depth of cut of $100\mu\text{m}$; (b) feed per tooth at cutting speed of $62.8\text{ m}/\text{min}$ and depth of cut of $100\mu\text{m}$; (c) tool coating ..	131
Figure 5.15 The comparison between the flank wear and specific cutting force with the effect of feed per tooth at the cutting speed of $62.8\text{m}/\text{min}$, depth of cut of $100\mu\text{m}$	132
Figure 5.16 Surface roughness under effected by (a) cutting speed at feed per tooth of $3\mu\text{m}/\text{tooth}$ and depth of cut of $100\mu\text{m}$; (b) feed per tooth at cutting speed of $62.8\text{ m}/\text{min}$ and depth of cut of $100\mu\text{m}$; (c) tool coating at feed per feed per tooth of $3\mu\text{m}/\text{tooth}$, cutting speed of $62.8\text{m}/\text{min}$ and depth of cut of $100\mu\text{m}$	134
Figure 5.17 Top view of worn endmill obtained at Tool #4 (cutting speed of $62.8\text{m}/\text{min}$, feed per tooth of $0.75\mu\text{m}$ and depth of cut of $100\mu\text{m}$)	135
Figure 5.18 Built-up edge formed on cutting edge corner at Tool #3 (cutting speed of $125.6\text{m}/\text{min}$, feed per tooth of $3\mu\text{m}$ and depth of cut of $100\mu\text{m}$)	135
Figure 5.19 Burr formation at varying Experiment: (a)Experiment.1, cutting speed of $31.4\text{m}/\text{min}$, feed per tooth of $3\mu\text{m}/\text{tooth}$; (b) Experiment 2, cutting speed of $62.8\text{m}/\text{min}$, feed	

per tooth of $3\mu\text{m}/\text{tooth}$; (c) Experiment 3, cutting speed of $125.6\text{m}/\text{min}$, feed per tooth of $3\mu\text{m}/\text{tooth}$; (d) Experiment 4, cutting speed of $62.8\text{m}/\text{min}$, feed per tooth of $0.75\mu\text{m}/\text{tooth}$; (e) Experiment 5, cutting speed of $62.8\text{m}/\text{min}$, feed per tooth of $1.5\mu\text{m}/\text{tooth}$ at constant depth of cut of $100\mu\text{m}$ 136

List of Tables

Table 2.1 Representative reinforcements for MMCs (Chawla and Chawla, 2013)	2
Table 2.2 Reinforcement materials, particle size/ volume fraction, grain size and mechanical properties of Al-based nano-MMCs (Kim et al., 2017)	6
Table 3.1 Micro endmill specifications	46
Table 3.2 Cutting conditions for 1 st test	47
Table 3.3 Cutting condition for 2 nd test	48
Table 3.4 MMCs specimen parameters	49
Table 3.5 Cutting parameters used in full factorial designed experiment	49
Table 3.6 Experimental matrix of micro milling of MMCs with TiB ₂ and Ti in first experiment and response	50
Table 3.7 Experimental matrix of micro milling of MMCs with TiB ₂ and Ti in first experiment and response	51
Table 3.8 ANOVA for surface roughness of Mg/TiB ₂ MMCs	53
Table 3.9 ANOVA for surface roughness of Mg/Ti MMCs	53
Table 4.1 Machining parameters in FE model	78
Table 4.2 Mechanical properties and materials constant in J-C model for magnesium matrix (Ulacia et al., 2011)	79
Table 4.3 Mechanical and brittle cracking properties for SiC particle.....	79
Table 4.4 Mechanical properties of aluminium matrix, SiC particles and PCD tools	93
Table 4.5 Johnson-Cook constitutive model parameters for aluminium.....	93
Table 4.6 Johnson-Cook damage parameters for aluminium.....	93
Table 4.7 Machining parameters used in both FE models	104
Table 4.8 Mechanical properties and materials constant used in J-C model for aluminium alloy	105
Table 4.9 Material properties for SiC particles	106
Table 5.1 Mechanical properties of 1.98 Vol.% Mg/Ti MMCs (Meenashisundaram and Gupta, 2014).....	120
Table 5.2 Cutting parameters for each set of experiment.....	122

Nomenclature

\overline{F}_x	Average cutting force in X direction (Normal cutting force)
\overline{F}_y	Average cutting force in Y direction (Feed cutting force)
$F_{average}$	The Root Mean Square (RMS) values of in-plane force
N	Number of flutes of end mill
K_{rc} and K_{tc}	Cutting constants contributing to shearing action
K_{rc} and K_{te}	Cutting constants contributing to the ploughing action
π	ratio of a circumference of circle to its diameter
ϕ	Tool rotation angle
ϕ_{st}	Entry angle
ϕ_{ex}	Exit angle
\overline{F}_{yc} and \overline{F}_{xc}	Slope of line functions
\overline{F}_{xe} and \overline{F}_{ye}	Offsets of line functions
n	Spindle speed
f_t	Feed per tooth
a_p	Depth of cut
R_a	Surface roughness (average)
$\beta_0, \beta_1, \beta_2,$ and β_3	Constants in regression equations
v_c	Cutting speed in m/min
V_{rem}	Removed chip volume
t_c	Cutting time
u_c	Specific cutting energy
V_B	Flank wear
D_E	Effective tool diameter
$\bar{\sigma}$	Flow stress
$\bar{\epsilon}^{pl}$	Plastic strain
$\dot{\bar{\epsilon}}^{pl}$	Plastic strain rate
$\dot{\epsilon}_0$	Reference strain rate
T	Workpiece temperature
T_{melt}	Melting temperature
T_{room}	Ambient temperature
A	Yield strength
B	Hardening modulus

C	Strain rate sensitivity coefficient
n	Hardening coefficient
m	Thermal softening coefficient
$C_0 - C_5$	Materials constants determined through experiments
ω_D	State variable
$\overline{\varepsilon}_f^{pl}$	Equivalent plastic strain at failure
p	Pressure stress
q	Mises equivalent stress
η	Stress triaxiality
$d_1 - d_5$	Fracture parameters
$\dot{\varepsilon}_0$	Reference strain rate
D	Damage parameter
C	Critical damage value
G_f	Energy required to open a unit area of crack
L	Characteristic length
$\bar{\mu}^{pl}$	Equivalent plastic displacement
σ_y	Yield strength
$\bar{\mu}_f^{pl}$	Equivalent plastic displacement at failure
d	Damage variable
t_u	Uncut chip thickness
α	Rake angle
β	Clearance angle
$\tau_{sticking}$	Friction shear stress along the sticking region
$\tau_{sliding}$	Friction shear stress along sliding region
τ_{lime}	Limiting shear stress
μ	Friction coefficient
σ_n	Normal stress distribution along the rake face
k_{chip}	Average shear flow stress in the chips

Chapter 1 Introduction

1.1 Background and motivation

With the increasing demands on the components with superior mechanical properties, pure metals and alloys hardly satisfy the strict requirements in number of extreme applications due to the relatively low elastic modulus, ductility, creep resistance and high density. Therefore, composite materials with low weight and admirable mechanical properties are attracting increasingly attention from numerous areas. In the last two decades, the metal matrix composite materials (MMCs) have been studied and widely used in plenty of industrial areas such as the aerospace, automobile, electronics and biomedical due to their superior mechanical and thermal properties.

Like all composite materials, metal matrix composites consist of two or more phases of materials with different physical and chemical properties. The strengthening mechanism such as grain reinforcement strengthening and load transfer strengthening which is attributed to addition of hard particles produce desirable properties significantly superior to either of the individual phases (Miller and Humphreys, 1991; Taya, 1991; Zong *et al.*, 2007). As one of the most commonly used composite materials, conventional MMCs (micro-MMCs), such as Aluminium-based (Al/MMCs) and Magnesium-based (Mg/MMCs) reinforced with micro-sized particles (Φ :0.1-500 μ m) provide superior mechanical properties such as high specific strength and stiffness, excellent wear and creep resistance and low coefficient of thermal expansion, which make them replacing conventional metals at various engineering applications (Wang, Chen and Lloyd, 1993; M. El-Gallab and Sklad, 1998) . Fig. 1.1 shows several specific applications demanding the high strength to weight ratio of MMCs in macro scale.

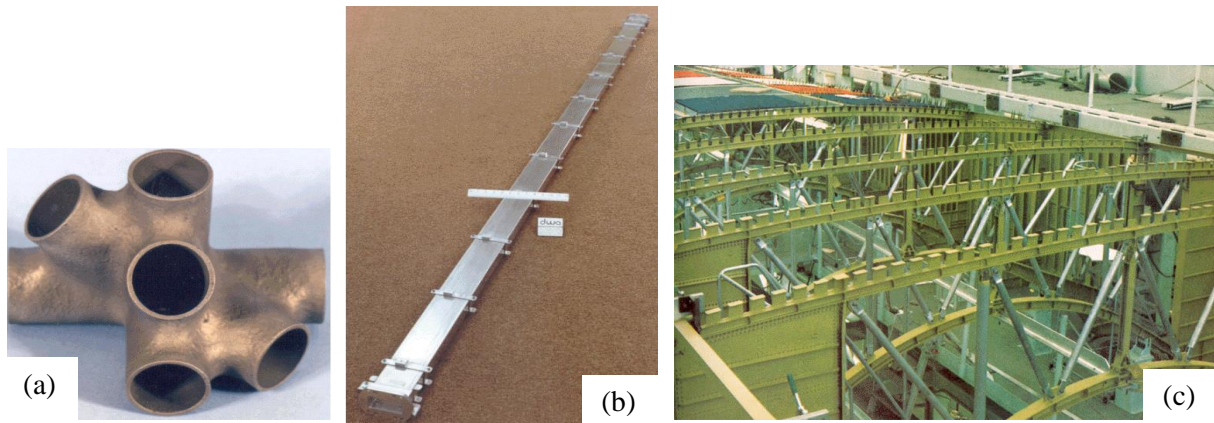


Figure 1.1 Macro scale applications of MMCs (Rawal, 2001) (a) B/Al tubular used as mid-fuselage structure of space shuttle orbiter; (b) The P100/6061 Al high-gain antenna wave guides/boom for the Hubble Space Telescope; (c) Cast SiCp/Al multi-inlet fittings for a truss node.

Normally, the improvement of ultimate tensile and yield strengths of matrix can be achieved by adding the micro-sized particles. However, some restriction of conventional micro-MMCs in specified applications are discovered due to the sacrifice in ductility caused by the large volume fraction of particles when compared to their matrix material (Ye and Liu, 2004; Mazahery, Abdizadeh and Baharvandi, 2009). In recent years, MMCs reinforced with nanoparticles (nano-MMCs) as promising materials are receiving increasing attention in both academia and industries. It is noticed that the MMCs with small volume fraction of nanoparticles are found to exhibit even better mechanical properties and temperature creep resistance than those reinforced with larger volume fraction of micro-sized particles without compromising in ductility (Gupta and Wong, 2016). Unlike the most commonly used particle size ranging from 50 to 500 μm in conventional micro-MMCs, the size of particles reinforced within nano-MMCs is usually less than 100 nm. Recently, magnesium receives increasing attention from biomedical area due to its biocompatibility, biodegradability and similar mechanical properties to human cortical bone (Staiger *et al.*, 2006; Li and Zheng, 2013). Magnesium-based nanocomposites therefore show the great potential in use for implant materials, microclips and suture wire (Gupta and Wong, 2015) due to their improved corrosion resistance

Normally, MMCs components are fabricated in near net shape process. But conventional machining process such as turning, milling and grinding is indispensable in order to achieve the high dimensional accuracy and complex shapes when compared to non-conventional machining methods such as electric discharge machining (EDM), laser beam machining (LBM) and abrasive water jet machining (ABJM). At the same time, the enhanced mechanical properties and tool-like hardness of reinforced particles make MMCs become very difficult-to-cut materials. The deteriorative machined surface finish and excessive tool wear have been

recognised as the main obstacles during machining of MMCs due to their heterogeneous and abrasive nature (Monaghan and Brazil, 1998; Ozben, Kilickap and Çakir, 2008).

The demand for miniaturised components with complex features and admirable mechanical properties in micro scale has rapidly increased in many applications such as bioengineering, aerospace, medical, and electronics in the last decade. Fig. 1.2 indicates some specific micro-scale applications which demand the miniature size and high dimensional accuracy made by MMCs. In order to satisfy such increasing demands, mechanical micro machining is recognised as one of the most versatile micro manufacturing process. With the decreasing ratio of either the uncut chip thickness or micro structure of workpiece material to the cutting edge radius, the grain size and material micro structure become the predominant factors which rise the issues such as size effect and minimum chip thickness effect during material removal process.

It is therefore believed that those aforementioned obstacles in conventional machining of MMCs will become significant in micro machining process. In addition, in the strengthening mechanism point of view, Orowan strengthening effect plays an important role in strengthening nano-MMCs, which is different to that for micro-MMCs due to the reduced particle size and volume fraction. Therefore, it is believed to make the material removal mechanism significantly different to their micro-sized counterparts. Researchers have been attracted by the development of conventional machining method on a variety of micro-MMCs materials for approximately two decades and large number of experiments and modelling related studies have been done. However, there is a gap existing in the development of micro machining on the magnesium-based MMCs reinforced with nanoparticle.

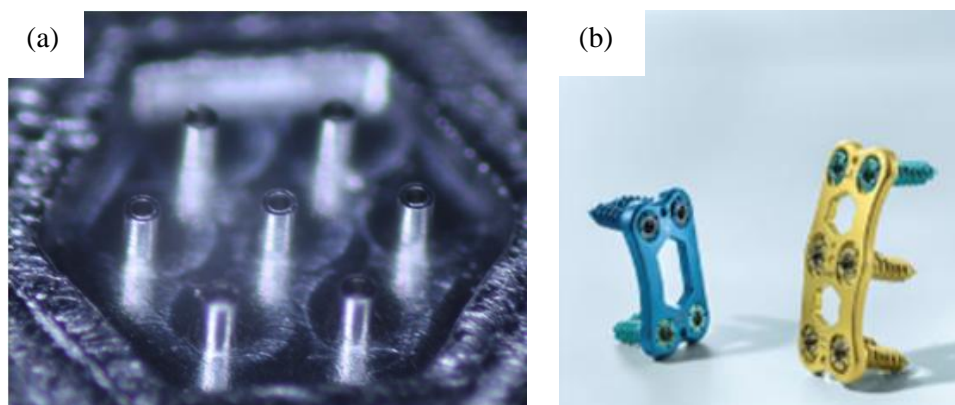


Figure 1.2 Micro-scale applications of MMCs: (a) micro machined electro spray atomizers (hole inner diameter 50 μ m fabricated in RISE lab) (Liu and China, 2011); (b) bio-implant: bone plates.

1.2 Aim and objectives

Within this study, both computational and experimental methods are carried out to comprehensively study the micro machinability of Mg-based MMCs reinforced with nanoparticles in terms of the machined surface quality, tool wear, and materials removal mechanism.

The specific objectives are set for achieving the overall aim of this PhD research:

1. To critically review the previous research on the conventional/non-conventional machining of metal matrix composites (MMCs) and establish a body of systemic knowledge and the state-of-the-art research status.
2. To investigate the effects of various types of reinforcement materials, volume fraction and cutting parameters on the machining characteristics including the surface morphology, burr formation, cutting force and specific cutting energy considering the change of micro structure within nano-MMCs.
3. To evaluate the size effect during the cutting process through both experimental and computational modelling approaches.
4. To obtain the comprehensive understanding regarding the change of cutting mechanism under various cutting condition with the tool wear progression in micro milling process. The tool-particles interaction behaviours obtained from simulation models explain the wear phenomenon observed from experiments. New wear mechanism are proposed for machining nano-MMCs.
5. To establish the finite element models to simulate the material behaviours such as tool-particles interaction, chip formation behaviours and machined surface morphology during machining of nano-MMCs and micro-MMCs in both macro and micro scale. To compare the machinability between micro and nano-MMCs in order to investigate the effect of particle size reduction on the material removal mechanism.

1.3 Scopus of this research

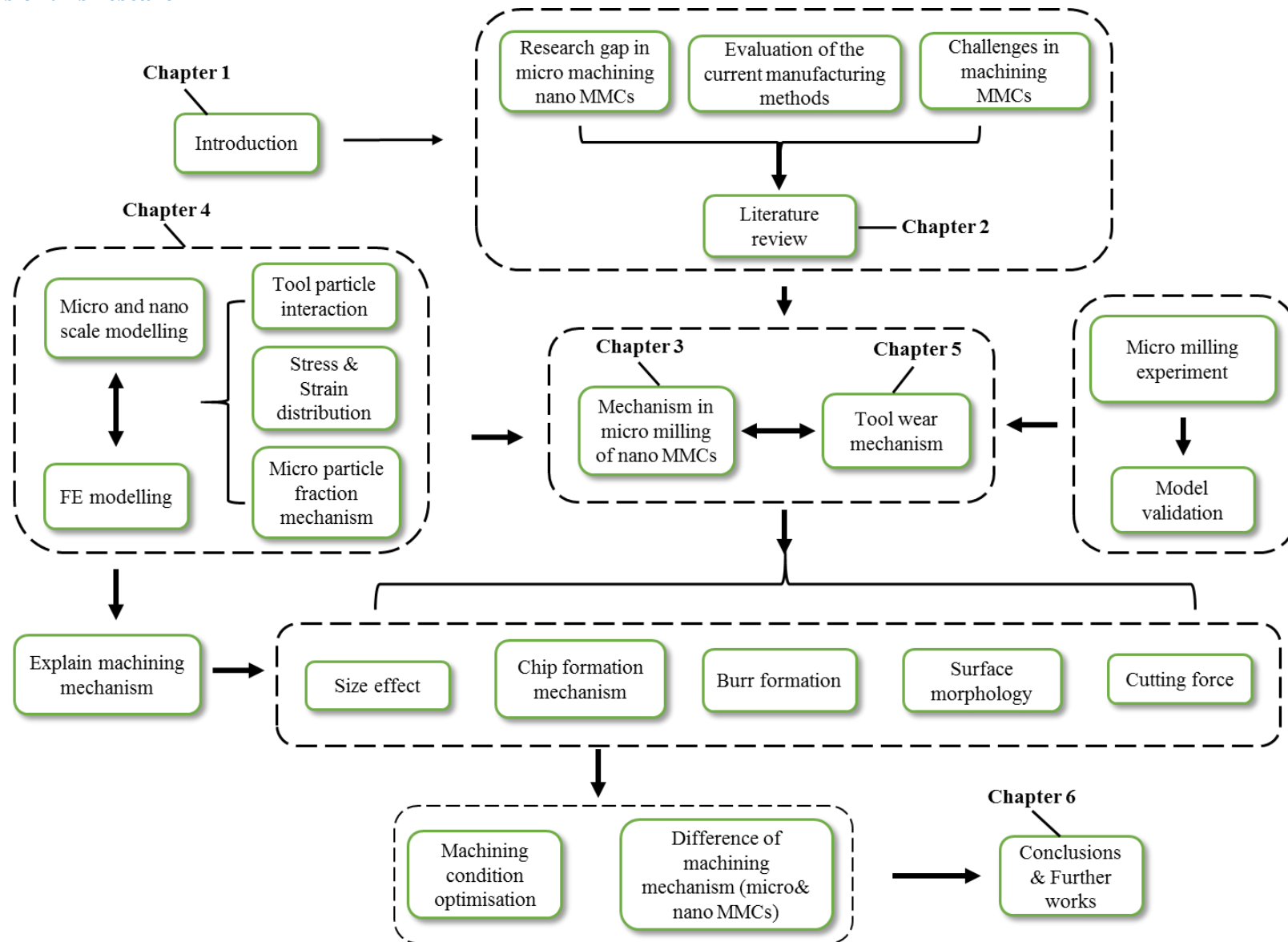


Figure 1.3 Schematic of research methodology

The schematic of research methodology is illustrated in Figure 1.3. This thesis is categorised into six chapters and the brief synopsis of reminder chapters is listed in the following:

Chapter 1 introduce the research background and motivations, and briefly review and evaluate various state-of-the-art machining method of metal matrix composites (MMCs) with consideration of scientific and technological challenges involved.

Chapter 2 presents discussion of the research background and a literature review on the aspects of micro milling technique, basic characteristics of MMCs and the machinability study of MMCs by experimental and simulation methods.

Chapter 3 comprehensively investigates the micro-machinability of Mg-based MMCs reinforced with nanoparticles (Mg/Ti, Mg/TiB₂, Mg/BN and Mg/ZnO) by conducting two individual micro milling experiments. The influence of cutting parameters on the surface morphology and cutting force was studied using Analysis of Variance (ANOVA). The specific cutting energy, surface morphology and the minimum chip thickness was obtained and characterised with the aim of examining the size effect. Moreover, the effect of reinforcement materials and volume fraction on the machinability of Mg/BN and Mg/ZnO MMCs are studied. The effect of microstructure change within MMCs workpiece due to the addition of nanoparticles is discussed by comparing with machining of pure Mg.

Chapter 4 proposes novel micromechanical finite element models to predict the behaviours of nano-MMCs and micro-MMCs during machining process (e.g. tool-particle interaction, chip formation, machined surface morphology etc.). The comparison of two types of MMCs is conducted in order to reveal the effect of significant reduced particle size from microscale to nanoscale on the machinability.

Chapter 5 investigates the tool wear mechanism in micro machining of Mg/Ti MMCs both quantitatively and qualitatively. The effect of cutting parameters on flank wear, reduction in tool diameter, cutting forces, surface roughness, and burr formation under the effect of tool wear progression is discussed.

Chapter 6 concludes this research and proposes future work in this field.

Chapter 2 Literature review

2.1 Overview of metal matrix composites (MMCs)

2.1.1 Background and characteristics of MMCs

The composite materials can be classified into polymer matrix composites (PMCs), metal matrix composites (MMCs) and ceramic matrix composites (CMCs) according to the matrix materials involved (Teti, 2002). The development of metal matrix composite materials started in the early 1960s with the aim of satisfying the need for materials with superior mechanical properties and reduced weight (Satyanarayana, 1989). In the early stages, the major applications of MMC materials were employed in aerospace engineering such as aircraft structures, missiles and space structures, but new applications were subsequently found in a wide range of areas including automotive, military, oil and gas (Teti, 2002). The form of reinforcement used can be classified as continuous fibre, discontinuous fibre (whiskers), particles, graphene or nanotubes. Some representative types of reinforcement in MMCs, as well as their aspect ratios and sizes are listed in Table 2.1. As a cost-effective and isotropic composite material, the particulate-reinforced MMCs have received close attention from both industries and academia (Chawla and Shen, 2001). Normally, the metallic materials such as aluminium, magnesium, titanium alloys and copper act as the matrix, and different metallic, intermetallic, ceramic or organic compound materials, including Cu, Ti, SiC, Al₂O₃, ZrO₂, B₄N and B₄C, act as reinforcement. Superior properties compared to the monolithic materials can be obtained, such as high strength to weight ratios, toughness, dimensional stability, and fatigue endurance and improved thermal and electrical conductivity (Shukla *et al.*, 2018).

Table 2.1 Representative reinforcements for MMCs (Chawla and Chawla, 2013)

Type	Aspect ratio	Diameter	Example
Particle	1-4	1-25 μm	SiC, Al ₂ O ₃ , BN, B ₄ C, WC
Short fibre or whisker	10-10,000	1-5 μm	C, SiC, Al ₂ O ₃
Continuous fibre	>1,000	3-150 μm	SiC, Al ₂ O ₃ , C, B, W
nanoparticles	1-4	<100nm	C, Ti, TiB ₂ , SiC, BN, ZnO
Nanotube	1,000	<100nm	C

Fabrication techniques for MMCs can be divided into two categories based on the processing phases involved namely, liquid phase and solid phase. Liquid phase techniques associated with a combination of molten metal with reinforcement during the fabrication process mainly include

squeeze and stir casting, liquid and pressure infiltration, and dispersion methods (Hashim, Looney and Hashmi, 1999; Chawla and Chawla, 2013). Solid phase techniques include powder metallurgy (PM), pressing and sintering. Casting has several advantages including near net shape, cost-effectiveness and faster rates of processing which have led it to become a widely used technique for batch manufacturing. Low processing temperature is the main advantage of the PM technique, which reduces the degree of undesired interaction between the matrix and reinforcement (Kim *et al.*, 2017).

Enhanced mechanical properties of micro-MMCs and nano-MMCs would be achieved through the activation of the main strengthening mechanisms, namely via the effect of load-bearing effect, Orowan effect, grain refinement effect, enhanced dislocation density effect, coefficients of thermal expansion effect (CTE) and/or elastic modulus (EM) mismatch effect. It is widely acknowledged that the load-bearing and CTE/EM effects play significant roles in strengthening MMCs reinforced with micro-sized particles. During the deformation process of micro-MMCs, the strengthening effect would take place where, due to its relatively large diameter and higher stiffness, the reinforcement would carry much of the load transferred from the matrix (Chawla and Shen, 2001). However, the Orowan effect is found to be the main strengthening mechanism for MMCs reinforced with nanoparticles (Yar *et al.*, 2009; Su *et al.*, 2012). The grain refinement effect is the primary mechanism for strengthening both micro- and nano-MMCs.

2.1.2 State-of-the-art of MMCs reinforced with nanoparticles

As opposed to conventional MMCs reinforced with micro-sized particles, MMCs containing nanoparticles (less than 100 nm) are very promising materials which are suitable for various functional and structural applications. As widely acknowledged, the size of particles and level of matrix-particles adhesion (Chaubey *et al.*, 2012) have a critical effect on determining mechanical properties such as failure mode, tensile strength and ductility. Large particles with diameter above 1.5 μm act as micro-concentrators of stress and thus increase the cleavage ability. Medium-sized particles (0.2-1.5 μm) generally cause the cavities through the interface. A relatively firm bonding between the matrix and nanoparticles below 0.1 μm in size could be achieved without the initiation of cavities. Accordingly, large ceramic particles reinforced within conventional MMCs were found to be easily cracked during mechanical loading, resulting in premature failure and a reduction in ductility (Tjong, 2007). Therefore, significant improvements in the mechanical performance of MMCs and reduced particle cracking could be obtained by decreasing particle size (Slipenyuk *et al.*, 2006). Researchers have found that reducing the reinforced particle size and/or matrix grains from the micrometre to nanometre

scale could further improve the mechanical properties of MMCs (Ma *et al.*, 1996; Tjong, 2000; Ferkel and Mordike, 2001). In this respect, their retention of superior mechanical properties without sacrificing ductility has led nano-MMCs to receive broad attention in recent years. Similar with conventional micro-MMCs, remarkable improvements in mechanical and physical properties of matrix materials in terms of yield strength, stiffness, wear resistance and damping properties can also be achieved through the addition of nano-reinforcement, but with less volume fraction (Poddar, Mukherjee and Sahoo, 2009).

The nanoparticles distribution uniformity within matrix is one of the key factors determining the mechanical properties of nano-MMCs. The main challenge in the fabrication process of ns is to achieve a homogeneous dispersion of nanoparticles within matrix. Nanoparticles tend to form clusters due to the low wettability within the molten metal matrix, which reduces their capability to disperse uniformly within matrix materials. The candidate matrix materials of nano-MMCs predominantly include Aluminium, Magnesium and Copper, etc. The most common reinforced particle materials are metallic and intermetallic materials and ceramic compounds.

Pure Al and its alloys are the most thoroughly investigated matrix materials for nano-MMCs. Ma *et al.* (Ma *et al.*, 1996) conducted one of the earliest studies on the fabrication of Al-based nano-MMCs reinforced with 1 Vol.% Si_3N_4 particles with diameter of 15 nm using PM technique. The ultimate tensile strength (UTS) and yield strength (YS) increased to 180MPa and 143.7 MPa compared to pure Al due to the addition of nano Si_3N_4 particles. It was found that the Al/1Vol.% Si_3N_4 (15nm) MMCs exhibit comparable UTS and higher YS when compared to that of Al/15 Vol.% SiC_p (3.5 μm). Al-based MMCs reinforced with different volume fraction of Al_2O_3 nanoparticles were fabricated by Kang *et al.* (Kang and Chan, 2004) using the PM method. The effect of nanoparticles on tensile strength and microstructure were investigated. They found that the tensile and yield strengths increase with volume fraction from 0-4% (Figure 2.1). A higher yield and tensile strengths were obtained for Al/4 Vol.% Al_2O_3 (50nm) when compared to that of Al/ 10 Vol.% SiC (10 μm). The Orowan strengthening mechanism becomes less dominant when the volume fraction of Al_2O_3 nanoparticles exceeded 4% because of the particle agglomeration. Figure 2.2 illustrates representative microstructures of pure Al reinforced with different volume fractions of Al_2O_3 nanoparticles. Particle aggregation was evident, and the size of particle clusters were approximately 100-400 nm and they increased with the particle volume fraction. The nanoparticles and clusters could pin grain boundaries, resulting in grain refinement. The grain size decreased with increasing volume fraction and then remained above 4 Vol.%. The wear behaviour of Cu/ Al_2O_3 nano-MMCs was

studied by Shehata et al. (Shehata *et al.*, 2009). An improvement in the wear resistance of the Cu matrix was found when Al_2O_3 nanoparticles were added and it increased with volume fraction. Kim et al. (Kim *et al.*, 2017) summarised the effect of matrix grain size, particle size and volume fraction on the mechanical properties of micro-MMCs and nano-MMCs. They revealed that grain refinement had a significant influence in strengthening the Al-based Nano-MMCs. The variations in mechanical properties with reinforcement type and content of Al-based nano-MMCs found in previous research are shown in Table 2.2.

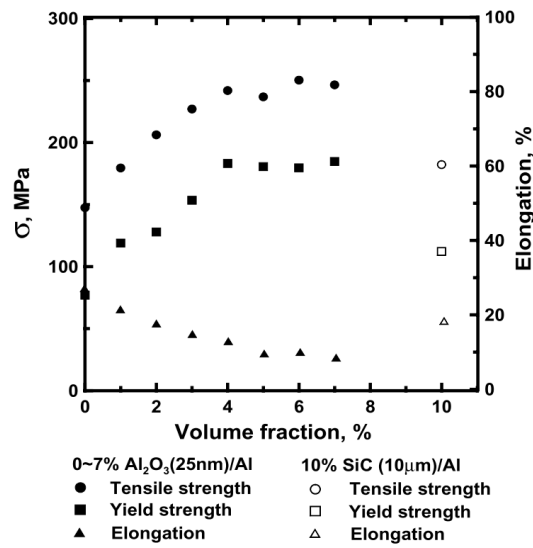


Figure 2.1 Effect of volume fraction on tensile properties of Al/MMCs. (Kang and Chan, 2004)

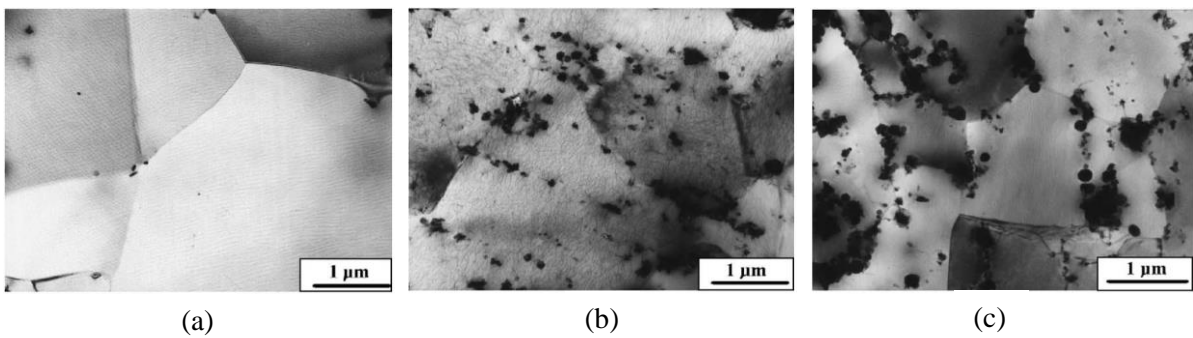


Figure 2.2 TEM images of: (a) pure aluminium; (b) Al/1 Vol.% Al_2O_3 ; (c) Al/4 Vol.% Al_2O_3 . (Kang and Chan, 2004)

Table 2.2 Reinforcement materials, particle size/ volume fraction, grain size and mechanical properties of Al-based nano-MMCs (Kim *et al.*, 2017)

Reinforcement materials	Particle volume fraction (Vol.%)	Particle size (nm)	Grain size (μm)	YS(MPa)	UTS (MPa)
SiC (Mohammad Sharifi, Karimzadeh and Enayati, 2011)	0	50	0.7	167	302
	1		0.35	207	385
	3		0.23	219	426
	5		0.17	258	436
	7		0.15	269	448
Al ₂ O ₃ (Kang and Chan, 2004)	0	50	4.6	75	150
	1		3	115	180
	2		2.3	125	210
	3		1.9	155	230
	4		1.2	180	245
	5		1.1	175	235
	6		1.2	170	250
	7		1.3	185	245
B ₄ C (Mohammad Sharifi, Karimzadeh and Enayati, 2011)		10-60			
	0		0.08	NA	NA
	5			324	371
	10			385	433
	15			420	485

2.1.3 Characterisation of Mg-based MMCs reinforced with nanoparticles

As the lightest structural metallic material, magnesium has a low density and it is approximately 34% lighter than aluminium alloy and 65% lighter than Ti alloys. Magnesium and its alloys exhibit high damping capacity, good electromagnetic shielding and good castability. With the growing demands for light weights in automotive, sports and aerospace applications, these unique features make magnesium received considerable attention. In recent years, biodegradable magnesium alloys are gaining in popularity in biomedical applications such as

orthopaedic implants because of their biocompatibility as well as strength and density similar to human cortical bone (Staiger *et al.*, 2006; Li and Zheng, 2013).

The limitations of the alloys include high corrosion rate, low ductility and poor creep and abrasive resistance, hindering applications using magnesium. These problems have been overcome by the development of magnesium-based MMCs and alloys (Gupta and Wong, 2015). Similar to other metal-based nano-MMCs, the addition of nanoparticles is found to not only improve mechanical properties but also maintain ductility (Cole, 2003; Gupta and Wong, 2016).

Ferkel and Mordike (Ferkel and Mordike, 2001) conducted the earliest research on the synthesis of the Mg/ 3 Vol.% SiC nano-MMCs using a powder metallurgical technique. The diameter of the SiC particle was 30nm, and the micro-structure and strengthening behaviour were investigated. Figure 2.3 shows the microstructure of Mg/3 Vol.% SiC nano-MMCs and a schematic diagram demonstrating the pattern of nanoparticle distribution within the Mg matrix. Grain refinement can also be observed in Mg-based nano-MMCs, and grain size is reduced with increasing volume fraction of the reinforcements (Figure 2.4).

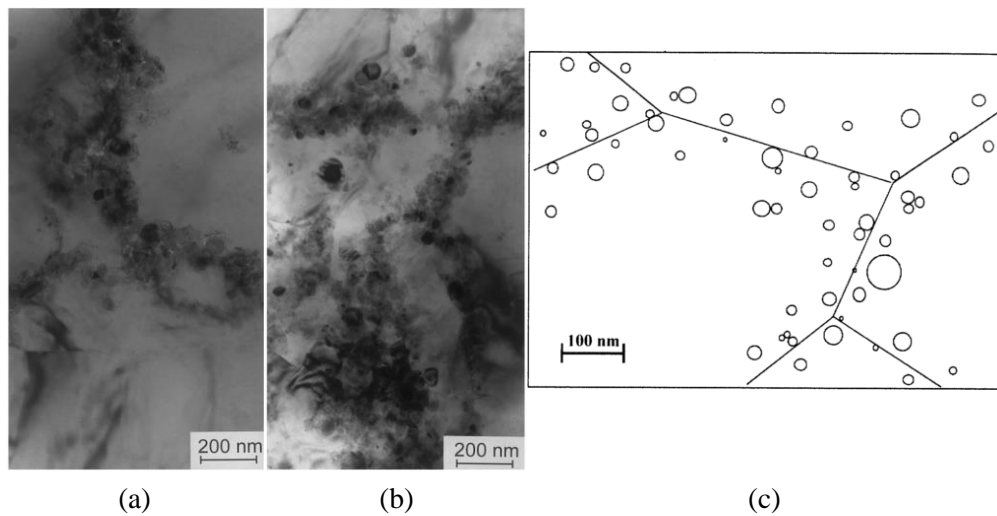


Figure 2.3 TEM micrographs of Mg/3 Vol.% SiC nano-MMCs: (a) after mixing; (b) after mixing and milling; (c) schematic diagram of nanoparticle distribution with the grain boundary of the Mg matrix.

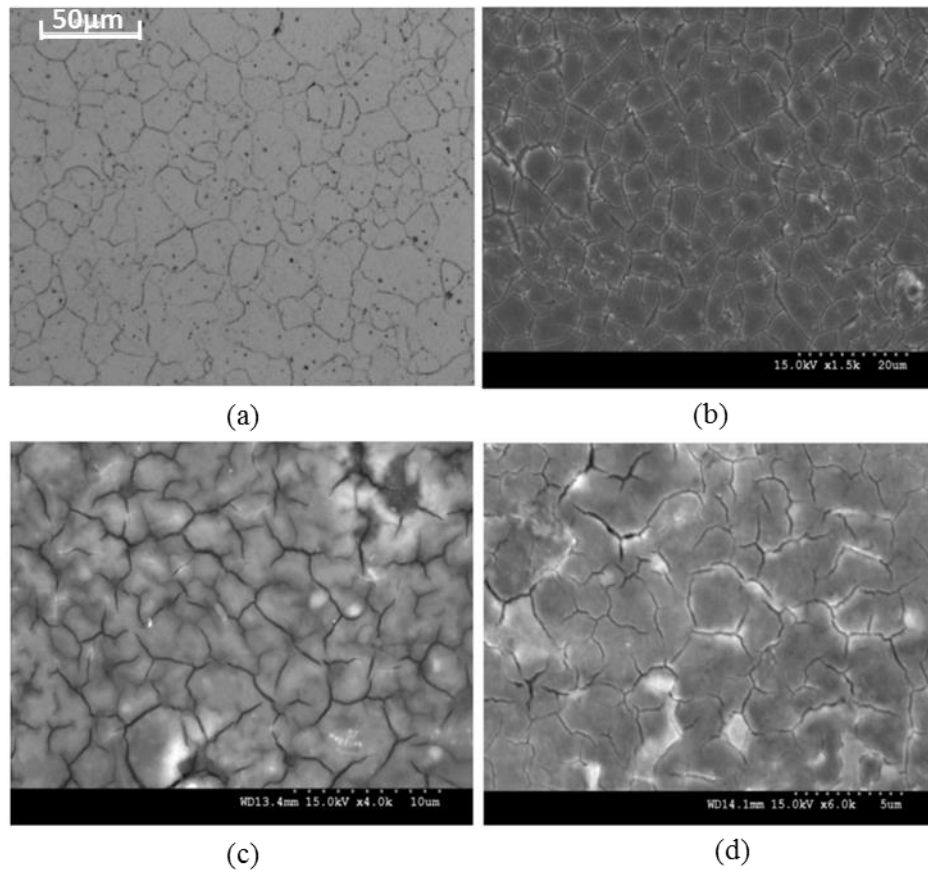


Figure 2.4 Microstructure of grain characteristic of: (a) pure magnesium; (b) Mg/0.58 Vol.% Ti; (c) Mg/0.97 Vol.% Ti; (d) Mg/1.98 Vol.% Ti. (Meenashisundaram and Gupta, 2014)

2.2 Machining of MMCs

2.2.1 Conventional machining

In order to accommodate the increasing demand for materials with a combination of light weight and high strength in various applications in precision engineering, a comprehensive understanding of the machinability of MMCs is highly desired. However, they bring significant challenges to the machining process due to the heterogeneous nature of MMCs and thus make it difficult-to-cut materials. The great tool wear and deteriorative machined surface finish can be introduced by abrasive particles with tool-like hardness. Therefore wider applications have been restricted by the difficulties associated with the machining process. Extensive research has been conducted on improving and quantifying the machinability of MMCs in terms of optimising cutting parameters, surface and sub-surface characteristics as well as the cutting tool selection etc. To achieve a cost-effective process of machining MMCs, the effects of cutting conditions such as cutting speed, feed rate, and depth of cut on the

machining characteristics of various types of MMCs have been investigated. The most important machining characteristics include cutting force, built-up edge (BUE), surface and sub-surface damage, and chip formation.

The earliest research on the machinability of aluminium alloy-based metal matrix composites reinforced with SiC particles (14 Vol.%) was conducted by Tomac et al. (Tomac, Tannessen and Rasch, 1992). They claimed that PCD tools can produce a very low cutting force as well as an excellent surface finish which is similar to that obtained from the grinding process. Moreover, segmented chip formation was obtained from machining MMCs. Also, narrow grooves caused by the ploughing of particles were observed to be typical surface defects that lead to deterioration in surface roughness.

Cutting speed and feed rate were identified as the major contributors to surface quality, cutting force and tool wear. The influence of various cutting parameters on cutting force and surface finish in turning Al/SiC MMCs was studied by Manna and Bhattacharayya (Manna and Bhattacharayya, 2003, 2005). They found that surface roughness decreases when the cutting speed increases within a specific range. High cutting speed, low feed rate and low depth of cut were suggested for achieving good surface quality.

El-Gallab and Sklad et al. (El-Gallab and Sklad, 2004) conducted a turning test on 20 Vol.% Al/SiC to investigate the effect of cutting parameters on surface quality. The pull-out PCD grains caused by tool wear were thought to be another reason causing grooves on the machined surface. Moreover, voids and cracks were induced near the particles because of plastic deformation. The voids would join up when feed rate increased causing chip segmentation. High cutting speeds were also found to reduce surface roughness. The positive effect of increasing cutting speed on surface finish has also been suggested in other research (Ozcatalbas, 2003; Palanikumar, Muthukrishnan and Hariprasad, 2008).

The specific power consumption was identified as an indicator of machinability by Muthukrishnan et al. (Muthukrishnan, Murugan and Prahlada Rao, 2008) and it was found to decrease with increasing cutting speed. Moreover, the better surface finish at high cutting speed was attributed to easier particle debonding.

Feed rate has been identified as the most significant factor influencing the cutting force and surface roughness (Manna and Bhattacharyya, 2004; Basavarajappa, Chandramohan and Davim, 2008; Muthukrishnan and Davim, 2009; Boswell *et al.*, 2017). Surface finish and integrity obtained in machining Al/SiC MMCs with different volume fractions (10 & 30 Vol.%)

were investigated by Dabade et al. (Dabade *et al.*, 2007). Their statistical analysis indicated that the feed rate was the most significant factor affecting the cutting force for both Al/30 Vol.% SiC and Al/10 Vol.% SiC, and the MMCs with higher volume fraction exhibited higher cutting force. Additionally, by increasing the feed rate, the surface roughness increased, which is similar to the conclusion obtained by Kilickap et al. (Kilickap *et al.*, 2005).

In order to reveal the mechanics and mechanism regarding the behaviour of MMCs during the cutting process, Kanna and Kishawy et al. (Kannan, Kishawy and Deiab, 2009) studied the deformation behaviour of the strain-hardened matrix materials and its relationship with cutting force during orthogonal machining. They stated that variation in average dislocation density can be characterised as one of the main factors that affects the cutting force, and it was determined by variations in the size and volume fraction of reinforcement and cutting parameters such as feed rate and cutting speed.

Many researchers have conducted investigations of the formation mechanism of built-up edge (BUE) and its effect on the machinability of MMCs in terms of surface finish and tool wear. The benefit of BUE for the machining process is still a controversial topic (Nicholls *et al.*, 2017). The BUE is caused by the melt material that builds up at tool tip, and therefore its formation is highly depended on the temperature at the tool-materials interface (Ramaswami, 1971). The occurrence of BUE is found to strongly depend on cutting speed. Kumar et al. (Kumar, Mahapatra and Jha, 2014) investigated the BUE formation during the turning of Al/4.5% Vol Cu-based MMCs reinforced with TiC particles in dry conditions. They found an almost 50% decrease in the height of BUE when cutting speed increases from 40 m/min to 120 m/min. The BUE formation under the effect of cutting parameters was studied by Manna and Bhattacharayya (Manna and Bhattacharayya, 2003). They found no BUE is formed at high cutting speed (225 m/min) and low depth of cut and it increased as increasing the depth of cut. Similar observations were obtained from a study conducted by Sahin (Sahin, 2005).

Muthukrishnan et al. (Muthukrishnan, Murugan and Prahlada Rao, 2008) studied the BUE formation in machining of Al/SiC MMCs using PCD cutting tools. The absence of BUE at high cutting speed can be attributed to the reduced adhesion characteristic due to the increased temperature. Moreover, extended tool life was obtained at a low cutting speed of 200 m/min. This can be attributed to the stable formation of BUE on the cutting edge, preventing it undergoing abrasive wear. Acting as a sacrificial layer which is constantly replenished, the BUE protected the cutting edge from abrasive wear caused by the relative motion between the tool and abrasive particles (Kannan, Kishawy and Balazinski, 2006; Pedersen and Ramulu, 2006).

However, a detrimental effect of BUE on tool life was claimed by Kadirgama et al. (Kadirgama *et al.*, 2011). They identified the built-up edge along with attrition/adhesion and oxidation as the main wear mechanism. This is because, when the BUE fall off from the tool tip, a portion of the tool material would be removed, leading to adhesion wear. The BUE wear mechanism would become more significant when the cutting tool or coating has high chemical affinity with workpiece materials.

In the respect of surface finish, it was also concluded by Muthukrishnan et al. (Muthukrishnan, Murugan and Prahlada Rao, 2008) that the formation of BUE cause the surface quality to deteriorate. This negative effect of BUE on surface finish has been verified by other researchers (Hung, Yeo and Oon, 1997; M. El-Gallab and Sklad, 1998; Ciftci, Turker and Seker, 2004a). The BUE would become unstable and fall off as the materials constantly build up. As a result, a portion of the broken BUE is smeared on the machined surface leading to a poor surface roughness.

Although plenty of studies have investigated the machinability of MMCs with micro-sized particles, very limited publications can be found on the machining of MMCs reinforced with nano-reinforcement (nano-MMCs). These researches are summarised below.

Liu (Liu, Li and Xu, 2013) conducted a micro-milling experiment on Mg-based nano-MMCs with relatively high content of SiC particles (5 Vol.%, 10 Vol.% and 15 Vol.%), and it was found that increasing SiC nano-reinforcements volume fraction improves the yield and fracture strength of MMCs and consequently results in an increased cutting force. Moreover, the cutting force profiles were not as smooth as those of pure Mg as a result of the existence of nanoparticles which influences the chip formation of Mg MMCs.

Teng et al. (Teng *et al.*, 2016) carried out an experimental investigation on the micro milling of nano-MMCs reinforced with nano-sized Ti and TiB₂ particles. Their results showed that chip adhesion effect which resulted in high cutting force and worse surface finish was more significant during machining MMCs reinforced with Ti particles compared to that with TiB₂ particles. Additionally, the increased volume fraction of reinforcement could lead to severe coating peeling off when coated tools were used.

El-Kady et al (Y. El-Kady, 2015) conducted a turning experiment on Al-based nano-MMCs with nano SiC particles. They found that, by increasing the content of SiC particles from 1wt.% to 5wt.%, surface finish improvement occurs and the cutting force is increased due to the increase in hardness. Moreover, the surface roughness decreased with increasing cutting speed.

This phenomenon is similar to that observed in the machining micro-sized particle reinforced MMCs.

The machining characteristics of the Al and Al-Si alloys (LM6 and LM25) and Al/Al-Si-based nano-MMCs reinforced with carbon nano tube were investigated by Gangadharan et al. (Gangadharan, Umashankar and Desai, 2011) using recurrence plots (RP) and recurrence quantification analysis (RQA) technique. Results indicated that the machinability in terms of vibration damping ability and stability of LM6 can be future improved by adding 0.5wt% CNT. The improved machinability of CNT reinforced nano-MMCs was also observed by Sasimurugan and Palanikumar (Sasimurugan and Palanikumar, 2011). They found that when compared to the ordinary hybrid Al/SiC-Al₂O₃ MMCs, the negative effect of increasing feed rate on surface finish is reduced in a large extent in machining Al/CNT- Al₂O₃ nano-MMCs.

The effect of the addition of graphite reinforcement on machining MMCs has been studied by various researchers. The negative effect of adding graphite reinforcement in Al/SiC MMCs on machined surface roughness was found by Basavarajappa et al. (Basavarajappa and Davim, 2013). This surface degradation was attributed to the voids generated on the surface caused by smearing and removal of graphite particles.

The optimization of cutting parameters in the turning of hybrid Al-based nano-MMCs reinforced with nano SiC particle and graphite was performed by Priyadarshi and Sharma (Priyadarshi and Sharma, 2016) using a response surface methodology. Positive effect of cutting speed on surface finish was also observed. Higher surface roughness could be induced at higher feed rate due to the increased heat generation. Moreover, the cutting force was significantly influenced by feed rate and depth of cut.

2.2.2 Non-conventional machining

Non-conventional machining processes such as electro discharge machining (EDM), laser beam machining (LBM) and abrasive water jet machining (AWJM) are increasingly being applied for the machining of particulate reinforced MMCs components. Some unique machining characteristic that cannot be found in conventional machining can be exhibited in non-conventional machining methods. For example, mechanical stresses, clatter and vibration problems can be eliminated by using nonconventional machining methods. However, machining the particulate-reinforced MMCs in conventional ways have been given higher priority than non-conventional machining in the last two decades, which results in a very limited understanding in the machining mechanism in non-conventional ways. Thus, further investigation of these methods is still highly desired for achieving the optimised machining

conditions and cost-efficient process with high levels of reliability and reproducibility [6]. Various material removal mechanisms such as vaporisation, melting and mechanical erosion are involved within every non-conventional machining methods, which exhibits distinct machining characteristics. The following section presents a general review on the up to date process understanding of non-conventional machining of particulate-reinforced MMCs.

2.2.2.1 Electric discharge machining (EDM)

Electrical discharge machining (EDM) is one of the most widely used non-conventional machining methods using thermal energy to manufacture geometrically complex parts made with materials which are difficult-to-cut using conventional machining process (Ho and Newman, 2003). Unlike the chips are produced through the plastic deformation of materials in conventional machining process, the materials are eroded by melting and evaporating produced by a channel of plasma between the tool and the workpiece with thermal energy. The temperature used can be as high as 20,000 °C (Ho and Newman, 2003). Although the materials mechanical properties such as hardness, toughness and strength would not be considered as the most important factors determining the material removal rate (MRR) as mechanical energy is not involved during EDM process (Benedict, 1987), the increased volume fraction of reinforced particles will still slow down the material removal rate. This can be attributed to the reduced thermal and electrical conductivity of MMCs workpiece because of the non-conductivity and high thermal resistance point of reinforced particles. During machining of MMCs, it is observed that the matrix materials are firstly removed and particles with sharp corners are still visible, indicating that the melting has not happened (Gatto and Iuliano, 1997). It can be suggested that the matrix materials are predominantly removed by melting and vaporising along with the particles detachment. In other words, the particles shield the matrix from being removed during the EDM of MMCs (Müller and Monaghan, 1997). Moreover, the interaction between particles and wire brings additional complexity to machining process. Pramanik (Pramanik, 2014) proposed three scenarios (Figure 2.5) based on the relative location of particle to the path of the wire. In the first, particles are fully located within wire path, secondly particles are partly embedded within solid material and partly within the projection of wire diameter, thirdly, particles are partly embedded in solid material and partly in melted material. In the first case where the particle is fully located within wire path, when the particle comes into contact with the wire, the matrix materials behind it would be the last portion to be melted and vaporized after the material located at the side and front of particle before the particle detachment happens. Thus the direct contact between the particle and wire causes scratch mark which is one of the main reason causing the wire failure (Hwa Yan *et al.*, 2005). Moreover, abnormal arcing is

more likely to be induced due to the conductive path formed between the electrodes. When the detached particle traps a certain amount of molten droplets of matrix material, a conductive path would be formed under inadequate flushing conditions (Müller and Monaghan, 2000). In the case where the particles lie partly within the projection of the wire diameter, the particles staying in the wire path will interact with the wire which contributes to the tool failure. The particles partly located in the melted material will be exposed to the machined surface after the wire has passed. The diffusion of Si element can be induced at the extremely high temperatures generated during the EDM process (Hwa Yan *et al.*, 2005). As mentioned earlier, the materials are removed mainly by melting and evaporating in a channel of plasma at extremely high temperature. The main materials removal process takes place during the interruptions of the discharge. Within this process, small amounts of melted materials are re-solidified at a high rate due to the flushing by the dielectric. Consequently, a re-cast layer is formed (Rozenek, Kozak and Da, 2001). Figure 2.6 shows the microstructure of the re-cast layer obtained from the EDM of Al/SiC MMCs conducted by Muller (Müller and Monaghan, 1997). The white spots observed in the unaffected bulk of materials disappear in the re-cast layer. An EDS-XR analysis was conducted on the white spots observed in the scanning electron microscopy images, and revealed that they comprise of higher percentages of copper, iron and nickel element. Above all, it can be assumed that the iron, copper and nickel element diffuse into the aluminium within the re-cast layer which results in homogenised alloy structure during the melting and re-solidification process at discharge channel. The effect of reinforced particles in promoting the formation of the re-cast layer can be revealed by comparing with the non-reinforced machined surface microstructure where no distinct re-cast layer can be observed. As the shielding effect caused by reinforced particles slows down the removal efficiency, less of the material is superheated and melted. Also, the intact particles which have not melted during the machining process increase the viscosity of melt matrix materials. Only small amounts of molten materials are therefore flushed away by the electrolyte during the interruptions of the discharge, which results in a significant re-cast layer.

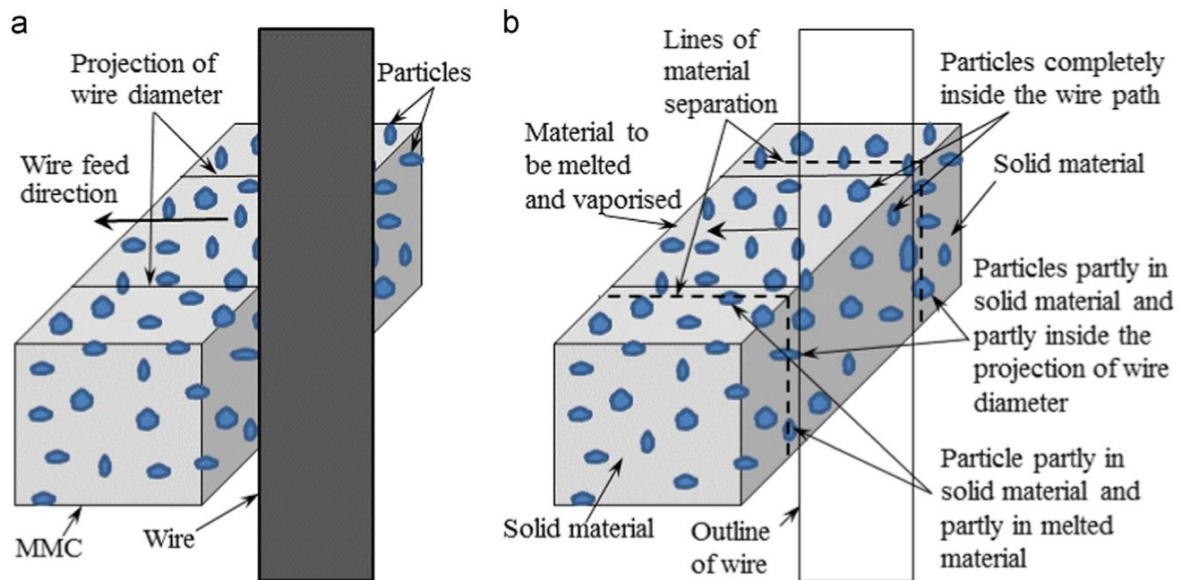


Figure 2.5 (a) Typical wire EDM process of particulate reinforced MMCs; (b) three scenarios based on the relative location of particle to path of wire. (Pramanik, 2014)

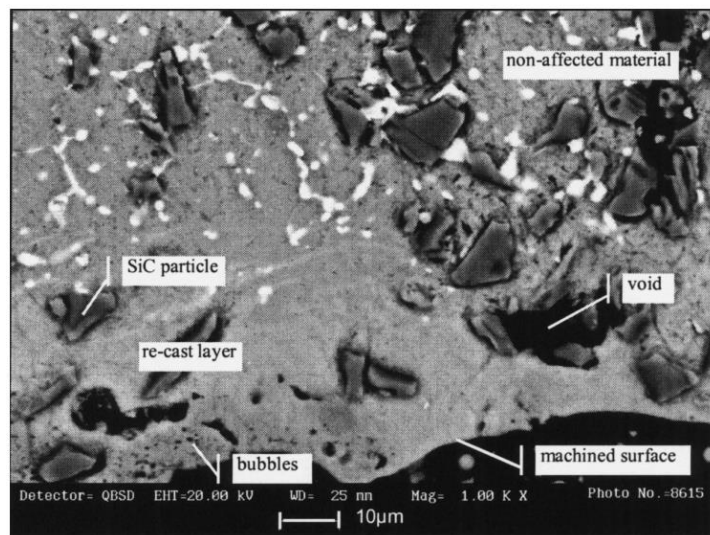


Figure 2.6 SEM micrograph of the re-cast layer of aluminium MMCs reinforced with SiC particles (AA2618Al/SiC). (Müller and Monaghan, 1997)

Random voids and micro craters generated on the re-cast layer are considered as the main characteristics contributing to the deteriorated surface quality obtained from the EDM process. They are thought to be related to the random spark discharge between electrodes. The formation of such surface defects can be attributed to the imperfect joining of the molten aluminium droplets and the porosity produced by gas bubble generated during the re-solidification process. As the optimisation of cutting parameters is always vital in experimental planning to achieve the cost-efficient process, researchers have conducted various EDM experiments to understand the effect of cutting parameters on surface roughness and removal rate and the underlying

mechanisms of different particulate-reinforced MMCs (micro-sized particle reinforced MMCs; Hybrid MMCs; nanoparticles reinforced MMCs).

Many researchers have indicated that surface roughness and material removal rate can be greatly affected by the discharge current and pulse-on time (Müller and Monaghan, 2000; Rozenek, Kozak and Da, 2001; Mahdavinejad and Mahdavinejad, 2005). The size of craters on the machined surface is mainly associated with the discharged energy which is a function of gap voltage, current and pulse-on time (Müller and Monaghan, 2000). One of the earliest studies conducted by Muller (Müller and Monaghan, 2000) reported that the surface roughness would increase with the discharge current and elongating pulse-on time (Figure 2.7). Higher current and longer pulse-on time caused a larger thermal loading and consequently larger amount of materials were melt and removed. Thus a larger crater size namely rougher surface finish was obtained. It is also interesting to note from Figure 2.7 that, Al-based alloy exhibited higher surface roughness than that of particulate-reinforced MMCs at the same conditions. This can be explained in terms of the reduced materials removal rate for particulate-reinforced MMCs. It can be thought that the presence of particles shared portion of energy of spark and thus less of the material was superheated which in turn reduces the crater size.

Similar results were obtained from experiments conducted by Rozenek et.al (Rozenek, Kozak and Da, 2001). The effect of current and voltage on the surface roughness when machining AlSi7Mg alloy reinforced with 20 Vol.% Al_2O_3 was studied, and it was found that with increases in either the pulse-on time, discharge current or voltage, the surface roughness would be increased to different extent. Among these three parameters, voltage contributed to the least changes in surface roughness. The materials removal rate was found to increase with the current at different pulse-on time (Figure 2.8). A higher pulse-on time resulted in an increased removal rate. Furthermore, different types of reinforcement material was another factor affecting the removal rate, where MMCs reinforced with SiC particles produced a faster removal rate compared to Al_2O_3 particles.

Mahdavinejad (Mahdavinejad and Mahdavinejad, 2005) found that increasing the pulse-on time when machining WC-CO composites would increase the instability of EDM process when using die sinking machines. A re-cast layer with cracks generating a rougher surface was developed which can be attributed to the increased amount of material being melted and recast.

Great tool wear at higher peak current and pulse-on time was found by Seo (Seo, Kim and Ramulu, 2006) during the EDM of SiCp/Al MMC. They proposed an optimal combination of peak current and pulse-on time which produce the maximum material removal rate.

An optimisation of WEDM parameters for Al/SiC particulate reinforced MMCs was conducted by Fard et al. (Fard, Afza and Teimouri, 2013) applying an adaptive neuro-fuzzy inference system (ANFIS). The machining experiments were designed using Taguchi's orthogonal array to reveal the effect of input parameters on the cutting velocity and surface roughness. Similarly, the authors also reported that discharge current and pulse-on time are the most significant factors contributing to the surface roughness according to the ANOVA and this was also confirmed by Gopalakannan (Gopalakannan, Senthilvelan and Ranganathan, 2013).

With the development of composite materials, metal matrix nanocomposites reinforced with nanoparticle or hybrid MMCs reinforced with carbon nano tubes (CNTs) have received increasing attention in different areas. Accordingly, the research into the EDM process on such nanocomposites has been conducted (Ponappa *et al.*, 2010; Gopalakannan and Senthilvelan, 2013). However, only a limited number of publication can be found.

Ponappa et al. (Ponappa *et al.*, 2010) optimised the cutting parameters (pulse-on time, pulse-off time, voltage gap and servo speed) in the EDM of Mg-based MMCs reinforced with alumina nanoparticles. Servo speed and pulse-on time were observed as the vital factors for surface roughness according to the ANOVA, which is in agreement with research on MMCs reinforced with micro-sized particles. The recast layer was minimised to 18µm.

An experimental study of the EDM of Al-based MMCs reinforced with B₄C nanoparticles using a response surface methodology was conducted by Gopalakannan et al. (Gopalakannan and Senthilvelan, 2013). Pulse current and pulse-on time showed the largest statistical significance on both electrode wear rate and surface roughness. Pulse-on time and current were considered as two important factors affecting material removal rate. Furthermore, an optimised combination of parameters was proposed to minimise the electrode wear rate and surface roughness.

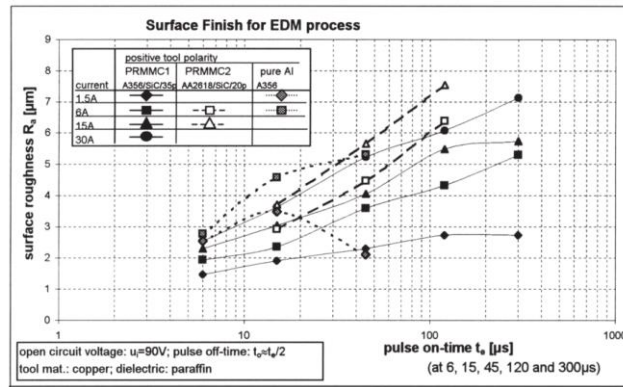


Figure 2.7 Effect of discharge current and pulse-on time on surface roughness when EDM of AA2618Al/SiC, A356Al/SiC and pure A356 Al. (Müller and Monaghan, 2000)

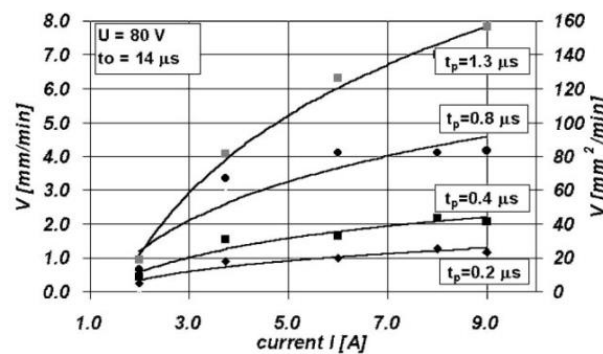


Figure 2.8 Effect of current on the material removal rate when machining AlSi7Mg with 20 vol.% SiC at different pulse-on times. (Rozenek, Kozak and Da, 2001)

Overall, although vibration and chatter is eliminated because of the non-contact nature of EDM, the heat affected zone and re-cast layer containing micro cracks and random voids can be found on machined surface due to the high energy of discharge deteriorates the surface finish and dimensional accuracy. Currently, the research on this method is mainly focused on the optimisation of process parameters. But the surface roughness is still difficult to reach to nano-meter level which can be easily obtained from conventional machining method. Therefore surface quality has been recognised as the main limitation for EDM machining of MMCs.

2.2.2.2 Laser beam machining (LBM)

Conventional machining using diamond cutting tools is costly and technically difficult, and electrical discharge machining is relatively slow. Therefore laser beam machining method has been considered as one of the alternatives to process the difficult-to-cut materials in the sheet form (Müller and Monaghan, 1997). The material removal rate in laser beam machining mainly depends on thermal conductivity and partly on optical properties. Thus mechanical properties of the workpiece such as hardness, elasticity, and ductility which play predominated role in conventional machining process can be ignored in the laser machining process. The stages of

material removal process in laser machining are firstly melting, vaporising and chemical degradation, then the removal of transformed materials by high-pressure inert gas jet and finally cooling down (Dubey and Yadava, 2008; Pramanik, 2014).

Striations are one of the typical surface characteristics produced from LBM and it is mainly caused by side way burning (Müller and Monaghan, 1997). The effect of the addition of reinforced particles on the striations formation in LBM was observed by Muller (Müller and Monaghan, 1997). A comparison of the surface morphology obtained from the LBM of non-reinforced aluminium alloy and particulate reinforced MMCs with SiC particles are shown in Figure 2.9. They reported that a smoother surface with striations was obtained with A2618/SiC particulate-reinforced MMCs compared to non-reinforced Al alloy. It was concluded that the presence of SiC particles increases the viscosity of molten aluminium, thus preventing the formation of striations. In addition, the sub-surface layer damage occurred due to excessive heating (Figure 2.10). An EDS analysis was performed on the damaged area revealing that copper and zinc were deposited along the aluminium grain boundary. Increasing feed rate would decrease the depth of the damaged area but increase the surface roughens as the cutting process tends to be intermittent (Lau, Lee and Pang, 1990).

The micro structural changes at the surface and sub-surface were also characterised by Hong et al. (Hong, Vilar and Youming, 1997). Al_4C_3 / Al_4SiC_3 plat/needle-like phases in the machined surface caused by the chemical reaction between Si and Al were observed based on the dissolution-recrystallization mechanism (Viala, Fortier and Bouix, 1990). The size of the plat/needle phase was found to increase from the top of the kerf downward (from 3-5 μm to 10-20 μm). The grain refinement occurred during the solidification process. The damaged sub-surface was divided into three distinct zones based on the morphology of particles and the plate-like phase. In addition, in the laser drilling of blind holes, the extent of damaged sub-surface layer would significantly increase due to the inefficient removal of molten materials (Pramanik, 2014).

Sharma et al. (Sharma and Kumar, 2018b) statistically studied the quality characteristics of the laser cutting of Al/SiC particulate-reinforced MMCs. They claimed that the cutting speed, volume fraction of SiC particles and arc radius are the most significant parameters determining the kerf width and dross height.

The optimal input parameters for producing the maximum material removal rate and minimising the taper in ytterbium fibre laser drilling of Al/ Al_2O_3 MMCs was obtained by

Ghosal et al. (Ghosal and Manna, 2013) using RSM. The mathematical models were developed for the evaluation of material removal rate and taper angle.

Another experimental study of the thermal effect of SiC particles on surface roughness and kerf deviation in the laser machining of Al2025/SiC was conducted by Sharma et al. (Sharma and Kumar, 2016). The formation of Al_4C_3 was again observed at the cut kerf area due to the large amount of heat produced from machining process causing the breakdown of SiC particles. The formation of Al_4C_3 compounds tended to weaken the bonds between particle-matrix phases which in turn causes the voids and cracks in the microstructure and thus the cut edge quality deteriorated. As a result, the surface quality was found to increase with the increasing content of SiC particles.

Later on, the output characteristics in the laser machining of particulate-reinforced MMCs with various particle materials (SiC, Al_2O_3 , and ZrO_2) were compared by Sharma et al. (Sharma and Kumar, 2018a). A higher rates of crack formation could be observed in Al/ ZrO_2 compared to other particulate reinforced MMCs. Furthermore, the lowest values of dross height and kerf deviation were found in the cutting of Al/SiC and Al/ ZrO_2 particulate reinforced MMCs respectively. The above phenomena can be explained in terms of the agglomeration of particles due to the wetting effect.

As mentioned above, similar to EDM method the relatively poor surface quality resulting from laser beam machining compared to the conventional machining method is considered as the main factor hindering its wide application in processing components with strict requirements for surface finish. The problem is due to its thermally based nature of process, where the surface roughness is usually related to the surface damage characteristics such as striations, dross attachment to the bottom of the cut, and heat-affected sub-surface damage during the laser machining process. Also, its inability to produce complex 3D features is another limitation. At the present time, only limited research can be found concerning the laser machining of particulate-reinforced MMCs. Most researchers focus on the optimisation of cutting parameters using statistical methods. However, research on the laser machining of nano-particles reinforced MMCs is still lacking.

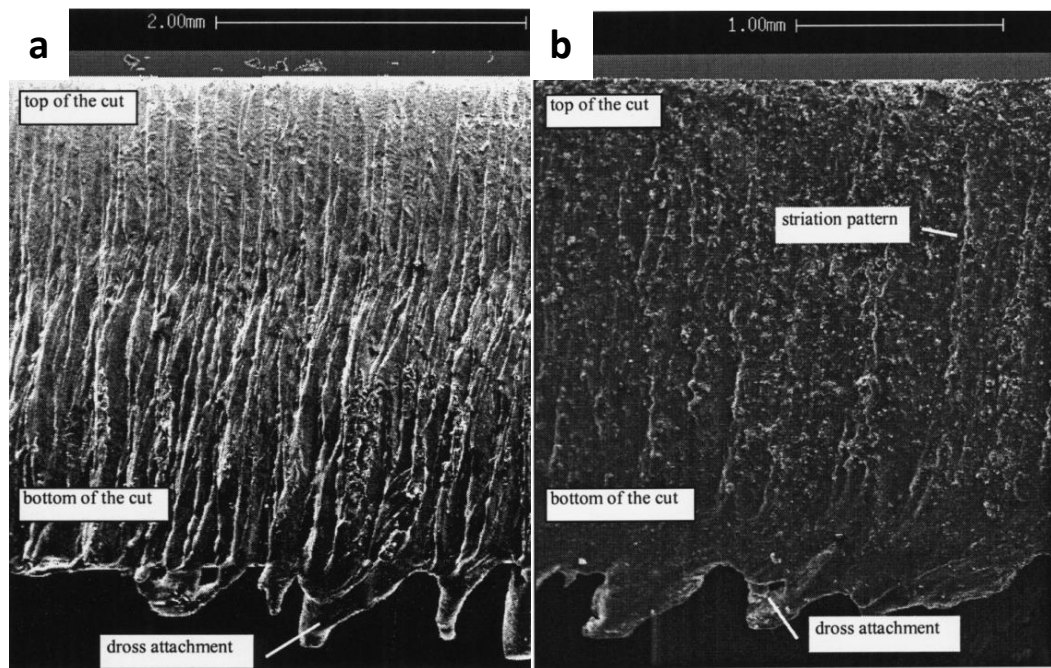


Figure 2.9 Surface morphology obtained from the LBM of (a) aluminium alloy; (b) AA2618/SiC particulate reinforced MMCs. (Müller and Monaghan, 1997)

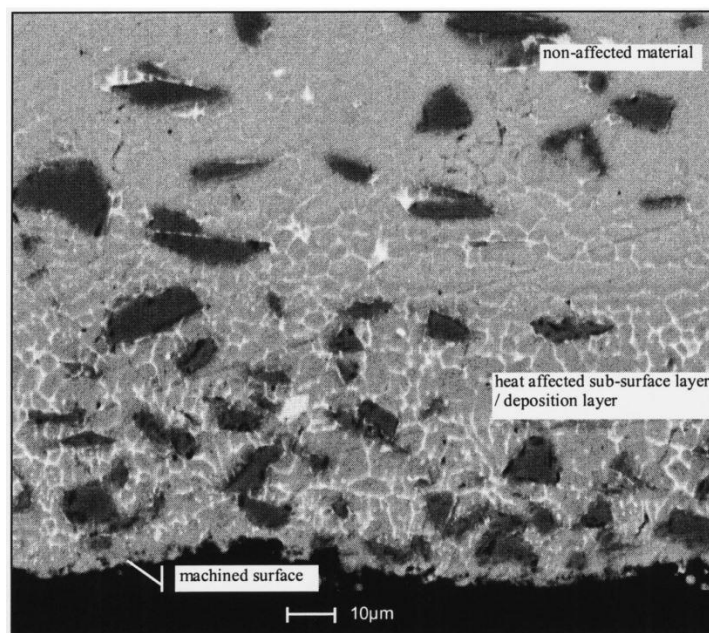


Figure 2.10 Damage to sub-surface layer caused by excessive heating. (Müller and Monaghan, 1997)

2.2.2.3 Abrasive water jet machining (AWJ)

The absence of thermal effect and relatively highly efficient material removal process have been recognised as the main advantages of abrasive water jet machining (AWJM) compared to EDM and LBM (Müller and Monaghan, 1997). The material is eroded by the impact of high speed abrasive water jet by means of plastic deformation without melting, wrapping or

distorting. (Müller and Monaghan, 2000; Srivastava *et al.*, 2017). The application of AWJ can be found not only in the contour cutting of sheet materials, but also in other machining methods such as turning, milling, drilling etc. due to its versatility (Kovacevic *et al.*, 1997). It can be used in machining a wide range of difficult-to-cut and thermally sensitive materials.

The interactions between the abrasive particles in the high speed slurry and reinforced particles within the matrix significantly alters the materials removal mechanism of particulate-reinforced MMCs compared to that of homogeneous materials. Harder particles offer higher resistance to the high speed abrasive jet in machining process (Srinivas and Babu, 2012) when the size of the abrasive particles becomes comparable to that of the reinforced particles. The size of particles plays a significant role in processing particulate-reinforced MMCs. Pramanik (Pramanik, 2014) summarised three scenarios based on the size of abrasive particles, namely where they are larger, similar to or smaller than the reinforced particles. The specific behaviours of reinforced particles are predominant in affecting the machining process, namely particle fracture and pull out, indentations to the matrix and being progressively removed in the three cases respectively. In other words, the ability of abrasive particles to remove the reinforced particles from the matrix was found to decrease with decreasing of the relative size of the abrasive particles.

Piercing and slot cutting experiments were conducted by Hamatan et al. (Hamatani and Ramulu, 1990) in studying the AWJ machinability of Al/SiC particulate-reinforced MMCs. Machining performance was characterised by the kerf taper ratio and surface roughness. The kerf taper ratio was found to increase with increasing of cutting speed up to 200mm/min at every abrasive particle size (80, 100 and 150 mesh). Moreover, it was interesting to note that, with increasing abrasive particle size, the critical cutting speed to produce a slot without a taper decreased. The surface roughness would rose with increasing cutting speed. Among all the abrasive particle size, the 150 mesh generated the highest rate of change in surface roughness with cutting speed at abrasive rate of 9g/sec.

Srinivas et al. (Srinivas and Babu, 2012) studied the penetration ability of abrasive water jets on Al alloy-based MMCs reinforced with various weight fractions of SiC particles. It was found that the penetration depth increases when increasing the jet flow rate. The effect of input various parameters on the penetrability was also explained in details.

Mardi et al. (Mardi *et al.*, 2017) reported that increasing the cutting speed contributed to the grooving effect by the abrasive particles sliding over the machined surface, which was more

evident in the AWJ machining of Mg-based MMCs reinforced with Al_2O_3 nanoparticles. This was attributed to the insufficient cutting by the abrasive particles at higher speed.

A study of the surface integrity in the abrasive water jet turning of hybrid MMCs with B_4C and Al_2O_3 particles was carried out by Srivastava et al. (Srivastava *et al.*, 2017). The residual stress and micro hardness on the machined surface and sub-surface were analysed. The maximum compressive stress was found at a depth of 50 μm and then decrease with increasing the cutting speed. In addition, the formation of crack, pit and fractured reinforced particles on machined surface was observed. By increasing cutting speed, the extent of cutting traces and such defects increased and thus the surface quality deteriorated.

When compared to other two non-conventional machining methods, the absence of thermally affect zone is the unique advantages of AWJ method. However, although the AWJ provides an efficient material removal rate and capability of machining difficult-to-cut materials, high surface roughness and deteriorative surface integrity in machining MMCs are its significant limitations due to the interaction mechanism between reinforced and abrasive particles (Müller and Monaghan, 2000).

2.3 Tool wear in machining particulate-reinforced MMCs

The hard particles embedded in the matrix materials bring tremendous challenges in the machining of MMCs leading to a very short tool life. During the cutting process, hard particles separated from the substrate slide over the cutting edge during machining. The direct contact between the cutting edge and particles which act as large numbers of small cutting edges, consequently leads to severe tool wear and reductions in accuracy (Weinert and Lange, 2001). The tool wear mechanisms affecting the machining performance can be generally classified as abrasive wear, chipping on the cutting edge, fractures and fatigue as a result of both thermal and mechanical load (Weinert and Lange, 2001; Takács, Verö and Mészáros, 2003). Plenty of studies can be found regarding the tool wear modes and mechanism in the conventional machining process of MMCs.

Most researchers suggested that abrasive wear is the predominant wear mechanism in the machining of MMCs. For a given tool, matrix and reinforcement materials, the tool wear mechanism will greatly depend on the cutting conditions as well as particle size and volume fraction. Ozben et al. (Ozben, Kilickap and Çakir, 2008) studied the effect of particle volume fraction and cutting speed on the tool wear in the machining of Al/SiC MMCs with different volume fractions. TiN-coated cemented carbide tools were used. It was reported that at lower feed rate, tool wear rate would increase. This can be explained in terms of the increased contact

length between the cutting tool and the abrasive particles at lower feed rate. They also found that the lowest flank wear can be found at a low cutting speed of 50m/min, and when cutting speed is increased to 150 m/min, flank wear increases. This can be attributed to the protective behaviours of the stable formation of BUE at low cutting speed. The importance of cutting speed is especially significant when machining MMCs with coarse particles. (Yanming and Zehua, 2000) Additionally, increased particle volume fraction from 5% to 15% resulted in increased tool wear. A similar observation was made by Sahin (Sahin, 2005) where increasing either particle content or cutting speed leads to an increased tool wear when machining Al alloy-based MMCs reinforced with SiC particles. Mild abrasion and edge chipping were defined as the major wear mechanisms. Li and Seah (Li and Seah, 2001) also reported that the tool wear become severe when the particle volume fraction exceeds a threshold. An investigation of tool wear under the effect of reinforced particle size using coated and uncoated cemented was carried out by Ciftci (Ciftci, Turker and Seker, 2004b). Al/SiC MMCs with constant volume fraction of 16 % and various particle sizes of 30, 45 and 110 μm were used as specimens. Particle size was found to have a negative effect on the tool wear. This observation was supported by Kannan (Kannan, Kishawy and Balazinski, 2006).

Coated and uncoated cemented carbide, cubic boron nitride and Polycrystalline Diamond (PCD) are the major cutting tool materials used in the machinability studies of MMCs. Many studies have indicated that carbide tools generally exhibit a rapid tool wear while machining MMCs, which means that carbide tool is not an ideal cutting tool for machining such materials (Heath, 2001; Manna and Bhattacharayya, 2003; Aramcharoen *et al.*, 2008; Ozben, Kilickap and Çakir, 2008). Carbide tools were found to be suitable in economic and short time run machining for roughing operation (Hung *et al.*, 1995; Narahari, Pai and Pillai, 1999). Among these studies, carbide tools demonstrate a catastrophic failure when cutting speed exceeds 350m/min, and thus the maximum cutting speed for such tools is limited to 300m/min. Boswell *et al.* (Boswell *et al.*, 2017) determined the optimum machining parameters in machining titanium-based MMCs reinforced with 20 Vol.% B_4C using uncoated carbide tools. They concluded that the carbide tool is useful for its ability to produce a desired surface quality and its tool life is satisfactory. Hung (Hung *et al.*, 1995) *et al.* suggested to use tungsten carbide tool in roughing process and PCD tools in finishing process. Kannan *et al.* (Kannan, Kishawy and Balazinski, 2006) studied the progression of flank wear in machining of Al6061 alloy-based MMCs reinforced with SiC particles. It was concluded that low cutting speed and high feed rate can be used to maximise tool life. Ghani *et al.* (Ghani, Haron and Kasim, 2015) investigated the milling

and turning process of AlSi/AlN MMCs using carbide cutting tools. Their results showed that uniform flank wear caused by abrasion was the dominant wear mechanism.

In order to prolong the tool life, carbide tools with various ceramic coatings have been used in the machining of MMCs by many researchers. It was found by Sun et al. (Sun *et al.*, 2004) that TiNAl- coated carbide tools demonstrate a satisfactory wear resistance with the cutting speeds from 10-40m/min in the high speed milling of Al/SiC MMCs with volume fraction of 15%. Quigley et al. (O. Quigley, J. Monaghan, 1994) studied the machinability of Al/SiC MMCs in terms of surface finish and tool wear using uncoated carbide tools and TiN-coated tool. The TiN-coated tools delivered improved wear resistance but worse surface finish when compared to uncoated carbide tools. Songmene and Balazinski (Songmene and Balazinski, 1999) investigated the performance of TiCN-coated tools in terms of flank wear and tool life in the machining Al-based MMCs reinforced with different types of particle materials. As the hardness of Al₂O₃ particles, at 2100-2300HV, is lower than that of TiCN coating (3000HV), the abrasive mechanism was not observed in the machining Al/Al₂O₃ MMCs leading to the longest tool life and lowest flank wear rate. When machining the Al-based MMCs reinforced with SiC particles whose hardness is higher than TiCN coating, the cutting tool exhibited the shortest tool life and high flank wear rate. Overall, carbide tools with ceramic coating offer slight advantages in machining MMCs compared to uncoated tools. The wear resistance mainly depends on the reinforcement materials used.

The carbide cutting tools with diamond coating made by chemical vapour deposition (CVD) have been identified as one of the most suitable cutting tool for machining MMCs. By comparing with PCD, CVD diamond is harder and it presents a lower friction coefficient, higher thermal conductivity and better thermal stability. However, the main concern with CVD cutting tools is considered as the adherence between the coating and substrate carbide tool. Davim (Davim, 2002) compared the performance of CVD diamond-coated and PCD tools in the machining of A356/SiC MMCs. The time taken for flank wear becoming visible in CVD tools was 10 times faster than that in PCD. The better performance of PCD in machining MMCs compared to CVD was also confirmed by Andrews et al. (Andrewes, Feng and Lau, 2000). Kremer et al. (Kremer *et al.*, 2008) performed dry turning tests on Al/SiC MMCs using CVD diamond-coated tools. A range of relatively high cutting speed of 400-900 m/min was used. The predominant wear mechanism was found to be coating failure caused by a process where the built-up edge welded onto the coating surface is regularly scratched away by hard SiC particles. Coating failure was also investigated by Chou and Liu (Chou and Liu, 2005). They looked into the effect of cutting temperatures at the flank face of CVD cutting tools in the

machining of Al/SiC MMCs. Greater interfacial stress was induced between the coating and substrate due to the different thermal expansion, which contributed to the coating pull-out mechanism.

Very limited research has been conducted on the tool wear of tools made of cubic boron nitride (CBN) when machining MMCs (Nicholls *et al.*, 2017). Ding et al. (Ding, Liew and Liu, 2005) studied the machinability of MMCs using various types of PCBN and PCD cutting tools in machining Al-based MMCs with SiC particles of 12.8 μm and 20% volume fraction. The built-up edge was found to be significant with PCBN tools, which in turn led to increased notch wear and deteriorated surface quality. PCBN tools exhibited a shorter tool life than PCD tools.

The performance of various cutting tools including tungsten carbide, CBN and PCD in machining Al/SiC were tested by Hung et al. (Hung *et al.*, 1996). CBN and PCD tools fractured the SiC particles along their crystallographic planes, which in turn led to minimum subsurface damage. The PCD tool lasted five times longer tool life than the CBN tool while machining at a cutting speed of 6m/min, a feed rate of 0.07mm/rev and a depth of cut of 5mm.

Ciftci et al. (Ciftci, Turker and Seker, 2004a) studied the effect of particle size on cutting performance of CBN tools while turning Al/SiC. Tool fracture as well as abrasive and adhesion wear were identified as the primary wear mechanisms at particle sizes of 110 μm and 30 μm . It was concluded that CBN tool is not suitable for cutting MMCs with the larger particles (110 μm).

Among those tools made from different materials, PCD cutting tools are the most preferred due to their an acceptable life compared to others (Lin, Bhattacharyya and Lane, 1995; M El-Gallab and Sklad, 1998; El-Gallab and Sklad, 2000; Yanming and Zehua, 2000). This can be attributed to the low friction coefficient of PCD and its low chemical affinity with workpiece materials as well as the fact that the hardness of PCD tools is greater than most commonly used particle materials such as SiC and Al_2O_3 (Paulo Davim and Monteiro Baptista, 2000; Davim, 2002). These unique features make it an ideal tool material for the machining of MMCs.

Muguthu et al. (Muguthu, Dong and Ikua, 2013) found that PCD tools exhibited lower power consumption and higher wear resistance when compared to polycrystalline cubic boron nitride (PCBN) in the turning of $\text{Al}_2\text{O}_3/\text{SiC}_p$ MMCs. While the PCD tools provided an admirable performance in machining of MMCs, the machining cost is also significantly higher due to manufacturing costs, and thus consequently restricts their use (Lin, Bhattacharyya and Lane, 1995; M El-Gallab and Sklad, 1998; Ding, Liew and Liu, 2005).

Huang et al. (Huang *et al.*, 2012) conducted a drilling experiment on Al/SiC_p with a high volume fraction (56%). Average particle size is 60 µm. Extremely rapid flank wear was found on PCD drills, and it was concluded that the primary mechanisms include abrasive and adhesive wear. The results indicated that PCD tool is suitable for machining Al/SiC_p MMCs with high volume fractions and large particle size.

An abrasive wear mechanism was identified in earlier work conducted by Tomac and Tonnessen (Tomac, Tannessen and Rasch, 1992). The results obtained from their research showed that the PCD tool exhibits over 30 times longer tool life than the carbide tool with the same cutting parameters. El-Gallab and Smlad (M El-Gallab and Sklad, 1998) machined Al/SiC MMCs using PCD tools and found abrasion to be the main wear mechanism, which was verified by the flank face with grooves parallel to the chip flow direction. They attributed the formation of grooves to the following three reasons: 1) Aluminium seizure and the pull-out process of PCD grains, 2) formation of Al₂O₃ on the cutting edge, 3) SiC abrasive particles.

2.4 Overview of the micro machining process

2.4.1 General review of the micro machining process

In order to meet the increasing demand for micro components with high precision features and complex shapes in areas such as electronics, medicine, optics and biotechnology, increasing attention has been paid to the development of micro manufacturing technology. Based on the various geometric and functional requirements of micro components, the micro manufacturing technologies can be classified into two categories, namely MEMS-based and non-MEMS-based processes. MEMS micro manufacturing techniques are lithography-based and are normally used to fabricate the MEMS devices such as micro sensors, micro actuators, transducers and other microelectronics products using silicon as the substrate material. Although it is capable of achieving a relatively high accuracy in machined products, wider application is still restricted by the limited workpiece material choices (silicon and a few metals) and the geometrical complexity involved (planar or 2.5D).

As a relatively new technique that has been developed in the past two decades, non-lithography based micro manufacturing including micro EDM, laser beam machining, micro stamping and micro mechanical cutting, *e.t.* are capable of manufacturing with wider range of workpiece materials and producing components with complex 3D shapes. Micro cutting involves a mechanical material removal process used to machine highly accurate 3D components with dimension or feature size ranging from several microns to hundreds of microns on a variety of

engineering materials including metals, polymers, glasses, ceramics and composites. The processes can be categorised as micro turning, micro milling, micro drilling, and micro grinding.

Micro milling is recognised to be one of the most flexible and versatile micro mechanical cutting processes with high accuracy, and thus it has received considerable attention in the last decade (Cheng and Huo, 2013). In order to produce micro features, micro endmills ranging from 50-1000 μm are typically used. Although micro milling is kinematically similar to its conventional counterpart, a number of issues including size effect and minimum chip thickness arise from the fact that uncut chip thickness is comparable to the cutting edge radius in micro milling (Cheng and Huo, 2013). The attainable accuracy as well as the surface quality and the integrity of products can be influenced by numerous factors such as cutting edge geometry, material micro structure and strengthening mechanisms and so on. These issues mean that the material removal mechanism in micro milling is different from that in conventional milling. These problems encountered with micro milling also limit its industrial applications.

2.4.2 Size effect and minimum chip thickness

In conventional macro milling process, the cutting edge can be assumed to be ideally sharp as the cutting edge radius is much smaller than the uncut chip thickness. In this case, the effect of cutting edge radius can be neglected and the shearing mechanism dominates the material removal process. In micro milling process, with the decreasing of uncut chip thickness dimensionally close to the same magnitude as the cutting edge radius, the effective rake angle becomes highly negative, which changes the material removal mechanism from shearing to ploughing (X. Liu, DeVor, *et al.*, 2004). In this case, the materials being ploughed off mainly undergo an elastic deformation which in turn produces a large frictional force between the cutting tool and the workpiece. As a result, the specific cutting energy (energy consumed in removing a unit volume of material) would suffer a nonlinear increase when the uncut chip thickness decreases below a certain value. This normally has a significant effect on aspects of the cutting process such as surface finish, surface integrity and tool wear. Therefore, the size effect caused by the decreasing ratio of uncut chip thickness to cutting edge radius is considered as the one of the main factors affecting the cutting mechanism in micro milling process.

In the micro cutting process, minimum chip thickness plays significant role in the chip formation mechanism. When the uncut chip thickness is less than the minimum chip thickness, chip formation does not occur. Ploughing dominates the cutting mechanism. The workpiece will fully recover to its original position as the tool passes. As the uncut chip thickness becomes close to the minimum chip thickness, the materials removal mechanism is dominated by both

shearing and ploughing. In this case, the workpiece material is removed intermittently. Thus, only a portion of the material is plastically removed and other portions recover to their original position elastically. When the uncut chip thickness is larger than the minimum chip thickness, plastic deformation governs the cutting process and chip formation occurs.

One of the earliest studies on the size effect was conducted by Yuan et.al (Yuan, Zhou and Dong, 1996). They performed an experimental investigation into the relationship between cutting edge radius and minimum chip thickness and its effects on the machined surface integrity using a diamond turning on aluminium alloys. It was found that the quality machined surface would become worse with increasing of the cutting edge radius, which is attributed to the size effect. In addition, the minimum chip thickness was determined to be in the range of 20-40% of the cutting edge radius. Moreover, varying the cutting edge radius also affected the micro hardness, residual stress and dislocation density of the machined surface.

Weule et al. (Weule, Hüntrup and Tritschler, 2001) proposed the existence of the minimum chip thickness and verified its influence on the machined surface quality in the micro milling of SAE 1045 steel. Assessment of the saw-tooth-like machined surface profile verified the effect of minimum chip thickness (Figure 2.11). Also it was recommended that the homogeneity of the workpiece material is a key factor in achieving stable a machining process.

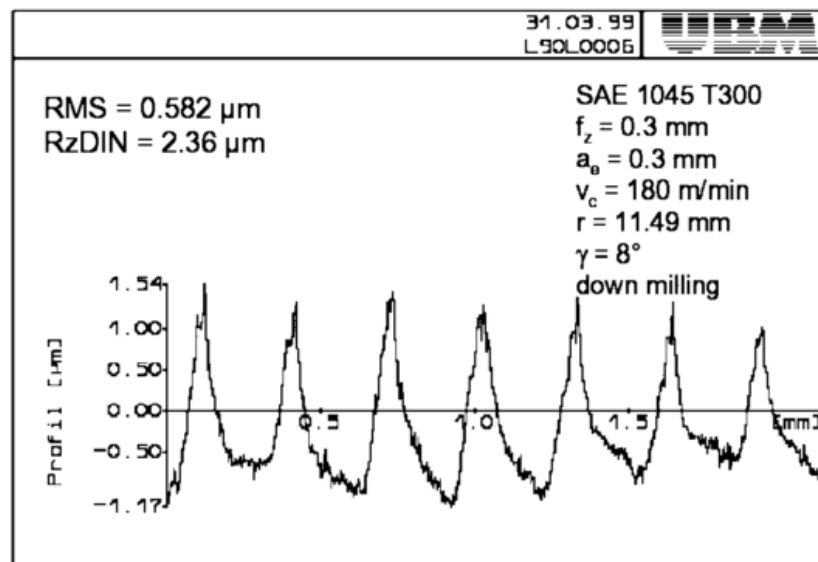


Figure 2.11 Saw-tooth-like machined surface profile under the effect of minimum chip thickness. (Weule, Hüntrup and Tritschler, 2001)

Bissacco et al. (Bissacco, Hansen and De Chiffre, 2006) attributed the deterioration in surface quality with lower ratio of uncut chip thickness to cutting edge radius to the accumulation of

workpiece materials on the tool and the machined surface during the machining process. Negative effect of increased cutting edge radius on the surface quality was also observed by Biermann and Kahnis (Biermann and Kahnis, 2010) while micro milling of hardened tool steel 40CrMnMo7.

Liu et al. (Liu and Melkote, 2007) further investigated the effect of edge radius on the size effect in the orthogonal micro cutting of Al5083-H116 in terms of materials deformation process. They concluded that there are two ways in which cutting edge radius influences the size effect: the first is the change in material flow patterns near the tool tip caused by shear zone expansion, and the second is the increased duration of tool-workpiece contact leading to increasing energy dissipation.

Essentially, the size effect can lead to higher cutting force, premature tool breakage, and worse machined surface quality. Therefore, it is important to determine the minimum chip thickness in order to eliminate such effects, and to select appropriate machining parameters (Goo *et al.*, 2010).

Vogler et al. (Vogler, Kapoor and DeVor, 2004) utilised a finite element (FE) model to determine the minimum chip thickness of steel workpiece with ferrite and pearlite phases. In this model, values of cutting edge radius ranging from 2-7 μm and uncut chip thickness ranging from 0.1-3 μm were selected to determine the ratio of minimum chip thickness to cutting edge radius, which varied from 14%-26% for pearlite and 29%-43% for ferrite.

Liu et al. (Xinyu Liu *et al.*, 2004; Liu, DeVor and Kapoor, 2006) established an analytical model to predict the minimum chip thickness in the micro machining process. The thermal softening and strain hardening were considered within this model. The results obtained indicated that, when the cutting speed and edge radius increase, the minimum chip thickness also increases. The ratio of minimum chip thickness to the edge radius in the machining of various materials (Al6082-T6, AISI1018 and AISI1040) was determined. Figure 2.12 illustrates the extracted surface profiles obtained from experimental validation showing the values of minimum chip thickness $t_{c\min}$.

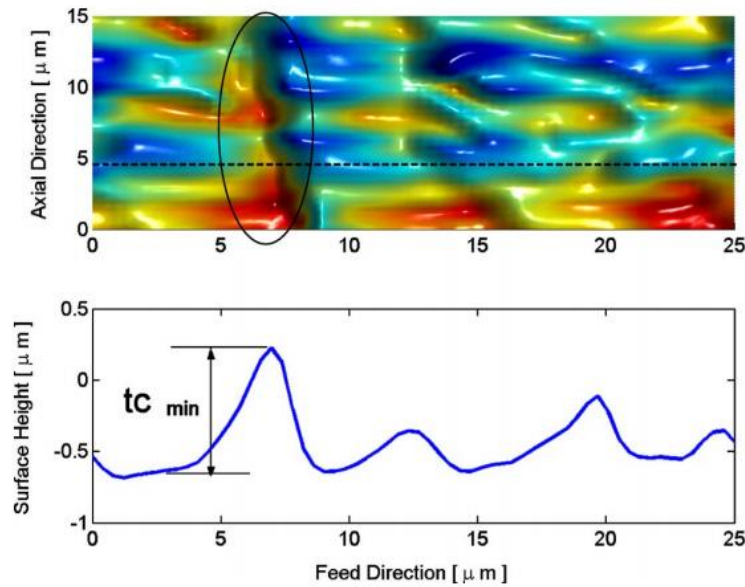


Figure 2.12 Extraction of the minimum chip thickness from the surface profile. (Liu, DeVor and Kapoor, 2006)

Aramcharoen et.al and Mativenga et.al (Aramcharoen and Mativenga, 2009) conducted a micro milling experiment on H13 hardened tool steel to investigate the size effect. The sign of the size effect was observed by studying the effect of the ratio of uncut chip thickness to tool edge radius on the specific cutting energy, surface quality and burr formation. The experimental results revealed that the best surface finish can be achieved when setting the uncut chip thickness close to the same magnitude as the cutting edge radius. By doing this, a balanced status between ploughing and shearing mechanisms occurred.

2.4.3 Microstructure effect

In the macro machining process, because the cutting edge is considered as ideally sharp, the chip formation is performed by shearing a bulk piece of material, while the workpiece is normally considered to be homogeneous and isotropic. The typical grain size of engineering materials such as steel, copper, aluminium ranges from 100 nm to 100 μm . In micro machining, the workpiece is no longer treated as homogeneous and isotropic when the uncut chip thickness or/and depth of cut become comparable in size to the micro structural characteristics such as grain size, where material deformation occurs by fracturing each individual grain as shown in Figure 2.13 (Bissacco, Hansen and De Chiffre, 2006; Lee, Mayor and Ni, 2006; Cheng and Huo, 2013). Moreover, the grain boundary effect has to be taken into account in the micro machining of single crystal materials (Cheng and Huo, 2013). In this case, the micro cutting process in terms of chip formation, cutting force characteristics and surface generation will be negatively affected (To, Lee and Chan, 1997; Lee, Mayor and Ni, 2006).

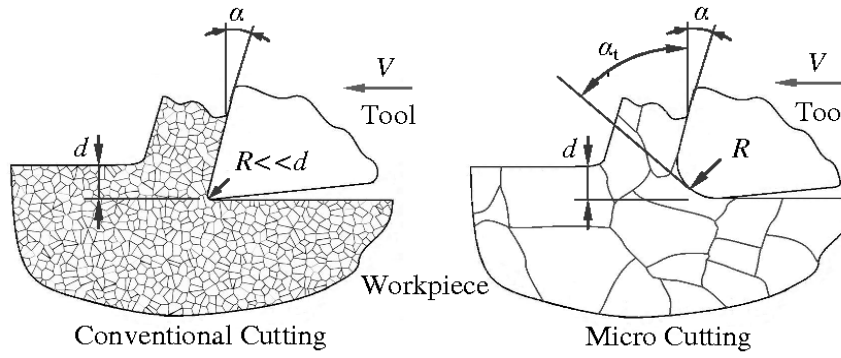


Figure 2.13 Schematic diagram of micro structure size effect in the micro machining process. (Cheng and Huo, 2013)

Much research has been conducted to investigate the effect of micro structural size effect on the micro machinability of different materials. Furukawa and Moronuki (Furukawa and Moronuki, 1988) experimentally investigated the cutting mechanism of poly-crystal, single crystal and amorphous materials and discussed cutting force with consideration of the size effect. They found that the specific cutting force varies significantly at uncut chip thickness below $3\text{ }\mu\text{m}$ and then tends to be stable at larger values. In addition, they suggested that using an uncut chip thickness which is ten times larger than grain size can eliminate the negative effect of crystallographic features on the surface finish.

The effect of a multiphase microstructure on cutting force was studied by Vogler et al. (Vogler, DeVor and Kapoor, 2003) in the slot micro milling of ferrite and pearlite single-phase and ductile iron multi-phase workpiece materials. They found that the heterogeneous microstructure of ductile iron leads to high frequency forces. In contrast, the low frequency cutting forces were observed in single phase material.

Simoneau et al. (Simoneau, Ng and M. A. Elbestawi, 2006b; Simoneau, Ng and M.A. Elbestawi, 2006; Simoneau, Ng and Elbestawi, 2007) conducted a series of experimental and simulation studies investigating the effect of various microstructure of workpiece materials on chip formation mechanism. Experimental results obtained from the micro orthogonal cutting of AISI 1045 show that a quasi-shear-extrusion chip, which is comprised of alternating layers of pearlite and ferrite, was observed when the uncut chip thickness approached to the smallest average grain size. This phenomenon indicated that these two different phases (ferrite and pearlite) govern distinct plastic deformation behaviours. (Simoneau, Ng and M.A. Elbestawi, 2006). It was also found that the varying size of microstructure features could alter the scale of cutting between micro, meso and macro (Simoneau, Ng and M. A. Elbestawi, 2006b; Simoneau, Ng

and Elbestawi, 2007). Chip and surface defect formation was illustrated by developing heterogeneous finite element (FE) models that included ferrite and pearlite phases.

The importance of the effect of materials homogeneity on machined surface integrity in micro scale has been noticed by many researchers. The effect of different grain size of Al5083 alloy on surface roughness and integrity was investigated by Popov et al. (Popov *et al.*, 2006) through micro milling experiments. By employing the equal channel angular pressing (ECAP), the workpiece was modified metallurgically and mechanically and the grain size was refined from 100-200 μm to 0.6 μm . It was found that the grain refinement and reduced anisotropy contributed to a threefold improvement in surface roughness. Similar conclusions regarding the positive effect of grain refinement on surface roughness and defects were drawn by Pham et al. (Pham *et al.*, 2009) in the micro milling of copper. Dimples were formed on the machined AISI 1045 workpiece in the research conducted by Simoneau et al. (Simoneau, Ng and M. A. Elbestawi, 2006a). This could be explained by the larger strain at the grain boundary of softer ferrite caused by the early and large absorption of cutting energy, which in turn caused a mismatch in plastic strain between the ferrite and pearlite phases. The authors also suggested that by refining the grain size, the surface quality can be improved.

The machinability of multiphase AISI 1045 that has a relatively coarse grain microstructure with average size of 10 μm was investigated by Mian et al. (Mian, Driver and Mativenga, 2009). Unlike the results obtained from other studies where grain refinement tends to improve surface quality, the surface roughness obtained at undeformed chip thickness ranging from 0.02 μm to 15 μm was lower than the grain size and surface quality did not exhibit significant deterioration at uncut chip thickness close to grain size. This improvement in surface quality can be explained in terms of grain polishing and fracture. The use of uncut chip thickness equal to the grain size was also recommended when rough micromachining of coarse-grained materials in order to minimise burr size and to maximise material removal rates.

2.4.4 Tool wear mechanism in micro machining

The size effect caused by scaling effects in micro milling play an important role in the material removal mechanism and the underlying mechanics during machining process. The size of the ploughing region where material elastically deforms and recovers to its original position after the tool passes cannot be neglected in micro milling. Consequently, high friction and stress is induced between the cutting tool and the materials which in turn makes the cutting edge the most loaded portion of micro endmills (Li *et al.*, 2011). Therefore unpredictable tool life and

the premature failure of micro endmills have been recognised as the major barriers of micro milling (Tansel *et al.*, 1998).

The flank wear is considered as the main wear criterion in conventional milling process, but it becomes less significant in micro milling process. The wear mechanisms and failure types in micro milling are diverse and complex. Additionally, tool wear measurement is challenging due to miniaturised size of endmills in micro milling. A literature survey shows that the current state-of-the-art lacks generic tool wear criteria and assessment methods in micro milling. Some attempts in investigating tool wear mechanisms in the micro milling of engineering materials are summarised below.

Tansel *et al.* (Tansel *et al.*, 1998) studied the wear mechanism of micro endmills when machining aluminium and mild steel and concluded that tool wear was mainly caused by fatigue and stress induced chip-clogging breakage. Another subsequent study (Tansel *et al.*, 2000) established a relationship between tool wear and cutting force characteristic based on a neural-network method in micro milling of aluminium and steel. A steady increase in cutting force with the progression of tool wear was observed in the machining of soft materials made of aluminium, which caused a loss in effectiveness/sharpness of the cutting edge. The wear condition could be estimated accurately by observing variation in cutting force. Conversely, a sudden increase in cutting force occurring before tool failure was induced in the machining of hard material (steel) leading to the difficulty in estimating tool wear.

Rahman *et al.* (Rahman, Senthil Kumar and Prakash, 2001) also investigated the effect of development of tool wear on cutting forces in the micro machining of pure copper using a micro grain carbide endmill. Increasing cutting speed from 35m/min to 45m/min was found to accelerate the tool wear significantly. Non-uniform wear and chip adhesion were observed on both major and minor cutting edges. This resulted in an increase of cutting forces and led to an early tool failure.

The abrasion wear which was found to be the dominant wear mode during the micro milling of copper 101 using a tungsten carbide tool was reported by Filiz *et al.* (Filiz *et al.*, 2007) (Figure 2.14). The stress acting on the cutting edge was found to dramatically increased when the material was elastically removed due to the size effect at low feed per tooth. Therefore, the greatest tool wear in the form of flank wear was experienced at the lowest feed per tooth. An improvement in tool wear was found when cutting speed increases from 40 m/min to 120 m/min at all feed per tooth, which was in contrast to results reported by Rahman *et al.* (Rahman, Senthil

Kumar and Prakash, 2001). The reduction in tool diameter was utilised as a measure of tool wear.

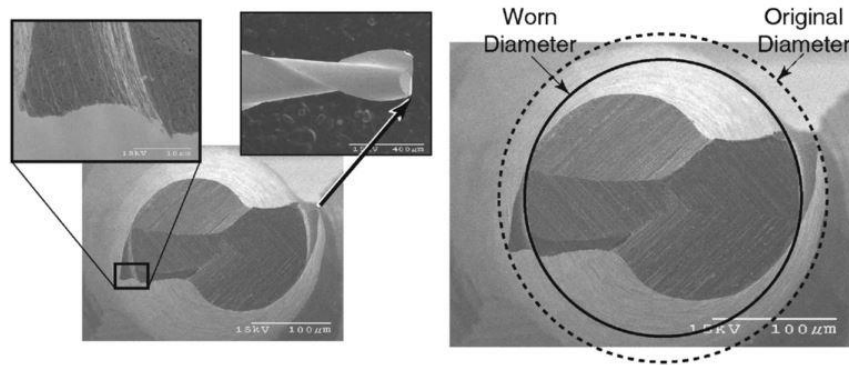


Figure 2.14 SEM images of severely worn endmill. (Filiz *et al.*, 2007)

Ucun *et al.* (Ucun, Aslantas and Bedir, 2013) compared the performance of endmills with different coatings (AlTiN, TiAl&AlCrN, AlCrN, TiAl&WC/C and DLC) during the micro milling of Inconel 718 super alloy. Effective tool diameter and cutting edge corner were measured to quantitatively define tool wear condition (Figure 2.15). Flank wear due to abrasion and chipping were reported as the dominant wear modes. Also, local fractures resulting from fatigue and burr formation were observed due to the excessive friction on a part where smeared by workpiece material, and this was dominated by the size effect at small uncut chip thickness. DLC and TiAlN&WC/C coatings exhibited better wear resistance compared to others.

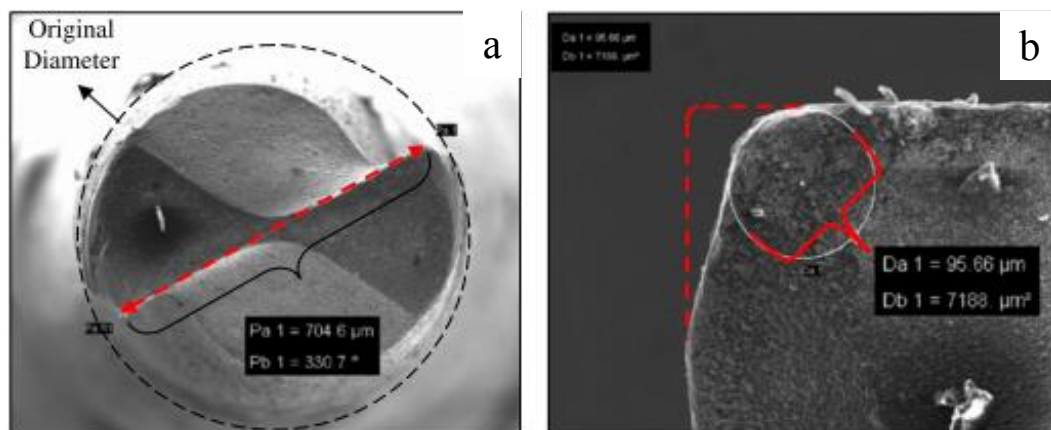


Figure 2.15 Tool wear criteria: (a) effective tool diameter; (b) cutting edge radius. (Ucun, Aslantas and Bedir, 2013)

Imran *et al.* (Imran *et al.*, 2014) stated that the abrasion was initially experienced on a TiN coated tool in wet drilling, followed by cyclic workpiece adhesion onto the cutting edge. Finally,

the micro chipping which gradually increased the edge blunting was observed near the cutting edge due to the diffusion of workpiece materials into the WC-Co binder with the assistance of adhesion effect.

Overall, previous studies have investigated tool wear mechanisms-based only on the experimental methods. Moreover, diverse wear mechanisms have been reported in the machining of different engineering materials but only a few publications have investigated wear mechanisms during the machining of MMCs reinforced with nanoparticles.

When compared to the non-conventional machining methods mentioned in previous sections, the relatively high dimensionally accuracy and the flexible and controllable nature make micro machining a promising method to produce MMCs parts with complex 3D features and high surface quality. However it is believed that the enhanced mechanical properties of MMCs would make machining process more challengeable than that in conventional machining process. Therefore, it is crucial to comprehensively understand the material removal mechanism in micro machining of nano MMCs.

2.5 Finite element modelling on machining of MMCs

2.5.1 Numerical formulation in FEM of machining process

As one of the most common numerical simulation methods, the finite element (FE) modelling technique has been widely employed in the studies of the metal machining process to give a better understanding of material removal mechanism. FE modelling have the capability of predicating the cutting force, stress, strain, temperature and chip formation during the cutting process. The particular complexities of the machining process limit the utilization of other modelling methods such as empirical and analytical modelling (Markopoulos, 2013). Firstly, the high strain rates which occurs during the cutting process leads to strain and strain rate hardening effects which playas significant roles in determining cutting performance. However, these phenomena are not considered in many analytical models. Additionally, plastic deformation and friction in the tool-workpiece contact zone could result in a rise in temperature and consequently change the mechanical properties of material. Therefore, a coupling of thermal and mechanical effects should be included in the analysis. The non-linear nature of the machining process could be accommodated using the finite element modelling method owing to its inherent characteristics.

Basically, non-linearity and large deformation were involved in the finite element modelling process of machining. Therefore, appropriate formulations are necessary to describe the relationship between the mesh and underlying workpiece materials in terms of continuum

mechanics. Three formulations have been proposed, namely Lagrangian, Eulerian and Arbitrary Lagrangian-Eulerian (ALE).

2.5.1.1 Lagrangian formulation

In the Lagrangian formulation, the mesh elements are attached to the underlying material. The position of nodes in the mesh will be changed simultaneously with the deformation of material in the machining process. In this formulation, the underlying surface can be easily tracked and the introduction of boundary conditions is simplified. An initial chip formation to a steady-state conditions can be simulated with the Lagrangian formulation. However, because of the mode of connection between materials and mesh, distortion in the mesh can occur when the material undergoes large plastic deformation, resulting in a poor results. Moreover, several strain, strain rate and temperature dependent models for the workpiece material should be applied.

2.5.1.2 Eulerian formulation

In the Eulerian formulation, the finite element mesh is fixed in space and covers a control volume. During the simulation, the variables are converged and the geometry of chips is updated by applying an iterative procedure. The material can flow through the mesh without constraint. The mesh element would not flow with the underlying materials during the deformation process which in turn avoids excessive distortion. Therefore, re-meshing and chip separation criteria are not needed with the Eulerian formulation. However, its main disadvantage is that the shape of chips in the initial stage, contact condition between tool and workpiece and the shear angle must all be known prior to starting the simulation, either from experiments or assumption.

2.5.1.3 Arbitrary Lagrangian Eulerian (ALE)

In the Arbitrary Lagrangian Eulerian formulation, the advantages of two aforementioned formulations are combined (Movahhedy, Altintas and Gadala, 2002; Arrazola and Ozel, 2008). By utilizing the ALE formulation, the nodes move arbitrarily in such a way that combines the features of both the Lagrangian and Eulerian formulations. During the simulation process, the boundary nodes flow with the material boundaries and the interior nodes move relatively with deformed underlying materials. The distortion is therefore minimised. The ALE formulation reduces the extent of the mesh-material attachment with the Lagrangian formulation while retaining the independence of the mesh in the Eulerian formulation. As a result, excessive distortion could be reduced and prior assumptions concerning the geometry of chips is not required.

2.5.2 Finite element modelling of machining particulate-reinforced MMCs

Various numerical techniques have been used to model the machining process of MMCs in the past two decades. The modelling process can be achieved at two levels, namely in macro-mechanical and micro-mechanical models. Within macro-mechanical models, MMCs are treated as macroscopically anisotropic materials without considering fundamental characteristics such as particle size, interfaces between particles and matrix, and the fracture properties of particles. On the other hand, micro-mechanical models focus on the materials' local behaviour during machining process, and thus they can predict the behaviour of particles such as debonding and fracturing during tool-particles interaction. The finite element (FE) method exhibits better capability in predicting actual machining characteristics such as the behaviour of the matrix and interactions between the cutting tool and particles, and therefore it produces more visible details about the materials removal mechanism when compared to experimental approaches. As one of the most commonly used numerical approaches, finite element modelling has received growing attention in investigating machining mechanism of MMCs in the past two decades.

Different materials removal mechanism can be found in the machining of MMCs which can be classified as follows: 1) the nucleation of voids due to debonding at the interface between particles and matrix, 2) particles failure. 3) growth and merging of voids in the matrix (Dandekar and Shin, 2012). Those unique failure mechanisms in the machining of MMCs means that their behaviour is different from that of homogeneous materials. According to numerous studies of finite element modelling on MMCs, it has been proven that various phenomena can be successfully simulated during the cutting process including: particle failure, the flow of the particles in the tool-workpiece contact zone, debonding of the reinforcement in the secondary and primary deformation zones, and tool-workpiece interaction which leads to severe and premature tool wear.

In an early attempt, Monaghan et al. (Monaghan and Brazil, 1997, 1998) conducted a numerical investigation of the micromechanics involved during the machining of A356 aluminium alloy with 35% volume fraction of SiC particulate-based MMC using FORGE2 code. They split the whole simulation process into two stages. A homogeneous material was modelled to obtain the hydrostatic pressure in the first stage, and the resultant loading output was applied in the second stage which is accomplished using ANSYS, an elastoplastic FEA code. By using pressure data from aluminium alloy simulations, the failure at the particle-matrix interface, sub-surface damage, tool wear and residual stress were studied.

Later, a transient dynamic finite element model was established by Ramesh et al. (Ramesh *et al.*, 2001) to investigate the diamond turning process of Al6061/SiCp MMCs. They studied the normal and shear stresses field in four different cases, namely tool facing/ploughing of aluminium matrix/SiC element respectively, and found that the relative position of the SiC element and cutting tool motion produced different magnitudes and patterns of stress.

Zhu and Kishawy (Zhu and Kishawy, 2005) presented a plane-strain thermo-elasto-plastic finite element model of orthogonal machining of Al6061/ Al_2O_3 MMCs (Figure 2.16). Temperature dependent material properties were incorporated into this simulation. The effective and shear stresses on reinforcements and different machining deformation zones were investigated. The interface failure model between the matrix material and particles (e.g. particle debonding) was used to explain the development of tool wear. Although reinforcement was considered in this model, detailed cutting behaviours such as tool-particles interaction and the effect of particles on the chip formation process were not simulated.

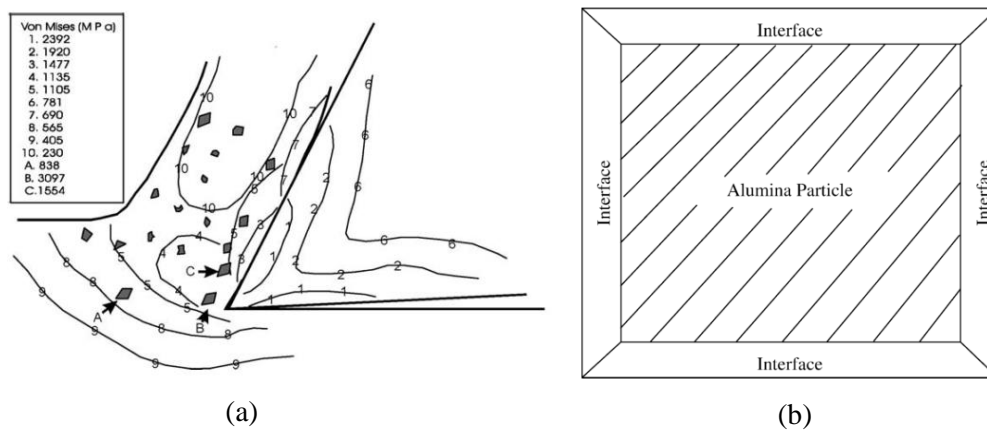


Figure 2.16 (a) Von Mises stress distribution within matrix material; (b) modelling of particle interface. (Zhu and Kishawy, 2005)

Unlike in previous research work, a more comprehensive model describing the behaviour of workpiece materials in machining was established by Pramanik et al. (Pramanik, Zhang and Arsecularatne, 2007). The interaction between particles and the cutting tool was studied through three scenarios with particles either above, along or below the cutting path (Figure 2.17). The variations in tensile and compressive stresses at the particles and the surrounding matrix as the tool advanced was investigated in these three scenarios, and were used to explain the occurrence of particles fracture and debonding from the matrix. Additionally, the machined surface was considered to be hardened owing to the indentation of particles in the machined surface caused by interaction with the cutting tool.

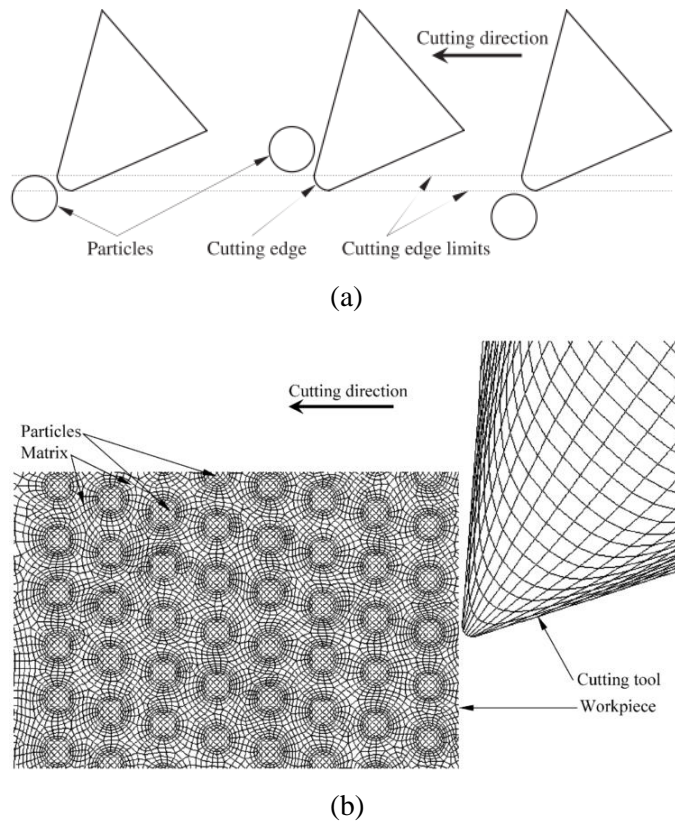


Figure 2.17 (a) Three scenarios of tool-particles interaction; (b) Schematic representation for MMCs machining simulation. [131]

Later, a multi-step 3D finite element model of production of sub-surface damage after the machining of MMCs was provided by Dandekar and Shin (Dandekar and Shin, 2009) (Figure 2.18). The cutting data obtained from the initial step using an equivalent homogenous material (EHM) model was applied to a local multi-phase model. This multi-step method provided an accurate prediction of particle fracture behaviour and the relationship between cutting force and depth of sub-surface damage.

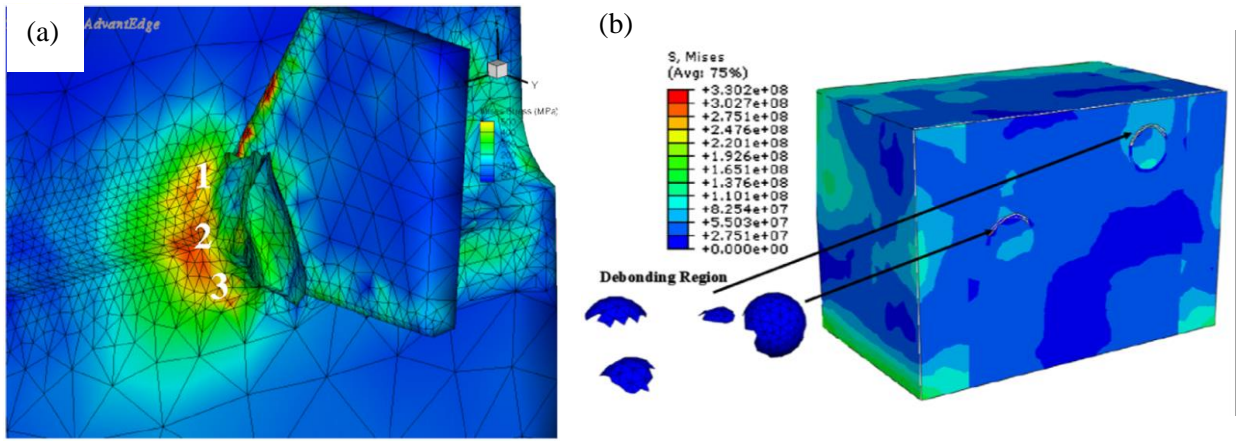


Figure 2.18 (a) Stress distribution obtained from machining EHM model; (b) sub-surface damage a depth of 40.7 μm .

Recently, Zhou et al. (Zhou *et al.*, 2011) presented a better understanding of particles removal mechanism by studying the von Mises equivalent stress distributed locally within matrix and particle phases. However, this simulation model exhibited an inability to globally simulate the chip formation process and stress/strain distribution under the effect of particles. To overcome this problem, they studied the edge defects near the exit of orthogonal cutting by creating a FE model with randomly distributed particles in later work (Zhou *et al.*, 2014). The brittle fracture of particles and plastic flow of matrix were found in the simulation process resulting in fragmented chips.

Wang et al. (Wang *et al.*, 2016) established a meso-scale FE model on milling process of Al/SiC MMCs with high volume fractions. Their research showed that the formation mechanism of machined surface defects is contributed by particles failure behaviours such as debonding, micro fracture, big cleavage and cutting through of particles.

Comparative studies were conducted by Umer et al. (Umer *et al.*, 2015) by developing the heterogeneous finite element models with and without the cohesive zone element when machining Al/SiC. They found that the model with cohesive zone element more accurately predicted cutting forces and chip morphology compared to the model without cohesive zone.

In order to obtain an in-depth understanding of the chip formation process and tool-particles interaction, Ghandehariun et al. (Ghandehariun *et al.*, 2016a, 2016b, 2017) conducted a series of comprehensive simulation studies by developing micro-mechanical models using the cohesive element method. They presented a comprehensive analysis on details of local material behaviours such as tool-particles interaction considering the effect of cutting speed by

incorporating all phases of MMCs, including the matrix, particles and the interface between matrix and particles. Moreover, plastic deformation in the machining of Al6061/Al₂O₃ MMCs was analysed using the adaptive meshing technique to avoid mesh quality deterioration. So far, in-depth investigation of machining MMCs with micro-sized particles using finite element modelling have been conducted by previous researchers, but little such research seems to have been conducted on nano-MMCs.

To fill this gap, Teng et al. (Teng *et al.*, 2018) established a two-dimensional micromechanical finite element model to simulate the micro orthogonal machining of Mg-based MMCs reinforced with nanoparticles considering the size effect. It was found that, unlike the fragmented chips obtained in the machining of MMCs with micro-sized particles, continuously formed chips with a saw tooth appearance was predominant. It is clear that the reduction in particle size could induce significant changes in the material removal mechanism.

2.6 Summary

This chapter provided a comprehensive review on the state-of-the-art machining methods of metal matrix composites with emphasis on conventional and micro machining process, and the main challenges involved in material removal process. The mechanism and suitability for machining MMCs in each machining method was evaluated. In addition, the development of MMCs and works regarding FE modelling of machining process on MMCs have also been surveyed. Some conclusions can be drawn, but not limited to:

- Magnesium based MMCs reinforced with nanoparticles shows great potential in the resolving the current limitation in magnesium alloy in the biomedical applications.
- Plenty of research has been done on the machinability study of conventional micro-MMCs, but little can be found on nano-MMCs. Therefore, knowledge related to the material removal mechanism in machining nano-MMCs is relatively limited.
- Current investigation on non-conventional machining methods on MMCs mostly focus on machining parameters optimisation, in-depth understanding on material removal mechanism is still needed.
- Poor surface quality is recognised as the main limitation in non-conventional machining of MMCs. Based on the evaluation of state-of-the-art machining methods, micro machining has been recognised as one of the most potential method achieving better surface finish and complex 3D features.
- Knowledge related to the tool wear study in micro machining process is limited. There is no mature standard to quantitatively define the wear state of micro endmill.

- A micro mechanical model revealing the mechanism in micro machining process of nano-MMCs, including the chip formation, tool-particle interaction and surface generation is desired in order to provide a more comprehensive understanding the effect of dramatically reduced particle size on their machinability.

Chapter 3 Comprehensive micro-machinability study of Mg based MMCs reinforced with nanoparticles

3.1 Introduction

The MMC components are normally fabricated in near net shapes, however conventional machining, such as turning, milling and drilling is necessary to achieve desired accuracy and produce complex features. The mechanical properties of MMCs are improved significantly due to the hard reinforcement materials such as ceramics or metallic particles. Therefore, improved mechanical properties and its nature of heterogeneous structure make MMCs a very difficult-to-cut material. Numerous research have been carried out on conventional machining of a variety of metal matrix composites in the past two decades. However, little published research regarding to the investigation of micro machining especially micro milling of MMCs with nano reinforcements can be found.

This chapter presents comprehensive studies of micro machinability of Mg based MMCs reinforced with nanoparticles. Two individual micro milling experiments are included in this chapter. The first experiment (experiment A) conducts the investigation on the influence of cutting parameters on the cutting force and surface morphology in micro milling of magnesium-based MMCs reinforced with two types of nanoparticles, namely titanium (Ti) and titanium diboride (TiB_2). The size effect and the minimum chip thickness according to the specific cutting energy and surface morphology at different feed per tooth is studied. Moreover, a mechanistic model was established to predict the cutting force during machining. The experiment results present an attempt to fill the gap and provide a comprehensive understanding on the micro machinability of Mg-based MMCs reinforced with nanoparticles.

For the second experiment (experiment B), the micro machinability of two types of magnesium-based nano-MMCs (Mg/BN & Mg/ZnO) with different volume fractions is investigated. Micro milling is performed on each specimen using AlTiN coated tungsten carbide end mills. The effect of cutting parameters including spindle speed, feed per tooth and depth of cut on the cutting force and surface morphology are studied. Moreover, the influence of volume fraction and reinforcement materials on the cutting force are evaluated and the phenomena observed are explained in detail considering microstructure change of MMCs. Additionally, the chip morphology and its formation mechanism were discussed.

3.2 Experimental setup

3.2.1 Machine tool

Experiment A&B

Micro machining experiments were carried out on an ultra-precision desktop micro machine tools (MTS5R) which is fitted with a high speed spindle driven by a continuous power of 100W(240V), with the rotation speed ranging from 20,000rpm to 80,000rpm. It has the capability of using high feedrate and cutters with small diameter. This ultra-precision micro machine tools consists of 3 axes (X, Y, Z) which are controlled by DC servo motors with smallest feed of 0.1 μ m. The micro machining tool with axis movement fitted with a Kistler cutting force dynamometer (9256C2) is given in Figure. 3.1. Ultra-precision collets are fitted to clamp the micro end mills to ensure the run out of spindle within 1 μ m.

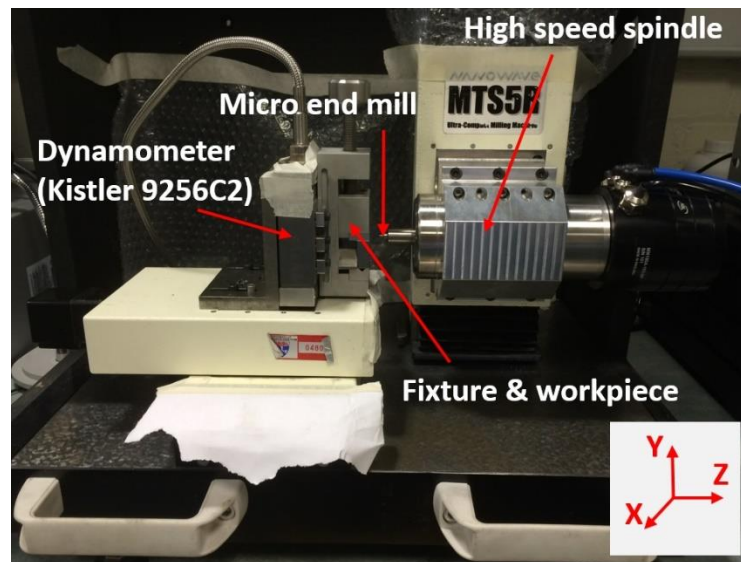


Figure 3.1 Configuration and machine tool with Kistler dynamometer

3.2.2 Workpiece materials

Experiment A

In this experiment, two specimens including Mg-based MMCs reinforced with 1.98 Vol.% of nano-sized Ti and TiB₂ reinforcements were used. Both specimens are synthesised and supplied by National University of Singapore (NUS). Magnesium with 99.9% purity, supplied by ACROS Organics, New Jersey, USA are used as the base matrix. Reinforcements consist of pure titanium powder of 30-50 nm supplied by US Research Nanomaterials and titanium

diboride powder of ~60nm supplied by NaBond Co.Ltd. Both MMCs are synthesized using the disintegrated melt deposition (DMD) technique.

Experiment B

Two types of magnesium-based MMCs reinforced with nano-sized BN and ZnO particles are utilized during this experiment. Both specimens are synthesised and supplied by National University of Singapore (NUS). The weight fraction for each type of MMCs specimen is 0.5 wt%, 1.5 wt% and 2.5wt% respectively. Disintegrated melt deposition (DMD) technique is employed to synthesise the MMCs specimens.

3.2.3 Micro end mills

Experiment A&B

2-flutes AlTiN coated tungsten carbide micro end mills (Figure 3.2) with tool diameter of 1 mm and shank diameter of 3mm were utilised. In order to reduce tool deflection in the experiment, a relative large tool diameter was selected since a wider range of feed rates were used in this experiment. The geometry of all the new tools used in the experiment was examined by SEM before milling. The cutting edge radius was estimated to be 1.5 μ m by SEM measurement. Table 3.1 illustrates the specifications of micro endmills used in this experiment.

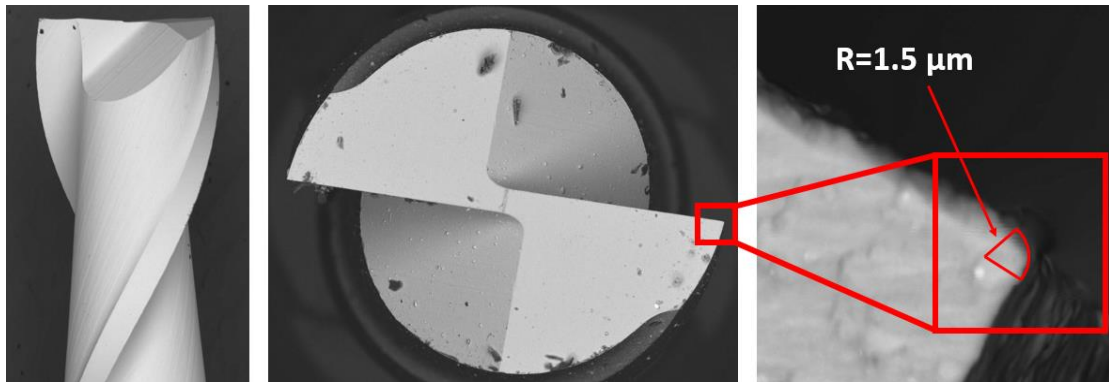


Figure 3.2 AlTiN coated Tungsten carbide micro end mill used with cutting edge radius

Table 3.1 Micro endmill specifications

Properties	Values
Nominal diameter (mm)	1
No. of flute	2
Helix angle (°)	25
Flute length (mm)	1.5
Rake angle (°)	0
Clearance angle (°)	17
Tool edge radius (μm)	1.5

3.3.4 Experimental Procedure

Experiment A

Two individual fullslot (1mm width and 5mm length) micro milling tests were conducted respectively on each type of Mg-based MMCs. Each machining condition was repeated once. Full factorial design was employed in the first experiment. Three controlled quantitative factors were used in this experiment, spindle speed n (rpm), feed per tooth f_t ($\mu\text{m}/\text{tooth}$) and depth of cut a_p (μm). 24 slots milling with various cutting conditions (illustrated in Table 3.2) was used to study the effect of cutting parameters on the cutting force and surface roughness. Table 3.3 shows the cutting conditions in the second test, there are 16 slots milling with various feed per tooth and constant depth of cut and spindle speed with the aim of investigating the specific cutting energy and size effect.

In this experiment, quantitative and qualitative investigation on the morphology of machined surface are conducted to produce a more confident analysis. For the quantitative study, the white light interference analyser (Zygo New View5020) are employed to measure the surface roughness of machined surface, which is employed to be statistically analysed by ANOVA to obtain the cutting parameters which contribute the most effect on the surface quality. The machined surface under different cutting conditions are qualitatively studied using scanning electron microscope (Hitachi TM3030) with the aim of obtaining the set cutting parameters which results in an optimized surface integrity. A piezoelectric dynamometer (Kistler 9256C2) assisted with a four channel charge amplifier of 5070A was used to acquire the cutting force along the X, Y, and Z axis during the machining. The DynoWare software is used to demonstrate and analyse the cutting forces. Based on maximum cutting speed used in this study (60,000 rpm), the sampling rate is set to be 20,000 Hz in order to acquire sufficient sampling points during each tool pass.

Table 3.2 Cutting conditions for 1st test

Cutting parameters	Level. 1	Level. 2	Level. 3	Level. 4
Spindle speed, n(rpm)	20000	40000	60000	N/A
Depth of cut, a_p (μm)	150	300	N/A	N/A
Feed per tooth, f_t (μm)	1	2	3	4

Table 3.3 Cutting condition for 2nd test

Exp No.	Feed rate	Spindle speed	Depth of cut	Feed per tooth
	$f_z(\text{mm/min})$	$n(\text{rpm})$	$a_p(\mu\text{m})$	$f_t(\mu\text{m/tooth})$
1	4	40000	150	0.05
2	8	40000	150	0.1
3	12	40000	150	0.15
4	16	40000	150	0.2
5	24	40000	150	0.3
6	32	40000	150	0.4
7	40	40000	150	0.5
8	64	40000	150	0.8
9	88	40000	150	1.1
10	112	40000	150	1.4
11	136	40000	150	1.7
12	160	40000	150	2
13	240	40000	150	3
14	320	40000	150	4
15	400	40000	150	5
16	480	40000	150	6

Experiment B

Specimen preparation is carried out to cut the rod into cuboid shape (with the dimension: 6mm x 6mm x 38mm). Prior to the machining experiments, dial gauge with resolution of 1 μm was used to adjust the levelness of specimens to limit the deviation within 10 μm . To eliminate the negative effect of levelness of deviation of the depth of cut, a layer of material with thickness of 15 μm was then removed using the micro machine tool. Zero position of the cutting tool relative to the surface of specimen is adjusted using Kislter dynamometer to set up the depth of cut within 1 microns that is possible due to the resolution of axes of 0.1 μm .

Full immersion slot micro milling is carried out in this work. Seven types of specimens with different reinforcement materials and weight fraction are involved in this experiment and they are listed in Table 3.4. 24 full immersion micro milled slots are carried out on each specimen in this work. Three controlled quantitative factors are utilised in this experiment, namely spindle speed, feed per tooth and depth of cut. Full factorial design is used and the cutting parameters with different levels are illustrated in Table 3.5.

Table 3.4 MMCs specimen parameters

No.	Matrix material	Reinforcement materials	Weight fraction
1	Pure Mg	N/A	N/A
2	Mg	ZnO	0.5%
3	Mg	ZnO	1.5%
4	Mg	ZnO	2.5%
5	Mg	BN	0.5%
6	Mg	BN	1.5%
7	Mg	BN	2.5%

Table 3.5 Cutting parameters used in full factorial designed experiment

Cutting parameters	Level 1	Level 2	Level 3	Level 4
Spindle speed, n (rpm)	6,000	8,000	10,000	N/A
Feed per tooth, f_t (μm)	1	2	3	4
Depth of cut a_p (μm)	30	60	N/A	N/A

3.4 Results and discussions (Experiment A)

3.4.1 Surface roughness analysis

The average surface roughness of the bottom machined surface of the micromachined slots was obtained. Three measurements on different position of each slot were carried out with the aim of reducing the measurement uncertainty and assessing repeatability. Mean value of R_a was used for analysis. The experimental matrix of micro milling of MMCs with TiB_2 and Ti and response in two experiments are listed in Table 3.6 and Table 3.7.

Table 3.6 Experimental matrix of micro milling of MMCs with TiB₂ and Ti in first experiment and response

Experiment No	Experimental Matrix	Response			
		MMCs with TiB ₂	MMCs with Ti		
	Spindle speed n	Depth of cut a _p	Feed per edge f _t	Surface roughness Ra (average)	
	rpm	μm	μm/t	μm	
1	20000	150	1	0.158	0.1217
2	20000	150	2	0.137	0.1417
3	20000	150	3	0.152	0.1347
4	20000	150	4	0.185	0.1623
5	40000	150	1	0.121	0.1280
6	40000	150	2	0.183	0.1250
7	40000	150	3	0.162	0.1623
8	40000	150	4	0.142	0.1637
9	60000	150	1	0.156	0.2097
10	60000	150	2	0.216	0.1747
11	60000	150	3	0.306	0.2143
12	60000	150	4	0.212	0.2247
13	20000	300	1	0.091	0.2047
14	20000	300	2	0.11	0.1997
15	20000	300	3	0.155	0.1967
16	20000	300	4	0.117	0.2083
17	40000	300	1	0.081	0.1927
18	40000	300	2	0.087	0.2280
19	40000	300	3	0.109	0.2327
20	40000	300	4	0.134	0.2983
21	60000	300	1	0.13	0.1990
22	60000	300	2	0.11	0.2460
23	60000	300	3	0.211	0.2143
24	60000	300	4	0.181	0.2473

Table 3.7 Experimental matrix of micro milling of MMCs with TiB₂ and Ti in first experiment and response

Experiment No	Experimental Matrix			Response			
				MMCs with TiB ₂	MMCs with Ti	MMCs with TiB ₂	MMCs with Ti
	Spindle speed n	Depth of cut a _p	Feed per tooth f _t	Cutting force (average)		Surface roughness Ra (average)	
	rpm	μm	μm/t	N		μm	
1	40000	200	0.05	0.923	4.000	0.167	0.182
2	40000	200	0.1	0.812	4.200	0.140	0.215
3	40000	200	0.15	0.8	4.100	0.164	0.288
4	40000	200	0.2	1.435	4.298	0.161	0.249
5	40000	200	0.3	0.582	3.881	0.103	0.254
6	40000	200	0.4	0.647	4.046	0.145	0.197
7	40000	200	0.5	0.638	3.728	0.199	0.202
8	40000	200	0.8	0.65	3.993	0.082	0.193
9	40000	200	1.1	0.684	3.727	0.095	0.200
10	40000	200	1.4	0.742	3.665	0.097	0.189
11	40000	200	1.7	0.826	3.646	0.089	0.218
12	40000	200	2	0.837	3.475	0.074	0.190
13	40000	200	3	1.167	3.685	0.090	0.207
14	40000	200	4	1.447	3.594	0.093	0.214
15	40000	200	5	1.634	3.967	0.110	0.205
16	40000	200	6	1.894	3.870	0.124	0.253

3.4.1.1 Main effect of cutting parameters on surface roughness

Main effects of cutting parameters on the surface roughness for Mg/TiB₂ and Mg/Ti MMCs were plotted in Figure. 3.3. (a) and (b) respectively. Unlike the inverse proportional variation trend of surface roughness with respect to spindle speed observed in the previous research conducted on the conventional turning of Al/SiC and Al/Cu-TiC MMCs (Suresh Kumar Reddy, Kwang-Sup and Yang, 2008; Kumar, Mahapatra and Jha, 2014), a proportional relation was found between surface roughness and spindle speed for Mg/Ti MMCs. This could be due to the continuous semi-circular tool marks which is known as side flow in turning, on machined surface in full slots milling as a result of squeeze between the corner edges of endmill and the material at the relatively small uncut chip thickness to cutting edge radius ratio in micro milling. High heat was generated at high spindle speed of 20k – 60k rpm (linear speed = 10.46 – 31.4m/s) and consequently soften the material which assists the formation of semi-circular tool marks. The surface roughness, however, was observed to decrease when increasing the spindle speed from 20,000 to 40,000 rpm, then increase rapidly when spindle speed increase to 60,000rpm

for Mg/TiB₂ MMCs. Lower depth of cut should be selected to minimise the surface roughness in machining of Mg/Ti MMCs. For machining Mg/TiB₂ MMCs, however the higher depth of cut results in a lower surface roughness value and this tendency is contrary to micro milling of metallic materials. An increase in feed per tooth from 1 to 3 $\mu\text{m}/\text{tooth}$ results in increase of surface roughness values in both materials. Overall, the machined surface quality of Mg/TiB₂ MMCs was superior than that of Mg/Ti MMCs in terms of surface roughness value. This might be contributed to the higher cutting force induced in cutting process of Mg/Ti MMCs.

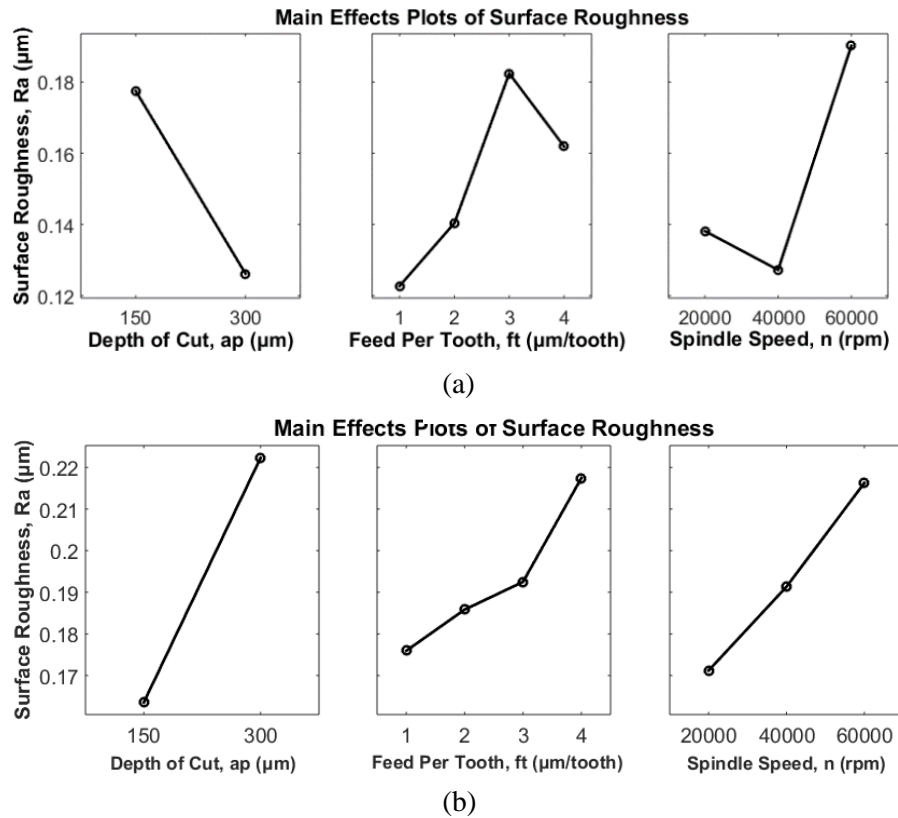


Figure 3.3 Main effects of cutting parameters on the surface roughness. (a) Mg/TiB₂ MMCs; (b) Mg/Ti MMCs.

3.4.1.2 ANOVA analysis

ANOVA for the first experiment of two materials was carried on the surface roughness to isolate main effects of each source of variations and determine effects of interactions (Table 3.8 and Table 3.9). It can be concluded that the depth of cut and spindle speed have significant influence on surface roughness in both materials. The contribution ratio for the spindle speed and depth of cut is 33% and 29 % for machining Mg/TiB₂ MMCs, 19% and 49% for the

machining Mg/Ti MMCs. The interactions between two cutting parameters are found to be not significant to the results.

Table 3.8 ANOVA for surface roughness of Mg/TiB₂ MMCs

Source of variation	Degree of freedom	Sum of square (x10 ⁻³)	Mean of square (x10 ⁻³)	F Value	P Value	% Contribution
n	2	18.094	9.047	10.87	0.01	33%
a_p	1	15.794	15.794	18.97	0.005	29%
f_t	3	12.079	4.026	4.84	0.048	22%
n&a_p	2	0.624	0.312	0.37	0.702	1%
n&f_t	6	6.776	1.129	1.36	0.36	12%
f_t&a_p	3	1.397	0.466	0.56	0.661	3%
Error	6	4.994	0.832			
Total	23	59.757				

Table 3.9 ANOVA for surface roughness of Mg/Ti MMCs

Source of variation	Degree of freedom	Sum of square (x10 ⁻³)	Mean of square (x10 ⁻³)	F Value	P Value	% Contribution
n	2	8.146	4.073	9.06	0.015	19%
a_p	1	20.709	20.709	46.06	0.001	49%
f_t	3	5.64	1.88	4.18	0.064	13%
n&a_p	2	5.269	2.634	5.86	0.039	12%
n&f_t	6	1.677	0.279	0.62	0.711	4%
f_t&a_p	3	1.225	0.408	0.91	0.491	3%
Error	6	2.698	0.45			
Total	23	0.045363				

3.4.1.3 Regression analysis

The MINITAB statistical software was used to generate the simple regression analysis to identify the fitness of the experimental measurement surface roughness. Within this study, first order nonlinear polynomial model was obtained. The general mathematical expression is illustrated below.

$$Y = \beta_0 + \beta_1 n + \beta_2 a_p + \beta_3 f_t \quad (1)$$

Where β_0 , β_1 , β_2 , and β_3 are constants, Y denotes surface roughness and A, B, C, are spindle speed, depth of cut and feed per tooth.

The regression equation for Mg-based MMCs with TiB₂ particles is

$$\text{Surface roughness} = 0.1369 + 0.000001n - 0.000342a_p + 0.01595f_t \quad (2)$$

The regression equation for Mg-based MMCs with Ti particles is

$$\text{Surface roughness} = 0.027 + 0.000001n - 0.000392a_p + 0.01312f_t \quad (3)$$

3.4.2 Cutting force analysis

Measurement of cutting force is imperative to understand the machinability and cutting mechanics of materials. The main effect of three cutting parameters on the average cutting force of F_x and F_y in machining of two types materials is illustrated in Figure 3.3. The Root Mean Square (RMS) values of in-plane force ($F_{\text{average}} = \sqrt{F_x^2 + F_y^2}$) were calculated and used as the average cutting force.

3.4.2.1 Main effect of cutting parameters on cutting force

The average cutting force can be observed to be increased by increasing both feed per tooth and depth of cut in both Mg/TiB₂ and Mg/Ti MMCs (Figure 3.4). This is because more resistance is acted on the cutting tool due to the increased cross sectional area of chip and therefore lead to higher machining force with vibration which facilitates higher surface roughness. Additionally, it can be seen that the cutting force for Mg/Ti MMCs are more sensitive with the variation of depth of cut and feed per tooth compared to Mg/TiB₂.

For Mg/TiB₂ MMCs, the cutting force decreases when the spindle speed increase from 20,000rpm to 40,000rpm until a minimum value achieved, and a rapid increase in the cutting force is followed with the increasing of spindle speed from 40,000 rpm to 60,000 rpm. But for Mg/Ti MMCs when spindle speed increase from 20,000rpm to 60,000rpm, there is an approximate linear increase in the average cutting force from 2N to 4.5N. Same tendency can be obtained in the variation of surface roughness with spindle speed for both MMCs. The strength of materials could be dominated by two factors which are temperature and strain rate. For cutting Mg/TiB₂ MMCs, the material strength and cutting force would decrease due to the thermal softening of the material at spindle speed from 20,000 rpm to 40,000 rpm. However the strength of materials would increase with strain rate during fast cutting speed. It was found that

the strain strengthening becomes more dominant than thermal softening when spindle speed increased from 40,000 rpm to 60,000 rpm. During cutting Mg/Ti MMCs, strain strengthening might play the dominant role in determining strength of the material. Mg/Ti MMCs may present greater strain rate sensitivity than Mg/TiB₂ and other aluminium-based MMCs. Lower level of spindle speed and feed per tooth therefore should be selected to minimise the cutting force while improving the machined surface quality. However, it is important to note that, the feed per tooth should not be smaller than the minimum uncut chip thickness otherwise cutting edge size effect would cause ploughing action governing the cutting process, which would deteriorate surface generation. Size effect will be discussed in the next section.

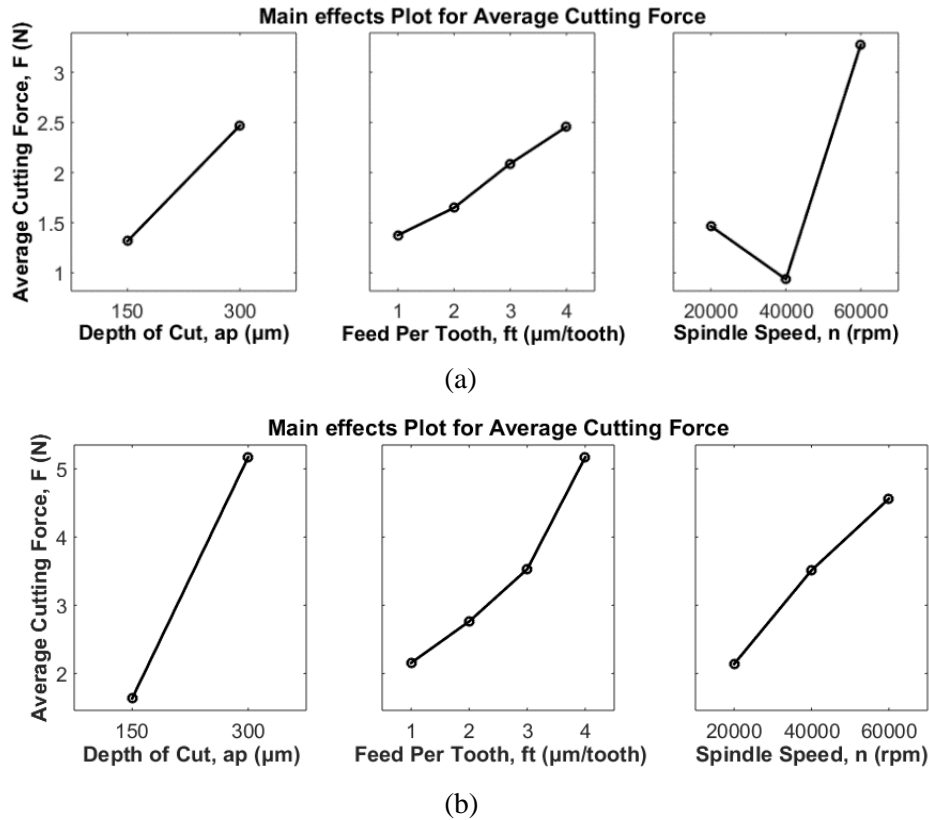


Figure 3.4 Variation of cutting force with three cutting parameters. (a) Mg/TiB₂ MMCs; (b) Mg/Ti MMCs.

Figure. 3.5 shows the comparison in the variation of cutting force with feed per tooth between Mg/TiB₂ and Mg/Ti MMCs at constant depth of cut of 150 μm , spindle speed of 40,000rpm. The cutting force for the Mg/Ti MMCs is much higher than that for Mg/TiB₂.

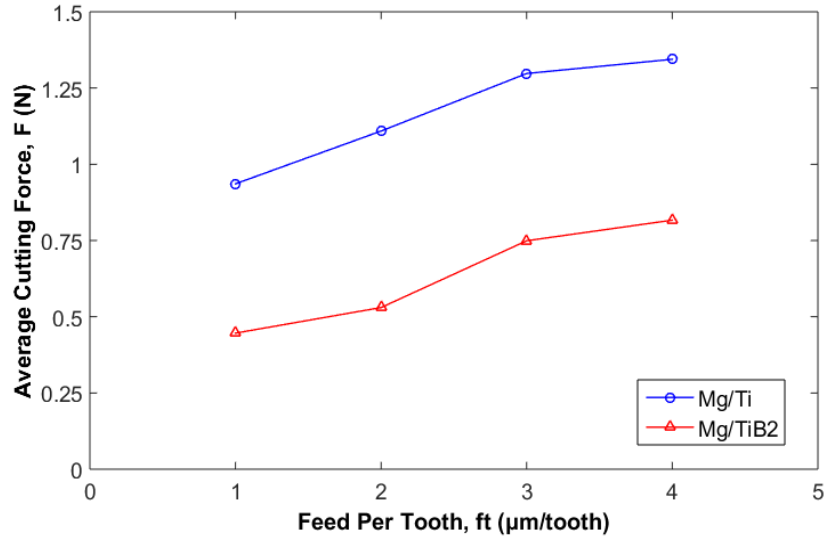


Figure 3.5 The influence of reinforcement material on average cutting force at spindle speed: 40,000rpm, depth of cut: 150μm.

3.4.2.2 Mechanistic model

The mechanistic model proposed by Budak et al. (Budak, Altıntaş and Armarego, 1996) was utilised to determine the cutting constants and to generate the simulated cutting force during the micro milling of Mg/TiB₂ and Mg/Ti MMCs. The average cutting force in the X, Y direction were determined as shown in Eq. (4) and (5).

$$\overline{F}_x = \left\{ \frac{Na_p f_t}{8\pi} [K_{tc}(2\phi - \sin 2\phi) + K_{rc} \cos 2\phi] - \frac{Na_p}{2\pi} [K_{te} \cos \phi + K_{re} \sin 2\phi] \right\}_{\phi_{st}}^{\phi_{ex}} \quad (4)$$

$$\overline{F}_y = \left\{ \frac{Na_p f_t}{8\pi} [K_{tc} \cos 2\phi - K_{rc}[2\phi - \sin 2\phi]] + \frac{Na_p}{2\pi} [-K_{te} \sin \phi + K_{re} \cos 2\phi] \right\}_{\phi_{st}}^{\phi_{ex}} \quad (5)$$

Where N is number of flutes of endmill, K_{rc} and K_{tc} are the cutting constants contributing to shearing action, K_{re} and K_{te} are cutting constants contributing to the ploughing action, ϕ is tool rotation angle, f_t is the feed per tooth, a_p is the axial depth of cut (edge contact length). For the full slot milling, the entry and exit angle are $\phi_{st} = 0$ and $\phi_{ex} = 180^\circ$ respectively. When above conditions are applied to equation 4 and 5, the average forces per tooth pass can be obtained as follows:

$$\overline{F}_x = -\frac{Na_p}{4} K_{rc} f_t - \frac{Na_p}{\pi} K_{re} \quad (6)$$

$$\overline{F}_y = +\frac{Na_p}{4} K_{tc} f_t + \frac{Na_p}{\pi} K_{te} \quad (7)$$

As a result, the value of cutting constants (K_{rc}, K_{re}, K_{tc}, K_{te}) can be obtained by fitting above equations into average cutting force curve with feed per tooth

Extra set of experiments on Mg/TiB₂ MMCs with feed per tooth of 3 and 4 $\mu\text{m}/\text{tooth}$, depth of cut of 300 μm and spindle speed of 40000rpm were conducted to perform the verification. The comparison between the simulated and measured cutting force in feed and normal direction are shown in Figure 3.6. The prediction force shows a good agreement with the measured force for F_x at both levels of feed per tooth. In terms of the maximum cutting force, the error of prediction cutting force is 3-4% in F_x and 45-65% in F_y at 3 and 4 $\mu\text{m}/\text{tooth}$. The difference in the maximum value of measured cutting forces generated from two tool pass in each period can be attributed to the non-uniformity existing in the geometries of two cutting edges.

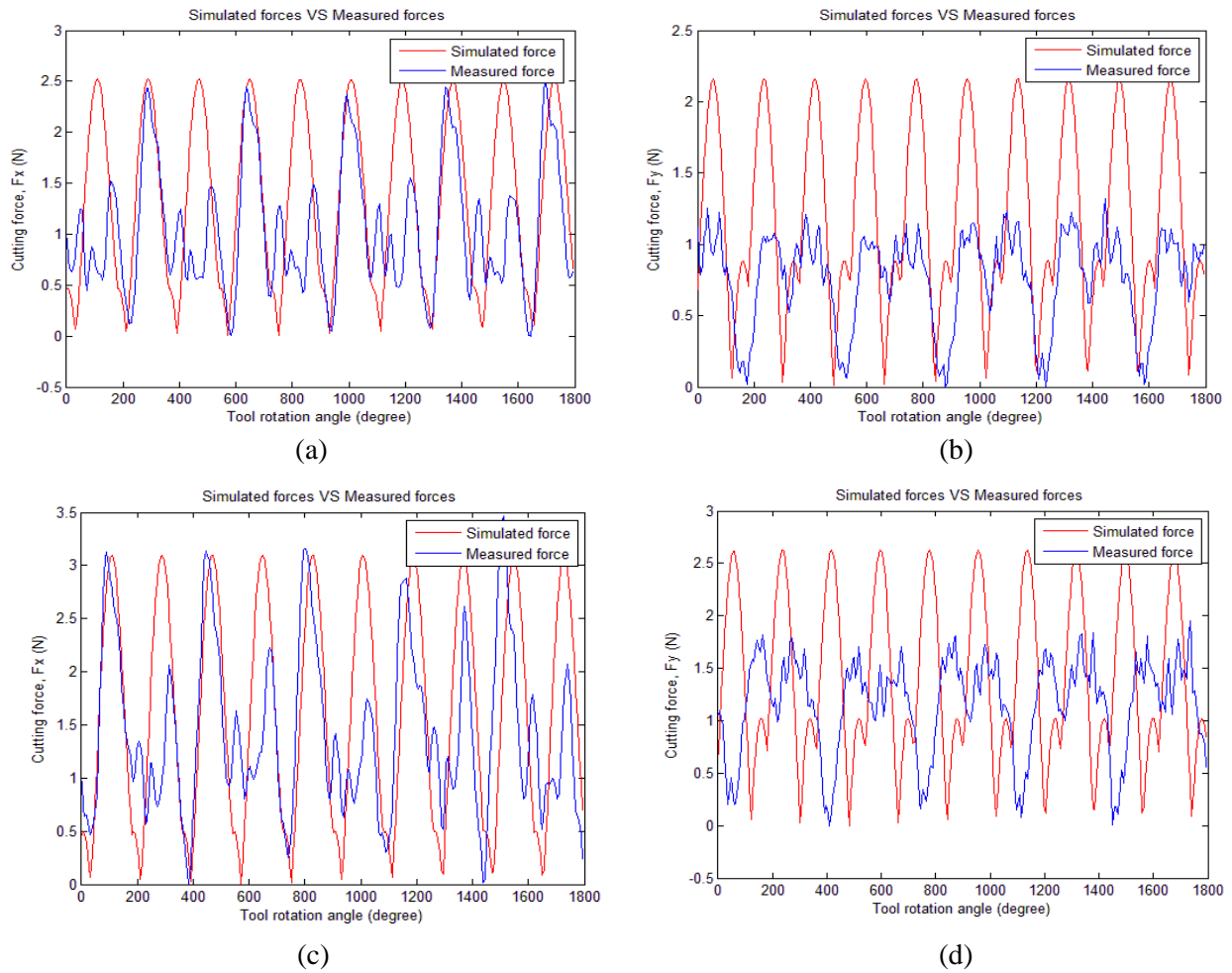


Figure 3.6 Comparison of simulated and experimental measured cutting force for machining Mg/TiB₂ MMCs at depth of cut: 300 μm , spindle speed: 40000rpm; feed per tooth: 3 $\mu\text{m}/\text{tooth}$ (a) cutting force in cross feed direction, F_x ; (b) cutting force in feed direction, F_y and at feed per tooth of 4 $\mu\text{m}/\text{tooth}$; (c) cutting force in cross feed direction, F_x ; (d) cutting force in feed direction, F_y .

3.4.3 Size effect

With the decreasing of uncut chip thickness which is dimensionally close to the cutting edge radius of the cutting tool, size effect becomes a dominant factor that leads to a transitional

regimes associated with intermittent shearing and ploughing during the machining (X. Liu, DeVor, *et al.*, 2004). Essentially, the size effect can lead to a negative effect on the cutting process such as higher cutting force, premature tool breakage, and worse machined surface quality. The investigation of size effect is carried out according to two aspects which are specific cutting energy and surface morphology, and the value of minimum chip thickness for such materials were determined.

3.4.3.1 Specific cutting energy

Specific cutting energy can be defined as the energy consumed in removing a unit volume of material. The specific cutting energy for each materials is calculated through equation 8, where $\overline{F_x}$ and $\overline{F_y}$ are the cutting force component in X and Y direction, v_c is the cutting speed in m/min, V_{rem} is removed chip volume, t_c is the cutting time.

$$u_c = \frac{v_c}{V_{rem}} \int_0^{t_c} \sqrt{\overline{F_x}^2 + \overline{F_y}^2} dt \quad (8)$$

Figure 3.7 shows the variation of the specific cutting energy with feed per tooth for Mg/TiB₂ and Mg/Ti MMCs at a spindle speed of 40,000rpm and a depth of cut of 200μm. Size effect can be observed according to the non-linear decrease of the specific cutting energy with feed per tooth. As illustrated in Figure 3.7, as the ratio of feed per tooth to the cutting edge radius increases, the specific cutting energy decreases rapidly, and transits to a stable value at the feed per tooth between 1 and 2 μm/tooth. The high specific cutting energy at small feed was attributed to that the material undergo an elastic deformation and deformed material fully recovers to its original position, as a consequence an uneven distribution of stress is caused by the interaction of workpiece and cutting tool. A transition for the specific cutting energy approaching to a stable value is expected at where the feed per tooth is close to the critical uncut chip thickness. Finally, when the feed per tooth is larger than the critical chip thickness, the material deforms plastically by shearing, and continuous chips are formed. In addition, by comparing these two materials, it can be reported that much more energy is required to cut Mg/Ti MMC than Mg/TiB₂ when the feed per tooth is below the critical value. This leads to a worse machined slot edge for Mg/Ti MMCs with more burrs as shown in Figure 3.8

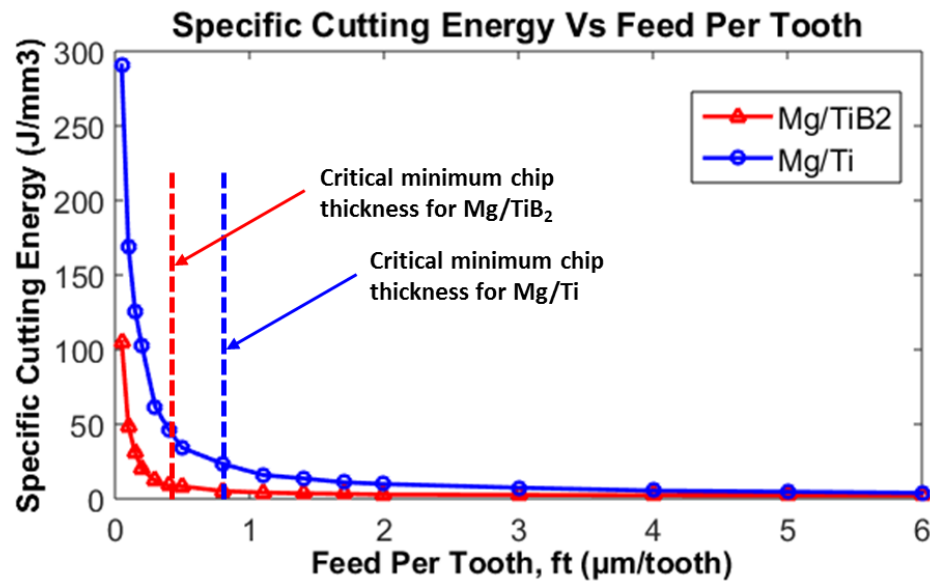


Figure 3.7 Specific cutting energy of Mg/TiB₂ and Mg/Ti MMCs obtained at spindle speed: 40,000rpm, depth of cut: 200 μm .

3.4.3.2 Machined surface morphology

Observation of machined surface in Figure 3.8 revealed that for both Mg/TiB₂ and Mg/Ti MMCs, various types of surface defects were formed during machining. Severe top burr formation, worse surface and large area of cracks were observed on the slot edges and machined surfaces at small feed per tooth of 0.15 and 0.3 $\mu\text{m/tooth}$ (example are Figure 3.8 (a)(b)(e)(f) and (k)). The burr formed during machining process considerably affect not only the dimensional accuracy and functionality of produced product but also tool wear due to the size of burr approaching to half of slot width at small feed per tooth. However, the machined surface without burrs and surface defects are obtained when the feed per tooth increases to 0.8 $\mu\text{m/tooth}$ for Mg/Ti MMCs and 0.5 $\mu\text{m/tooth}$ for Mg/TiB₂ MMCs respectively (example are Figure 3.8 (d)(g) and (j)). The materials toward the cutting direction was squeezed and therefore deformed plastically at small feed per tooth when ploughing took place instead of shearing action. Then partial of fractured materials remained at slot edges and burrs were formed.

The results show an excellent agreement with the findings that higher forces incurred in small feed per tooth due to size effect may result in high value of surface roughness as well as the worse surface quality. It can also be seen from Figure 3.8 that the material in the same position was cut more than once, which results in overlapping tool marks generated on the surface and indicates that the material was elastically ploughed off due to the size effect. Therefore, based on all the work done in this chapter the minimum chip thickness for cutting Mg/TiB₂ and Mg/Ti MMCs can be determined as 0.8 μm and 0.5 μm respectively and the ratio of minimum chip thickness and cutting edge radius is approximately as 53% and 33%.

By comparing the two Mg MMCs, more top burrs on slot edges and worse surface quality with evenly distributed crack on the surface were found Mg/Ti MMC. As the reinforcement material, titanium and its alloy exhibit low thermal conductivity, high ductility and adhesion. These characteristics and strain hardening of composite materials lead to adhesion and high burr formation during micromachining. Meanwhile, the thermal softening of both matrix and reinforcement materials caused by high temperature also facilitate this phenomenon. As a result, large and continuous burr was formed along the slot edges.

Less burrs were formed at the up milling side according to Figure. 3.8 (b), (g) and (h). Additionally, it can be seen from Figure 3.8 (f) that a more defective slot edge could be generated at down milling side compared to that at up milling side. The cutting direction and the tool feed direction is opposite in both up and down milling, therefore the characteristics is different in surface and burr formation in the up milling and down milling (Liu, Li and Xu, 2014).

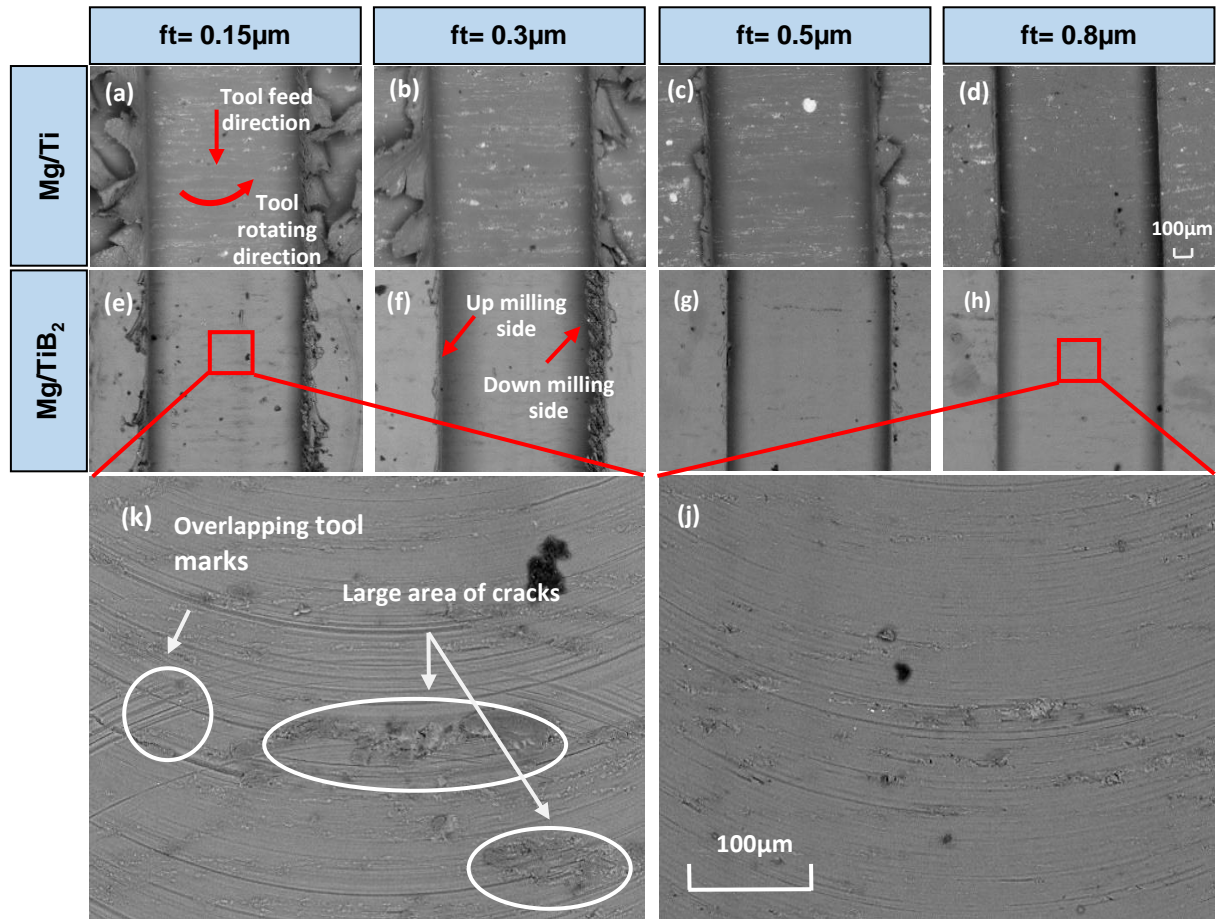


Figure 3.8 SEM micrographs of micro machined slots for Mg/TiB₂ MMCs and Mg/ Ti MMCs, (a) & (e) at feed per tooth of 0.15μm/tooth; (b) & (f) 0.3 μm/tooth; (c) & (g) 0.5 μm/tooth; (d) & (h) 0.8 μm/tooth and spindle speed: 40,000rpm, depth of cut: 200μm; (k) magnified image of (e); (j) magnified image of (h).

3.5 Results and discussion (Experiment B)

3.5.1 Influence of nanoparticles contents and materials on cutting force

When the spindle speed of 10,000 rpm and depth of cut of 60 μm are employed, the effect of feedrate on the cutting force in machining pure Mg and its composites with different weight fraction is shown in Figure 3.9 (a). Similar to the machining of traditional MMCs with micro-sized particles (Kannan, Kishawy and Deiab, 2009; Kumar, Mahapatra and Jha, 2014), as expected the increase in the feed per tooth from 1 to 4 $\mu\text{m}/\text{tooth}$ results in a corresponding increase in cutting forces. For the case of machining Mg/1.5 wt.% ZnO, a slight decrease in cutting force can be observed from 3 to 4 $\mu\text{m}/\text{tooth}$. As illustrated in Figure 3.9 (b), when depth of cut of 60 μm and feed per tooth of 3 $\mu\text{m}/\text{tooth}$ was used, the effect of spindle speed on the cutting force for various types of specimen was obtained. A significant drop in the cutting force from 6,000 to 8,000 rpm indicating that material softens at higher spindle speed due to the large amount of heat generated at the tool-chip interface and consequently less force is needed. For the Mg/0.5wt.% BN and Mg/2.5wt.% BN, cutting forces continuously decrease until a maximum spindle speed of 10,000 rpm is reached. A reverse trend, however, was observed for pure Mg, Mg/1.5wt.% BN, and all Mg/ZnO specimens. Figure 3.9 (c) shows the trend of cutting forces which is obtained under the feed per tooth of 3 μm and spindle speed of 10,000 rpm. As expected, the cutting force increases with the increase of depth of cut from 30 to 60 μm for all specimens.

The cutting force of Mg/ZnO MMCs is much higher than Mg/BN MMCs under the same machining conditions. The cutting force of each Mg-based MMCs specimen can be related to their compressive strength tested in previous research (Sankaranarayanan, Pranav Nayak, *et al.*, 2014; Sankaranarayanan, Sabat, *et al.*, 2014), namely Mg/ZnO MMCs with higher tensile strength could generate higher cutting force than that for Mg/BN MMCs. Based on Figure 3.9 (a), it can be seen that the cutting force of Mg/2.5wt.%ZnO is the largest among all the specimens. The cutting force of Mg/1.5wt.% ZnO is slightly larger than that of Mg/0.5wt.% ZnO from feed per tooth of 1 to 3 $\mu\text{m}/\text{tooth}$. For the Mg/BN MMCs, MMCs with weight fraction of 2.5% results in the smallest cutting force and there is not obvious difference can be found between MMCs with 1.5% and 0.5% weight fraction.

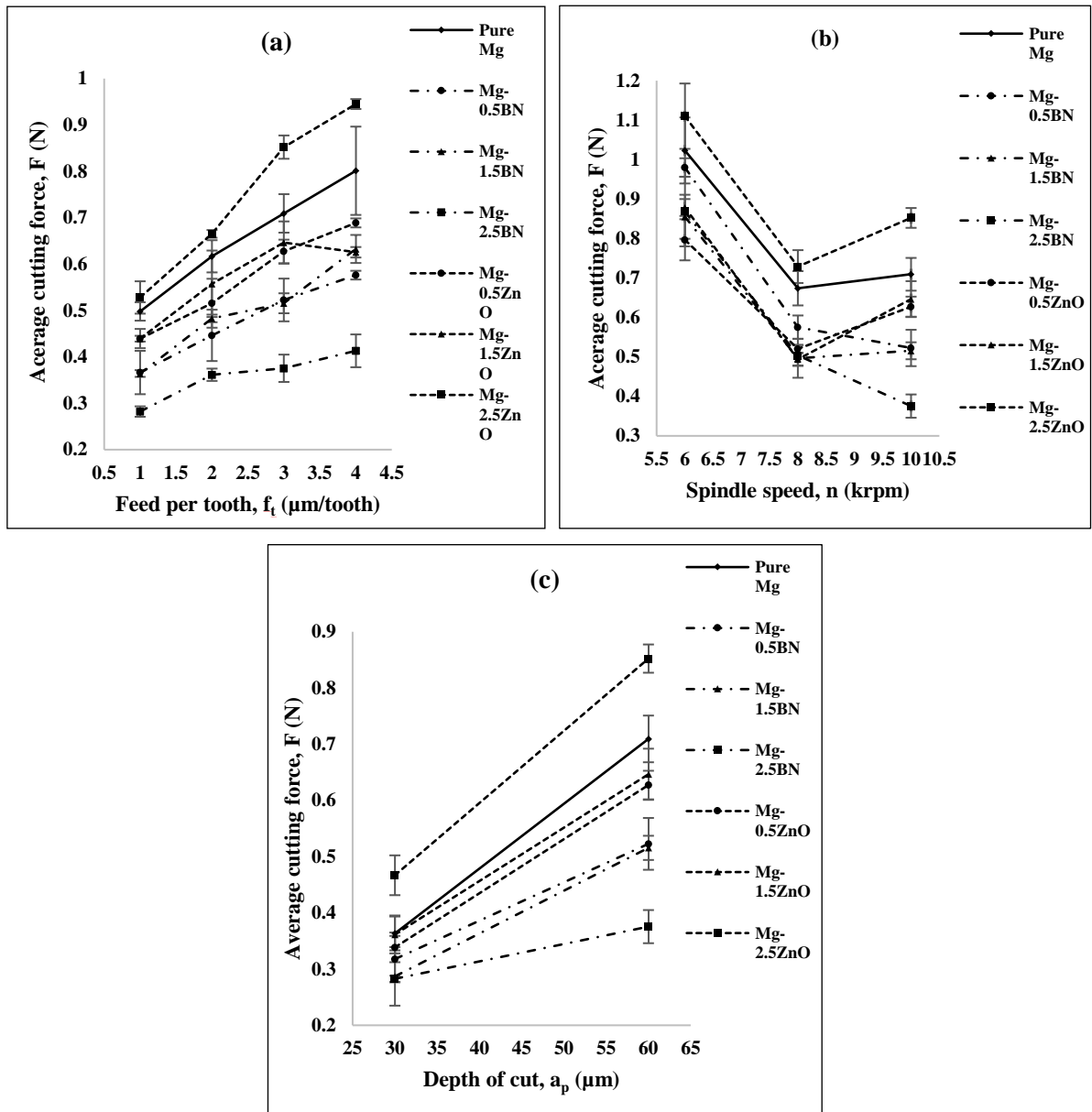


Figure 3.9 The effect of different cutting parameters on average cutting forces (a) effect of feedrate (depth of cut: 60 μm ; spindle speed: 10,000 rpm); (b) effect of spindle speed (feed per tooth: 3 $\mu\text{m}/\text{tooth}$; depth of cut: 60 μm); (c) effect of depth of cut (spindle speed: 10,000 rpm; feed per tooth: 3 $\mu\text{m}/\text{tooth}$)

Moreover, it is important to note that the cutting force for machining pure Mg is found to be higher than any other MMCs except Mg/2.5wt.% ZnO. This trend of cutting force is contrary to the results obtained from past investigation on machining of Mg MMCs with high volume fraction (5%, 10% and 15%) of nano-sized SiC particles [9]. This phenomenon can be explained by considering the increase of slip plane intensity in Mg MMCs attributed to the incorporation of nano-sized reinforcements. Generally, the motion of dislocations within materials is found to be one of the main mechanisms resulting in the occurrence of plastic deformation, wherein the slip plane within the material is recognised as the most preferred plane that the dislocations

can move along. Metals like magnesium with HCP crystal structure has relatively less slip systems and this feature makes it become less ductile than those materials with FCC or BCC crystal structure. In general, the number of dislocations will significantly increase during deformation. Therefore, large number of dislocations will multiply and accumulate in the shearing area adjacent to the cutting edge before the forming of a completed chip during machining process. For the Mg composites, the activation of new non-basal slips within composite materials due to the addition of nano-sized reinforcements could ease the movement of dislocations and therefore less cutting forces are required for chip formation. Conversely, for the pure Mg the mobility of dislocations is restricted owing to the lower intensity of slip systems compared to Mg nanocomposites (Seetharaman *et al.*, 2013; Sankaranarayanan, Pranav Nayak, *et al.*, 2014) and consequently dislocation density instantly increases at large deformation conditions. As a result, higher cutting forces are required to initiate the plastic deformation in machining process.

3.5.2 Influence of nanoparticles contents and materials on surface roughness and morphology

The effect of feed per tooth on the surface roughness of Mg and its nanocomposites was given in Figure 3.10 (a). Unlike the trend of cutting forces with various feed per tooth, a decreasing rate can be observed in surface roughness of all specimens with the feed per tooth increase from 1 to 2 μm . This is because when the feed per tooth is less than the cutting edge radius, an elastic recovery and minimum chip thickness will occur at the tool-chip interface resulting an increased surface roughness. For pure Mg and its nanocomposites with 2.5 wt.% ZnO and 2.5 wt.% BN, the surface roughness increase with feed per tooth from 2 to 3 $\mu\text{m}/\text{tooth}$ and then followed by a decrease from 3 to 4 μm , however a reverse trend for Mg/0.5 wt.%BN and Mg/0.5 wt.%ZnO is observed. According to Figure 3.10 (b), pure Mg and its composites with 2.5wt.% ZnO exhibits higher surface roughness than others specimens. The effect of depth of cut on surface roughness is illustrated in Figure 3.10 (c). It is noticed that value of surface roughness for machining Mg/2.5wt.%ZnO is more sensitive to machining parameters than other specimens. The general trend of surface roughness is increasing with the depth of cut for all specimens.

Prior to the SEM qualitative analysis, the machined specimens are cleaned by an ultrasonic cleaner with immersion of acetone with the aim to protect machined surface from oxidation. Figures 3.11 and 3.12 illustrate the SEM micrographs of machined surface and its magnified SEM pictures captured at an arbitrary position for pure Mg and Mg/2.5wt.% BN respectively. Distinct milling tool path can be observed on the machined surface for pure Mg. Micro defects

can be found at the tool path which broke its continuity. This might be caused by the scratching of residual chips at the tool-chip interface during high speed machining. This can be considered as one of the main reasons that deteriorates the quality of machined surface. As compared to the machined surface for Mg/2.5wt.% BN, the clear tool path and micro defects on pure Mg make it becomes deteriorative than that for Mg/2.5wt.% BN. This result shows a proper agreement with the finding that the surface roughness for machining pure Mg is higher than that for Mg/2.5wt.% BN.

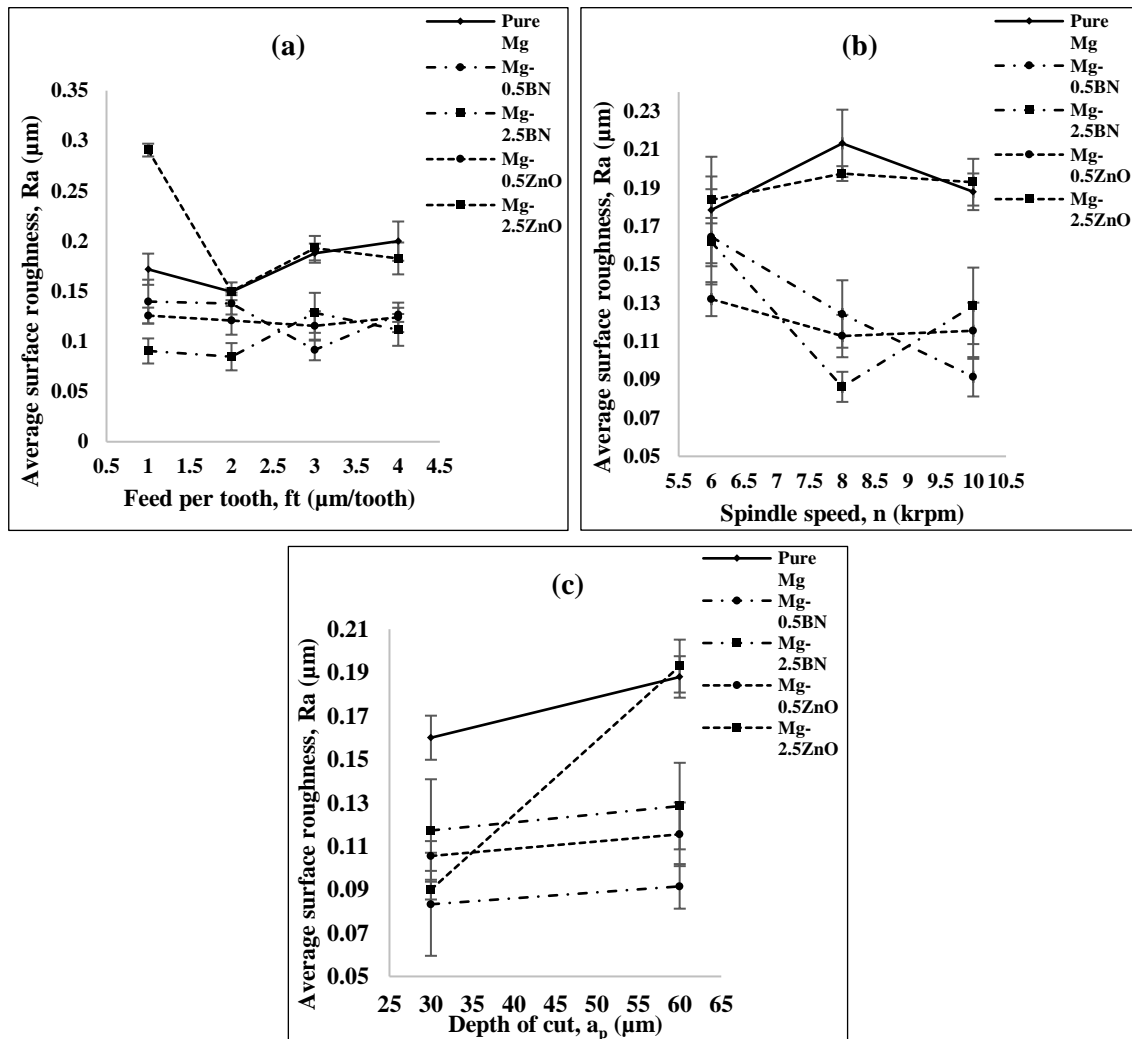


Figure 3.10 The effect of different cutting parameters on surface roughness in machining pure Mg and its nanocomposites (a) effect of feedrate at depth of cut of 60 μm and a spindle speed of 10,000 rpm; (b) effect of spindle speed at feed per tooth of 3 $\mu\text{m/tooth}$ and depth of cut of 60 μm ; (c) effect of depth of cut at spindle speed of 10,000 rpm and feed per tooth of 3 $\mu\text{m/tooth}$.

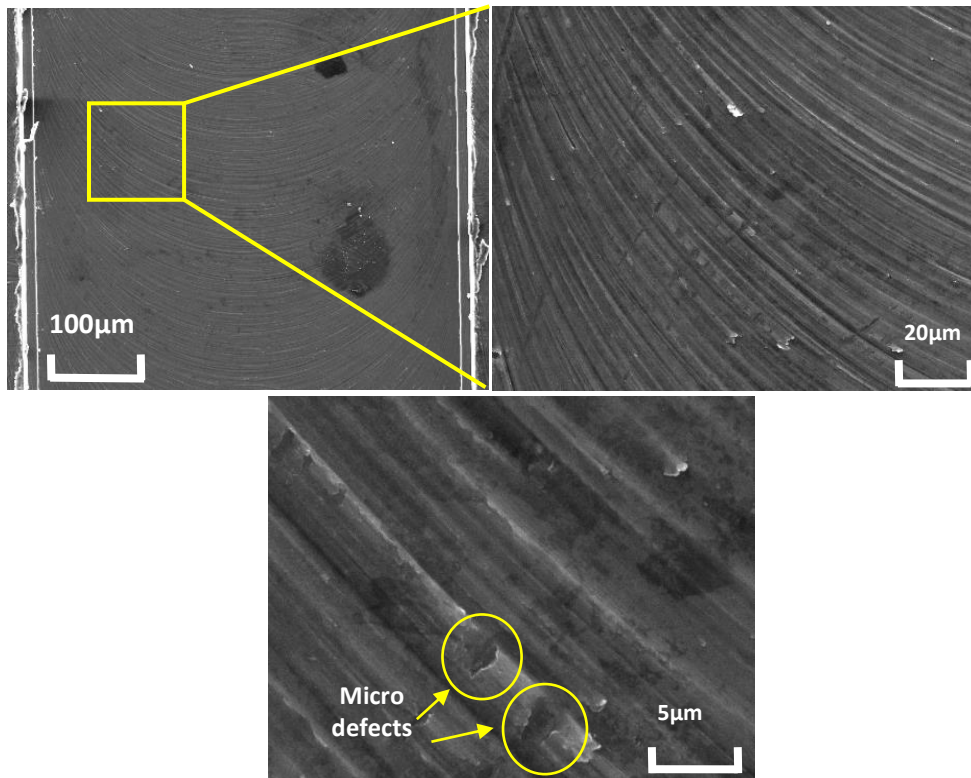


Figure 3.11 SEM micrographs of machined surface for pure Mg at feed per tooth of 1μm/tooth, spindle speed of 6,000rpm and depth of cut of 30 μm.

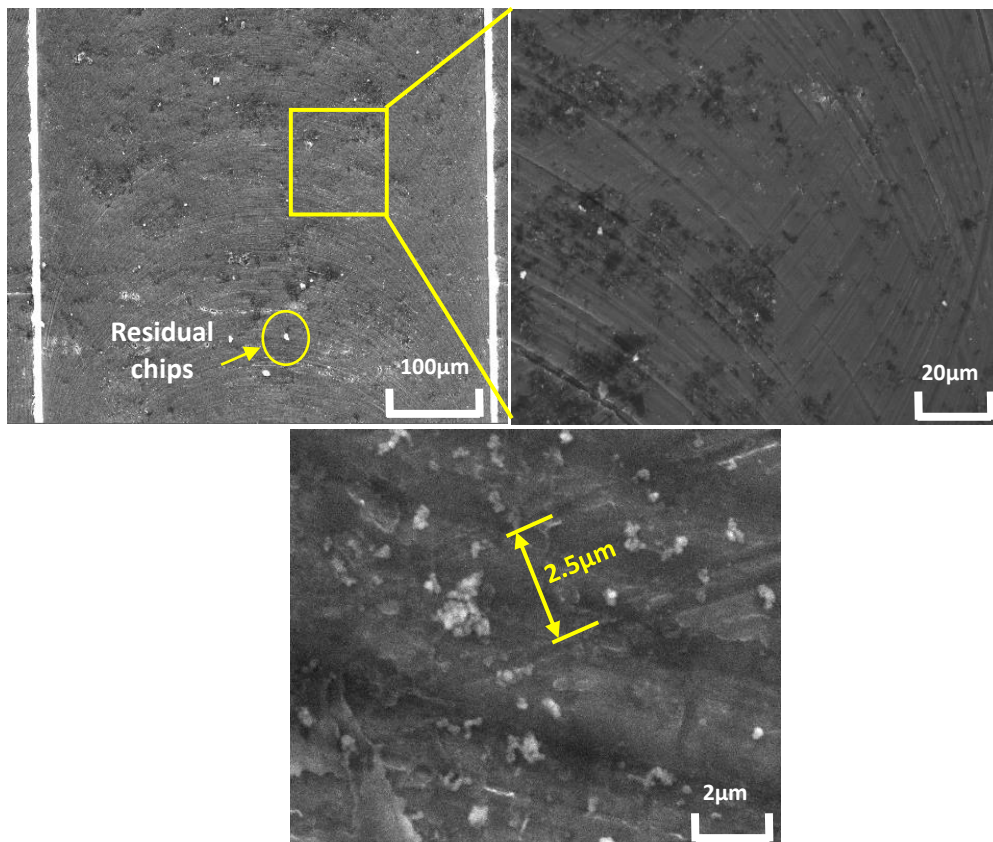


Figure 3.12 SEM micrographs of machined surface for Mg/2.5 wt.% BN at feed per tooth of 1μm/tooth, spindle speed of 6,000rpm and depth of cut of 30 μm.

A significant difference of surface morphology can be found between pure Mg and Mg/2.5wt.%BN. Unlike the regular tool path with large density on pure Mg, for the case of machining Mg/2.5wt.%BN the overlap of milling tool path can be found on the machined surface which is considered as the sign of the machined surface being cut repeatedly. As the value of feed per tooth is smaller than minimum chip thickness, a portion of material will be pushed by the cutting edge and then elastically recover to its original position after tool pass instead of being removed plastically. Consequently, the machined surface will be cut repeatedly. The tensile ductility is improved as compared to pure Mg due to the addition of nano-sized reinforcement and consequently facilitating the elastic recovery. For machining traditional MMCs with micro-sized particles, void marks could be left on the machined surface due to pulling out of particles. This is recognised as one of the reasons causing the poor surface finish. However, the void marks are absent on the machined surface in machining Mg/2.5wt.% BN with nanoparticles. This might be due to the following reason: i) the size of nanoparticles dramatically reduced to nano-scale, ii) lower volume fraction compared to micro particles which make them very difficult to be observed using SEM microscope. Also the lower surface roughness for Mg/2.5wt.% BN when compare to that for MMCs with micro-sized particles revealed a relatively good machinability.

3.5.3 Influence of nanoparticles contents and materials on chip formation

Figure 3.13 shows the SEM micrographs of chips during cutting pure Mg, Mg/2.5wt.%BN and Mg/2.5wt.%ZnO. As compared to the pure Mg, chips with different morphology can be found in machining MMCs. It is believed that the shape of chips formed is related to the material properties and the investigation on chip formation combining with metal machining theory is one of the effective way to reveal the material processing characteristic.

Segmented chip formation can be found in all three materials. According to the observation on Figure 3.13 (b) and (c), it can be seen that long spiral chips and long straight chips were found on machining pure Mg and Mg/2.5wt.%ZnO MMCs. Although the particles size is reduced to nano-size level and its weight fraction is significantly smaller than that for traditional MMCs, a high stress concentration induced around the particles as MMCs experiences high strain in primary shear zone might be thought as one of the main reasons initiating the fracture of chips.

For the Mg/2.5wt.%BN, Figure 3.13 (a) illustrates tightly curled and short shape chips comparing to pure Mg. It is well known that the material in front of cutting edge which is adjacent to the root of formed chips undergoes compressive stress, meanwhile, according to the mechanical test in previous research (Sankaranarayanan, Sabat, *et al.*, 2014), the compressive

ductility for Mg/2.5wt.%BN (17.6 ± 2.0 %) is less than that for pure Mg (20.7 ± 0.9 %). Therefore, this makes the chips become more brittle under compressive stress and easy to fracture when compare to that in machining pure Mg. Additionally, by relating the surface roughness with the morphology of formed chips it can be found that the longer chips produced from machining pure Mg and Mg/2.5wt.% ZnO could generate a rougher surface roughness.

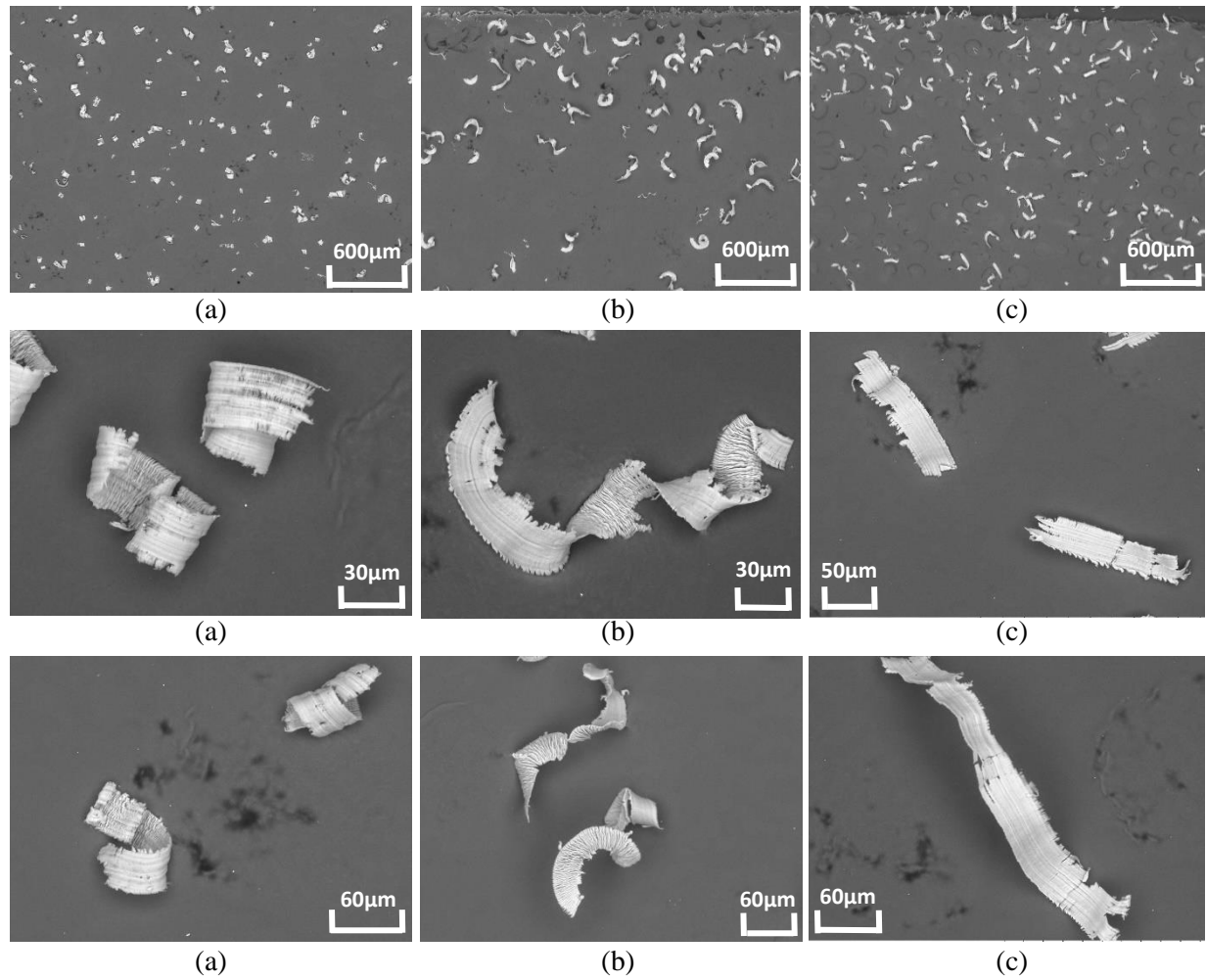


Figure 3.13 SEM morphology of chips of (a) Mg/2.5wt.% BN; (b) pure Mg; (c) Mg/2.5wt.% ZnO (at feed per tooth of $0.5\mu\text{m}$, depth of cut of $30\mu\text{m}$, spindle speed of 6,000rpm).

3.6 Conclusions

In this chapter, two individual micro-end milling experiments were conducted to comprehensively study the micro machinability of Mg-based metal matrix composites reinforced with nanoparticles using AlTiN coated carbide end mills. The influence of various experiment parameters on the cutting force and surface quality was analysed. The size effect was investigated and minimum chip thickness was obtained according to specific cutting energy

and surface morphology. Additionally, the effect of different weight fraction and reinforcement materials on the micro machinability of Mg-based MMCs was studied. Moreover, the machinability of Mg-based MMCs was compared with that of pure Mg in order to explain the effect of micro structure changes occurring within MMCs due to the addition of nanoparticles. The following conclusions can be drawn from this chapter:

- The cutting force would increase with the depth of cut and feed per tooth which is larger than the minimum chip thickness. An approximate 2 times larger cutting force was obtained in the machining of Mg/Ti MMC compared to that for Mg/TiB₂. The surface roughness would rise with the increase of feed per tooth and spindle speed, but the trend with depth of cut were opposite on cutting two MMCs. Based on the ANOVA, the spindle speed and depth of cut has significant influence on surface roughness.
- The minimum chip thickness is determined to be 0.8 μm and 0.5 μm for Mg/Ti and Mg/TiB₂ respectively which is 53% and 33% of the cutting edge radius in this experiment. Therefore, for machining Mg/Ti MMCs and TiB₂ MMCs feed per tooth under minimum chip thickness is not recommended.
- The Mg/TiB₂ MMCs exhibit better machinability compared to Mg/Ti MMCs in terms of surface morphology. More burrs could be found at slot edges after machining Mg/Ti MMCs. Up milling side could generate slot edges with better quality and less burrs in machining of Mg/Ti MMCs.
- The cutting force for machining pure Mg was found to be larger than other specimens except for Mg/2.5wt.%ZnO at all conditions. This could be explained as the addition of nanoparticles in MMCs facilitate the mobility of dislocation by increasing the density of slip planes in crystal plane and consequently reduce of the amount of force that required to initiate the plastic deformation.
- As expected, the cutting force would increase with the depth of cut and feed per tooth in all specimens. Among then, machining force for Mg/ZnO MMCs was much larger than that for Mg/BN MMCs.
- A surface morphology observation revealed a significant difference between the machined surface of pure Mg and Mg/2.5wt.%BN which was attributed to elastic recovery caused by the increased tensile ductility of Mg/2.5wt.%BN. Meanwhile, the common surface defect like void marks in machining traditional MMCs with micro-sized particles was not found in this experiment. Also a finer surface roughness could be generated by nano-sized Mg MMCs when compared to the traditional one.

- Different chip morphology was found in machining pure Mg and other two types of MMCs. Formed chips of Mg/2.5%wt.%BN exhibited the shortest and tightly curled shape feature due to its reduced compressive ductility.

Chapter 4 Modelling of machining micro-sized & nanoparticle reinforced MMCs

4.1 Introduction

In this chapter, a comprehensive investigation into the machinability of particulate-reinforced MMCs using finite element (FE) modelling is presented. The FE simulation is conducted using commercially available software ABAQUS/Explicit v6.14-4. The details of modelling procedure will be presented.

The machinability of MMCs reinforced with particle in different size, namely, nano-sized and micro-sized, will be discussed in details. Moreover, a comparison between machining micro and nano-MMCs and very detailed explanations are given for every different phenomenon. Model validation is conducted by performing machining experiment.

4.2 Overview of finite element (FE) method formulation

Several input factors for FEM such as assignment of workpiece material properties (material constitutive model), criteria of chip separation (fracture criteria), friction within tool-chip interface and strategies of mesh generation are essential to provide model that is close to realistic. The selection of appropriate factors critically affects the quality of output during the simulation. Among these factors, materials constitutive models, fracture criteria and friction models have been recognised as the three most important factors and receive plenty of attentions from researchers.

4.2.1 Materials constitutive modelling formulation

An accurate material constitutive model is one of the most critical aspects to describe the behaviour of material deformation during the machining process. In reality, the workpiece material during the machining process undergoes extreme conditions such as high strain, strain rate and increase in temperature. A high level of plasticity was observed in the primary and secondary shear zones. Meanwhile, a work hardening effect triggered by the fast strain rate of workpiece plays an important role in determine its instantaneous mechanical properties, whilst the material properties measured in quasi-static conditions no longer govern the plastic behaviour. Number of material constitutive models used for describing the response of stress and strain and also its dependence on strain and strain rate hardening and temperature softening effect has been proposed by researchers.

Among these material constitutive models, Johnson-Cook equation (Johnson and Cook, 1983) (equation 9) has been widely used in FEM with adiabatic transient dynamic simulations. The factors affecting the flow stress within workpiece were classified into three terms including the elastic-plastic term to represent the strain hardening, the viscosity which present the increase in flow stress with high strain rate and the temperature softening effect term (equation 9).

$$\bar{\sigma} = [A + B(\bar{\epsilon}^{pl})^n] \left[1 + C \ln\left(\frac{\dot{\bar{\epsilon}}^{pl}}{\dot{\epsilon}_0}\right) \right] \left[1 - \left(\frac{T - T_{room}}{T_{melt} - T_{room}} \right)^m \right] \quad (9)$$

Where $\bar{\sigma}$ is the flow stress, $\bar{\epsilon}^{pl}$ is the plastic strain, $\dot{\bar{\epsilon}}^{pl}$ is the plastic strain rate, $\dot{\epsilon}_0$ is the reference strain rate, T is the workpiece temperature, T_{melt} and T_{room} are the material melting and ambient temperature. Coefficient A is the yield strength, B is the hardening modulus, C is strain rate sensitivity coefficient, n is the hardening coefficient, m is the thermal softening coefficient and these material coefficients are determined by experiments.

By considering the crystal structure of material, Zerilli and Armstrong (Zerilli and Armstrong, 1987) proposed a material constitutive model (equation 10&11) based on the theory of dislocation mechanics. Two models based on the lattice structure of workpiece including the body centre cubic (BCC) and face centre cubic (FCC) was established, as described respectively.

$$\bar{\sigma} = C_0 + C_1 \exp[-C_3 T + C_4 T \ln(\dot{\bar{\epsilon}}^{pl})] + C_5 \bar{\epsilon}^{pl} \quad (10)$$

$$\bar{\sigma} = C_0 + C_2 \bar{\epsilon}^{pl} \exp[-C_3 T + C_4 T \ln(\dot{\bar{\epsilon}}^{pl})] \quad (11)$$

Where $C_0 - C_5$ are materials constants determined through experiments. T is the absolute temperature.

The selection of material constants in constitutive models can make a critical effect on the outcomes such as stress and strain distribution, cutting force, temperature field, and chip morphology. Acquisition of these constants experimentally is a relative complex process since the experimental data is necessary to be acquired under the deformation conditions that cover large range of strains, strain rate and temperature. A number of constitutive models are also available to model the workpiece such as Mecking-Kocks (Follansbee and Gray, 1989) model with 23 material constants and a physical based model with number of necessary constants from 8 - 12 presented by Nemat-Nasser (Nemat-Nasser *et al.*, 2001). As J-C model and Z-A model require less constants than the aforementioned two models, they are widely used in material

modeling studies. Additionally, numbers of research have been done to determine the constants for various materials and can be easily acquired from the past literatures.

4.2.2 Fracture criterion

As mentioned in section of 2.5.1, chip separation criterion must be employed in pure Lagrangian formulation. Materials separation is a complex process including many physical mechanism occurring at micromechanical level (Dandekar and Shin, 2012). Stress and strain were recognised as two main tensors that cause the initiation and evolution of materials fracture. In commercial FEM software, the fracture mechanism can be classified into ductile fracture and shear fracture. In ductile fracture, the voids would undergo the nucleation, growth and coalescence and eventually fracture. The mechanism in the shear fracture is mainly based on the shear band localisation. Recently, several fracture criteria for the ductile metal have been proposed and are widely used in various areas such as impact, fatigue analysis and metal forming process, which are (1) constant strain criterion and maximum shear stress criterion, (2) Johnson-Cook fracture criterion and (3) Cockcroft-Latham fracture criterion. Some of them are either built in commercial available software or implanted through user defined subroutine.

4.2.2.1 Constant strain criterion

Constant strain criterion (equation 12) has been employed in many researches regarding metal cutting and forming (Shi and Liu, 2006; Simoneau, Ng and M.A. Elbestawi, 2006; Pramanik, Zhang and Arsecularatne, 2007). This criterion is assumed to be satisfied when the equivalent plastic strain reaches a critical value (equivalent strain at onset of fracture) and the nodal point of workpiece in front of the tool tip will be separated resulting the separation of chips. The disadvantage of this fracture criterion requires high computational cost.

$$\omega_D = \int \frac{d\bar{\varepsilon}^{pl}}{\bar{\varepsilon}_f^{pl}} = 1 \quad (12)$$

Where ω_D is a state variable.

The equivalent plastic strain at onset of fracture is assumed to be a function of stress triaxiality and strain rate ('Abaqus/Explicit V6.14 User manual', 2016):

$$\bar{\varepsilon}_f^{pl}(\eta, \dot{\bar{\varepsilon}}^{pl}) \quad (13)$$

Where $\eta = -p/q$ is the stress triaxiality, p is the pressure stress, q is the Mises equivalent stress, $\dot{\bar{\varepsilon}}^{pl}$ is the equivalent strain rate.

4.2.2.2 Johnson-Cook fracture criterion

Johnson-Cook fracture criterion (equation 14) it is a function of strain and strain rate hardening effect and temperature softening. It has been widely used to define the fracture criterion in metal machining. The equivalent plastic strain at the onset of fracture, $\overline{\varepsilon}_f^{pl}$, is defined as

$$\overline{\varepsilon}_f^{pl} = (d_1 + d_2 e^{d_3 \eta}) \left[1 + d_4 \ln\left(\frac{\dot{\varepsilon}^{pl}}{\dot{\varepsilon}_0}\right) \right] \left[1 + d_5 \left(\frac{T - T_{room}}{T_{melt} - T_{room}} \right) \right] \quad (14)$$

Where $d_1 - d_5$ are fracture parameter obtained from experiments, $\eta =$ is the stress triaxiality and $\dot{\varepsilon}_0$ is reference strain rate.

A damage parameter D is defined in each analysis increment and the element would be deleted once damage parameter D reaches unit value.

$$D = \sum \frac{\Delta \varepsilon^{pl}}{\overline{\varepsilon}_f^{pl}} \quad (15)$$

Johnson-Cook semi-empirical fracture criterion and the constants can be determined through tensile test, shear test or Hopkinson bar torsion with extensive strain rate and temperature (Dandekar and Shin, 2012).

4.2.2.3 Cockcroft-latham fracture criterion

The Cockcroft-Latham fracture criterion was originally proposed for bulk forming operations (equation 16). However a modified criterion was applied in machining simulation by numerous researchers (Ceretti, Lucchi and Altan, 1999; Hua J and Shivpuri, 2002; Aurich and Bil, 2006). The main disadvantage of this criterion is that it can be only applied in small and negative triaxiality (Dandekar and Shin, 2012). Same as other aforementioned criterion, the onset of fracture initiates when the critical damage value, C , obtained through integral of the normalised maximum principal stress reaches the predefined value determined from tensile test.

$$C = \int_0^{\varepsilon_f} \sigma^* d\bar{\varepsilon} \quad (16)$$

where $\sigma^* = \frac{\langle \sigma_1 \rangle}{\bar{\sigma}}$, the value of σ_1 is defined to be unity within this function if $\sigma_1 > 0$, and zero if $\sigma_1 < 0$, $\bar{\sigma}$ is equivalent stress

4.2.2.4 Fracture criterion coupled with damage evolution step

Generally, damage evolution step which is based on the accumulation of stress and strain can be used in combination with the fracture criteria aforementioned to model the progressive

damage and failure of workpiece material. The materials failure process was divided into two steps, the first step introduces the damage imitation and second one introduces the damage evolution. Two approaches can be employed to define evolution process including dissipated energy and effective plastic displacement.

Figure 4.1 presents the stress-strain response during the damage process. From point A to B, the material undergoes plastic strain with hardening effect. Damage initiation is not satisfied at point B until the damage parameter D reaches unity, and σ_{y0} and $\bar{\epsilon}_0^{pl}$ are the yield stress and equivalent plastic strain. After point B, the material undergoes the damage evolution process whilst the load-carrying capability is reduced until reaches the failure state.

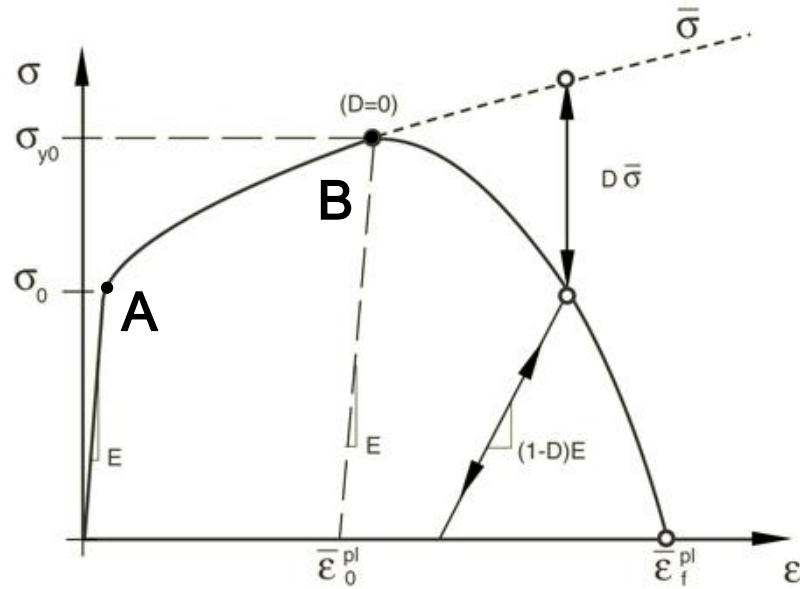


Figure 4.1 Stress-strain curve of damage evolution process. ('Abaqus/Explicit V6.14 User manual', 2016)

During the damage evolution process, strain-stress response cannot be used to illustrate the damage behaviour since it can cause a strong mesh-dependency based on strain localisation. Therefore, a fracture energy based approach (equation 17) was proposed by Hillergorg (Hillerborg, Mod  er and Petersson, 1976). The energy, G_f , was defined as a material parameter required to open a unit area of crack. By utilising this approach, the mesh dependency is reduced and the damage behaviour after the onset of fracture is decreased through a stress-displacement response.

$$G_f = \int_{\bar{\epsilon}_0^{pl}}^{\bar{\epsilon}_f^{pl}} L \sigma_y d\bar{\epsilon}^{pl} = \int_0^{\bar{\mu}_f^{pl}} \sigma_y d\bar{\mu}^{pl} \quad (17)$$

where L is the characteristic length, $\bar{\mu}^{pl}$ is the equivalent plastic displacement.

This approach introduces the equivalent plastic displacement, $\bar{\mu}^{pl}$ as the fracture work conjugate of the yield stress after the damage initiation point. The value of $\bar{\mu}^{pl}$ is defined as zero before the damage initiation and $\bar{\mu}^{pl} = L\bar{\epsilon}^{pl}$ once the damage initiation criterion is satisfied.

For the damage evolution defined in terms of equivalent plastic displacement, a damage variable d ($d=0$ at damage initiation point) was defined.

$$d = \frac{L\bar{\epsilon}^{pl}}{\bar{\mu}_f^{pl}} = \frac{\bar{\mu}^{pl}}{\bar{\mu}_f^{pl}} \quad (18)$$

Once damage variable d reaches unity, it can be thought that the load-carrying capability of material is fully degraded, namely the failure of workpiece would occur. With the damage evolution defined in terms of energy, the equivalent plastic strain at failure can be expressed as:

$$\bar{\mu}_f^{pl} = \frac{2G_f}{\sigma_{y0}} \quad (19)$$

4.2.3 Friction between tool-chip interface

The friction characteristic at tool-chip interface is one of the factors that greatly affect the simulated results. There are two shear zones taking place at the vicinity of cutting tool; primary shear zone due to the large strain and strain rate, secondary shear zone due to the friction at tool-chip interface. The friction characteristic is a very complex process. Large amount of heat can be generated due to friction at tool-chip interface with high cutting speed leading to a high temperature field, which eventually facilitate the process of excessive tool wear. The simplest way is to experimentally acquire a constant coefficient of friction and apply it along the tool-chip interface.

In most studies, Coulomb friction law combining with sticking-sliding theory is applied to simulate friction stress. Two regions including sticking and sliding are established along the tool-chip interface. A sticking region forms at the vicinity of cutting tool and the friction shear stress (equation 20) is equal to the average shear flow stress in the chips, k_{chip} (Maekawa.K *et al.*, 2000). Once the shear stress at interface reaches a critical value (limiting shear stress), sliding regime (equation 21) govern the friction process. Sliding region forms along the

remainder region along the interface and the friction shear stress can be determined using a coefficient of friction, μ .

$$\tau_{sticking} = k_{chip} \text{ when } \mu\sigma_n < \tau_{lime} \quad (20)$$

$$\tau_{sliding} = \mu\sigma_n \text{ when } \mu\sigma_n \geq \tau_{lime} \quad (21)$$

where τ_{lime} is the limiting shear stress, σ_n is normal stress distribution along the rake face, $\tau_{sticking}$ is friction shear stress along the sticking region, $\tau_{sliding}$ is friction shear stress along sliding region, μ is the friction coefficient.

4.3 Case i: Cutting mechanism of MMCs reinforced with nanoparticles

This case attempts to establish a novel micro-mechanical finite element (FE) model to simulate the micro machining process of nano Mg/SiC MMCs considering the cutting edge radius. Unlike the previous research using large volume fraction of micro particles, the nanoparticles (100nm in diameter) is modelled with a volume fraction of 1.5%. It is clear that the uncut chip thickness will make significantly effect on the machining process, especially in micro machining process under size effect. This case will particularly focus on the behaviour of MMCs such as chip formation mechanism, tool-particles interaction, stress distribution and cutting force at small depth of cut. A validation has been made with the experimental results for a range of uncut chip thickness.

4.3.1 FE modelling procedures

4.3.1.1 Simplification of 2D milling to orthogonal machining process

An assumption (Lai *et al.*, 2008) has been made for simplifying 2D micro milling process to orthogonal machining process. In micro milling experiment conducted within this study, the maximum uncut chip thickness t (less than 2 μm) is much smaller than the diameter of micro endmill (500 μm) as shown in Figure 4.2 (a), which results in relatively small variation of uncut chip thickness (2 μm) when compared with the travel distance of cutting edge in 180° of tool rotation (~392.5 μm), namely it can be thought that the variation of uncut chip thickness will not make significant influence on results (cutting force, chip morphology). Therefore, the uncut chip thickness in micro milling process can be considered to be equivalent to that in orthogonal machining process as shown in Figure 4.2 (b).

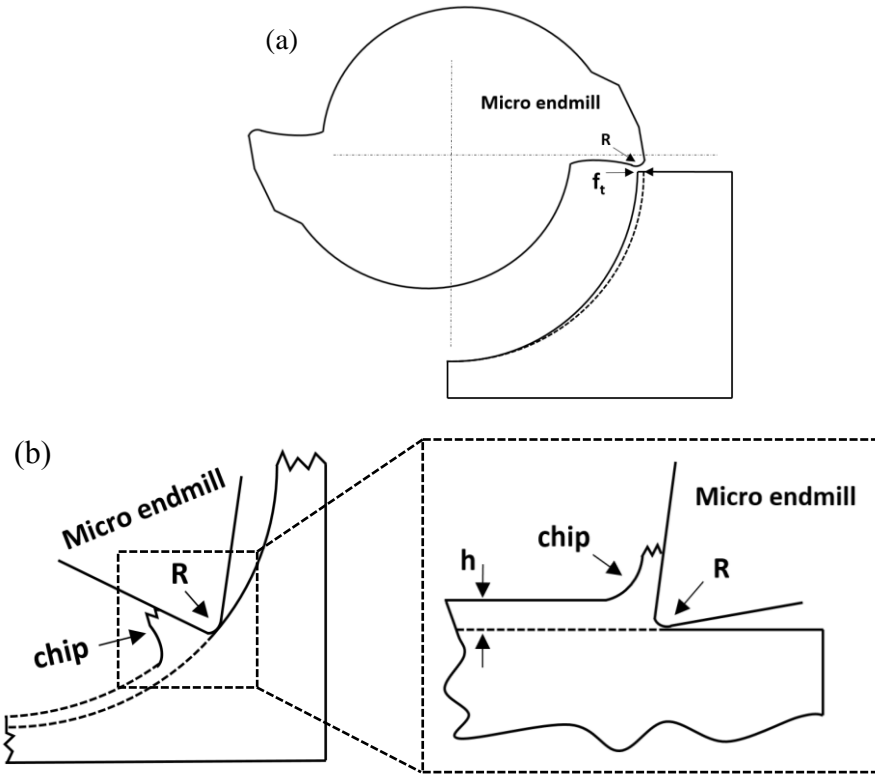


Figure 4.2 (a) Schematic diagram of 2D milling process in 180° of tool rotation; (b) Relationship between 2D milling process to orthogonal machining process [17].

4.3.1.2 Model setup

A two-dimensional micro-mechanical finite element model is established to simulate the micro-orthogonal machining process of nano Mg/SiC MMCs using commercially available software ABAQUS/Explicit v6.14-4. Since the nonlinearity, large strain and strain rate are involved in machining process, Arbitrary Lagrangian Eulerian (ALE) formulation is selected to avoid severe distortion of elements. The schematic representation of the established model is shown in Figure 4.3. Analytical rigid body is assigned to the cutting tool which moved horizontally into workpiece with a predefined speed. In order to get a better understanding of details of machining process, two phases materials including matrix and particles are assigned individually in this model. The particle diameter is defined as 100 nm with volume fraction of 1.5%. The machining parameters are listed in Table 4.1.

Table 4.1 Machining parameters in FE model

Cutting speed, V_c (m/min)	125.64
Uncut chip thickness, t (μm)	0.1, 0.2, 0.5, 1, 2
Tool rake angle, α (Degree)	10
Tool clearance angle, β (degree)	6
Cutting edge radius, (μm)	1

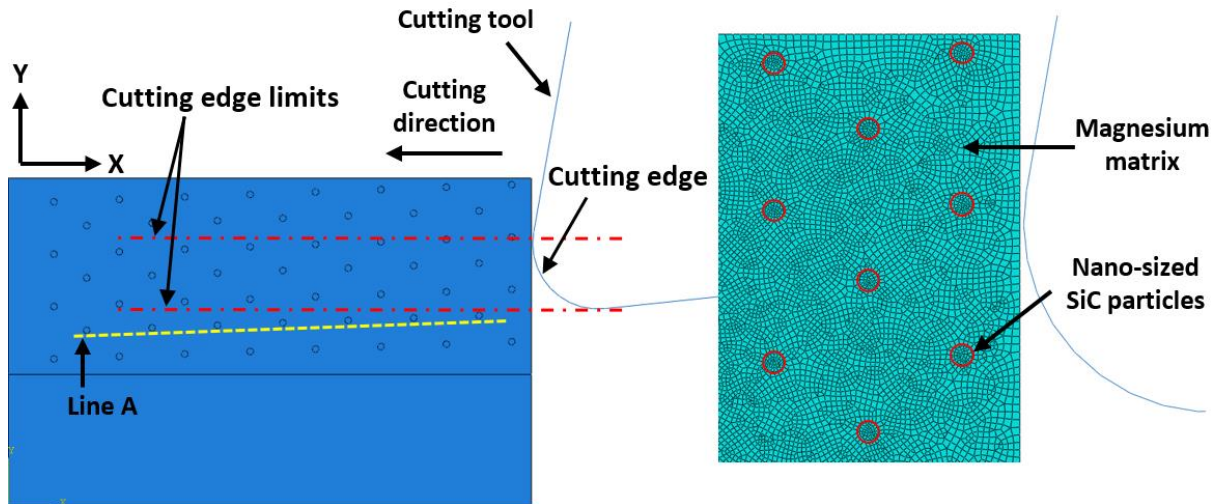


Figure 4.3 (a) Schematic representation of the established models for micro orthogonal machining of Mg/SiC MMCs; (b) local zooming of mesh element.

A particles distribution strategy that makes the particles distributed at different relative locations of cutting path is used in this model as shown in Figure 4.3 (a). Within this strategy, the distance between each particle in X and Y direction is same, while the distance between the uppermost particles and top surface of the workpiece is 50 nm larger in Y direction than the last column from right to left side. For example, particles along line A distribute further away from bottom cutting edge limits, which simulate the diversity of particles locations relative to the cutting path in reality.

4.3.1.3 Material modelling

Magnesium matrix is treated as a deformable thermo-elastic-plastic material with quadrilateral continuum element and fracture criteria. As one of the most commonly used constitutive models for predicting flow stress within metallic materials subjected high strain, strain rate and temperature, the Johnson-Cook constitutive model is used to describe the plasticity behaviour of magnesium matrix during machining process. Johnson-Cook fracture equation is used to

define the materials failure criterion for magnesium matrix. The mechanical properties and material constants of Mg in J-C model are listed in Table 4.2.

SiC particles were assumed to be brittle cracking body with brittle failure definition in order to investigate its behaviour during cutting process. The mechanical and brittle cracking properties are shown in Table 4.3.

Table 4.2 Mechanical properties and materials constant in J-C model for magnesium matrix (Ulacia *et al.*, 2011)

Density (ton/mm ³)	1378×10 ⁻¹²
Young's Modulus (MPa)	39820
Poisson's Ratio	0.35
T _{melt} (K)	873
T _{transition} (K)	293
Thermal expansion (K-1)	25×10 ⁻⁶
Thermal Specific Heat (mJ/ton*K)	914×10 ⁶
Conductivity (mW/mm*K)	156
A (MPa)	153
B (MPa)	291.8
n	0.1026
m	1.5
C	0.013
d ₁	0.5
d ₂	0.2895
d ₃	3.719
d ₄	0.013
d ₅	1.5

Table 4.3 Mechanical and brittle cracking properties for SiC particle

Density (kg/mm ³)	3200
Young's Modulus (MPa)	408000
Poisson's Ratio	0.35
Thermal Specific Heat (J/kg*K)	755
Conductivity (W/m*K)	120
Compressive Strength (MPa)	3900

4.3.1.4 Boundary condition and contact definitions

Free thermal-displacement quad-dominated meshing technique is used with combination of advancing front algorithm for both matrix and particles (Figure 4.2(b)). Mesh size of particles

and matrix surrounding particles is defined to be 25 nm and 40 nm. The bottom surface of the models was fixed in all directions.

Cohesive element and shared nodes are two common methods employed to model the interface between the particles and matrix. A cohesive layer with appropriate properties and fracture criterion is essential to generate accurate results. However, this method is not available for modelling Mg-MMC due to the absence in material properties. As a result, share nodes method was employed to model the interface. The interface nodes of magnesium matrix and SiC particles are tied together, resulting that the matrix and particles will exhibit the same behaviour at initial deformation. In order to implement shear node method, the pattern of particles were directly added on the workpiece using 'partition part' commend, which results in two main regions on the workpiece, namely matrix and particles. The properties of magnesium and SiC were then assigned onto these two regions respectively. The workpiece was finally globally meshed. Same implementation process for adding particles into matrix were used for the following two cases.

The surface-to-surface contact model is applied between the external surface of the tool and node points of machining area. In this study, due to the high cutting speed and high friction contributed by size effect, the high temperature generated is believed to make a significant contribution to plasticity behaviour of matrix material. This would make the sticking zone obvious during chip formation process. Therefore, Coulomb friction law combining with sticking-sliding theory is used to simulate friction stress.

4.3.2 Chip formation process analysis

According to previous studies on macro machining of micro MMCs (Zhou *et al.*, 2014; Wang, Xie and Wang, 2015; Ghandehariun *et al.*, 2016a, 2016b), addition of hard particles into matrix materials could greatly alter the cutting mechanism comparing with homogeneous materials. In fact, cutting tool edge radius is becoming one of the important factors governing the machining mechanism in micro machining process. In this section, the chip formation process in micro machining process will be studied in terms of chip morphology, stress/strain distribution within matrix and tool-particles interaction with consideration of cutting edge radius.

Figure 4.4 illustrates the simulated chip formation process under the uncut chip thickness of 1 μm . As shown in Figure 4.4 (a), when the tool firstly engages with the workpiece, a highly concentrated stress is induced leading to an irregular shear zone closely formed in front of the cutting edge, which is different from that in macro machining of MMCs where an obvious primary shear zone can be formed at initial cutting stage.

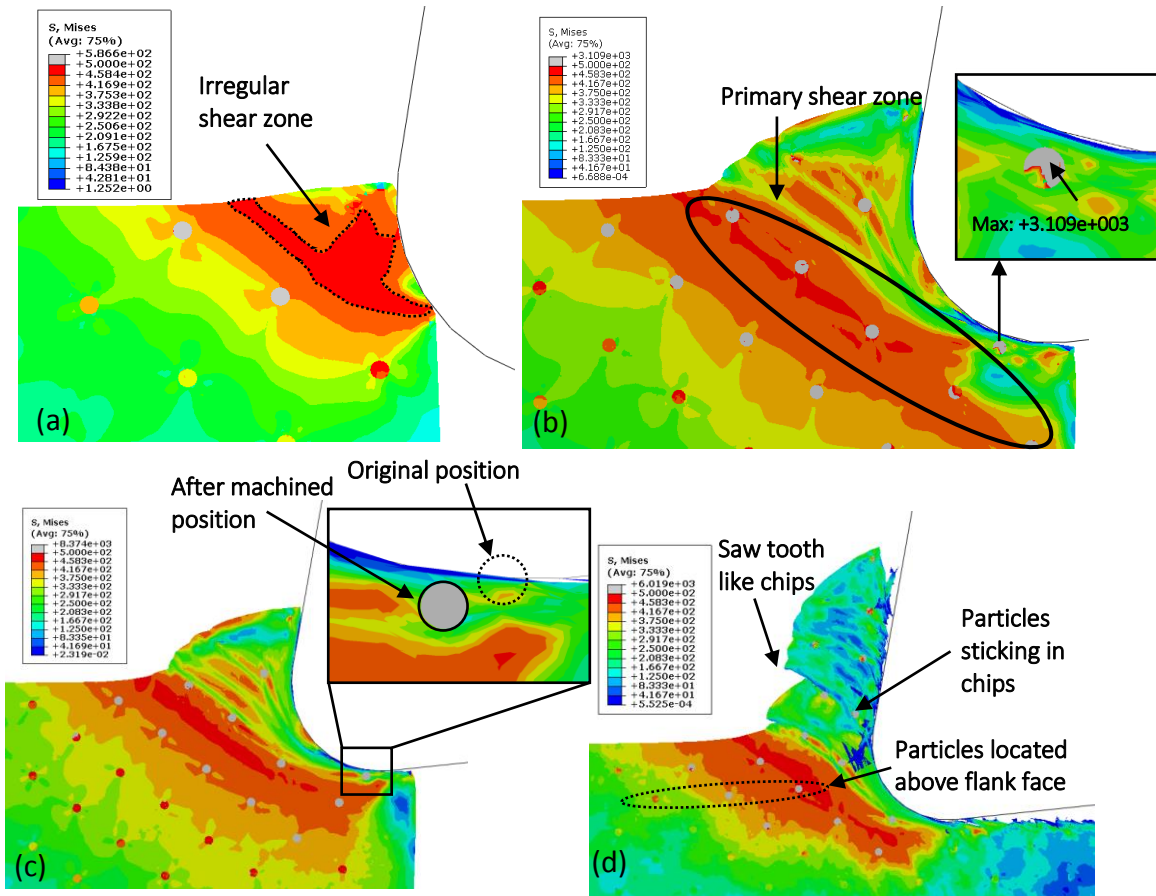


Figure 4.4 Chip formation process during micro-machining of nano Mg/SiC MMCs

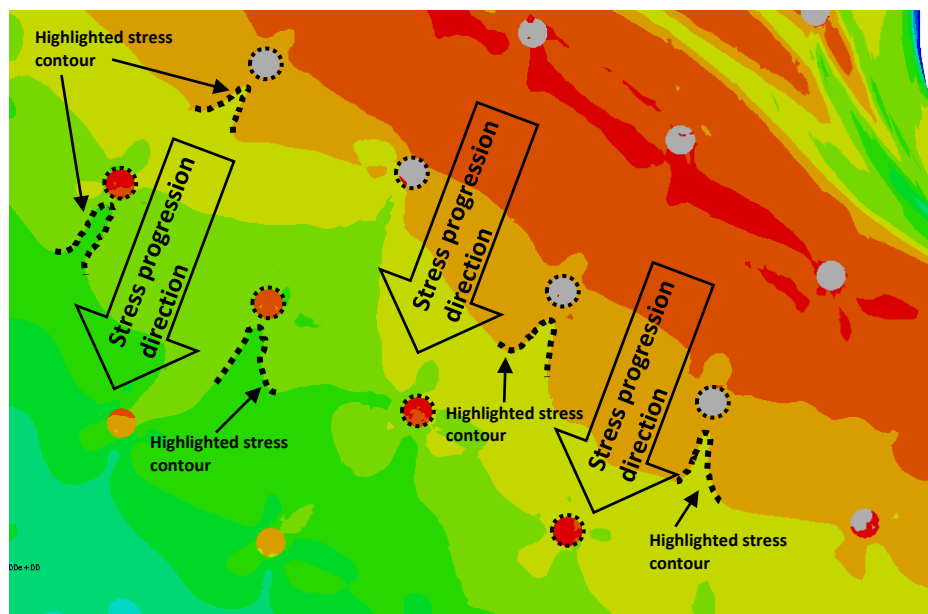


Figure 4.5 Effect of addition of nanoparticles on distribution pattern of von Mises stress contour

As the tool advances, the primary shear zone can be observed in Figure 4.4 (b). Additionally, it is clear that the particles take more stress than matrix material, especially those particles located near the primary shear zone. This might be attributed to the high elasticity of SiC particles. The maximum von Mises stress is found at the particles located under cutting edge which is 3109 MPa. This is different from that in machining monolithic materials where the maximum stress occurs in the primary shear zone. Moreover, another difference can be obtained through observing the von Mises stress distribution pattern in Figure 4.5. The addition of nanoparticles greatly alters the pattern of stress field within matrix. A distorted stress contour can be found at vicinity of each particle. This observation can be explained by the existence of particles in the matrix restricting the progression of plastic stress flow within matrix during machining. The stress is therefore accumulated and hence results in a high plastic strain field at particle interface as shown in Figure 4.6. The existence of nanoparticles also fragments strain field. Similar phenomena was reported by Pramanik et al. (Pramanik, Zhang and Arsecularatne, 2007) in machining of micro-sized Al/SiC MMCs.

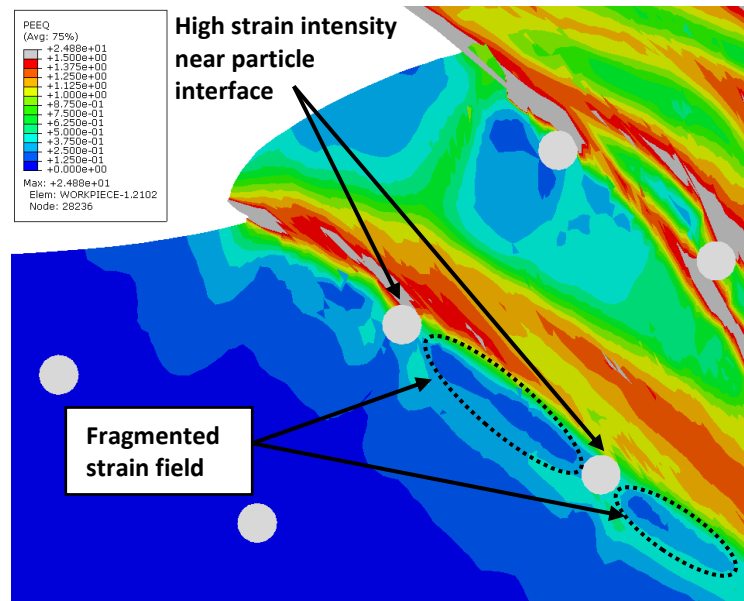


Figure 4.6 Distribution of equivalent plastic strain within nano Mg/SiC MMCs.

As the tool continuously moves, Figure 4.4 (c) shows the behaviour of particle located immediately under the flank face of the cutting tool when the tool is approaching to it. By comparing with the original position of this particle, it moves horizontally with the highly deformed matrix in cutting direction without any direct contact with the cutting edge. Evolution of von Mises stress on the matrix element surrounding the particle with approaching of cutting

edge is studied in Figure 4.7 in details. Initially, the von Mises stress is found to increase to maximum value of 454 MPa (C) with advancement of the tool. At this stage, the particle is found at primary shear zone. As mentioned earlier, this particle acting as a barrier restricts the progression of plastic stress within matrix which results in a high compressive stress acting on the matrix close to particle interface. This is different to macro machining process where the maximum stress usually happens at the matrix between cutting edge and particles due to the indentation caused by the cutting edge (Pramanik, Zhang and Arsecularatne, 2007). Consequently, this results in a concentrated stress ranging from 540 to 650 MPa acting at particles A sudden drop in von Mises stress is followed from C to E as the primary shear zone moves horizontally passing through this particle. At this period, the restricting behaviour on plastic stress flow of particle becomes less dominant as particles moves with surrounding matrix with further advancement of the tool. It is believed that the matrix element experiences a highly plastic deformation within this stress drop process (C to E). Finally, von Mises stress releases and decreases to 0 MPa when the cutting edge is passing through it, resulting in a failure of matrix surrounding this particle. As a result, this particle is subjected to debonding from matrix.

The premature tool wear caused by the high contact stress between cutting tool and hard particles has been recognised as one of the important factors affecting the machinability of MMCs. The interaction process between cutting tool and particles should be better analysed to predict the tool wear. Figure 4.8 (a-d) illustrates the stress distribution on the particles located immediately below the cutting edge with advancement of the tool. Based on the observation of Figure 4.8 (a) and (b), the increase in von Mises stress can be observed on the particle due to the compressing of surrounded matrix with tool approaching to the particle. The direct contact between tool and particles can be found in Figure 4.8 (c). A highly concentrated stress on the upper part of particle is generated due to the ploughing between particle and flank face. This particle is then debonded and slide over the flank face (Figure 4.8 d). During the sliding process, particle acting like a sharp cutting edge scratches the flank face leading to abrasive wear. Smoother wear at flank face is expected due to the nanoparticles. Additionally, it is evident from this figure that the particle is still intact which is different with that in machining of micro-sized MMCs where particle fracture is observed.

Upon the advancement of cutting tool, the chip is completely formed (Figure 4.4 d). A complete chip-tool contact area is achieved with chip flow happening along the rake face. In this stage, the particles located above the flank face of cutting tool initially move with surrounding matrix and enter into the formed chips as the cutting edge approaches. Figure 4.4 (d) also illustrates a continuous chip with saw tooth appearance. This phenomenon can be explained by studying

the equivalent plastic strain distributed in the chip as shown in Figure 4.9. A large deformation is observed at the interface of chip and cutting tool. Moreover, it can be seen that several highly strained bands are distributed across the chips at vicinity of particles, which can be considered as the main reason contributing to the lamellate structure of chips. Essentially, those highly strained bands are caused by localised high plastic von Mises stress bands (Figure 4.10). Figure 4.10 illustrates the formation of high stress bands within chip with advancement of cutting tool. At initial stage, primary shear zone is observed in Figure 4.10 (a). As the tool further moves, transition stage is achieved (Figure 4.10 b). The concentrated stress field is observed at interface of particles as primary shear zone passing through due to particles' restricting behaviour to plastic stress flow as mentioned earlier. Figure 4.10 (c) shows eventually the high stress bands is formed within chips.

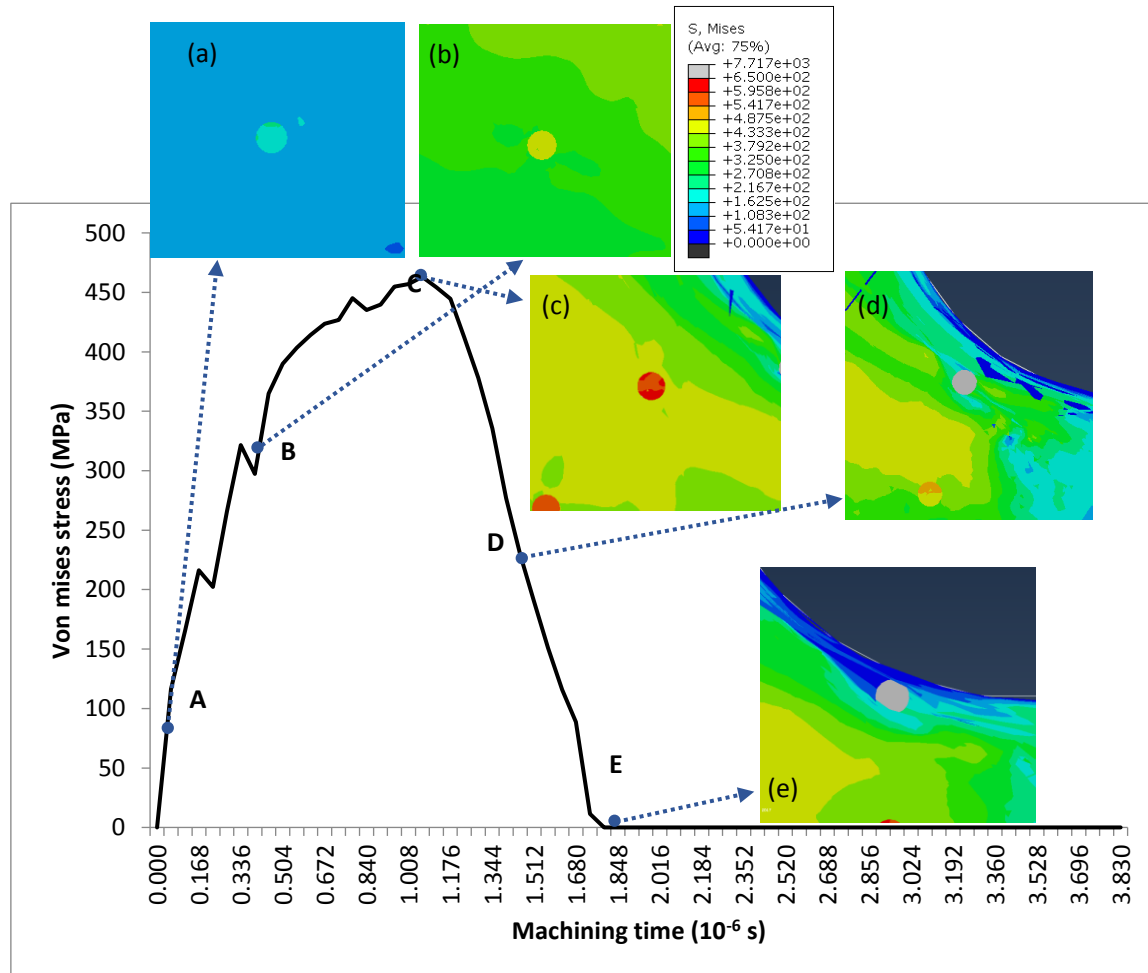


Figure 4.7 Evolution of von Mises stress distribution on the matrix element close to interface of particle

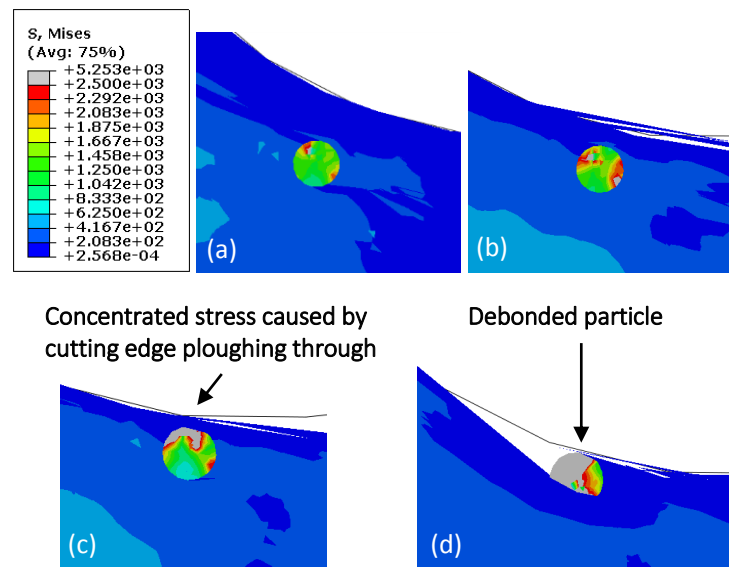


Figure 4.8 Evolution of von Mises distribution on the particle located immediately below cutting edge with advancement of cutting tool

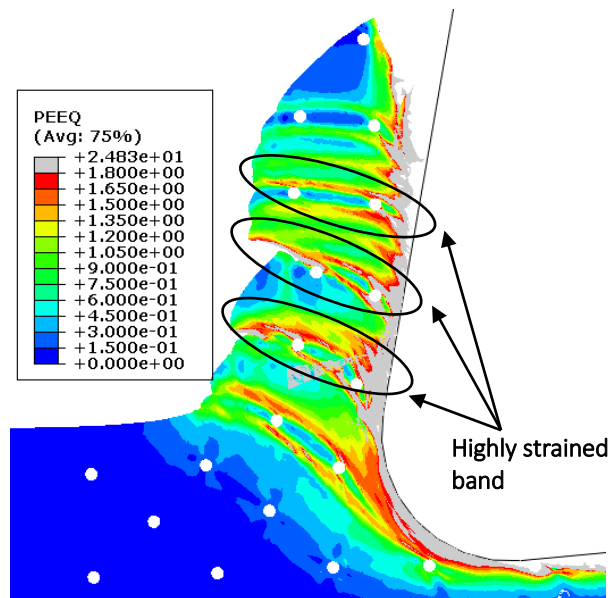


Figure 4.9 Distribution of equivalent plastic strain within formed chips

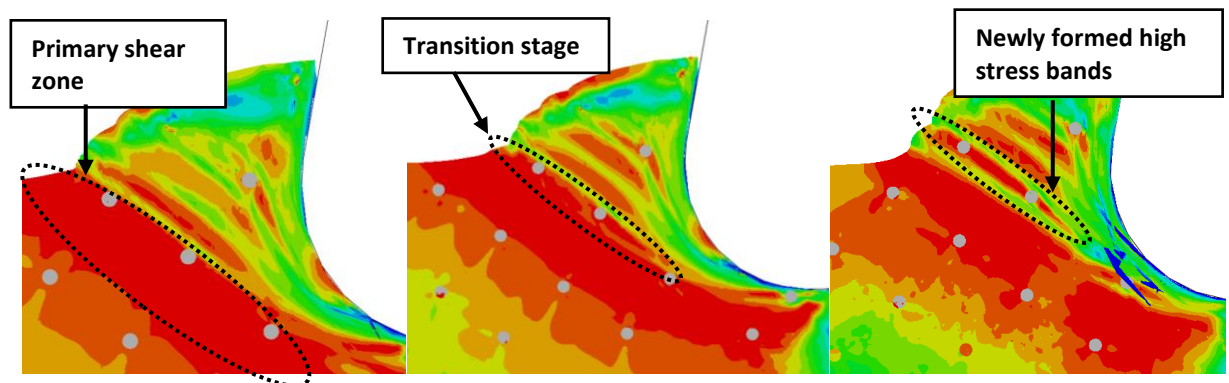


Figure 4.10 Formation of high stress bands within chips with advancement of cutting tool

4.3.3 Model validation

A validation of the finite element model is performed by comparing the simulated cutting force and chip morphology with experimental results. Figure 4.11 illustrates the cutting force obtained from simulation and experiment under different uncut chip thickness. As expected, the cutting force is found to increase with increase of uncut chip thickness. A satisfying agreement can be obtained between the predicted and experimental cutting force. At lower uncut chip thickness of 0.1 μm , the absolute average percentage error is 39.3% for the predicted cutting force. As the uncut chip thickness increasing, the absolute average percentage error decreases to 30.2%, 26.5%, 20.3% and 15.6% at uncut chip thickness of 0.2, 0.5, 1 and 2 μm respectively. It can be attributed to the constant friction coefficient used in this model which should be larger in realistic machining at small uncut chip thickness due to the ploughing effect. Moreover, because of the ideally sharp cutting edge without considering tool wear used in this model, the simulated cutting force is observed to be smaller than that obtained from experiment at each defined uncut chip thickness which meet the expectation.

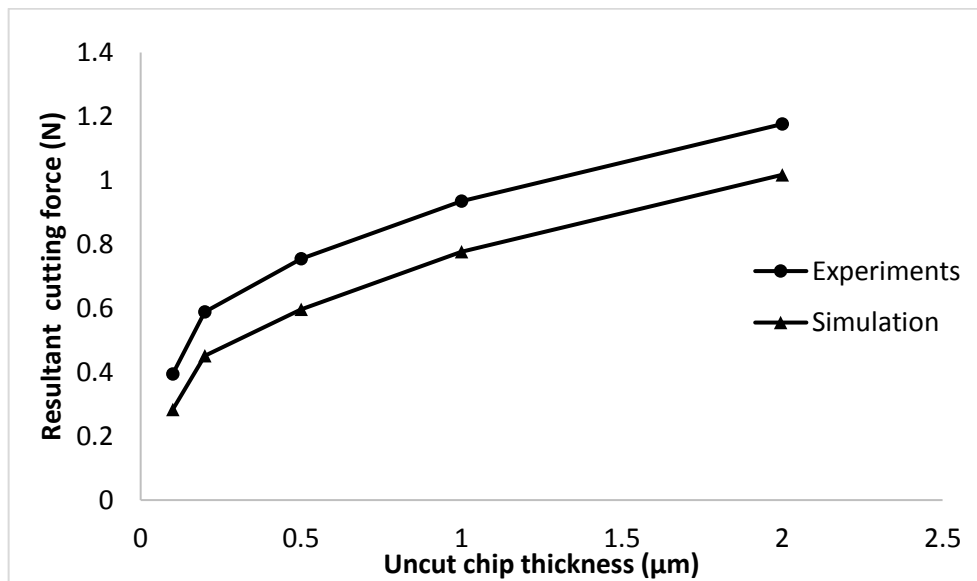


Figure 4.11 Comparison between simulated and experimental cutting force at different uncut chip thickness

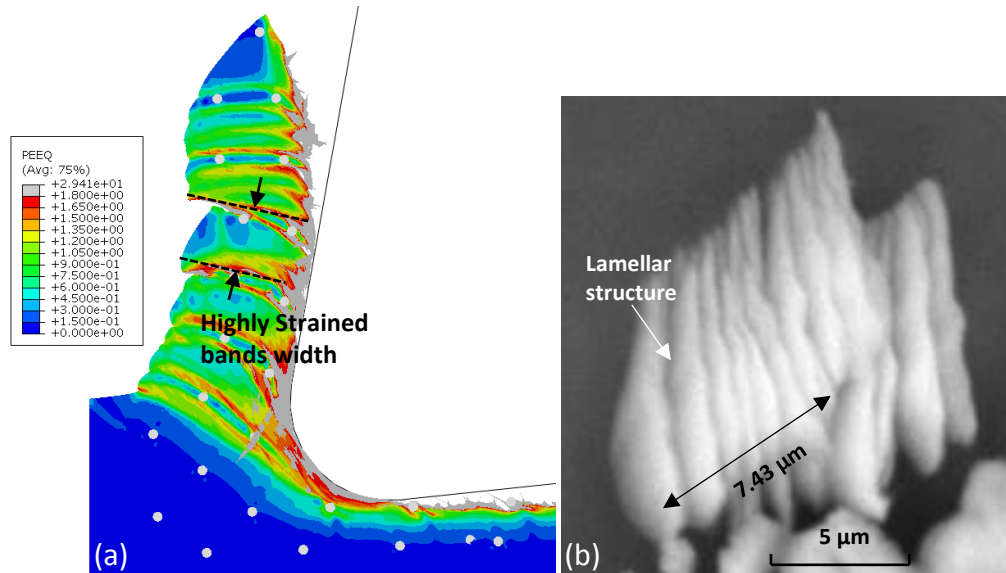


Figure 4.12. Chip morphology comparison between (a) simulation; (b) experiments

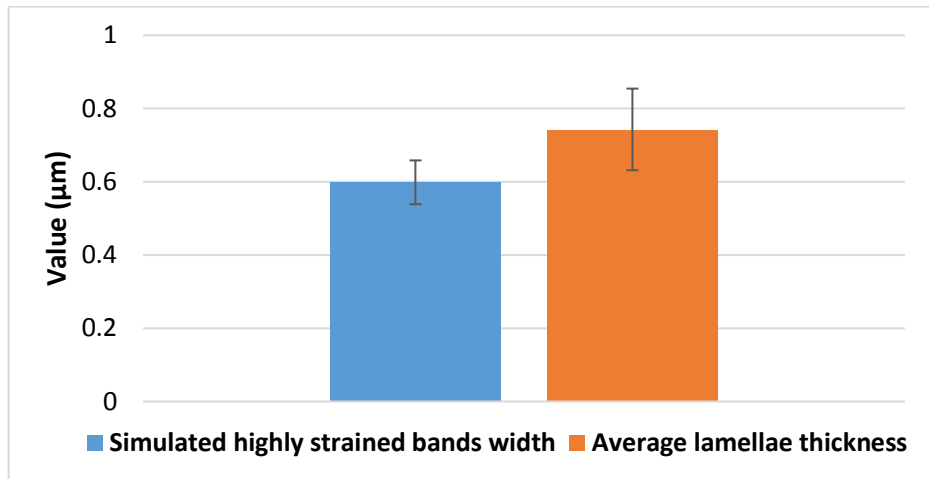


Figure 4.13 Band width comparison between simulation and experiments

FE model is also quantitatively validated in terms of the chip morphology. Small and fragile chips are collected from the micro milling experiment on nano Mg/SiC MMCs at uncut chip thickness of 1μm (Figure 4.12 (b)). The distinct lamellar structure is observed on the free surface of the chips. As mentioned earlier, highly strained bands distributed across the chips at vicinity of particles obtained from simulation can be considered as the main reason contributing to the lamellate structure of chips. Therefore, the validation is performed by comparing the thickness of lamellae on the chip obtained from experiment (Figure 4.12 (b)) with the width of highly strained bands from simulation results (Figure 4.12 (a)). The thickness of each lamellae is calculated by averaging the thickness of ten lamellar structure. Comparison results are shown in Figure 4.13. The average difference between simulation and experiment is 20.4%.

4.3.4 Effect of uncut chip thickness

4.3.4.1 Specific cutting force analysis

Figure 4.14 shows the specific cutting force at different uncut chip thickness obtained from machining experiment and simulation model. Specific cutting force is calculated by dividing the resultant cutting force by the section area of cutting area. Based on observation, size effect can be found according to the non-linear decrease of specific cutting force with increase of uncut chip thickness.

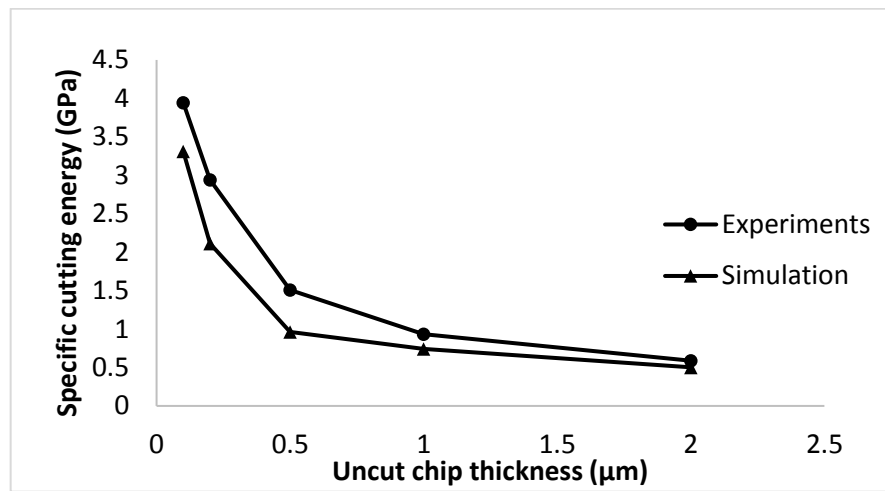


Figure 4.14 Specific cutting force at different uncut chip thickness

4.3.4.2 Chip morphology analysis

Several differences will appear when the machining features decrease from macro to micro scale. One of the significant concerns is the size effect leading a transitional regime associated with intermittent shearing and ploughing in material removal process (X. Liu, Devor, *et al.*, 2004). In this section, chip morphology of micro machining on nano Mg/SiC MMCs under various uncut chip thickness is investigated through FE models (Figure 4.15). Minimum chip thickness is determined based on the studying of chip morphology. The uncut chip thickness is selected to be 0.1, 0.2, 0.5, 1 and 2 μm. As shown in Figure 4.15, the highly concentrated stress region which can be considered as primary shear zone can be observed within workpiece materials with different location underneath the cutting edge at all uncut chip thickness.

At uncut chip thickness of 0.1 μm, it can be found from Figure 5.15 that there is no continuous chip formed in the cutting process. The small amount of material is initially elastically ‘pushed’ and accumulated in front of cutting edge (Figure 4.16 (a)). With the tool continuously moves, the equivalent

strain at the chip root increase resulting the onset of plastic deformation. Figure 4.16 (c) illustrates the continuous cutting stage. The maximum equivalent plastic strain is distributed at the accumulated material which finally leads to a complete failure and stress within workpiece is released. The fragmented chip is therefore formed by this discontinuous removal mechanisms. The chip formation process at uncut chip thickness of 0.2 μm exhibits the similar behaviour as that in uncut chip thickness of 0.1 μm . When the uncut chip thickness increase to 0.5 to 2 μm , an irregular segmented chip is formed. Based on these results, the minimum chip thickness can be proposed to be 0.5 μm (0.5R) under the input parameters utilised in this FE model. This result is consistent with that obtained from research carried by Teng et al. (Teng *et al.*, 2016), which is 0.53R in micro machining of Mg/Ti with volume fraction of 1.98%. Moreover, an increase in the shear angle can be found with the uncut chip thickness (Figure 4.17).

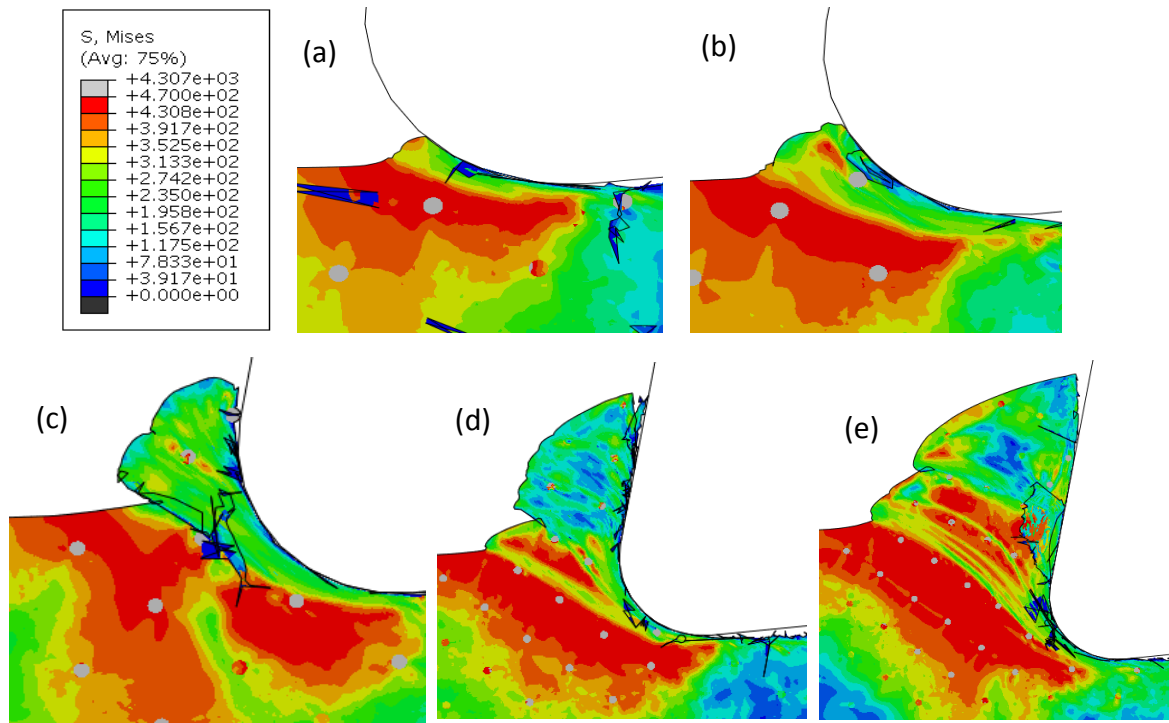


Figure 4.15 Chip morphology at uncut chip thickness of (a) 0.1 μm ; (b) 0.2 μm ; (c) 0.5 μm ; (d) 1 μm ; and (e) 2 μm .

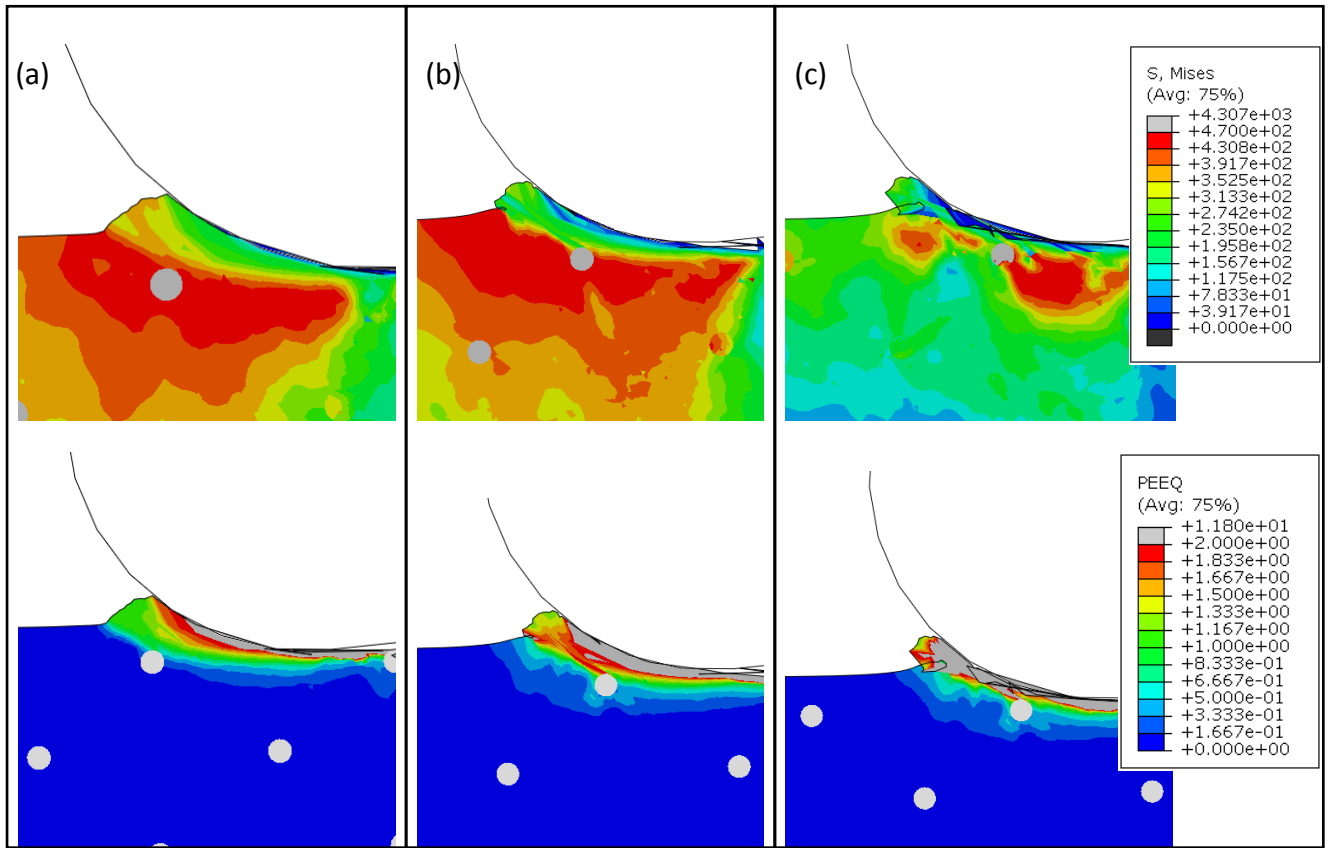


Figure 4.16. Stress and strain distribution within workpiece at material removal process under uncut chip thickness of $0.1 \mu\text{m}$

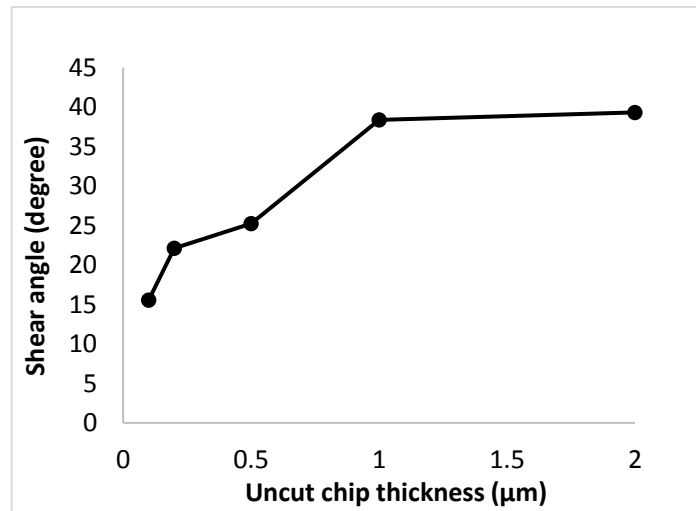


Figure 4.17 The variation of shear angle with uncut chip thickness in FE model

4.4 Case ii: Cutting mechanism of MMCs reinforced with micro-sized particles

In the case, a three-dimensional (3D) micro-mechanical FE model is established to simulate the orthogonal turning of aluminium-based metal matrix composites with micro SiC particles. Most of researchers studied the machinability of MMCs by established two-dimensional (2D) models.

However, by establishing 3D models, some of the important phenomenon such as machined surface morphology can be realistically exhibited, which is difficult to achieve in 2D models. The machined surface defects caused by different particle fracture behaviours under the effect of relative position of particles to cutting path are analysed. Von Mises stress distribution on the particles with the fracture progression is used to reveal the particles fracture mechanism. Model validation is conducted by comparing the simulated machined surface topography with the results obtained from turning experiments.

4.4.1 FE modelling procedure

In this case, a three dimensional finite micro structure-based element modelling is developed for simulating the orthogonal cutting of aluminium MMCs reinforced with SiC particles. The schematic representation diagram with XYZ coordinate system is shown in Figure 4.18 (a). The free adaptive meshing technique with thermal-displacement (C3D8RT) is used for mesh generation. Eight-node hexahedron and four-node tetrahedral finite elements are used to model the workpiece and cutting tool respectively. The workpiece is constrained in the X-Z plane at bottom surface.

The aluminium matrix and SiC particle are assigned separately in this model and the mechanical properties for these two phases are shown in Table 4.4. The particle with 40 μm diameter are uniformly distributed within the matrix. The SiC particle is modelled as a perfectly linear elastic material and brittle cracking model is used to define its fracture criterion. Two phases are defined to be perfectly bonded with tied node at their interface. The cutting process is performed by using PCD cutting tool with rake angle of 5° ; clearance angle of 5° and cutting edge radius of 1.5 μm . It is moving in the cutting direction with cutting speed of 1675 mm/s. In this model, different depth of cut is utilised in order to investigate the effect of relative position of particle to the cutting path on the cutting mechanism. Depth of cut of 2 μm , 4 μm , 6 μm , 8 μm , 10 μm , 15 μm , 20 μm and 25 μm is used (Figure 4.18 (b)).

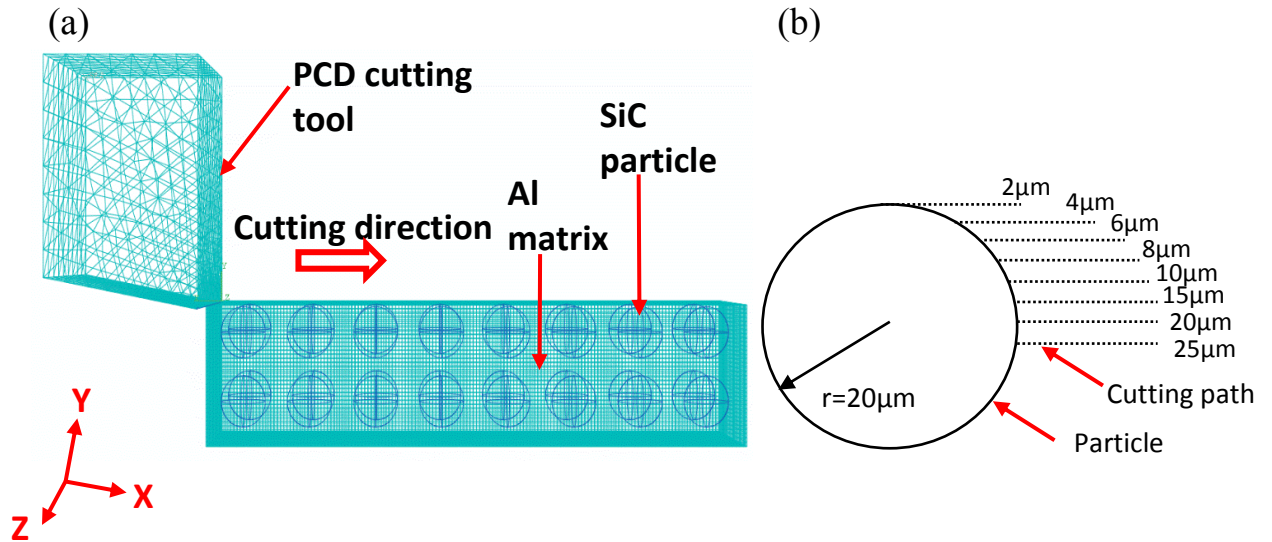


Figure 4.18 (a) Schematic representation diagram of FE model setup on orthogonal turning of aluminium-based MMCs reinforced with SiC particles; (b) Different relative position of particles to the cutting path.

Penalty contact between the cutting tool with matrix and particles is defined with the aim of enabling the tool-particle interaction. The friction coefficient μ is defined to be 0.5 in this study. J-C constitutive material model is used to predict the stress and strain distribution. J-C damage model defines the chip separation. Material constants are listed in Table 4.5 and Table 4.6.

The model validation is conducted by comparing the machined surface topography obtained from turning experiments and simulation. The turning experiments under the same cutting speed used the simulation model are conducted on an ultraprecision machine tool (Nanoform700, Precitech, USA) with maximum rotation speed of 10,000 rpm. The machine tool and PCD turning insert used is illustrated in Figure 4.19



Figure 4.19 ultraprecision machine tool (Nanoform700, Precitech, USA) with PCD turning insert

Table 4.4 Mechanical properties of aluminium matrix, SiC particles and PCD tools

	PCD	Al	SiC
Young's Modulus (MPa)	1147000	70600	420000
Poisson's Ratio	0.08	0.34	0.14
Density (ton/mm ³)	4.25E-09	2.70E-09	3.13E-09
Thermal Conductivity (mW/mm*K)	2100	180	81
Thermal expansion (K ⁻¹)	4.00E-06	2.36E-05	4.90E-06
Thermal Specific Heat (mJ/ton*K)	5.25E+08	8.80E+08	4.27E+08
Inelastic heat fraction	0.9	0.9	0.9

Table 4.5 Johnson-Cook constitutive model parameters for aluminium

A (MPa)	B (MPa)	n	m	Melting Temp (K)	Transition Temp (K)	C
265	426	0.183	0.895	923	293	0.001

Table 4.6 Johnson-Cook damage parameters for aluminium

d ₁	d ₂	d ₃	d ₄	d ₅
0.13	0.13	-1.5	0.011	0

4.4.2 Effect of relative position of particles to cutting path on the cutting mechanism

In machining MMCs reinforced with micro-sized particles, the large volume fraction (10-50 % Vol.) and particle size (2 μ m – 70 μ m) make the tool-particles interaction become one of the important factors contributing to the machining mechanism of MMCs in terms of the tool wear and machined surface topography. The following part discusses the formation mechanism of representative machined surface topography with various particle fracture behaviours along the cutting path at different depth of cut ranging from 2 μ m to 25 μ m.

Figure 4.20 shows the machined surface topography under the depth of cut of 2 μ m. In this model, a 2 μ m gap is left between the particle upper interface and top surface of workpiece. It can be seen from Figure 4.20 that the top layer of aluminium matrix materials is removed without engagement with particles when the cutting tool passes through the workpiece. It is clear that the particles are still intact. The matrix material near particle interface is heavily deformed resulting in shallow cavity surrounding each particle. The intact particles embedded

within matrix surrounded by shallow cavity can be observed in Figure 4.21 which shows the agreement with simulated results. This might be attributed to the existence of particles with high elasticity restricts the plastic deformation of surrounding matrix materials in cutting direction when the cutting tool get passed. This restricting behaviour of particles also makes part of the aluminium matrix deform in the cutting direction and partially cover the particles.

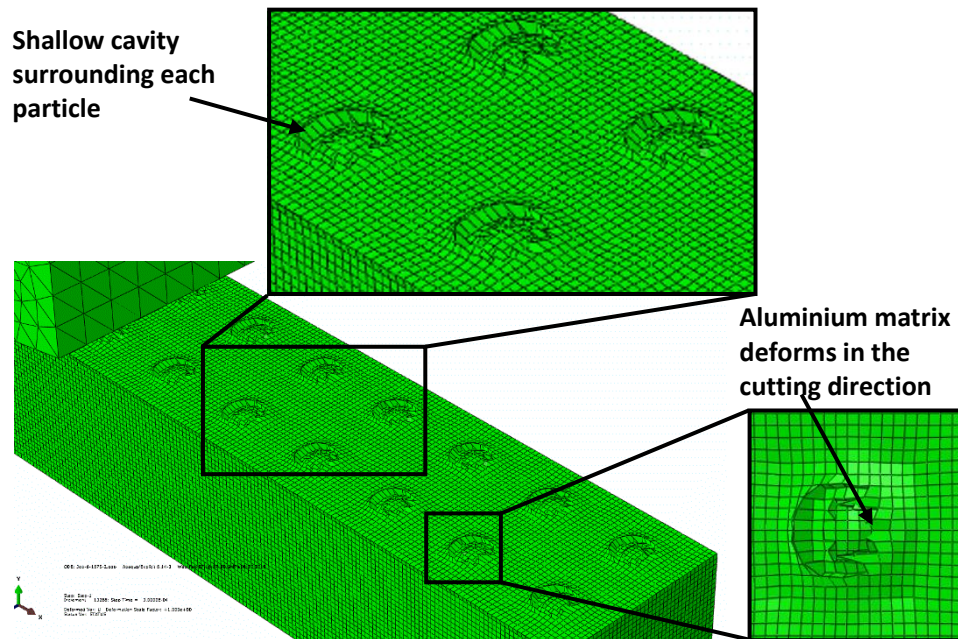


Figure 4.20 Simulated machined surface topography with particle behaviours under depth of cut of $2\mu\text{m}$.

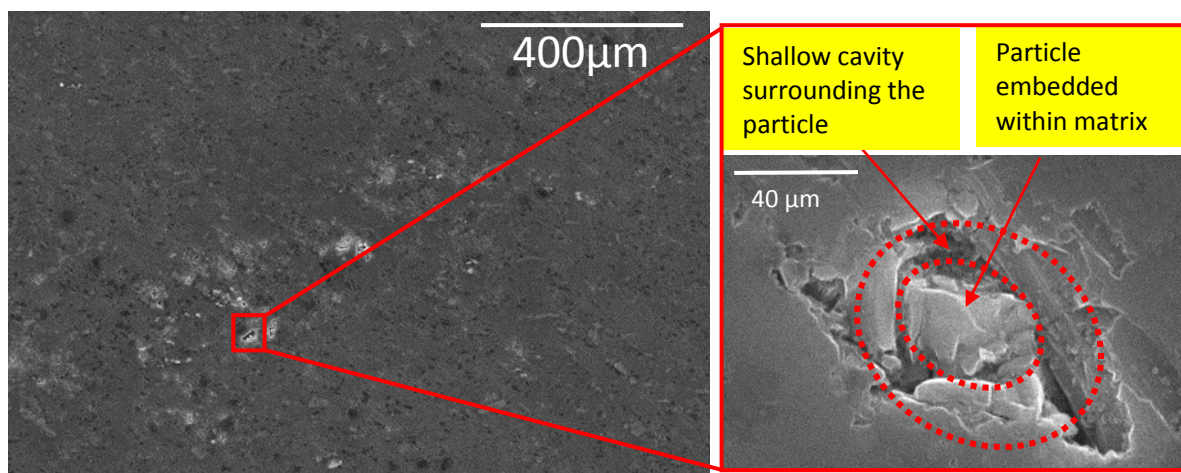


Figure 4.21 SEM image of machined surface obtained from turning experiment showing the shallow cavity surrounding the intact particle.

Partially fracture was observed on the tool-particles engagement area (top side of particle) when the depth of cut increases to 4 μm (see Figure 4.22). In addition, based on the observation of distorted mesh element on the machined surface, a more deteriorative surface quality with burrs located at edge of workpiece is found when compared to that obtained from depth of cut of 2 μm . The particle fracture process is investigated in detail by observation the von Mises stress distribution on particle during machining (see Figure 4.23). As shown in Figure 4.23(a), a high localised stress zone is found at the tool-particles contact area when the cutting tool firstly engages with particle. As the tool advances, the maximum localised stress zone with larger amplitude moves to the top side of particle which leads to the fracture initiation (see Figure 4.23 (b)). Then, the maximum stress zone is transferred to the right side of particle with continuous movement of cutting tool (see Figure 4.23 (c)). Finally, the deletion of mesh element on the top side of particle indicates a completed fracture when cutting tool passed, while the maximum stress distributed on particle drops from 7.92 to 3.5 GPa (see Figure 4.23 (d)). Moreover, the load is transferred from particle to surrounding matrix material which causes a severe mesh distortion. This might cause irreversible plastic deformation which is the main reason causing residual strain. Also, the elasticity of particles would reduce.

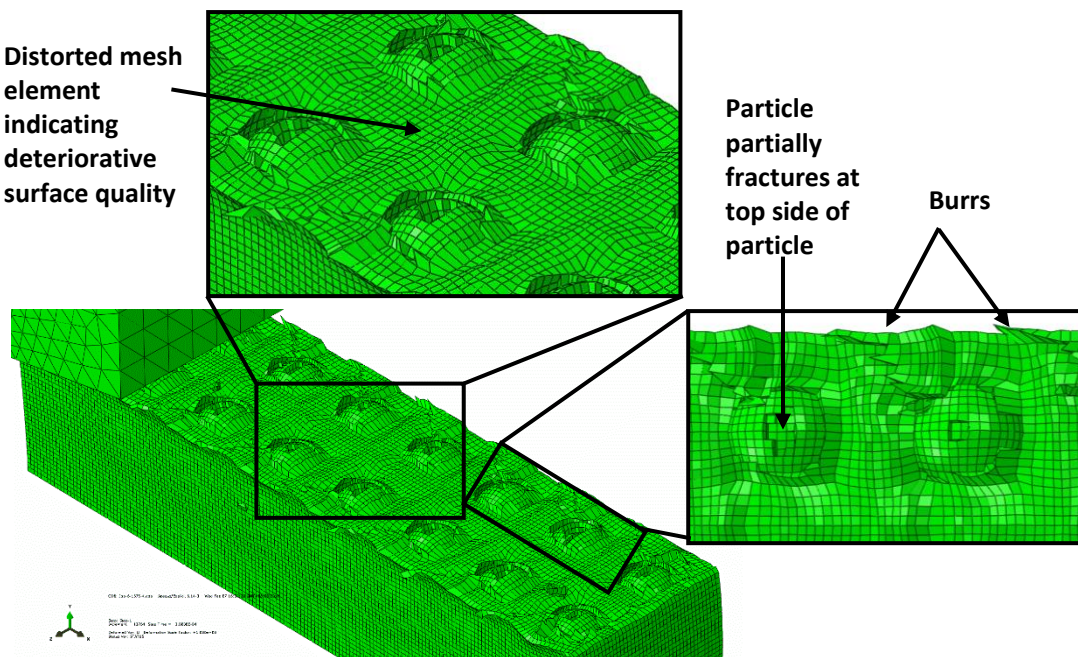


Figure 4.22 Simulated machined surface topography with particle behaviours under depth of cut of 4 μm .

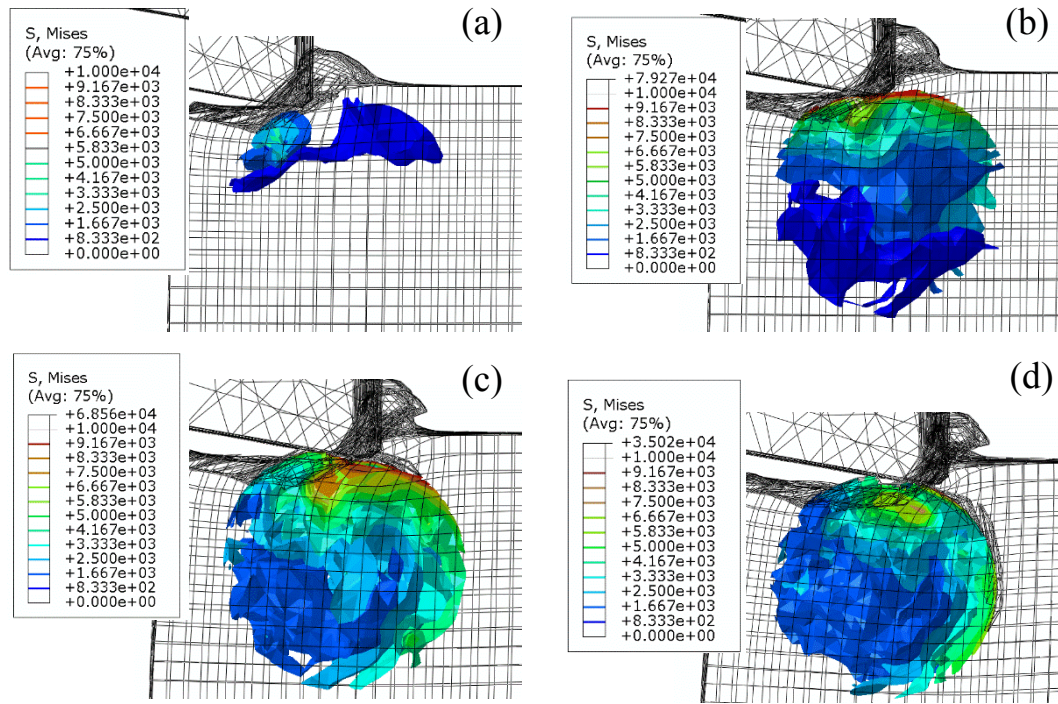


Figure 4.23 von-Mises stress distribution on particle at depth of cut of 4 μ m.

As the depth of cut increases from 4 μ m to 6 μ m, particle fracture becomes more evident (see Figure 4.24). It is clear that the fracture behaviour of particles located near the entrance of cutting is more severe than others. In Figure 4.25, the stress distribution in the particle during the interaction process between cutting tool is illustrated. Figure 4.25 (a)-(c) show the stress variation on the particles located at entrance of cutting. When the particle firstly engages with the cutting tool, the matrix materials near the top right side of particles are squeezed which leads to a localised failure at the particle interface (Figure 4.25 (a)). With the tool moves, the load is transferred to other side of the particle and finally completed fracture initiates resulting the fragmented particle embedded with machined surface (Figure 4.25 (b-c)). During this process, particle rotation phenomenon is presented with the plastic flow of surrounding matrix with the tool movement. Figure 4.25 (d)-(f) illustrate the process of partially fracture of particles. Unlike the fracture area observed at the top side of particles, in this case the fracture area is found at one side of particles. The particle rotation phenomenon is further proved in this case.

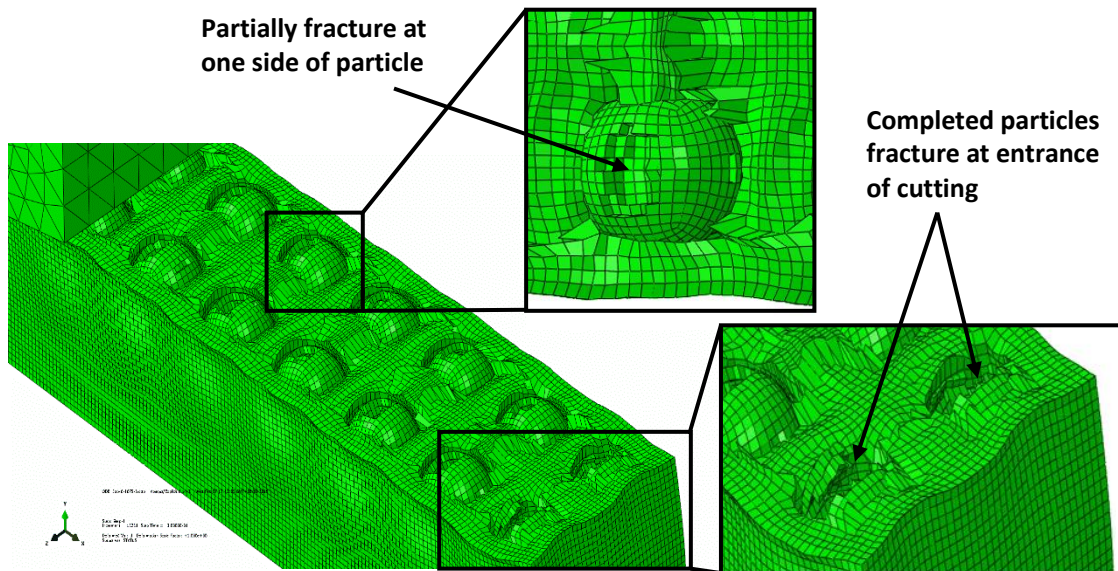


Figure 4.24 Simulated machined surface topography with particle behaviours under depth of cut of $6\mu\text{m}$

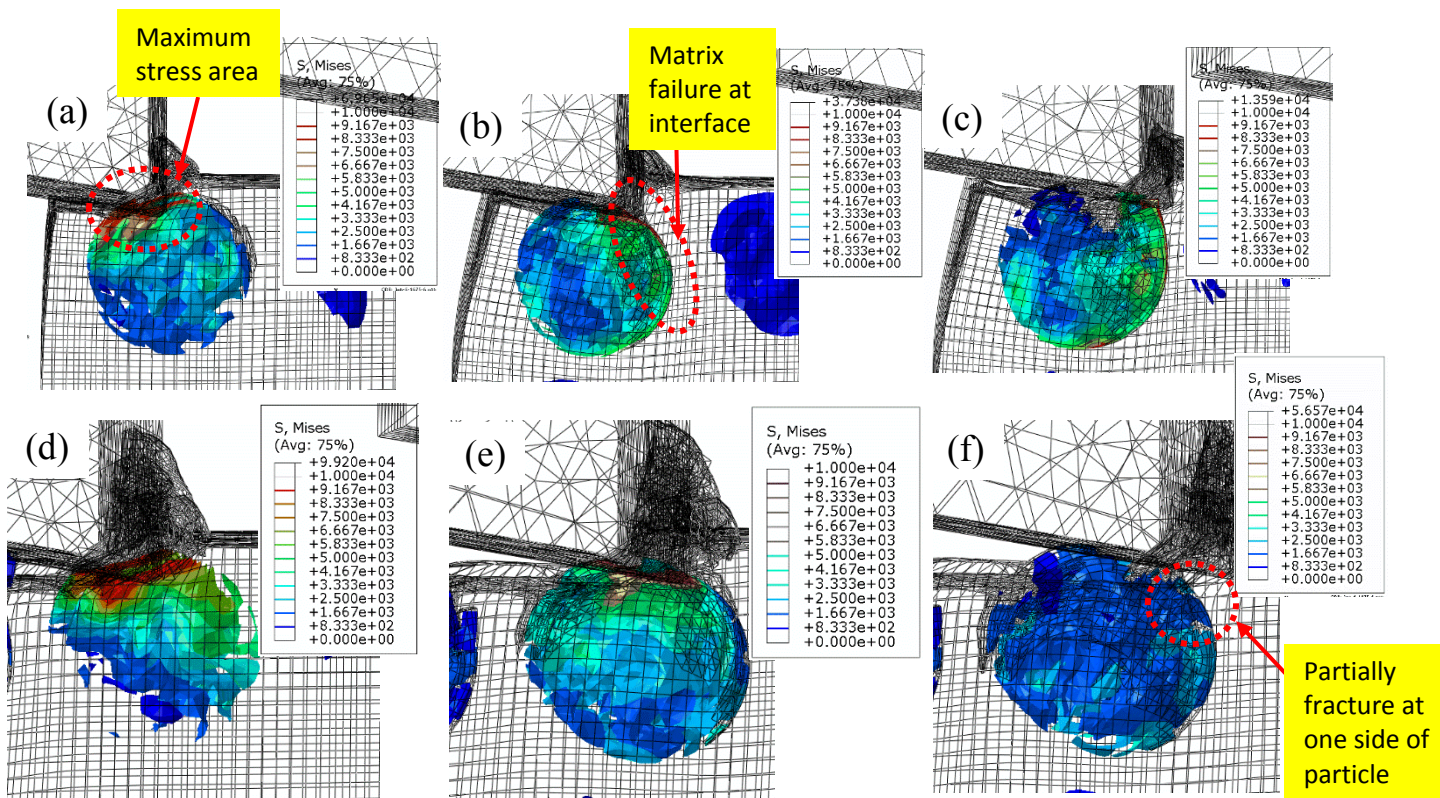


Figure 4.25 Von-Mises distribution of (a)-(c) completed fractured particle at entrance of cutting; (e)-(g) partially fractured particle at depth of cut of $6\mu\text{m}$.

Various machined surface topography with particle behaviours under the effect of depth of cut ranging from $8\mu\text{m}$ to $15\mu\text{m}$ are shown in Figure 4.26. The deteriorative machined surface

quality with particles fracture and debonding behaviours are becoming more evident with increasing depth of cut. In addition, the cutting tool tends to press the particles into the machined surface, which in turn causes the severe plastic deformation at matrix materials surrounded by particles (see Figure 4.26 b&c). Based on observation on the Figure 4.27 which shows the von-Mises distribution on the particle at depth of cut of 10 μ m and 15 μ m. More machining details such as particles cleavage, chip formation under the effect of fragmented chips and severe plastic deformation around cavity can be noticed. As the depth of cut increase to 10 μ m, unlike the top side of particles being partially fractured in a small portion in depth of cut of 6 μ m the particle experiences a completely cleavage after the cutting tool passing through (Figure 4.27 (b)). The cutting tool then forces the part of fragmented particle moving ahead of the rake face to squeeze the matrix material underneath the chip root resulting in failure of matrix materials (Figure 4.27 (c)). As a result, dramatically change take place in the chip formation mechanism. This is believed to be one of the cases leading to the discontinuous chips in machining micro-MMCs. With increase in depth of cut to 15 μ m, the edge distortion at the entrance of cutting is becoming more obvious (Figure 4.27 (e)). This might be attributed to the component force parallel to the cutting direction acting on the spherical surface of particles increases with increase of relative depth of cutting tool to the particles. Due to the non-uniform deformation between two distinct phases, a severe deformation on matrix near the entrance of cutting is caused. This assumption also can be used to explain the evolution of severe plastic deformation around the cavities on machined surface caused by particles debonding and fracture with increasing depth of cut (Figure 4.26 (b & c)). As shown in Figure 4.27 (f), the large part of fragmented particles embedded within machined surface is pressed by cutting edge, leading to severe and irreversible plastic deformation around the cavity. The cavity filled with particle fragments can be found in the machined surface from turning experiment (Figure 4.28). The EDS spectra of machined surface further prove the existence of particle fragments within cavity. As a result, a residual strain is generated on the machined surface which significantly deteriorates the surface quality.

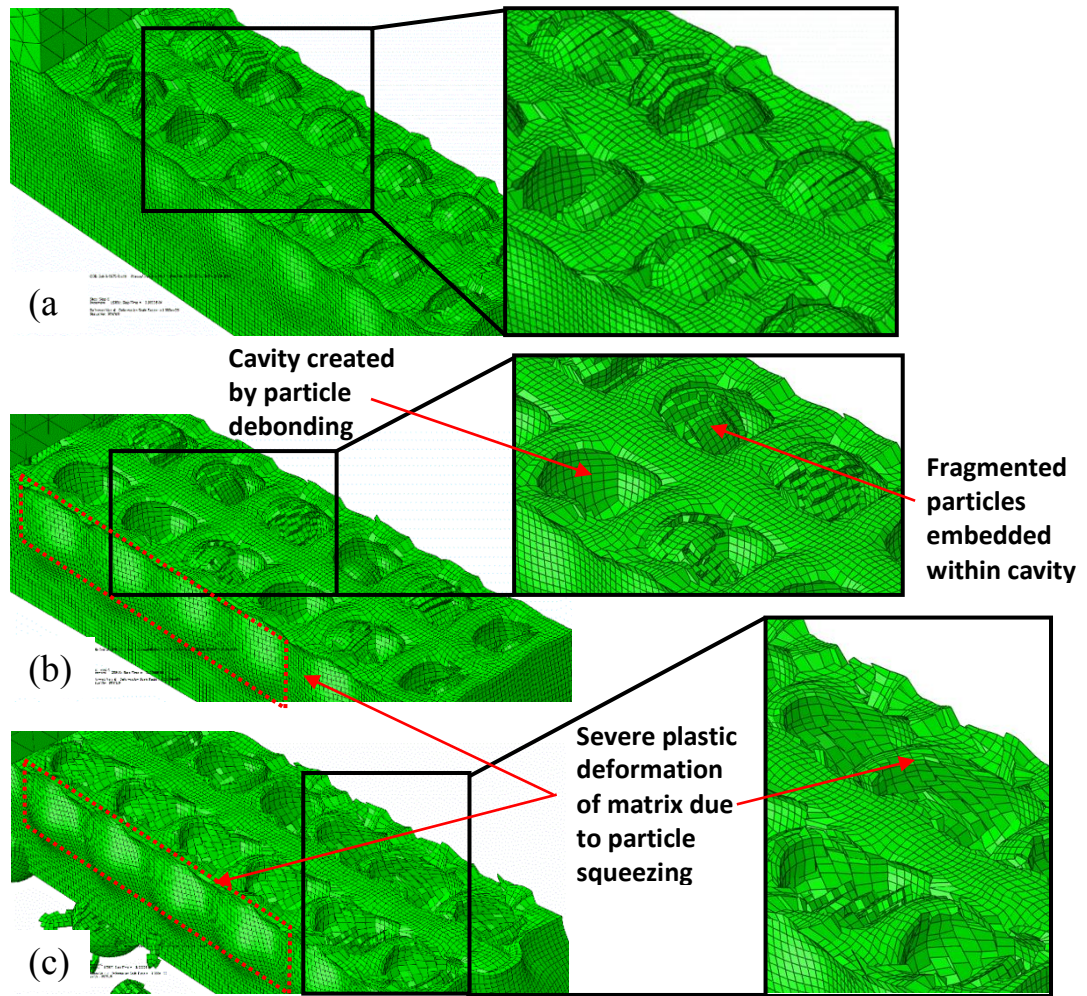


Figure 4.26 Simulated machined surface topography with particle behaviours at the depth of cut (a) 8μm; (b) 10 μm; (c) 15 μm.

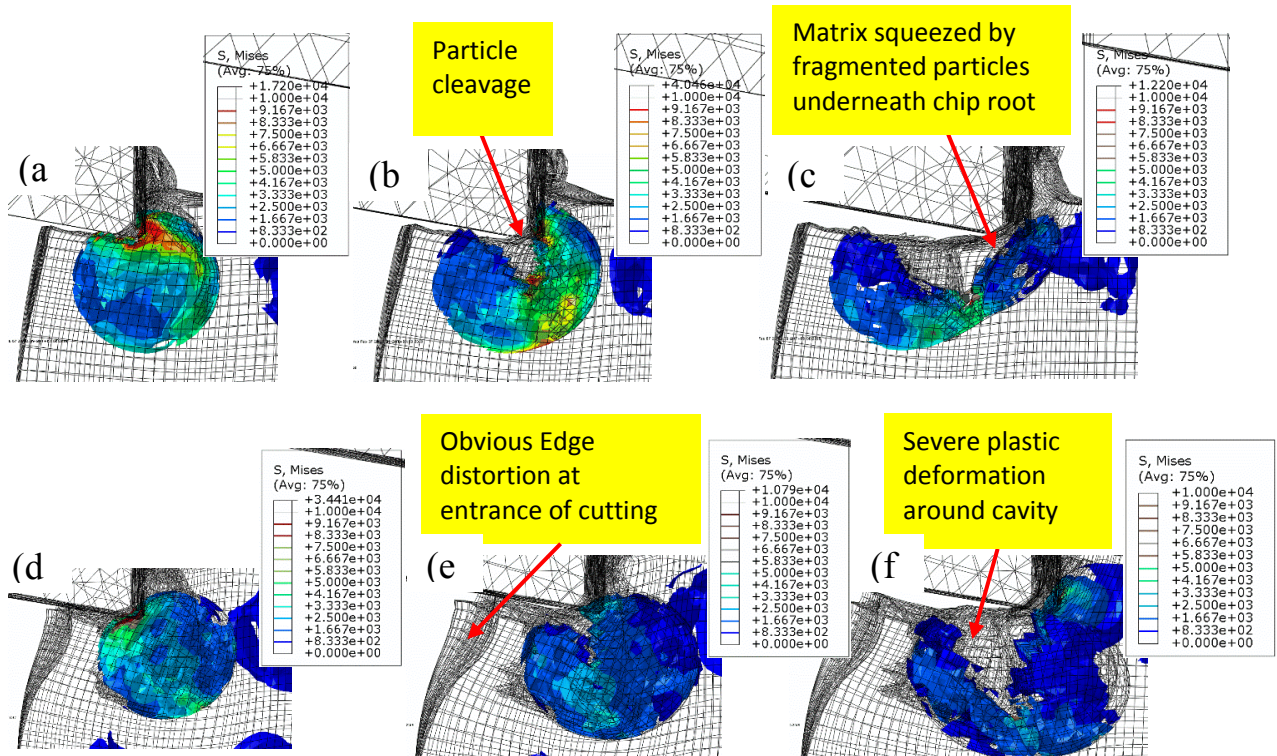


Figure 4.27 Von-Mises distribution on particles at depth of cut (a-c) 10 μm; (d-f) 15 μm

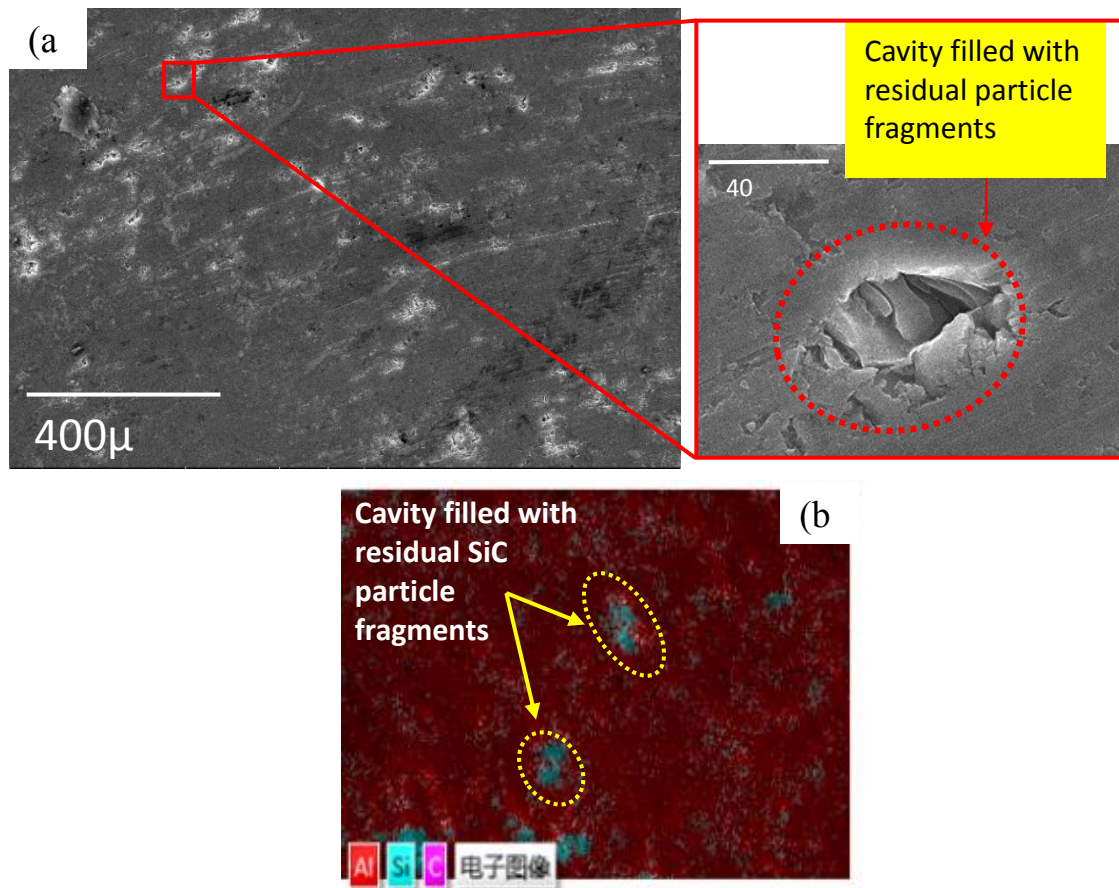


Figure 4.28 (a) SEM image of machined surface obtained from turning experiment showing the cavity filled with residual particle fragments; (b) EDS spectra of machined surface.

Figure 4.29 shows the machined surface topography at the depth of cut of 20 μm and 25 μm . It is clear that the complete particles debonding without any residual fragments in cavities take place when the cutting path located near the half height of the particle.

It can be said that the depth of cut shows a significant influence on the machined surface topography. A continuous improvement in the surface topography can be found as increasing the depth of cut from 15 μm to 25 μm . When the depth of cut is ranged from 8 to 15 μm (see Figure 4.26), fracture takes places on some of the particles leaving the deep cavities filled with particles fragments, which results in a deteriorative machined surface. When the depth of cut increases from 15 μm to 25 μm , the machined surface is significantly improved. The particles are completely removed from machined surface which results in shallow cavities without residual particle fragments embedded in. The debonding process with von Mises stress distribution on particle at depth of cut of 25 μm can be observed in Figure 4.30. Initially, a concentrated stress zone is found at the contact area between the rake face of cutting tool and particle (Figure 4.30 (a)). As the tool advances, particle debonding is initiated. The particle is

squeezed along cutting direction leading to failure at the particle-matrix interface (see Figure 4.30 (b)). With the tool further moves, the particle is subsequently dislodged from the matrix leaving a cavity on the machined surface (see Figure 4.30 (c)). The cavity caused by the complete particle debonding also can be observed in SEM image of machined surface in Figure 4.31. The debonded particle is then pushed by the rake face of cutting tool causing plastic deformation of matrix in front of the particle (Figure 4.30 (c)).

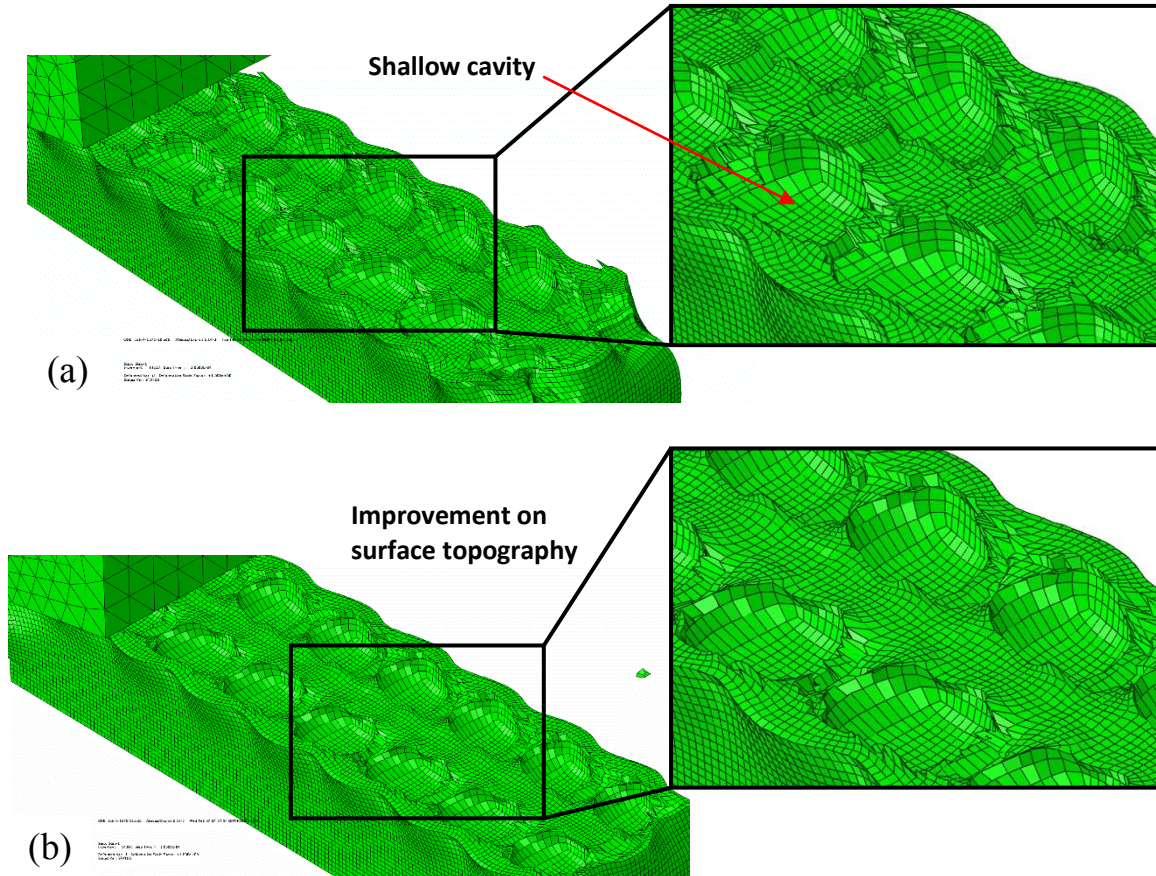


Figure 4.29 Simulated machined surface topography with particle behaviours at the depth of cut (a) 20µm; (b) 25 µm.

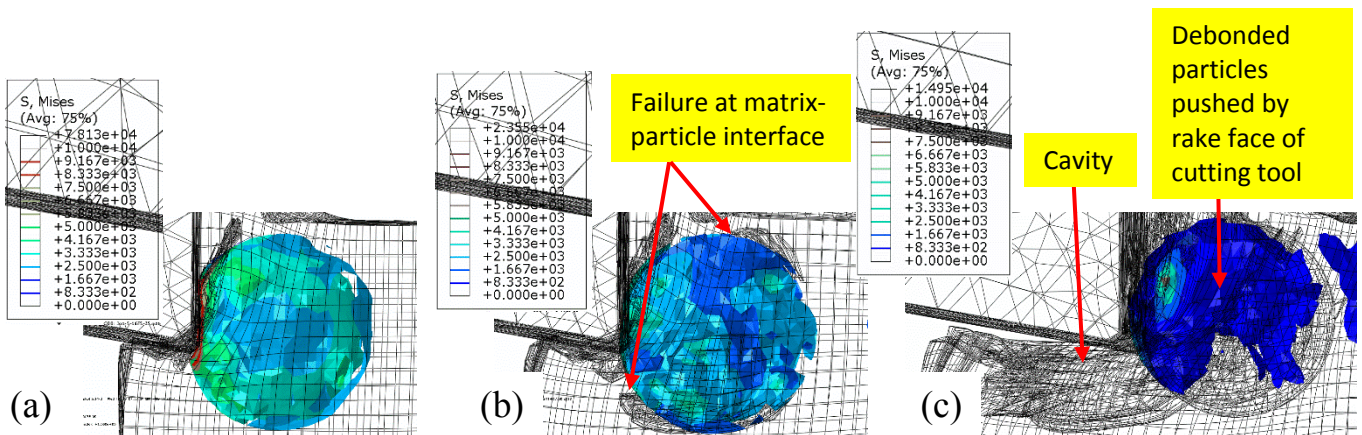


Figure 4.30 Von-Mises distribution on particles at depth of cut 25 µm.

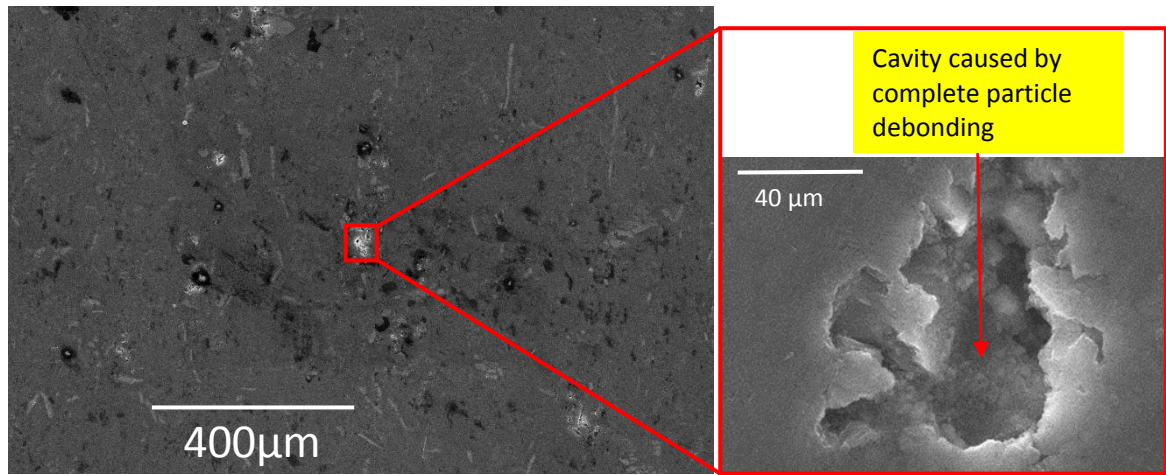


Figure 4.31 SEM image of machined surface obtained from turning experiment showing the cavity caused by complete particle debonding.

4.5 Case iii: Comparison of cutting mechanism when machining micro and nanoparticles reinforcing SiC/Al MMCs

In this case, simulation models when machining of two types of MMCs reinforced with micro-sized and nanoparticles were developed respectively. This case presents a comparison between machining of micro and nano-MMCs in terms of chip formation, stress/strain distribution, tool-particles interaction and machined surface morphology. Finally, validation of FE models is conducted by investigating tool wear, chip morphology and machined surface morphology obtained from micro milling experiment.

4.5.1 Modelling procedures

The same assumption simplifying the 3D micro milling process to 2D micro orthogonal machining process used in case i has been applied in these models. Microstructure-based two dimensional finite element (FE) models are established. As the large deformation and deformation rate in the workpiece is involved in the cutting process, arbitrary Lagrangian-Eulerian (ALE) formulation with the advancing front algorithm is used to provide the mesh distortion control in every analysis increment to avoid excessive mesh distortion. Free thermal-displacement quad-dominated meshing technique is used to generate mesh. The schematic representation of FE models is shown in Figure 4.32. For both models, a strategy of particles distribution is established to make the particles distributed at different relative locations of cutting path (Figure 4.32). Thus, more realistic models that predict all possible particles behaviours during tool-particle interaction process can be achieved. The cutting tools are treated as analytical rigid body and move horizontally into the fixed workpiece with a predefined speed.

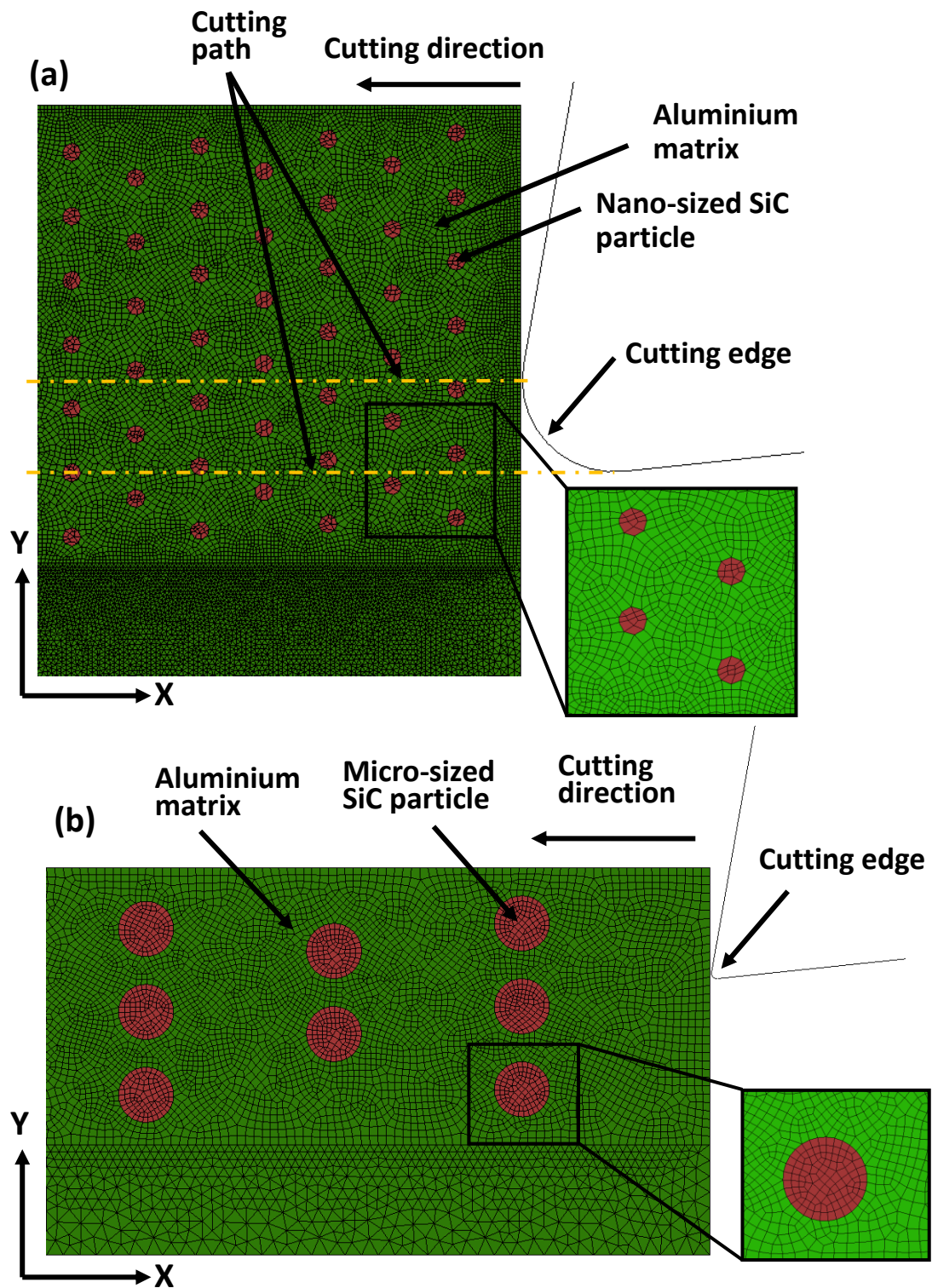


Figure 4.32 FEA model setup for orthogonal aluminium-based MMCs reinforced with (a) nano-sized SiC particles, (b) micro-sized particles.

The aluminium matrix and SiC particle phases are assigned separately in both models. Two phases are assumed to be perfectly bonded and their interface nodes are tied together. The particle diameter is defined as 200 nm with 10% volume fraction in the nano-MMCs model, and 10 μm particle diameter with 10% volume fraction of is used in micro-MMCs models. Table 4.7 lists all machining parameters used in the two models. Due to the scale-difference between two types of reinforcements (nano & micro scale) and the fact that the cutting edge radius of cutting tool is approximately eight times larger than the diameter of nanoparticles, it would be computational expensive to apply the same uncut chip thickness in both models. Therefore, different uncut chip thicknesses are used in order to present the typical and distinct tool-particles interaction behaviours. For the model of machining nano-MMCs, severe deformation of matrix element and large amount of mesh element generated due to the nanoparticles which make the computational process expensive. Therefore, mass scaling option is used to overcome this problem.

Table 4.7 Machining parameters used in both FE models

	Nano-MMCs	Micro-MMCs
Cutting speed, V_c (m/min)	125.64	125.64
Uncut chip thickness, t (μm)	4	20
Tool rake angle, α (Degree)	10	10
Tool clearance angle, β (degree)	6	6
Cutting edge radius, (μm)	1	1
Particle size, (μm)	0.2	10

The experimental validation was conducted on an ultra-precision desktop micro machine tools (MTS5R). 2-flutes uncoated tungsten carbide micro end mills with tool diameter of 0.5 mm were used. The worn end mills, machined surface and chips morphology were examined by scanning electron microscope (Hitachi TM3030).

Aluminium alloy matrix is assumed to be a deformable thermo-elastic-plastic material with failure criterion in both models. Johnson-Cook (J-C) constitutive equation is used to explore the von-Mises stress distribution during the high speed machining process. Material properties and J-C model parameters for aluminium matrix used in this work are listed in Table 4.8. Chip separation criterion of matrix material in the simulated machining process is defined using

Johnson-Cook damage equation. The reinforcement phase is modelled as a perfectly elastic material. Brittle cracking model available in Abaqus material model library is used to define reinforcement fracture criterion. Mechanical and brittle cracking properties are illustrated in Table 4.9.

Table 4.8 Mechanical properties and materials constant used in J-C model for aluminium alloy

Density (ton/mm ³)	2820×10 ⁻¹²
Young's Modulus (MPa)	70600
Poisson's Ratio	0.35
T _{melt} (K)	900
T _{transition} (K)	290
Thermal expansion (K ⁻¹)	23.6×10 ⁻⁶
Thermal Specific Heat (mJ/ton*K)	880×10 ⁶
Thermal Conductivity (mW/mm*K)	180
<i>A</i> (MPa)	224
<i>B</i> (MPa)	426
<i>n</i>	0.2
<i>m</i>	0.859
<i>C</i>	0.003
<i>d</i> ₁	0.13
<i>d</i> ₂	0.13
<i>d</i> ₃	-1.5
<i>d</i> ₄	0.011
<i>d</i> ₅	0

Table 4.9 Material properties for SiC particles

Density (ton/mm ³)	3200×10^{-12}
Young's Modulus (MPa)	408000
Poisson's Ratio	0.35
Thermal Specific Heat (mJ/ton*K)	755×10^6
Thermal Conductivity (mW/mm*K)	120
Compressive strength (MPa)	3900

4.5.2 von-Mises stress distribution in cutting area

Chip formation process when micro machining of Al/SiC MMCs reinforced with nano-sized and micro-sized particles were illustrated in Figure 4.33 and 4.34 respectively. Figure 4.33(a) and Figure 4.34(a) show the initial contact stage between the deformed workpiece and cutting tool prior chip formation. Particles distributing at the matrix experiencing with highly concentrated stress zone bear the greatest stress at both models. It proves the fact that hard SiC particles bear most of the load transferred from matrix materials. This can be attributed to the high elasticity of SiC particles. A different phenomenon in terms of von Mises stress distribution pattern within matrix can be found between these two models. When machining nano-MMCs (Figure 4.33 (a)), a narrow straight primary shear zone which can be commonly found in machining homogeneous materials is not obvious. Instead, an irregular highly concentrated stress zone was observed in tool-workpiece interface and the stress from the tool tip progresses to the upper surface with decreasing magnitude. With the cutting tool advances (Figure 4.33 (b&c)), a wider primary shear zone when compared to that in machining homogeneous matrix materials (Figure 4.35) becomes evident. In contrast, the primary shear zone can be observed when the cutting tool firstly engage with workpiece and lasts during chip formation process in the model of machining micro-MMCs (Figure 4.34(a)). The difference in the von Mises stress distribution between the two models implies that the location and size of particles play significant role in determining the stress propagation mechanism with advancement of cutting tool.

In the model of machining nano-MMCs, a significant reduction in particle size tends to increase the number of particles involved in the machining area (uncut chip thickness) when compared to that in machining of micro-MMCs. Unlike the highly concentrated stress region confined to the narrow primary shear zone in machining homogeneous materials (Figure 4.35), these particles acting as barriers restrict the propagation of stress and force the highly concentrated stress propagate to surrounding area. This is believed to be the main reason leading to an irregular stress zone at tool-workpiece interface at initial cutting stage and wider shear zone with advancement of cutting tool. A detailed study on restricting behaviour of nanoparticles is conducted through observing the primary shear zone propagation as shown in Figure 4.36. With the propagation of primary shear plane, higher magnitude stress attempts to bypass the nanoparticle, which in turn causes the irregular stress contour at the interface of each particle. As a result, a fragmented plastic strain field within matrix materials is formed due to the ability of the matrix to deform plastically and particles' inability, see Figure 4.37. The stress is therefore accumulated near the interface of particles and causes the highly concentrated plastic strain filed.

When the ratio between particle diameter to uncut chip thickness increases, the effect of existence of particle on stress distribution would be more dominated than that in nano-MMCs. By observing the von Mises stress pattern in the model of machining micro-MMCs, a significant difference when compared to that in machining nano-MMCs is that the particle size becomes comparable with the width of primary shear zone (Figure 4.34 (b-d)). Similarly micro-sized particles act as barrier restricting the propagation of primary shear zone. However the primary shear zone is broken into two regions with the similar area of particle and thus spread to surrounding when it is bypassing the micro-sized particle. Thus, greater compressive stress is generated on the particles under the squeezing action of cutting tool and matrix which results in a concentrated stress zone and maximum plastic strain on the tool-particle interface as shown in Figure 4.38.

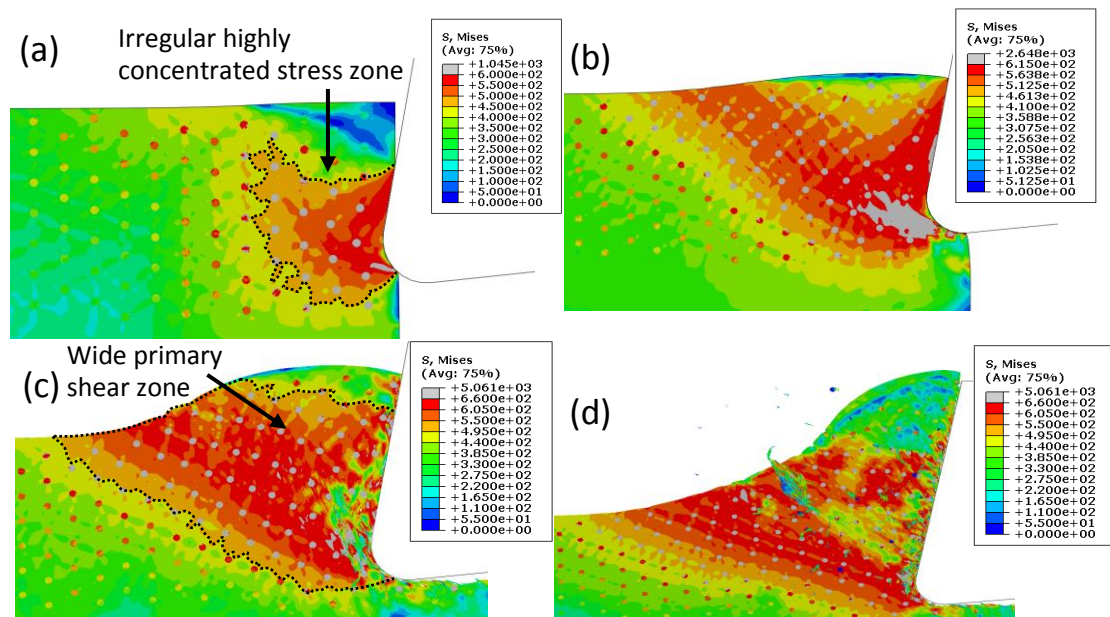


Figure 4.33 Chip formation when micro machining of Al/SiC MMCs reinforced with nano-sized particles (0.2 μm diameter).

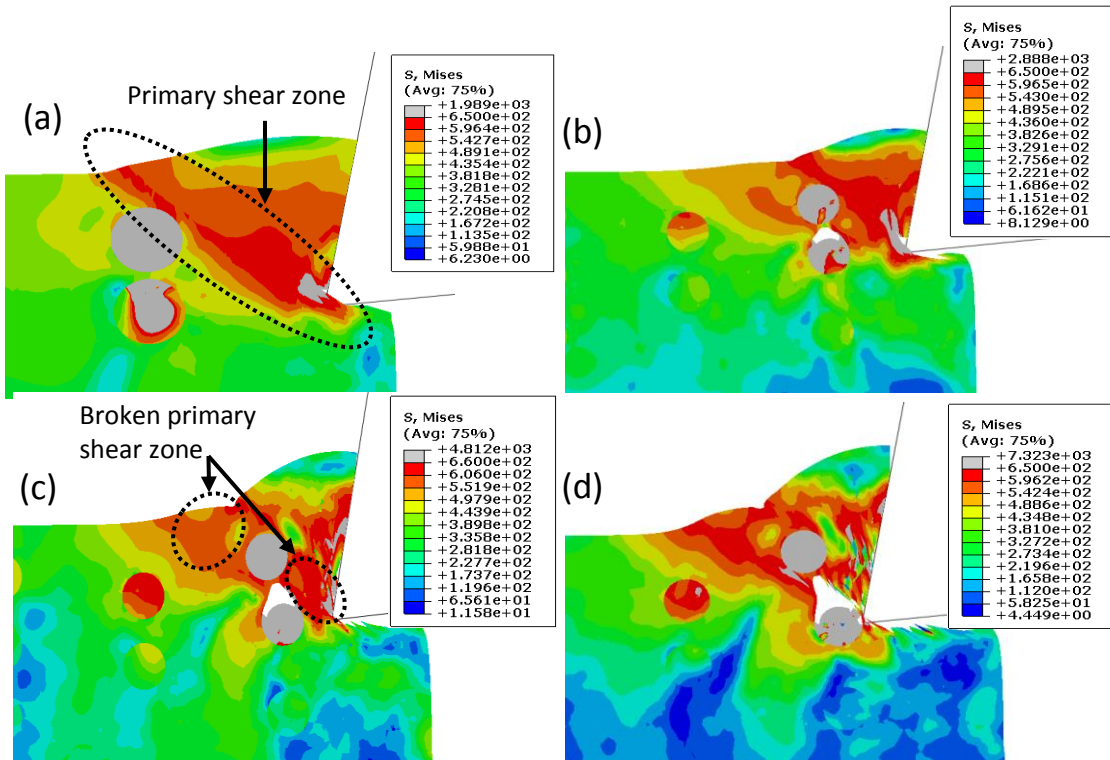


Figure 4.34 Chip formation when micro machining of Al/SiC MMCs reinforced with micro-sized particles (10 μm diameter).

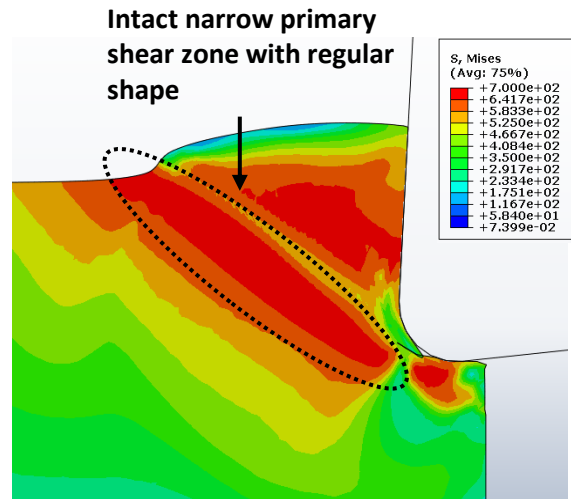


Figure 4.35 Von Mises stress contour in machining pure Aluminium using the same cutting parameters of nano Al/SiC MMCs machining

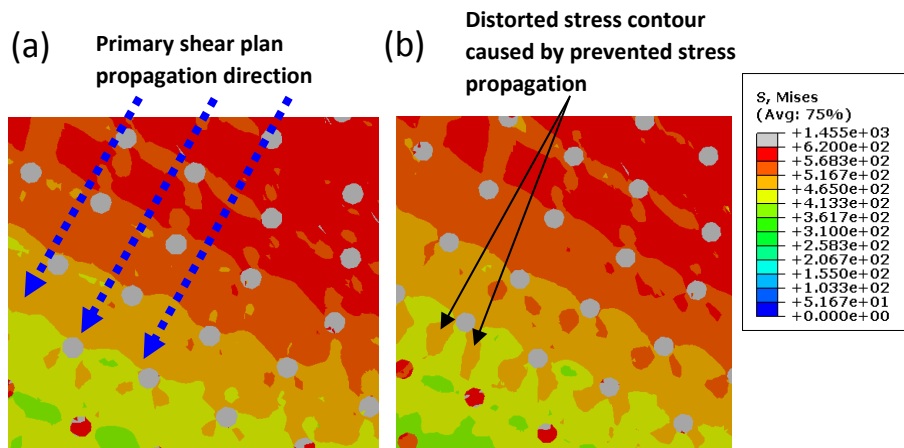


Figure 4.36 Effect of nano-particles on primary shear zone propagation (a) primary shear zone propagation direction; (b) distorted stress contour caused by prevented stress propagation.

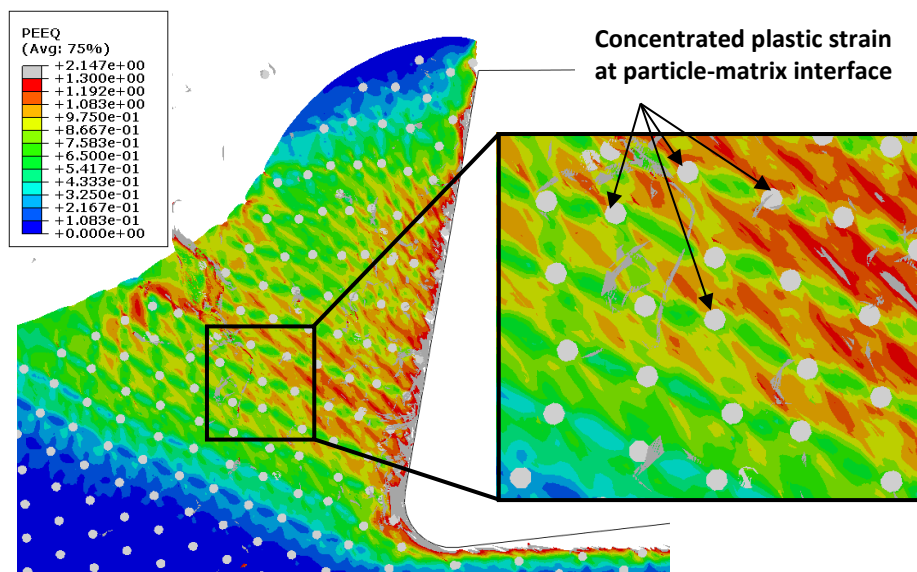


Figure 4.37 Distorted plastic strain field in machining nano Al/SiC MMCs

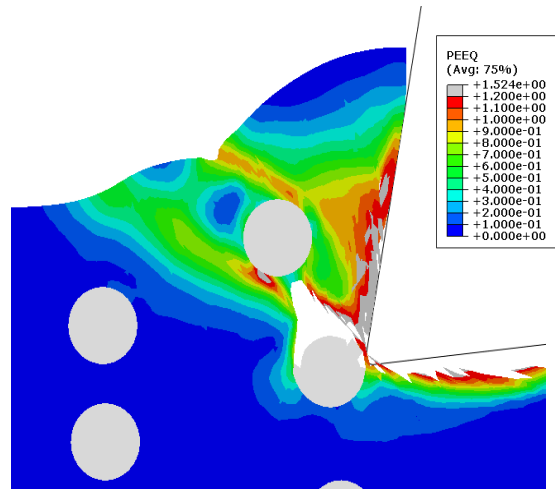


Figure 4.38 Distribution of plastic strain filed in machining of micro Al/SiC MMCs

4.5.3 Chip formation process

To analyse the chip morphology characteristics in machining the two MMC materials, it is necessary to understand the stress distribution within matrix. Basically, the size and location of particles play a significant role in the stress distribution pattern in machining process. Figure 4.39 demonstrates the fragmented chips formation with stress distribution immediately after chip formation shown in Figure 4.34. Initially, the particles along the cutting path partially deboned without any direct contact with tool tip, see Figure 4.34 (b). With the tool advances, bypassing of the primary shear plane occurred due to restricting behaviour of particle initiated. Then, a highly concentrated stress zone is formed connecting between the particle interface and upper surface of workpiece in the shear plane and lead to a crack initiation in the matrix as shown in Figure 4.39 (a). This crack initiation can be further proved by observing the high plastic strain field near this particle in Figure 4.38 as the MMCs workpiece behaviour in machining is mainly governed by the plastic deformation. As the tool advances, the matrix crack propagates towards the upper workpiece surface as shown in Figure 4.39 (b). Figure 4.39 (c) shows the fragmented chips form.

Chips were collected from micro and nano-MMCs machining experiments to validate the chip formation models. The increased discontinuity can be observed at the saw tooth structure of the chips obtained from machining of micro-MMCs (Figure 4.40(a)), whereas continuous chips with saw tooth structure were found in machining nano-MMCs (Figure 4.40(b)). Same observation was obtained from the experimental work conducted by Teng et al. (Teng *et al.*, 2018). It should be noted that although fragmented chips are formed in 2D FE simulation, because the axial depth of cut in the milling experiment is much greater than the micro-sized particle and also the micro-sized particles are randomly distributed in the matrix, the actual

chips may not break along the width of the chip. Therefore, when observing a crossed section of the actual chips, the simulated chips morphology of micro and nano-MMCs shows a good consistency with experimental results.

In addition, the highly concentrated stress zone can be found at particle-matrix interface in both models as mentioned earlier. Therefore, it might not be the main reason that lead to fragmented chips in micro-MMCs machining process. In fact, the chip formation mechanism in machining micro-MMCs is basically depend on the size and location of particles which is the main factor determining the way of stress propagation. By comparing the width of primary shear zone with particle size in these two models, it can be found that the shear zone is keeping intact during chip formation process in nano-MMCs rather than being fragmented in micro-MMCs. The existence of nanoparticle only affect the stress distribution pattern and it does not significantly affect overall integrity of primary shear zone during its propagation. In other words, the restricting behaviour of micro-sized particles is more dominant than that in nanoparticles, which results in a poor mobility of particles within matrix deformation. This might be due to the large uncut chip thickness to particle diameter in machining nano-MMCs. It can be thought that the location of nanoparticles has little effect on the chip formation mechanism in nano-MMCs machining process. Therefore, the ratio of uncut chip thickness to particle size might be considered as the fundamental reason determining the chip formation mechanism. Finally, the intact primary shear zone means that the material removal is achieved by shear sliding in nano-MMCs machining process. For micro-MMCs, as the result of strong restricting behaviour of micro-sized particles, the particle detachment from matrix caused by highly concentrated stress at its interface can be recognised as one of the factors promoting formation of fragmented chips.

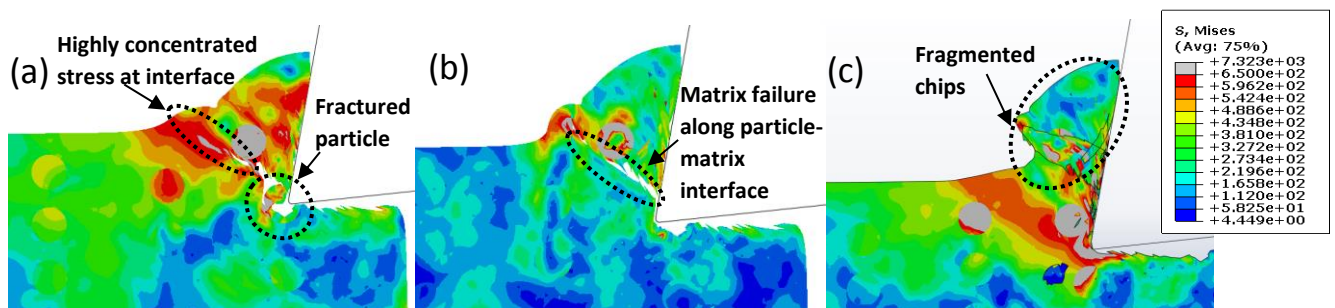


Figure 4.39 Fragmented chips formation when micro machining of micro Al/SiC MMCs.

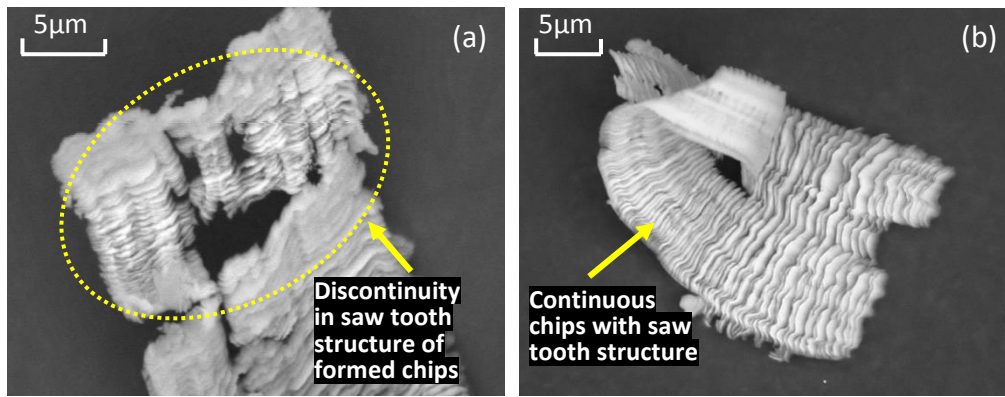


Figure 4.40 SEM images of chips obtained from machining Al/SiC MMCs reinforced with Vol.10 % (a) micro-sized particles (Φ :10 μm); (b) nano-sized particles (Φ :0.2 μm) under feed per tooth of 4 $\mu\text{m/tooth}$, cutting speed of 125.64 m/min and depth of cut of 30 μm

4.5.4 Tool-particle interaction process

It is believed that the significant reduction in particle diameter from micro to nanoscale not only influence the chip formation mechanism but also the tool-particle interaction. Figure 4.41 & 4.42 illustrate the tool-particle interaction in machining nano-MMCs and micro-MMCs respectively. It can be observed from Figure 4.41 that with the formation of continuous chip, the particle embedded within formed chips slides over the rake face generating a high localised stress at the tool-particle contact zone, which is similar as that for micro-MMCs. However, the nanoparticles are more likely to be squeezed by cutting edge due to their significantly large size difference, which leads to a relatively even distribution within particles. Also, the nanoparticles exhibit a good mobility within matrix as mentioned earlier. As a result, nanoparticles keep intact without cleavage and fracture. In contrast, the micro-sized particles are observed to experience fracture.

Different behaviours of particle interacting with cutting tool in micro-MMCs machining process are shown in Figure 4.42. It can be seen that the partially debonded particle is embed within fragmented chips and slide along the cutting tool, resulting in the particle sliding behaviour on the tool rake face and a high localised contact region (Figure 4.42 (a)), which in turn would contribute to the tool wear. The particle located in the cutting path suffers fracture and it was partially imbedded within the newly formed machined surface which might be considered as one of the main factors contributing to surface deterioration (Figure 4.42(b)). Some particles located along or below the cutting path are pressed into the matrix (Figure 4.42 (c)). These particles acting as sharp cutting edge lead to the increased residual stress or severe plastic deformation on machined surface. The particle detachment from machined surface

leading to the cavity can be observed from Figure 4.42 (d). This phenomenon is widely acknowledged by previous researchers in both experimental and simulation works.

In addition, the tool particle interaction can be visualised by analysing characteristics of cutting force profile obtained from these two models (Figure 4.43). Cutting forces obtained from machining the homogeneous matrix material under the same cutting parameters are also plotted in Figure 4.43. A larger cutting force fluctuation caused by the tool-particles interaction and fragmented chips formation is observed in micro-MMCs machining process when compared to that in homogeneous matrix materials. By comparison, obvious fluctuation in cutting force obtained from machining nano-MMCs cannot be observed when compared to that in machining homogeneous matrix. The larger cutting force fluctuation in machining micro-MMCs can be explained as results of various tool-particles interaction behaviours and the increased kinetic energy of the large particles.

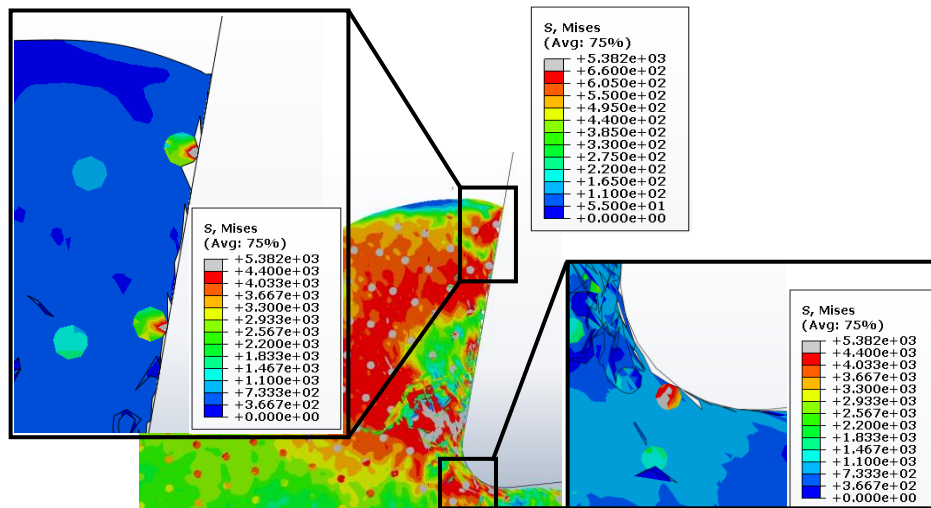


Figure 4.41 Nanoparticles interacting with cutting tool

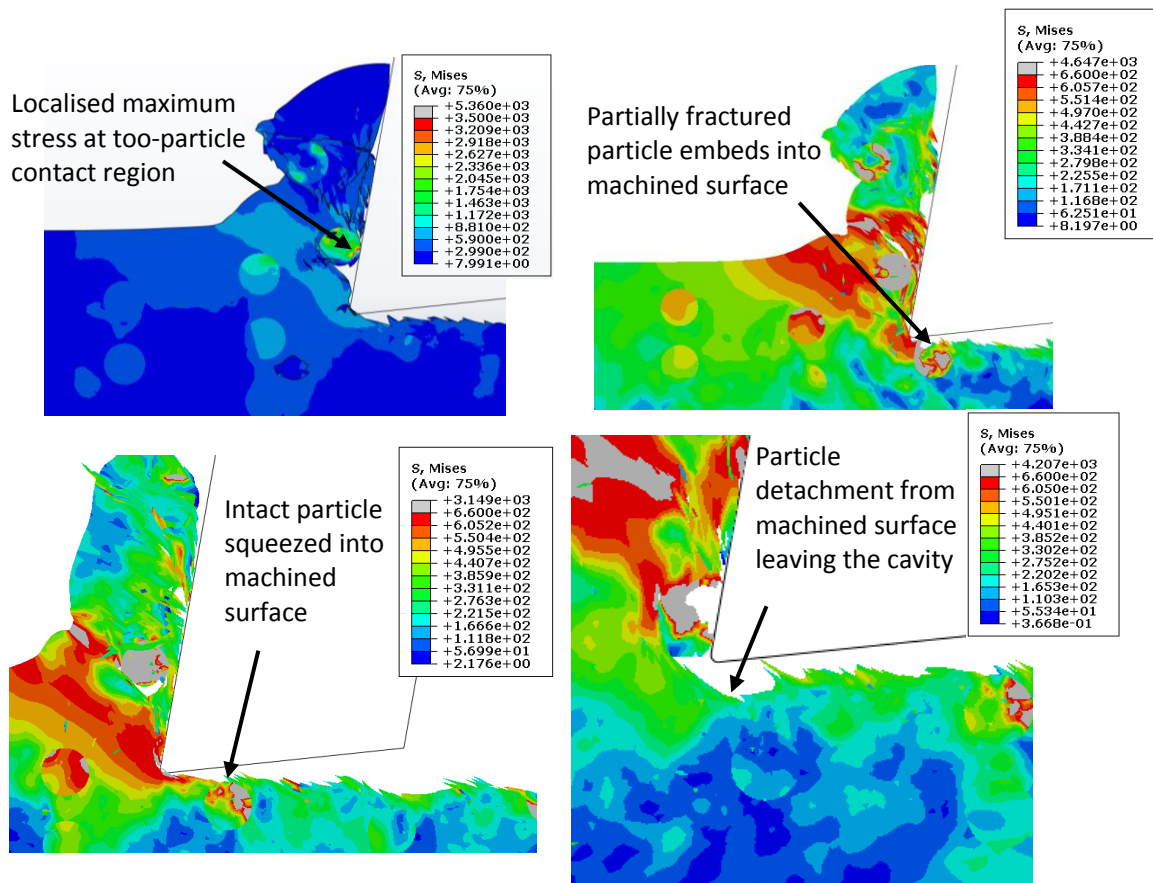


Figure 4.42 Different tool-particle interaction behaviours in machining micro Al/SiC MMCs.

Generally, the high contact stress at tool-particle interface has been recognised as the main reason causing the tool wear. Various tool wear patterns can be obtained from machining nano and micro-MMCs as shown in Figure 4.44. Tool tip rounding and relatively smooth abrasive wear can be observed on the flank face of the micro endmill in machining nano-MMCs (Figure 4.44(b)). This can be attributed to the relatively small size of nanoparticles resulting in a small kinematic energy when compared to micro-sized particles during tool-particles interaction. In addition, good mobility of nanoparticles with matrix deformation is another important factor contributing to the smooth abrasive wear pattern. However, the poor mobility of micro-sized particles within matrix materials and increased kinetic energy of micro-sized particles are believed to be the main reason that lead to a more severe edge chipping and fracture of tool tip on the endmill used in machining micro-sized MMCs (Figure 4.44(a)). Moreover, the unstable and fluctuating nature of machining process caused by different tool-particles interaction behaviours accelerates the wear process as well.

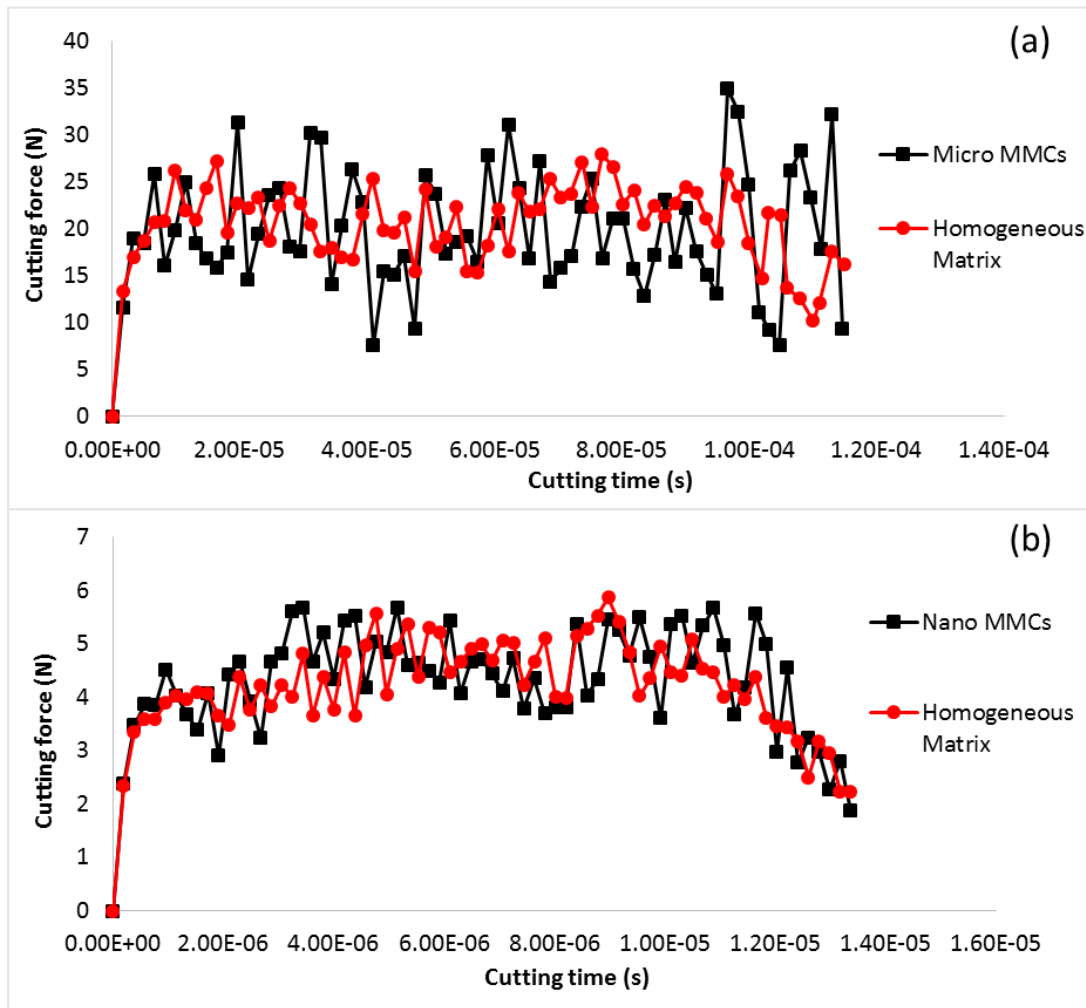


Figure 4.43 Simulated cutting forces of micro machining Al/SiC MMCs reinforced with (a) micro-sized particles; (b) nanoparticles.

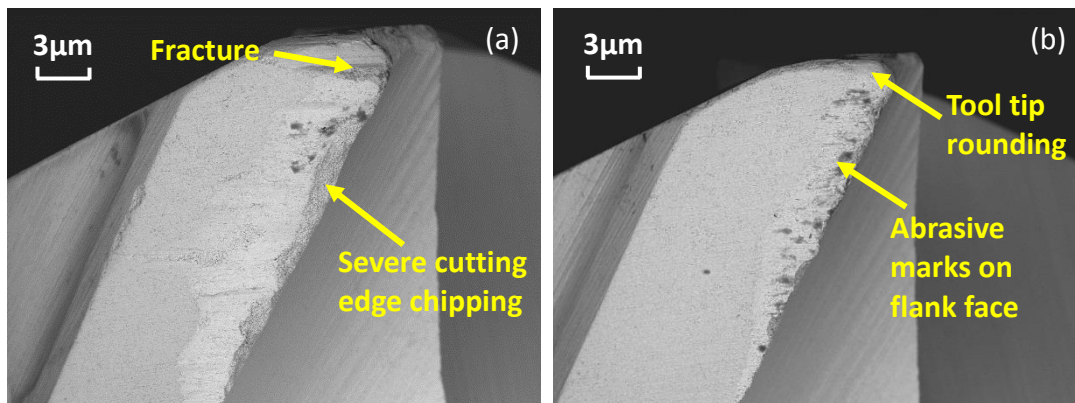


Figure 4.44 SEM micrographs of main cutting edge wear of micro endmill obtained from machining Al/SiC MMCs reinforced with Vol.10 % (a) micro-sized particles (Φ :10 μ m); (b) nano-sized particles (Φ :0.2 μ m) under feed per tooth of 4 μ m/tooth, cutting speed of 125.64 m/min and depth of cut of 30 μ m.

4.5.5 Machined surface morphology

Different tool-particles interaction behaviours can be found in machining nano and micro-MMCs, which in turn leads to different machined surface morphology. Figure 4.45 shows the simulated surface morphology in machining micro and nano-MMCs. The surface deterioration in machining micro-MMCs can be attributed to the surface defects such as cavities, scratch marks, fragmented particles embedded within matrix and particles pressed into matrix causing excessive strain, which in turn leads to a matrix failure (Figure 4.45 a). The abovementioned phenomenon obtained from simulation model can be easily observed from experimental results. It can be observed from Figure 4.46 (a) and (b) that the large cavity is formed when the majority of particles located in the cutting path are pulled away from the matrix during tool-particle interaction. Also, the fragmented particle embedded within matrix is observed in Figure 4.46 (a) which is consistent with simulated results. Excessive compressive stress would be caused by the particles pressed into the machined surface leading to the matrix failure or irreversible plastic deformation. Moreover, during the cutting process, scratch marks on machined surface will be formed when the fragmented particles acting as sharp cutting edge being ploughed through between the flank face of cutting tool and matrix. The magnified images of scratch marks marked in region i and ii can be found in Figure 4.46 (b). Similar surface morphology can be observed in the simulation model of machining nano-MMCs (Figure 4.45 (b)). However they are not observed in machined surface obtained from experimental works. Distinct milling tool path can be observed on the machined surface (Figure 4.46 (c)). Micro defects can be found at the tool path which broke its continuity. This might be caused by the scratching of residual chips containing nanoparticles at the tool-matrix interface during high speed machining. It can be said that the significant reduction in particles size is beneficial for improving the machined surface quality.

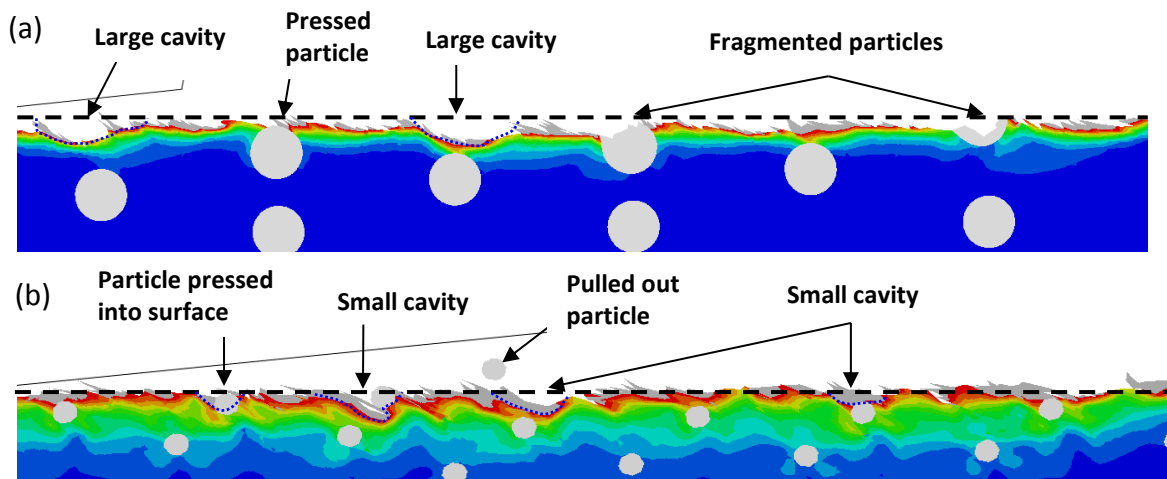


Figure 4.45 Simulated surface morphology from machining (a) micro-MMCs; (b) nano-MMCs.

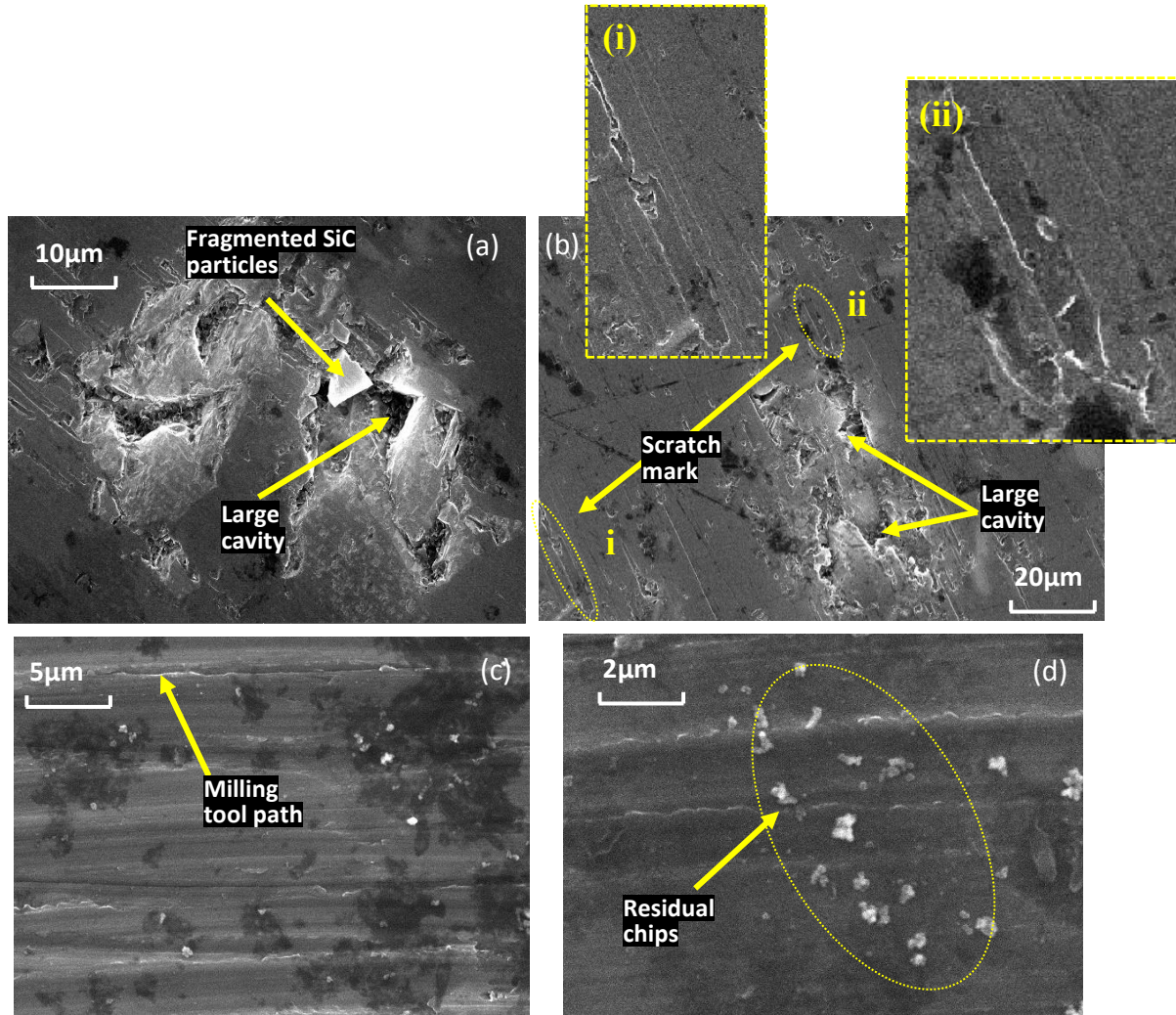


Figure 4.46 SEM micrographs of machined surface from experimental works (a)&(b) micro-MMCs; (c)&(d) nano-MMCs under the feed per tooth of 4 $\mu\text{m}/\text{tooth}$, cutting speed of 125.64 m/min and depth of cut of 30 μm .

4.6 Conclusion

In this chapter, the machinability of MMCs reinforced with SiC particles were studied using finite element cutting model. The MMCs reinforced with nano-sized and micro-sized particles were evaluated and compared in terms of the chip formation process, stress/strain distribution, tool-particles interaction, machined surface morphology. Model validation was conducted by comparing the cutting force, machined surface and chip morphology obtained from simulation model and micro milling experiments. A satisfying agreement was obtained. The assumption for the effect of particles on tool wear in simulation model has also been verified by observing the worn tool obtained from experiments. The following conclusion can be obtained:

- In machining nano-MMCs, the particles can be recognised as the obstacle restricting the progression of von Mises stress within matrix, resulting the highly strained field at particles interface. A continuous chip with saw tooth appearance is obtained at the uncut chip thickness above 1 μm . Highly strained bands at vicinity of particles are observed at chips, which can be recognised as the cause of this lamellate structure. Moreover, the investigation on tool-particles interaction provides a better understanding for premature tool wear. The concentrated stress acting on the nanoparticle is generated due to the ploughing between particle and flank face. During the machining process, nanoparticle is still intact without fracture.
- In machining micro-MMCs, with the effect of different relative position of particle to cutting path, various particle fractures behaviours such as slightly fracture at top side, residual fragments embedded within cavity, completely debonding can be found. These fractures behaviours result in different types of defects on the machined surface such as shallow cavity around embedded particles, severe plastic deformation around cavity and shallow cavity. Additionally, a severe plastic deformation and failure can be found in the matrix materials which are squeezed by the particle fragments with the advancement of cutting tool. Thus, the cutting mechanism is believed to be dramatically affected by particle fragments.
- By comparing the cutting mechanism of nano-MMCs and micro-MMCs, the following conclusions can be drawn:
 - The decrease in particle size leading to the different particle restricting behaviours exhibits a significant effect on the stress propagation within workpiece and it is concluded as the main reason causing the various von Mises stress distribution pattern in nano and micro-MMCs. The restricting behaviour would become more significant with increasing of particle size.
 - The stress propagation determined by the ratio of particle size and uncut chip thickness is considered as the main factor determining the chip formation mechanism. In machining of micro-MMCs, the size and location of particles play predominant role for chip formation mechanism due to the increased ratio of particle size and uncut chip thickness. In machining of nano-MMCs, due to the reduced size, the ratio of uncut chip thickness to particle size might be considered play little effect in determining the chip formation mechanism.
 - The better mobility of nanoparticle within matrix due to reduced size makes them being squeezed by cutting edge, which in turn produces evenly distributed

stress and less kinetic energy on nanoparticles during machining. This leads to intact particle which is different from the micro-sized particle showing cleavage and fracture. This observation has been verified by simulated cutting force profile and tool wear pattern obtained from experiments. The way of stress propagation mode within matrix under the effect of particle size is found to determine the chip formation mechanism. Continuous chip formation is observed in machining nano-MMCs, while chips obtained from machining micro-MMCs tends to be discontinuous.

- By comparing with the machined surface morphology obtained from machining micro and nano-MMCs, it can be concluded that the reduced particle size (nanoparticles) is beneficial for improving surface quality.

Chapter 5 Tool wear behaviours in micro milling of nano-Mg/Ti MMCs

5.1 Introduction

This chapter presents a comprehensive experimental investigation on the tool wear in micro milling of 1.98 Vol.% Mg/Ti MMCs under dry cutting condition. Tool wear is assessed by tool diameter reduction and flank wear. The wear mechanisms and effect of cutting parameters including feed per tooth and cutting speed on cutting force, surface roughness and burr formation is discussed by considering the size effect with the progression of tool wear. The performance of coated and uncoated cutting tool is compared. Modelling works from previous sections are introduced to obtain a clear understanding of the wear mechanism.

5.2 Experimental setup

5.2.1 Workpiece materials

Magnesium-based metal matrix composites (Mg/Ti MMCs) reinforced with 1.98 Vol.% nano-sized titanium particles (approx. 30-50 nm) is used as workpiece throughout the research. The workpiece is synthesized and supplied by National University of Singapore (NUS). The lightweight Mg-Ti nanocomposites has higher specific mechanical strength when compared to pure magnesium. Metallic reinforcements such as titanium with superior mechanical properties was found to produce an acceptable compromise in ductility compared to the addition of ceramic reinforcements SiC, Al₂O₃ and TiC MMCs. The mechanical properties of Mg/Ti MMCs are shown in Table 5.1.

Table 5.1 Mechanical properties of 1.98 Vol.% Mg/Ti MMCs (Meenashisundaram and Gupta, 2014)

Density (g/cm ³)	0.2 Yield Strength (MPa)	Ultimate tensile strength (MPa)	Ductility (%)	Microhardness (HV)	Grain size (μm)
1.793	162 ± 5	231 ± 12	7.7 ± 0.1	70±2	1.25 ± 0.25

Magnesium turnings of 99.9% purity, supplied by ACROS Organics, New Jersey, USA are used as the base matrix. Reinforcement consists of pure titanium powder of 30-50 nm supplied by US Research Nanomaterials. Mg/Ti MMC is synthesized using the disintegrated melt deposition (DMD) technique. The distribution of nano Ti particles within Mg/Ti MMCs was observed through Scanning electron microscope (SEM) in Figure 5.1.

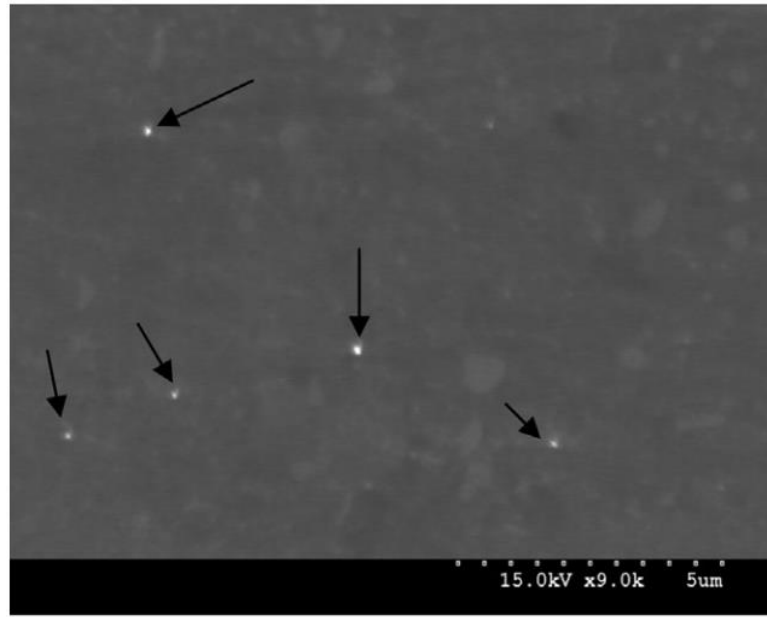


Figure 5.1 Distribution of nano Ti particles in Mg/Ti MMCs (Meenashisundaram and Gupta, 2014)

5.2.2 Experiments setup

Micro milling experiments were undertaken on an ultra-precision desktop micro-machine tool (Nanowave MTS5R). The spindle runout was measured to be less than $2\text{ }\mu\text{m}$. Total volume of 620 mm^3 of workpiece material was removed in each set of experiment. 6 sets of machining experiments and the cutting parameters for each set of experiment are detailed in Table 5.2. Brand new tools were measured before performing each set of experiments. Full-immersion slot milling with a constant axial depth of cut of $100\text{ }\mu\text{m}$ was employed in all experiments. For each set of experiment, a total volume of 620 mm^3 of workpiece material was removed at 4 even intervals, i.e. a volume of 155 mm^3 of workpiece materials in each interval. The tools were then measured after each interval. The cutting forces along the X, Y and Z axis was measured using a Kistler piezoelectric dynamometer (9256C2). A scanning electron microscope (SEM, Hitachi TM3030) was used to acquire the micrographs of the worn tools. A white light interferometer (Zygo NewView 5020) was employed to measure surface roughness of the machined slot.

Table 5.2 Cutting parameters for each set of experiment

Exp set/Tool #	Cutting speed, v_c (m/min)	feed per tooth, $f_t(\mu\text{m/tooth})$	Tool
1	31.4	3	uncoated
2	62.8	3	uncoated
3	125.6	3	uncoated
4	62.8	0.75	uncoated
5	62.8	1.5	uncoated
6	62.8	3	AlTiN-coated

5.2.3 Micro endmills and tool wear criteria

Two flutes uncoated and AlTiN coated micro-grain tungsten carbide endmills with nominal cutting diameter (D) of $0.5^{+0.00mm}_{-0.02mm}$ mm and helix angle of 20° are used. The dimension and geometry of the micro endmill are illustrated in Figure 5.2, 5.4 & 5.5. The cutting edge radius of new tools is measured using SEM and was estimated to be $2.0 \mu\text{m}$ in average (Figure 5.4 (b)). As the flank wear and reduction in effective tool diameter affect the machining accuracy and surface integrity, the effective tool diameter D_E and average flank wear V_{BA} are used as tool wear criteria and measured as shown in Figure 5.3. Flank wear V_B is defined as the band width in a direction perpendicular to the original cutting edge where the grinding marks from manufacturing process are removed by abrasive and chipping worn marks on the flank face of endmill. The measurement of flank wear is carried out at four consistent positions at different endmill and an average value, V_{BA} , is computed. All endmills were selected from the same batch to eliminate the effect of tool manufacturing errors.

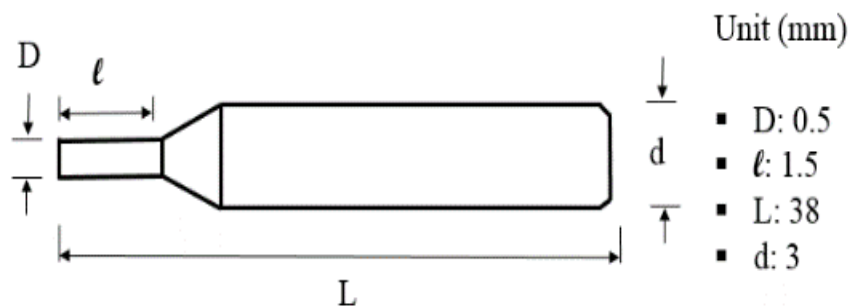


Figure 5.2 Dimension of the micro endmill (uncoated & coated)

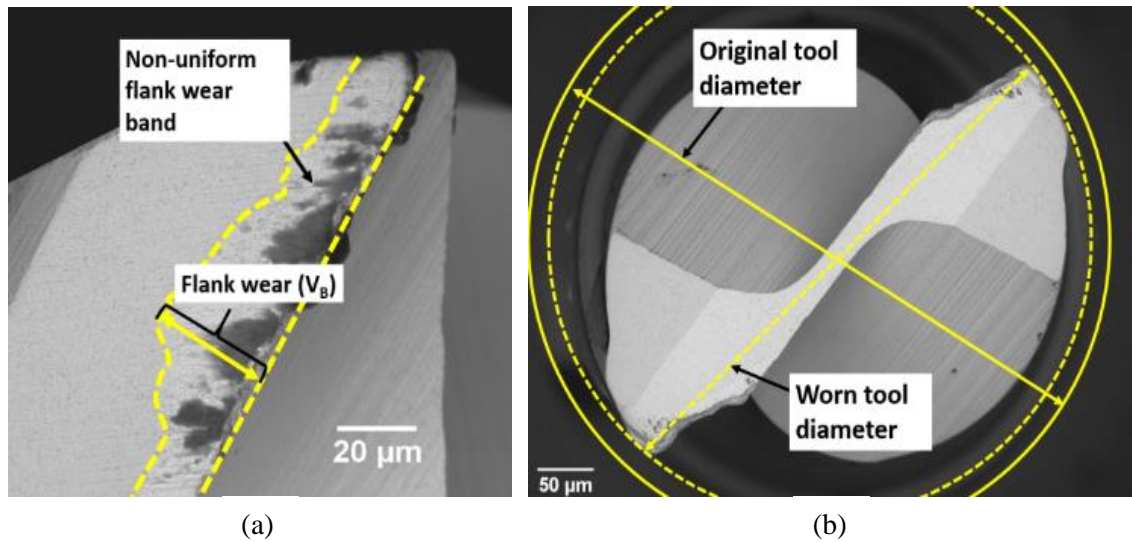


Figure 5.3 Measurement of (a) flank wear, V_B and (b) effective tool diameter (D_E)

5.3 Tool wear mechanism analysis

A better understanding of tool wear benefits from observing highly magnified SEM micrographs of the endmills. A significant reduction in the effective tool diameter is observed (an example is shown in Figure 5.3(b)) due to the decrease of cutting edge radius. All endmills used in this experiment exhibited similar wear behaviour. A significant amount of volume loss of tool material is found in the main cutting edge in all tools used in this experiment. A comparison between the new tool and worn tool (Tool #1) on the side and top view is illustrated in Figure 5.4 and Figure 5.5. Figure 5.6 shows the progression of tool wear against different cutting conditions. It is noted that a significant amount of tool wear with the combination of non-uniform flank wear and cutting edge chipping is found on the side cutting edge and flank face of all five uncoated endmills. For the AlTiN coated tools, delamination and flank wear were the dominant wear patterns.

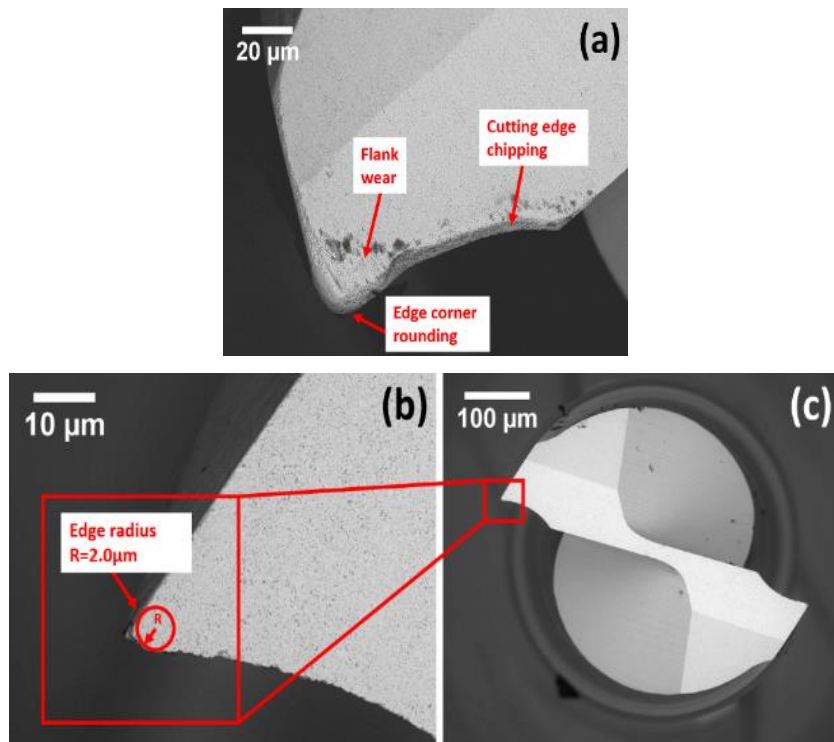


Figure 5.4 Top view of SEM micrograph for (a) worn tool (Tool #1); (b) & (c) new tool (uncoated endmill).

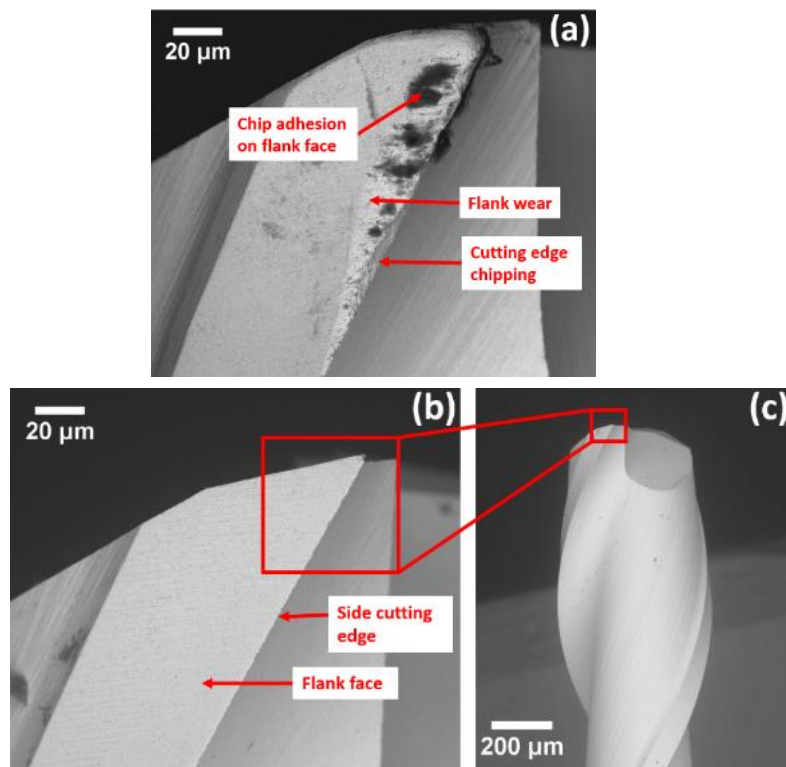


Figure 5.5 Side view of SEM micrograph for (a) worn tool (Tool #1); (b) & (c) new tool (uncoated endmill).

5.3.1 Effect of cutting speed

Figure 5.7 illustrates the effect of cutting speed on flank wear and reduction in tool diameter with the increasing cutting volume at constant depth of cut and feed per tooth. Understandably,

flank wear and reduction in tool diameter increases with cutting volume under all cutting parameters. As shown in Figure 5.7 (a), the largest wear was experienced at cutting speed of 31.4 m/min. The largest trend on the progression of flank wear was observed at the cutting speed of 62.8 m/min, namely this cutting speed produces the smallest wear after cutting volume of 155 mm³ and largest wear after cutting volume of 620 mm³ compared with other cutting speed. In addition, the flank wear obtained at 125.6 m/min provided the most stable trend and the smallest flank wear after cutting volume of 620 mm³ was measured. The smallest tool diameter reduction is obtained at the largest cutting speed of 125.6m/min (Figure 5.7(b)), which is consistent with the trend in flank wear.

Figure 5.8 and 5.9 illustrate the SEM micrographs and EDS spectra of the uncoated endmills after cutting volume of 620 mm³ of the workpiece material and at a constant feed per tooth of 3μm/tooth, depth of cut of 100 μm with cutting speed of 31.4m/min, 62.8m/min and 125.6m/min. Extensive abrasive marks and chipping wear along the flank face and cutting edges are observed from cutting speed of 31.4 and 62.8 m/min (Figure 5.8 (a & b)). In addition, the chip adhesion was observed on the flank face of Tool #1 and Tool #2 (Figure 5.8 (a & b)). The EDS spectra performed on flank face (Figure 5.8 (c & d)) shows the presence of excessive element of magnesium (Mg), and titanium (Ti). Chip adhesion can cause high friction during the interaction between the flank face and workpiece which is more evident in elastic dominated machining process. Additionally, the existence of titanium element on flank face from EDS spectra would confirm the abrasive effect contributed by hard reinforced particles. Based on this assumption, it is thought that local stressing would be induced on the cutting edge and flank face, which is a consequence of the hard reinforcement abrading through the cutting edge especially during elastic dominated cutting zone. The abrasive effect of hard particles during machining process has been verified in section 4.3.2 and section 4.5.4. Conversely, it can be seen from the EDS spectra obtained from the flank face (Figure 5.9(b)) that the chip adhesion effect is not evident and tool wear is considerably reduced at the cutting speed of 125.6m/min. Small amount of flank wear with only partial chipping is observed at cutting edge, which indicates that the gradual abrasive wear dominates the cutting process. At the initial cutting stage, small amount of adhered workpiece materials are found at flank face after cutting volume of 155 mm³ at cutting speed of 125.6m/min and feed per tooth of 3μm/tooth (Tool #3 at Figure 5.6). This adhered workpiece materials acting as similar role as BUE is believed to be the main reason to protect the cutting tool from chipping and flank wear. The friction condition at the tool-material interface is affected by the adhered workpiece materials that acts as a protecting

layer preventing the cutting edge being in contact with workpiece during machining process (Ramaswami, 1971).

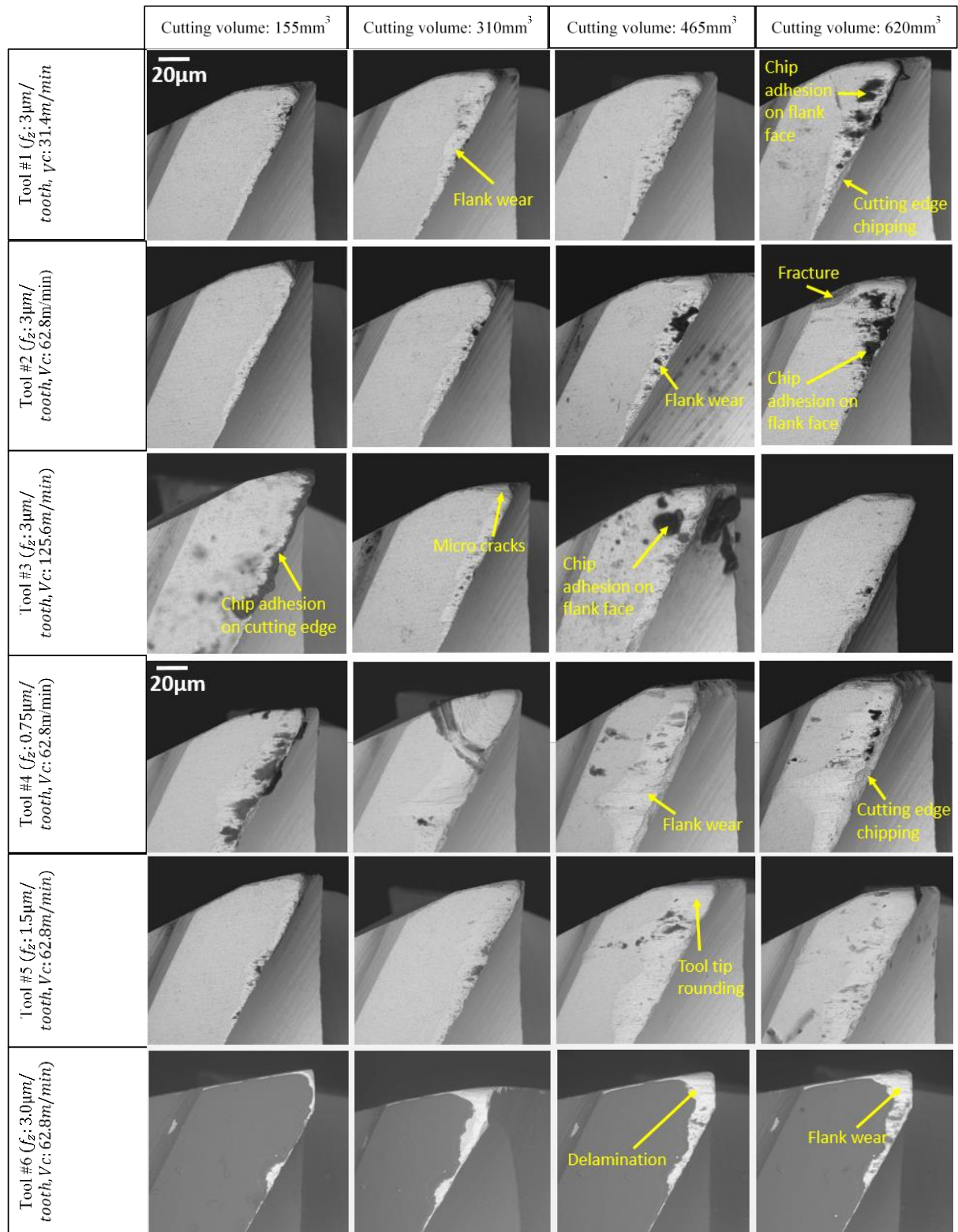


Figure 5.6 SEM micrographs of the tool wear progression under various cutting conditions.

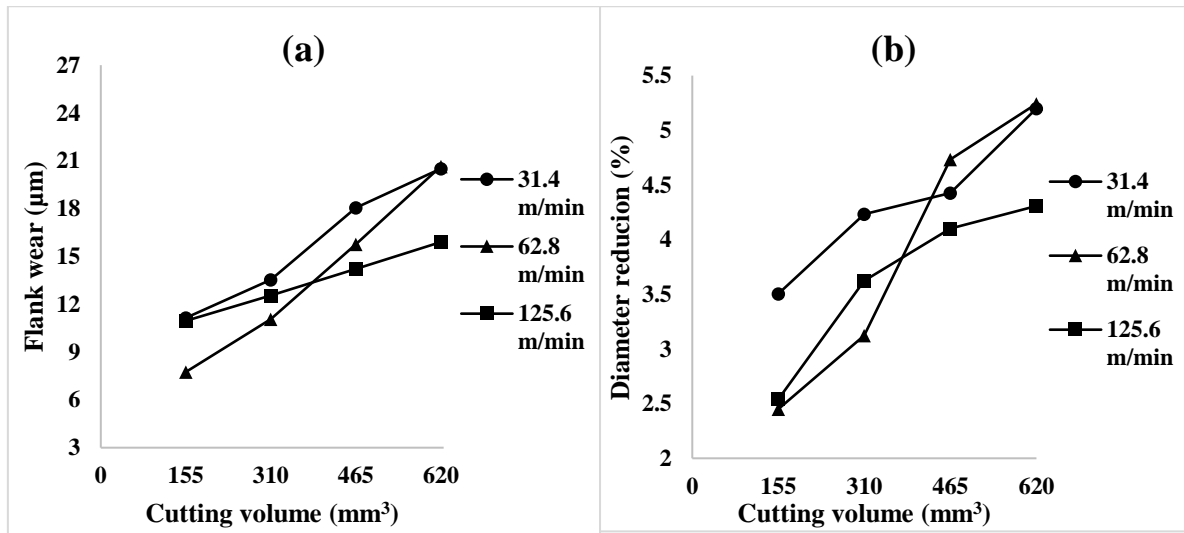


Figure 5.7 The effect of cutting speed on the progression of (a) flank wear; (b) reduction in tool diameter at constant feed per tooth of $3\mu\text{m}/\text{tooth}$ and depth of cut of $100\mu\text{m}$.

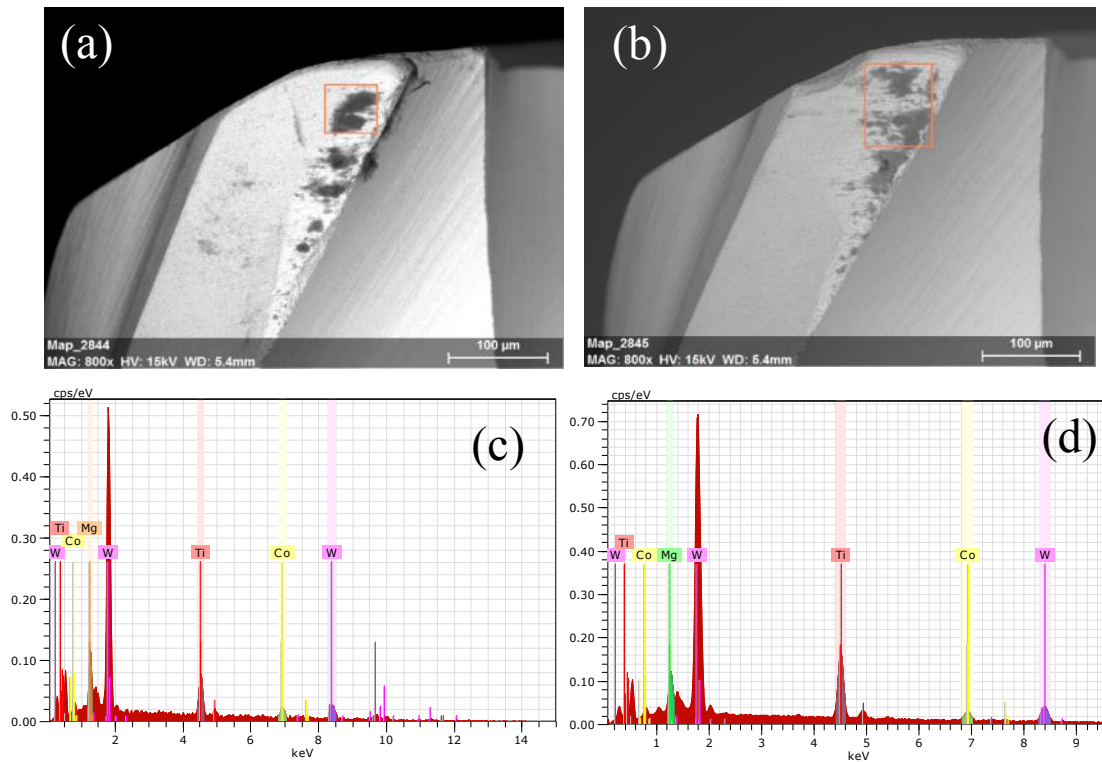


Figure 5.8 SEM micrographs and EDS spectra of uncoated endmills after cutting volume of 620 mm^3 from (a)(c) Tool #1 (cutting speed of $31.4\text{m}/\text{min}$); (b)(d) Tool #2 (cutting speed of $62.8\text{m}/\text{min}$) at feed per tooth of $3\mu\text{m}/\text{tooth}$ and depth of cut of $100\mu\text{m}$ (with adhesion effect).

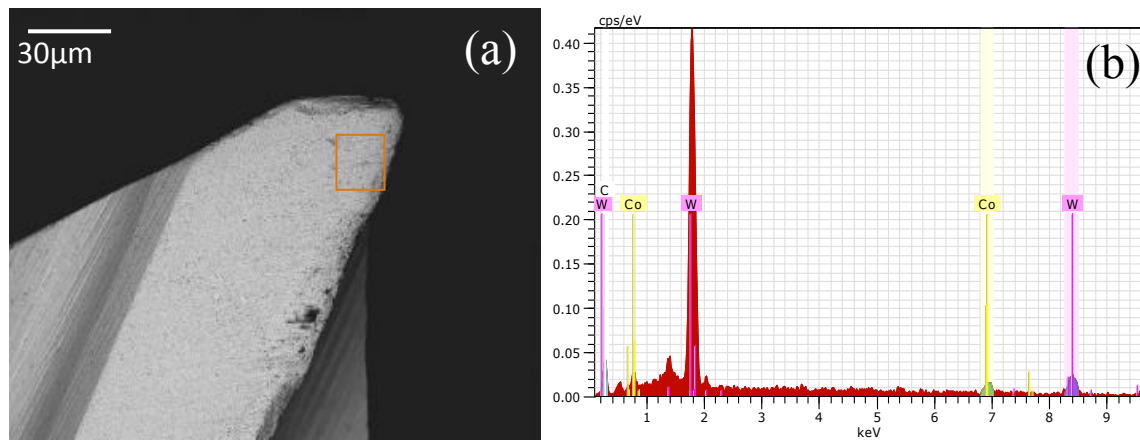


Figure 5.9 SEM micrographs and EDS spectra of uncoated endmill after cutting volume of 620 mm³ from Tool #3 (cutting speed of 125.6 m/min) at feed per tooth of 3µm/tooth and depth of cut of 100 µm (without adhesion effect).

5.3.2 Effect of feed per tooth

According to the observation on the effect of feed per tooth on the tool wear (Figure 5.10), it can be seen that flank wear and reduction in tool diameter increases with the decrease of feed per tooth. The largest wear was recorded at the smallest feed per tooth of 0.75µm/tooth while the largest feed per tooth of 3µm/tooth resulted in the smallest wear. SEM micrographs of the severely worn endmill (Tool #4) is shown in Figure 5.6. The most severe flank wear with edge chipping was found after cutting volume of 620 mm³. Based on the observation of EDS spectra (Figure 5.11), chip adhesion was not evident and an increasing volume loss of tool material was observed on the cutting edge and edge corner leading to the most severe wear in all experiments. This can be attributed to the cutting edge radius size effect. The instantaneous uncut chip thickness varies during each tool pass in slot milling. The uncut chip thickness starts from zero at the initial contact with the workpiece, followed by an increase to its maximum value as the tool rotates ninety degree, and then decrease to zero when cutting edge leaves workpiece. As a result, the ploughing region in each tool passing cycle at small feed per tooth is larger when compared with that at larger feed per tooth and the ploughing effect could dominate the cutting process when the uncut chip thickness is close to the minimum chip thickness. The ploughing effect could cause a significant portion of materials to be rubbed underneath the cutting edge and elastically deformed, and the workpiece material recovers to its original position without proper chip formation after the cutting edge passes, which induces a higher cutting force. Therefore, the abrasive wear mechanism resulting in a large flank wear and edge chipping is induced at small feed per tooth of 0.75µm. This can be contributed to the high frictional and normal stress experienced by cutting edge which exceeds the strength of the tool materials during each tool passing (Friedrich and Kulkarni, 2004). Additionally, unlike turning process,

the intermittent material removal mode and instantaneous changing uncut chip thickness in micro milling produce high frequency shocking loads to cutting edges and hence results in the edge chipping. This is believed to be another important contributing factor to higher tool wear rate. At higher feed per tooth, shear mode dominates most of the cutting process which leads to a uniform distributed stress on the cutting edge, resulting in a reduced tool wear rate.

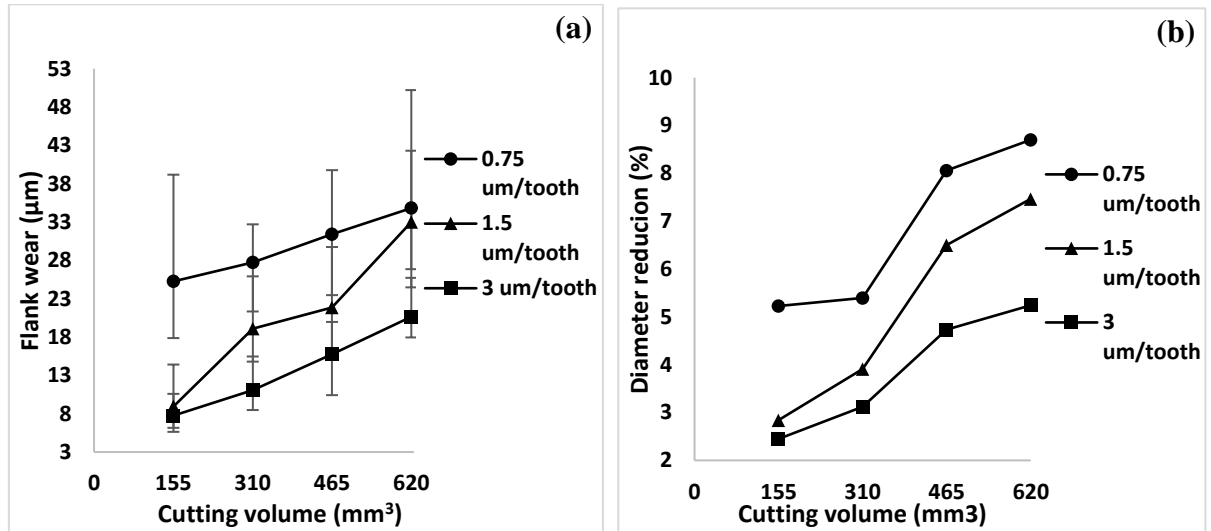


Figure 5.10 The effect of feed per tooth on the progression of (a) flank wear; (b) reduction in tool diameter at constant cutting speed of 62.8 m/min and depth of cut of 100 μm.

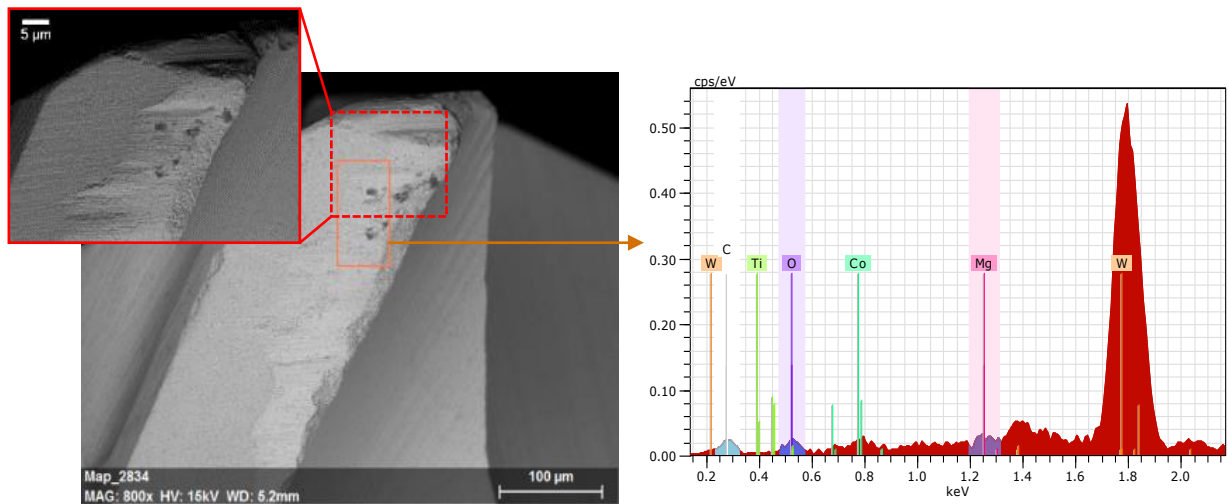


Figure 5.11 SEM micrographs and EDS spectra of uncoated endmill after cutting volume of 620 mm³ from Tool #4 (feed per tooth of 0.75 μm/tooth) at cutting speed of 62.8 m/min and depth of cut of 100 μm.

5.3.3 Effect of tool coating

Delamination was identified as the principal wear pattern on the coated tools. Chip adhesion and built-up edge are not observed on the coated tool. It can be noticed that the AlTiN coating

showed a better resistance to the chip accumulation under the cutting conditions used in this study. Figure 5.12 compares the performance of coated and uncoated tool in terms of reduction in tool diameter. A faster reduction rate was observed at the uncoated tool resulting in a higher value after cutting volume of 620 mm³ comparing with coated tool. Figure 5.13(a) shows SEM micrograph of the AlTiN coated tool after cutting volume of 620 mm³. A complete coating delamination was found along the flank face and cutting edge with the effect of machining stress. However, cutting edge was found intact without chipping which indicates a gradual abrasive wear. Additionally, a large presence of tungsten which is the main element of tool material was found on EDS spectra obtained from the area marked in Figure 5.13(a). The abrasive wear caused by hard titanium particles and the poor adhesion between the coating materials and the tool base substrate likely contributed to the coating delamination.

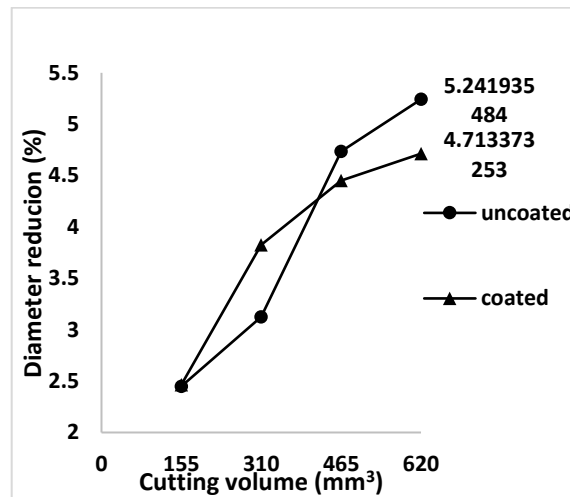


Figure 5.12 The effect of tool coating on the progression of reduction in tool diameter at constant feed per tooth of 3µm/tooth, cutting speed of 62.8 m/min and depth of cut of 100 µm.

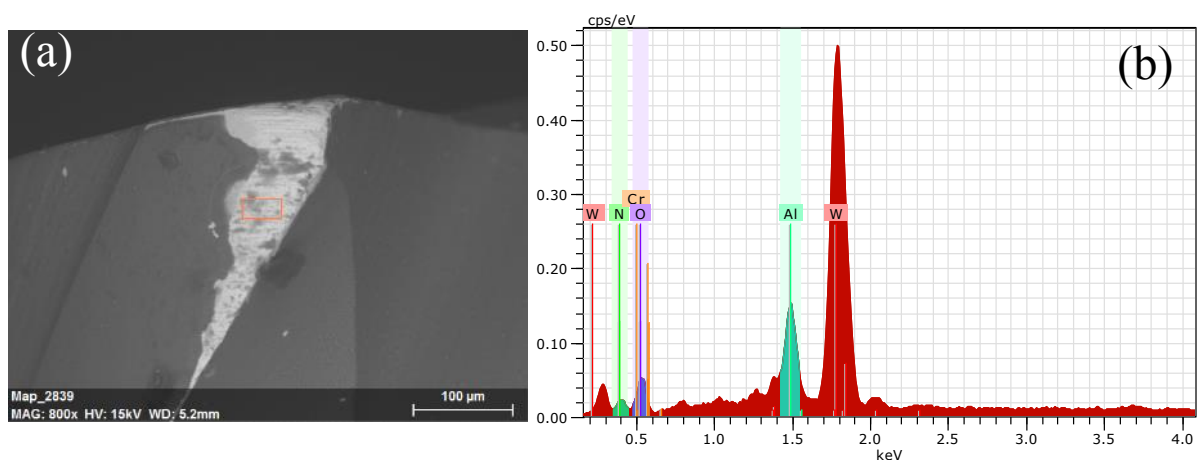


Figure 5.13 SEM micrographs and EDS spectra of coated endmill after cutting volume of 620 mm³ from Tool#6 at constant feed per tooth of 3µm/tooth, cutting speed of 62.8 m/min and depth of cut of 100 µm.

5.4 Effect of input parameters on cutting force with tool wear progression

To gain a better understanding of the effect of tool wear on the machinability, an average cutting force was calculated by collecting the peak-to-valley forces for each revolution and 500 revolutions was collected in total. Figure 5.14 presents the variation of average cutting force with the progression of tool wear under various cutting speed, feed per tooth and tool coating. The cutting force obtained from new tool was also captured (labelled at volume of 0 mm³). It can be seen from Figure 5.14 (a) that the largest cutting force is experienced at cutting speed of 31.4m/min after cutting volume of 620 mm³ although this cutting condition can produce the smallest tool wear in terms of flank wear and diameter reduction. A stable increase in the cutting force was observed from cutting volume 0 to 620 mm³ at the cutting speed of 125.6m/min that corresponds to the variation of flank wear.

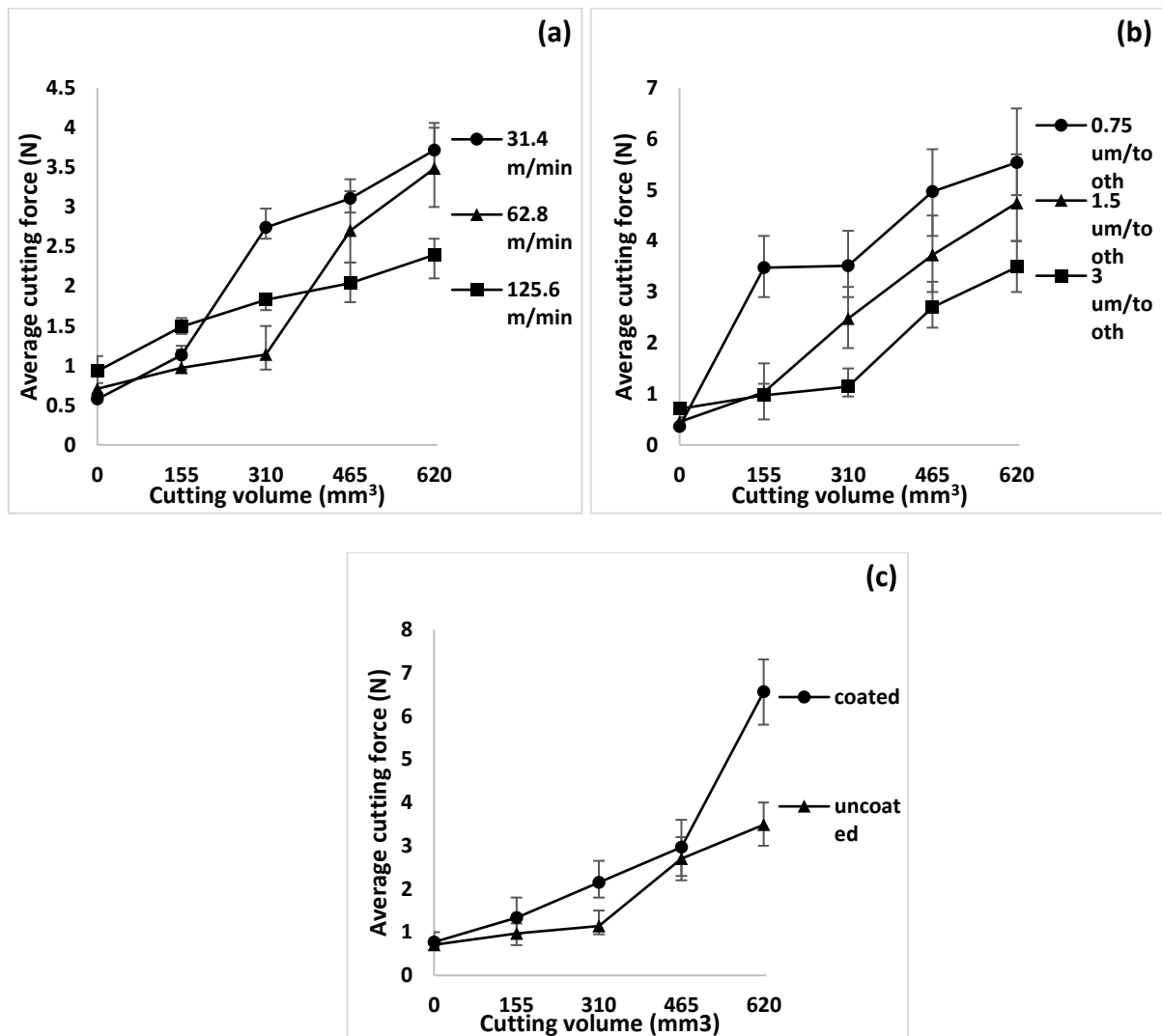


Figure 5.14 Variation of average cutting force with progression of tool wear under the effected by (a) cutting speed at feed per tooth of 3μm/tooth and depth of cut of 100 μm; (b) feed per tooth at cutting speed of 62.8 m/min and depth of cut of 100 μm; (c) tool coating

With regard to the influence of size effect on the tool wear, Figure 5.14 (b) shows the effect of feed per tooth ranging from 0.75 to 3 $\mu\text{m}/\text{tooth}$ (cover the minimum chip thickness) on the cutting force. It can be noted that the smallest feed per tooth of 0.75 $\mu\text{m}/\text{tooth}$ produced the largest cutting force, which can be considered as the main reason to cause the largest tool wear. Also, a sudden increase in the cutting force was seen from cutting volume 0 to 155 mm^3 , which was correlated to the observation where significant flank wear and chipping on endmill after cutting volume of 155 mm^3 (Tool #4, Figure 5.6) compared to other experiments. To further confirm the significant role played by size effect on the tool wear, Figure 5.15 compares the variation of flank wear and specific cutting force with the effect of feed per tooth. The specific cutting force can be defined as the chip load required to remove a unit volume of material and it was calculated by dividing the cutting force by the section area of chips. As illustrated in Figure 5.15, highest specific cutting force was experienced at lowest feed per tooth, while the specific cutting force at each feed per tooth increases with the flank wear. In addition, nearly 5 times larger of the specific cutting force (72.8 J/mm^3) at feed per tooth of 0.75 $\mu\text{m}/\text{tooth}$ can be found than that at 3 $\mu\text{m}/\text{tooth}$ (18.25 J/mm^3) after cutting volume of 620 mm^3 . By considering this information, it can be thought that the ratio of cutting edge radius to uncut chip thickness increases so that the material removal mechanism dominated by elastic deformation is becoming evident with the progression of flank wear.

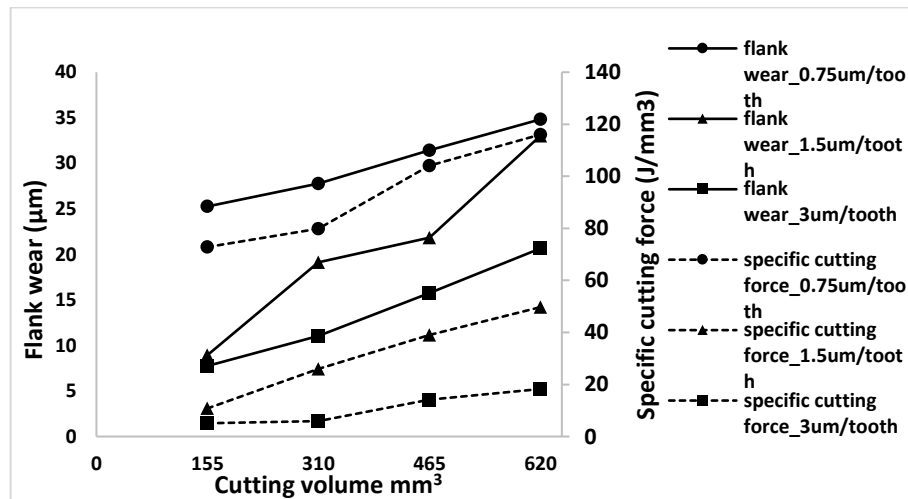


Figure 5.15 The comparison between the flank wear and specific cutting force with the effect of feed per tooth at the cutting speed of 62.8m/min, depth of cut of 100 μm .

For the effect of tool coating on the cutting force, it is interesting to note from Figure 5.14 (c) that the cutting force obtained from coated tool exhibits higher values from cutting volume 155

to 620 mm^3 than that from uncoated tool. This can be correlated with the delamination effect induced at the initial stage of cutting (cutting volume of 155 mm^3) which increases the cutting edge radius.

5.5 Effect of input parameters on surface roughness and burr formation

In order to clearly understand the relationship between the tool wear and surface quality, average surface roughness R_a was measured for all samples (Figure 5.16). It can be seen from Figure 5.16(a) that at the constant depth of cut of $100 \mu\text{m}$ with a feed of $3 \mu\text{m/tooth}$, cutting speed of 62.8 m/min generates the lowest surface roughness. In contrast, the surface roughness obtained at 125.6 m/min is the highest. As known that the deterioration can be induced on the surface roughness due to existence of BUE under certain machining conditions. This might be contributed to the adhesion effect of the BUE (Figure 5.18) on the machined surface. Some loose portion of BUE is thought to be adhered to the bottom surface of micro channels, which results in a deteriorated surface roughness. As expected, the highest surface roughness is obtained by the tool with large wear at smallest feed ($0.75 \mu\text{m/tooth}$). At this feed rate, the material is removed by relatively large cutting edge radius causing severe edge chipping (Figure 5.17). This indicates that the surface generation mechanism is dominated by ploughing and elastic deformation effect. The surface roughness decreases with increasing feed per tooth. This confirms the fact that the shearing mechanism becomes more dominant at larger feed rate. The results show a good agreement with the wear measurement. With regards to the effect of tool coating on surface roughness at Figure 5.16 (c), minor variation was observed in surface roughness results which indicate that coating has limited impact on surface quality.

To qualitatively compare burr formation at different cutting conditions and correlate its size with tool wear progression, SEM micrographs of the top burr at various cutting volumes were obtained (Figure 5.19). It can be seen that the burr formation is strongly dependent on tool wear conditions especially in the down milling side Figure 5.19 (a- d). At the feed rate of $3 \mu\text{m/tooth}$ (Figure 5.19(a-c)), an increased size of the top burrs was observed with the increase of tool wear. Additionally, cutting speed of 125.6 m/min (Figure 5.19 (c)) generates the slots with the smallest burr size, which corresponds to the smallest tool wear obtained at these cutting conditions. At the cutting speed of 62.8 m/min (Figure 5.19 b, e, d), the rise of feed per tooth from 0.75 to $3 \mu\text{m/tooth}$ results in a reduced burr size. The largest burrs formation is obtained at smallest feed per tooth of $0.75 \mu\text{m}$ Figure 5.19 (d).

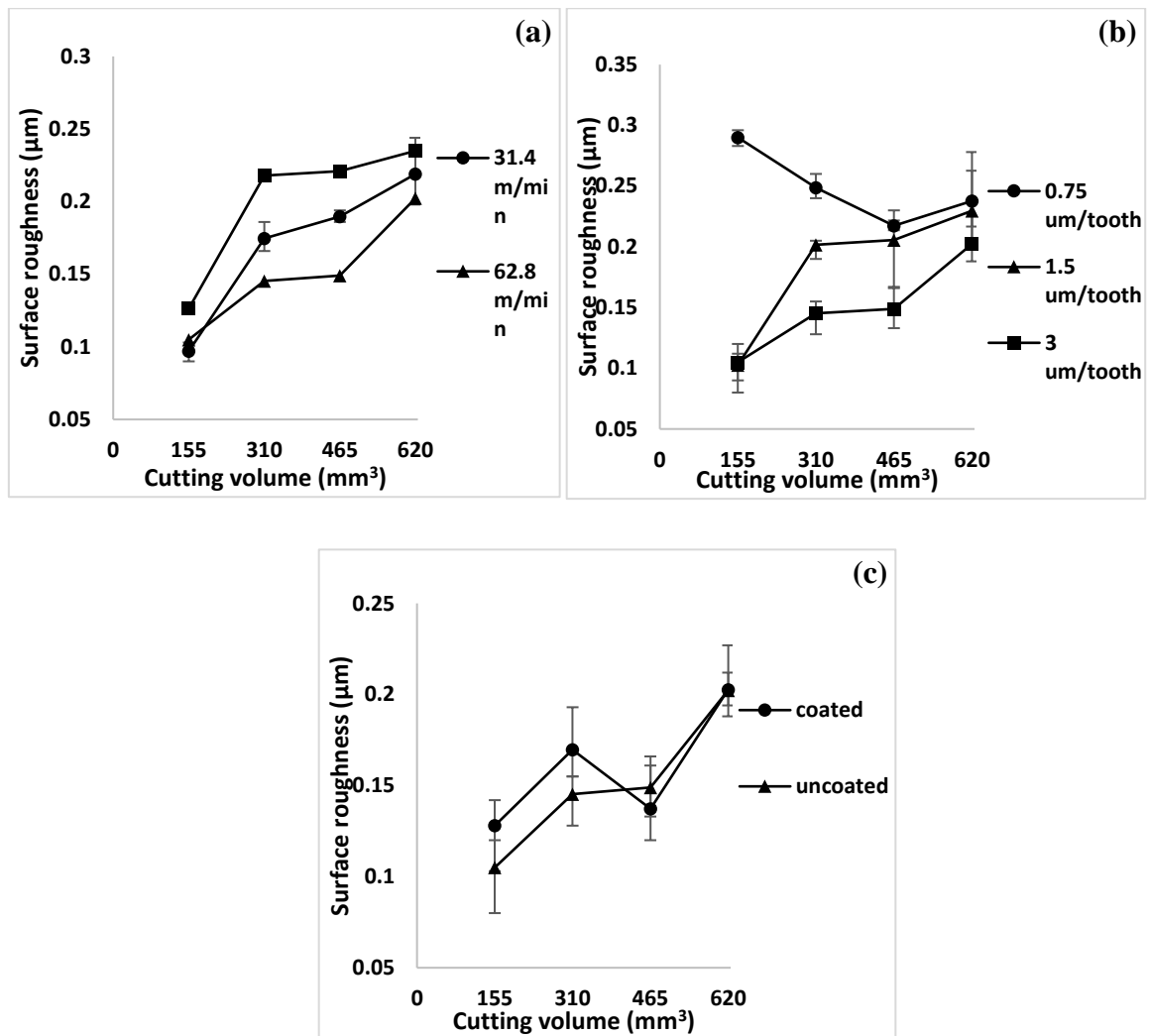


Figure 5.16 Surface roughness under effected by (a) cutting speed at feed per tooth of $3\mu\text{m/tooth}$ and depth of cut of $100\mu\text{m}$; (b) feed per tooth at cutting speed of 62.8 m/min and depth of cut of $100\mu\text{m}$; (c) tool coating at feed per feed per tooth of $3\mu\text{m/tooth}$, cutting speed of 62.8 m/min and depth of cut of $100\mu\text{m}$.

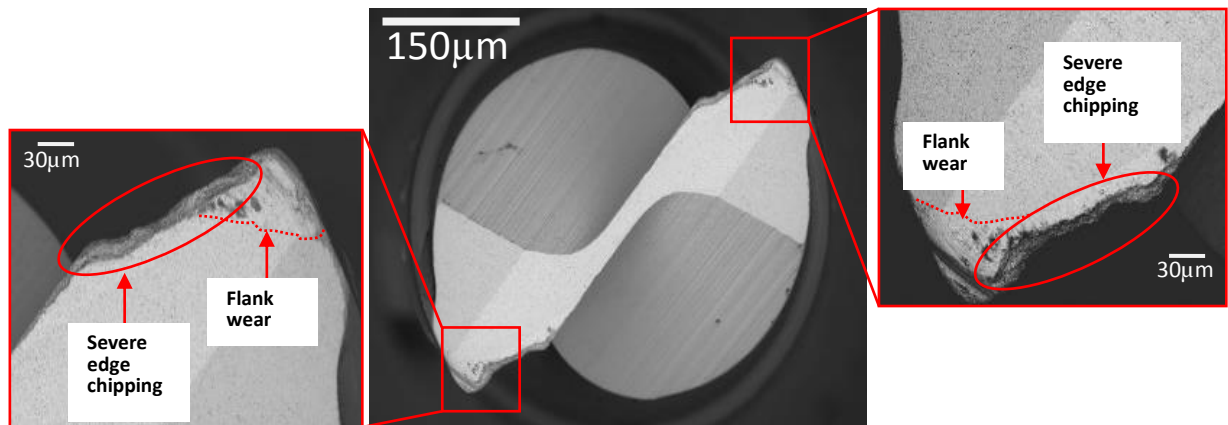


Figure 5.17 Top view of worn endmill obtained at Tool #4 (cutting speed of 62.8m/min, feed per tooth of 0.75 μm and depth of cut of 100 μm)

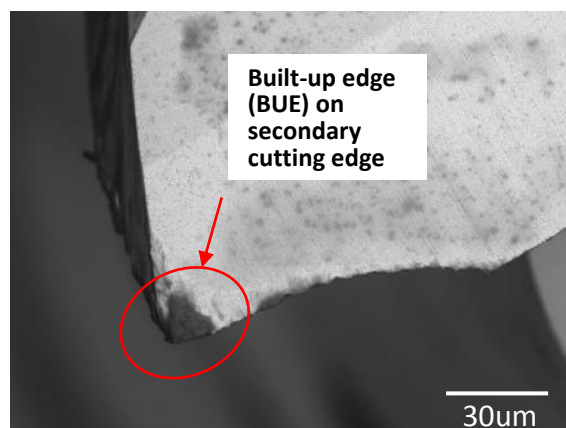


Figure 5.18 Built-up edge formed on cutting edge corner at Tool #3 (cutting speed of 125.6m/min, feed per tooth of 3 μm and depth of cut of 100 μm)

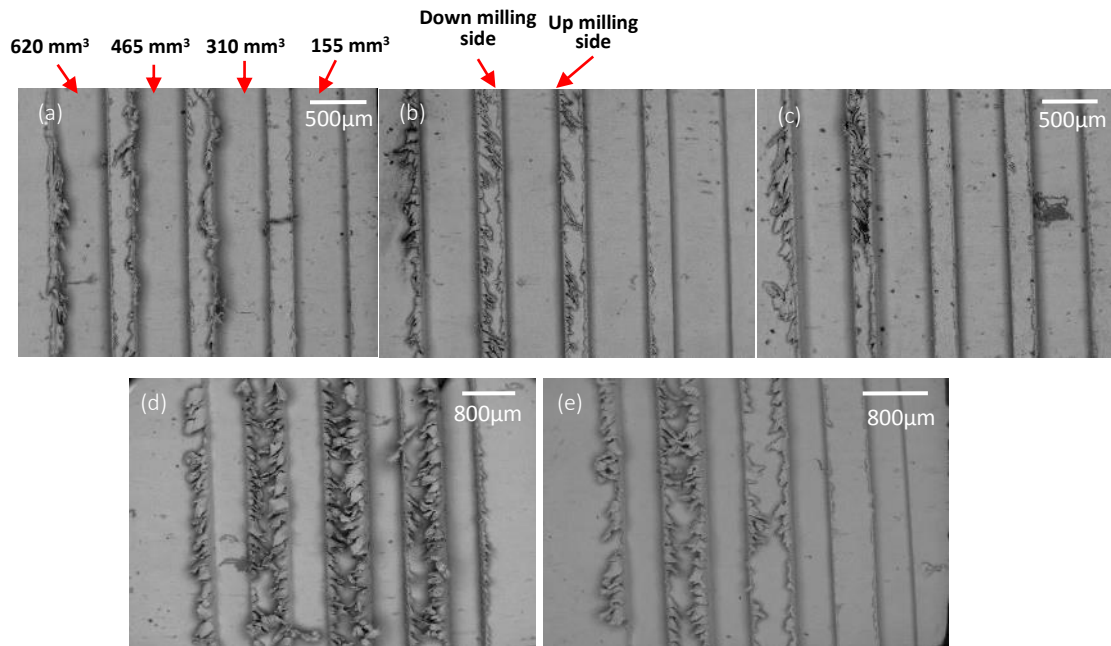


Figure 5.19 Burr formation at varying Experiment: (a) Experiment.1, cutting speed of 31.4m/min, feed per tooth of 3µm/tooth; (b) Experiment 2, cutting speed of 62.8m/min, feed per tooth of 3µm/tooth; (c) Experiment 3, cutting speed of 125.6m/min, feed per tooth of 3µm/tooth; (d) Experiment 4, cutting speed of 62.8m/min, feed per tooth of 0.75µm/tooth; (e) Experiment 5, cutting speed of 62.8m/min, feed per tooth of 1.5µm/tooth at constant depth of cut of 100 µm.

5.6 Conclusions

This chapter presents a comprehensive experimental investigation on the effect of cutting parameters and tool condition on the progression of tool wear in terms of flank wear and reduction in tool diameter when micro milling of 1.98 Vol.% Mg/Ti MMCs. The relation between tool wear and the cutting force, surface roughness and burr size was also investigated. Moreover, tool wear behaviour for uncoated and coated tools was compared. The following conclusions can be drawn:

- Flank wear and edge chipping due to abrasive wear and chip adhesion were observed as the main wear patterns during all cutting conditions for uncoated endmills. Abrasive wear mechanism has been confirmed by the chip formation process established using finite element modelling (FEM) from previous sections.
- The largest tool wear was generated at the lowest feed per tooth of 0.75µm/tooth whereas the smallest wear was experienced at the highest feed of 3 µm/tooth. Meanwhile, the highest average cutting force and surface roughness were obtained at the highest tool wear. This phenomenon was attributed to the elastically dominated materials removal mechanism in small feed, namely size effect.
- At 3 µm/tooth feed per tooth, depth of cut of 100 µm and cutting speed of 125.6m/min, small amount of adhered workpiece materials and BUE are found at the flank face of

major cutting edge and secondary cutting edge respectively. These adhered workpiece materials can be used to explain the smaller tool wear and highest surface roughness observed at cutting speed of 125.6m/min when compared to that at 62.8m/min and 31.4m/min.

- A faster reduction rate was observed at the uncoated tool resulting a higher value after cutting volume of 620 mm³ comparing with coated tool. Abrasive wear mechanism and poor adhesion of coating to the tool substrate were considered as the main reasons for coating delamination which was found to be the main wear mode. Chip adhesion was not observed on all cutting tools.

Chapter 6 Conclusions and further works

6.1 Summary and conclusions

With the development of MMCs, magnesium-based MMCs with small volume fraction of nanoparticle are found to exhibit even better mechanical performance than that reinforced with larger volume fraction of micro-sized particles without significant reduction in the ductility. However, the increased mechanical properties and abrasive reinforced particles also bring tremendous complexities in micro machining process. This research is mainly motivated by the increasing demands on the lightweight miniaturised components made with high strength materials. It presents a comprehensive analysis on the cutting mechanism of Mg-based metal matrix composites reinforced with nanoparticles in micro milling process. Both experimental and finite element simulation methods are applied to reveal the material removal mechanism considering the size effect and minimum chip thickness effect. Through this research, it fills in the gap existing in micro machinability study on nano-MMCs. A dramatically difference caused by the reduced particle size in the machinability of nano-MMCs has been revealed which greatly benefits for optimising the process parameters for micro milling. This is believed to eventually facilitate the application of nano-MMCs in various areas.

Based on the results and discussion from this research, the conclusions can be drawn as following:

1. The experimental investigation is conducted on the influence of cutting parameters on the cutting force and surface morphology when micro machining of Mg/Ti and Mg/TiB₂ with consideration of size effect and minimum chip thickness. The minimum chip thickness is determined to be 0.8 μm and 0.5 μm for Mg/Ti MMCs and Mg/TiB₂ respectively which is 53% and 33% of the cutting edge radius. Therefore, for machining Mg/Ti & TiB₂ MMCs feed per tooth under minimum chip thickness is not recommended. The experiment results presented an attempt to fill the gap and provide a comprehensive understanding on the micro machinability of Mg-based MMCs reinforced with nano reinforcements. Moreover, Mg/TiB₂ MMCs exhibit better machinability compared to Mg/Ti MMCs in terms of surface morphology. More burrs could be found at slot edges after machining Mg/Ti MMCs.
2. By considering the effect of microstructure change in MMCs due to the addition of nanoparticle, the effect of particle materials and volume fraction on the machinability of Mg/BN and Mg/ZnO is experimentally studied by comparing the results obtained

from pure Mg. The results show that the cutting force for machining pure Mg is larger than that for other MMCs specimen except of Mg/2.5wt.%ZnO. This can be explained as the addition of nanoparticle in MMCs facilitate the mobility of dislocation by increasing the density of slip planes in crystal plane and consequently reduce of the amount of force that required to initiate the plastic deformation. Also, MMCs reinforced containing ZnO particles exhibit higher cutting force than that containing BN particles. Moreover, compared to the pure Mg, chips with different morphology can be found in machining MMCs.

3. The tool wear in micro milling of Mg/Ti MMCs using 0.5mm diameter AlTiN coated and uncoated two-flute tungsten carbide micro endmills is studied. The tool wear is characterised both quantitatively and qualitatively by observing tool wear patterns and analysing the effect of cutting parameters on flank wear, reduction in tool diameter, cutting forces, surface roughness, and burr formation. The results indicated that the main wear patterns are identified as flank wear and edge chipping due to abrasive wear and chip adhesion mechanism in uncoated micro endmills. These wear mechanisms were confirmed by finite element (FE) modelling. It was also observed that the largest tool wear was occurred at smallest feed per tooth ($0.75\mu\text{m}/\text{tooth}$) and smallest wear was occurred at largest feed per tooth ($3\mu\text{m}/\text{tooth}$). Also, the effect of adhered workpiece materials acting the similar role as BUE on tool wear and surface generation is studied.
4. The simulation study on the cutting mechanism of Mg-based MMCs reinforced with SiC nanoparticles is conducted. A two-dimensional micromechanical finite element (FE) model is established using ABAQUS/Explicit to simulate the micro machining process with consideration of cutting edge radius. The simulated results present tool-particles interaction, chip formation process, cutting force, Von Mises stress and strain distribution within workpiece under the effect of uncut chip thickness. A continuous chip with saw tooth appearance is obtained at the uncut chip thickness above $1\mu\text{m}$. Highly strained bands at vicinity of particles are observed at chips, which can be recognised as the cause of this lamellate structure.
5. A three-dimensional (3D) micro-mechanical finite element model is established to simulate the orthogonal turning of Al-based MMCs with micro SiC particles. By establishing 3D models, some of the important phenomenon such as machined surface morphology can be realistically exhibited, which is difficult to achieve in 2D models.

Different depth of cut is adopted in this simulation to study the influence of relative position between the cutting tool and SiC particle on material removal and surface generation mechanism. Diverse particle behaviours such as slightly fracture at top side, residual fragments embedded within cavity, completely debonding are observed in this model which result in different types of defects on the machined surface such as shallow cavity around embedded particles, severe plastic deformation around cavity and shallow cavity. In addition, the fragments of particles squeezed by cutting tool during cutting process is found to change the chip formation mechanism.

6. The cutting mechanism comparison between SiC/Al metal matrix composites (MMCs) reinforced with micro and nanoparticles using finite element method is performed. The cutting mechanisms are investigated in terms of the von Mises stress distribution, tool-particles interaction, chip formation mechanism and surface morphology. It is found that the nanoparticles remained intact without fracture during the cutting process and are more likely to produce continuous chips, while the particles in micro size are easy to break and tend to form discontinues chips. Better machined surface quality with less defects can be obtained from nano size reinforced MMCs compared with their micro size counterparts. Therefore, cutting mechanism of nano-MMCs is believed to be different when compared to composites reinforced with micro particles.

6.2 Future work

Whilst this research has achieved the research aim and objectives, there are several recommendations that could be implemented to take this research further. The proposed future work includes:

1. Based on the literature review, the criteria describing the tool wear condition and define the tool life in micro machining are highly desired due to the significantly reduced scale. Therefore, investigation on the tool wear in the micro machining of particulate-reinforced MMCs using both experimental approaches and finite element modelling shows a great potential in filling this gap in order to reach a more cost-effective process in industry applications.
2. The current research investigates the tool wear mechanism of 2-flutes AlTiN coated and uncoated carbide micro endmills. However, a comparison with other endmill coatings and geometry is not only necessary in obtaining the most suitable cutting tool for better

machining quality of Mg-based MMCs, but also beneficial for advancing the knowledge in tool wear mechanism in micro machining process.

3. More realistic bonding mechanism between particles and matrix materials can be investigated by establishing a micro phase-field model. The finite element modelling with consideration of interfacial layer between two phases will be used as the primary method to reveal the details of material behaviour and its removal mechanisms in machining most of composite materials (metal & polymer-based) in a microcosmic scale. An accurate interface model is believed to not only make significant contribution on the state-of-the-art machining theory on composites but also provide a guidance on improving machined surface quality of composites. It will also expand the applications of composites miniaturized products in micro and nanotechnology.
4. Through investigating the relationship between the machined surface characteristics with the degradation rate and biocompatibility of Mg-based nanocomposites, this proposed research may also help to resolve the current limitations of magnesium alloy for use in biomedical science.

Reference

‘Abaqus/Explicit V6.14 User manual’ (2016).

Andrewes, C. J. E., Feng, H. and Lau, W. M. (2000) ‘Machining of an aluminum / SiC composite using diamond inserts’, *Journal of Materials Processing Technology*, 102, pp. 25–29.

Aramcharoen, A. and Mativenga, P. T. (2009) ‘Size effect and tool geometry in micromilling of tool steel’, *Precision Engineering*, 33(4), pp. 402–407. doi: 10.1016/j.precisioneng.2008.11.002.

Aramcharoen, a. *et al.* (2008) ‘Evaluation and selection of hard coatings for micro milling of hardened tool steel’, *International Journal of Machine Tools and Manufacture*, 48(14), pp. 1578–1584. doi: 10.1016/j.ijmachtools.2008.05.011.

Arrazola, P. J. and Ozel, T. (2008) ‘Numerical modelling of 3D hard turning using arbitrary Lagrangian Eulerian finite element method’, *International Journal of Machining and Machinability of Materials*, 4(1), p. 14. doi: 10.1504/IJMMM.2008.020907.

Aurich, J. C. and Bil, H. (2006) ‘3D Finite Element Modelling of Segmented Chip Formation’, *CIRP Annals - Manufacturing Technology*. Elsevier, 55(1), pp. 47–50. doi: 10.1016/S0007-8506(07)60363-1.

Basavarajappa, S., Chandramohan, G. and Davim, J. P. (2008) ‘Some studies on drilling of hybrid metal matrix composites based on Taguchi techniques’, *Journal of Materials Processing Technology*, 196(1–3), pp. 332–338. doi: 10.1016/j.jmatprotec.2007.05.043.

Basavarajappa, S. and Davim, J. P. (2013) ‘Influence of graphite particles on surface roughness and chip formation studies in turning metal matrix composites’, *Materials Research*, 16(5), pp. 990–996. doi: 10.1590/S1516-14392013005000098.

Benedict, G. F. (1987) *Nontraditional Manufacturing Processes*. Edited by G. F. Benedict. New York, USA: CRC Press.

Biermann, D. and Kahnis, P. (2010) ‘Analysis and simulation of size effects in micromilling’, *Production Engineering*, 4(1), pp. 25–34. doi: 10.1007/s11740-009-0201-1.

Bissacco, G., Hansen, H. N. and De Chiffre, L. (2006) ‘Size effects on surface generation in micro milling of hardened tool steel’, *CIRP Annals - Manufacturing Technology*, 55(1), pp. 593–596. doi: 10.1016/S0007-8506(07)60490-9.

- Boswell, B. *et al.* (2017) 'Effect of machining parameters on the surface finish of a metal matrix composite under dry cutting conditions', *Proceedings of the Institution of Mechanical Engineers, Part B: Journal of Engineering Manufacture*, 231(6), pp. 913–923. doi: 10.1177/0954405415583776.
- Budak, E., Altıntaş, Y. and Armarego, E. J. A. (1996) 'Prediction of Milling Force Coefficients From Orthogonal Cutting Data', *Journal of Manufacturing Science and Engineering*. American Society of Mechanical Engineers, 118(2), p. 216. Available at: <http://manufacturingscience.asmedigitalcollection.asme.org/article.aspx?articleid=1432575> (Accessed: 3 May 2015).
- Ceretti, E., Lucchi, M. and Altan, T. (1999) 'FEM simulation of orthogonal cutting: serrated chip formation', *Journal of Materials Processing Technology*, 95(1), pp. 17–26. doi: 10.1016/S0924-0136(99)00261-7.
- Chaubey, A. K. *et al.* (2012) 'Effect of particle dispersion on the mechanical behavior of Al-based metal matrix composites reinforced with nanocrystalline Al-Ca intermetallics', *Journal of Alloys and Compounds*. Elsevier B.V., 536(SUPPL.1), pp. S134–S137. doi: 10.1016/j.jallcom.2011.12.075.
- Chawla, B. N. and Shen, Y. (2001) 'Mechanical Behavior of Particle Reinforced Metal Matrix Composites', *Advanced Engineering Materials*, 3(6), pp. 357–370. doi: 10.1002/1527-2648(200106)3:6<357::AID-ADEM357>3.3.CO;2-9.
- Chawla, N. and Chawla, K. K. (2013) *Metal Matrix Composites*. Edited by N. Chawla and K. K. Chawla. New York, USA: Springer-Verlag New York. doi: 10.1007/978-1-4614-9548-2.
- Cheng, K. and Huo, D. (2013) *Micro Cutting: Fundamentals and Applications*. Edited by K. Cheng and D. Huo. Chichester, UK: John Wiley & Sons Ltd. doi: 10.1002/9781118536605.
- Chou, Y. K. and Liu, J. (2005) 'CVD diamond tool performance in metal matrix composite machining', *Surface and Coatings Technology*, 200(5–6), pp. 1872–1878. doi: 10.1016/j.surfcoat.2005.08.094.
- Ciftci, I., Turker, M. and Seker, U. (2004a) 'CBN cutting tool wear during machining of particulate reinforced MMCs', *Wear*, 257(9–10), pp. 1041–1046. doi: 10.1016/j.wear.2004.07.005.
- Ciftci, I., Turker, M. and Seker, U. (2004b) 'Evaluation of tool wear when machining SiCp-reinforced Al-2014 alloy matrix composites', *Materials & Design*, 25(3), pp. 251–255. doi:

10.1016/j.matdes.2003.09.019.

Cole, G. D. (2003) 'MAGNESIUM', *Chemical & Engineering News Archive*. American Chemical Society, 81(36), p. 52. doi: 10.1021/cen-v081n036.p052.

Dabade, U. A. *et al.* (2007) 'Surface finish and integrity of machined surfaces on Al/SiCp composites', *Journal of Materials Processing Technology*, 192–193, pp. 166–174. doi: 10.1016/j.jmatprotec.2007.04.044.

Dandekar, C. R. and Shin, Y. C. (2009) 'Multi-step 3-D finite element modeling of subsurface damage in machining particulate reinforced metal matrix composites', *Composites Part A: Applied Science and Manufacturing*, 40(8), pp. 1231–1239. doi: 10.1016/j.compositesa.2009.05.017.

Dandekar, C. R. and Shin, Y. C. (2012) 'Modeling of machining of composite materials: A review', *International Journal of Machine Tools and Manufacture*, 57, pp. 102–121. doi: 10.1016/j.ijmachtools.2012.01.006.

Davim, J. P. (2002) 'Diamond tool performance in machining metal-matrix composites', *Journal of Materials Processing Technology*, 128(1–3), pp. 100–105. doi: 10.1016/S0924-0136(02)00431-4.

Ding, X., Liew, W. Y. H. and Liu, X. D. (2005) 'Evaluation of machining performance of MMC with PCBN and PCD tools', *Wear*, 259(7–12), pp. 1225–1234. doi: 10.1016/j.wear.2005.02.094.

Dubey, A. K. and Yadava, V. (2008) 'Laser beam machining-A review', *International Journal of Machine Tools and Manufacture*, 48(6), pp. 609–628. doi: 10.1016/j.ijmachtools.2007.10.017.

El-Gallab, M. S. and Sklad, M. P. (2004) 'Machining of aluminum/silicon carbide particulate metal matrix composites: Part IV. Residual stresses in the machined workpiece', *Journal of Materials Processing Technology*, 152(1), pp. 23–34. doi: 10.1016/j.jmatprotec.2004.01.061.

El-Gallab, M. and Sklad, M. (1998) 'Machining of Al/SiC particulate metal matrix composites Part II: Workpiece surface integrity', *Journal of Materials Processing Technology*, 83(1–3), pp. 277–285. doi: 10.1016/S0924-0136(98)00072-7.

El-Gallab, M. and Sklad, M. (1998) 'Machining of Al / SiC particulate metal-matrix composites Part I: Tool performance', *Journal of Materials Processing Technology*, 83, pp. 151–158. doi: 10.1016/S0924-0136(98)00054-5.

- El-Gallab, M. and Sklad, M. (2000) 'Machining of Al/SiC particulate metal matrix composites. Part III: Comprehensive tool wear models', *Journal of Materials Processing Technology*, 101(1), pp. 10–20. doi: 10.1016/S0924-0136(99)00351-9.
- Fard, R. K., Afza, R. A. and Teimouri, R. (2013) 'Experimental investigation, intelligent modeling and multi-characteristics optimization of dry WEDM process of Al-SiC metal matrix composite', *Journal of Manufacturing Processes*, 15(4), pp. 483–494. doi: 10.1016/j.jmapro.2013.09.002.
- Ferkel, H. and Mordike, B. L. (2001) 'Magnesium strengthened by SiC nanoparticles', *Materials Science and Engineering A*, 298(1–2), pp. 193–199. doi: 10.1016/S0921-5093(00)01283-1.
- Filiz, S. *et al.* (2007) 'An experimental investigation of micro-machinability of copper 101 using tungsten carbide micro-endmills', *International Journal of Machine Tools and Manufacture*, 47(7–8), pp. 1088–1100. doi: 10.1016/j.ijmachtools.2006.09.024.
- Follansbee, P. S. and Gray, G. T. (1989) 'An analysis of the low temperature, low and high strain-rate deformation of Ti–6Al–4V', *Metallurgical Transactions A*, 20(5), pp. 863–874. doi: 10.1007/BF02651653.
- Friedrich, C. R. and Kulkarni, V. P. (2004) 'Effect of workpiece springback on micromilling forces', *Microsystem Technologies*, 10(6–7), pp. 472–477. doi: 10.1007/s00542-004-0375-6.
- Furukawa, Y. and Moronuki, N. (1988) 'Effect of Material Properties on Ultra Precise Cutting Processes', *CIRP Annals - Manufacturing Technology*, 37(1), pp. 113–116. doi: 10.1016/S0007-8506(07)61598-4.
- Gangadharan, K. V, Umashankar, K. S. and Desai, V. (2011) 'Machining Characteristics of Multiwall-CNT Reinforced Al/Al-Si Composites using Recurrence Quantification Analysis', *Jordan Journal of Mechanical and Industrial Engineering*, 5(4), pp. 345–351.
- Gatto, A. and Iuliano, L. (1997) 'Cutting mechanisms and surface features of WED machined metal matrix composites', *Journal of Materials Processing Technology*, 65(1–3), pp. 209–214. doi: 10.1016/S0924-0136(96)02264-9.
- Ghandehariun, A. *et al.* (2016a) 'Analysis of tool-particle interactions during cutting process of metal matrix composites', *International Journal of Advanced Manufacturing Technology*, 82(1–4), pp. 143–152. doi: 10.1007/s00170-015-7346-1.
- Ghandehariun, A. *et al.* (2016b) 'On tool-workpiece interactions during machining metal

matrix composites: investigation of the effect of cutting speed', *International Journal of Advanced Manufacturing Technology*, 84(9–12), pp. 2423–2435. doi: 10.1007/s00170-015-7869-5.

Ghandehariun, A. *et al.* (2017) 'On modeling the deformations and tool-workpiece interactions during machining metal matrix composites', *International Journal of Advanced Manufacturing Technology*. The International Journal of Advanced Manufacturing Technology, 91(5–8), pp. 1507–1516. doi: 10.1007/s00170-016-9776-9.

Ghani, J., Haron, C. and Kasim, M. (2015) 'Wear mechanism of coated and uncoated carbide cutting tool in machining process', *Journal of Materials*, (May 2016), pp. 1–7. doi: 10.1557/jmr.2015.382.

Ghosal, A. and Manna, A. (2013) 'Response surface method based optimization of ytterbium fiber laser parameter during machining of Al/Al₂O₃-MMC', *Optics and Laser Technology*. Elsevier, 46(1), pp. 67–76. doi: 10.1016/j.optlastec.2012.04.030.

Goo, C. *et al.* (2010) 'Micromachining of Polymer Composites Reinforced With Single-Walled Carbon Nano-Tubes', in *Proceedings of the 5th Int. Conf. on Micro-Manufacturing (ICOMM/4M)*. Madison, pp. 417–422.

Gopalakannan, S. and Senthilvelan, T. (2013) 'A parametric study of electrical discharge machining process parameters on machining of cast Al/B₄C metal matrix nanocomposites', *Proceedings of the Institution of Mechanical Engineers, Part B: Journal of Engineering Manufacture*, 227(7), pp. 993–1004. doi: 10.1177/0954405413479505.

Gopalakannan, S., Senthilvelan, T. and Ranganathan, S. (2013) 'Statistical optimization of EDM parameters on machining of aluminum Hybrid Metal Matrix composite by applying Taguchi based Grey analysis', *Journal of Scientific and Industrial Research*, 72(6), pp. 358–365. doi: 10.1016/j.measurement.2013.04.036.

Gupta, M. and Wong, W. L. E. (2015) 'Magnesium-based nanocomposites: Lightweight materials of the future', *Materials Characterization*. Elsevier Inc., 105, pp. 30–46. doi: 10.1016/j.matchar.2015.04.015.

Gupta, M. and Wong, W. L. E. (2016) 'An Insight into Processing and Characteristics of Magnesium Based Composites', in Alderman, M. *et al.* (eds) *Magnesium Technology 2014*. Cham: Springer International Publishing, pp. 423–428. doi: 10.1007/978-3-319-48231-6_78.

Hamatani, G. and Ramulu, M. (1990) 'Machinability of High Temperature Composites by

Abrasive Waterjet', *Journal of Engineering Materials and Technology*, 112(4), p. 381. doi: 10.1115/1.2903346.

Hashim, J., Looney, L. and Hashmi, M. S. J. (1999) 'Metal matrix composites: production by the stir casting method', *Journal of Materials Processing Technology*, 92–93, pp. 1–7. doi: 10.1016/S0924-0136(99)00118-1.

Heath, P. J. (2001) 'Developments in applications of PCD tooling', *Journal of Materials Processing Technology*, 116(1), pp. 31–38. doi: 10.1016/S0924-0136(01)00837-8.

Hillerborg, A., Mod  er, M. and Petersson, P.-E. (1976) 'Analysis of crack formation and crack growth in concrete by means of fracture mechanics and finite elements', *Cement and Concrete Research*. Pergamon, 6(6), pp. 773–781. doi: 10.1016/0008-8846(76)90007-7.

Ho, K. H. and Newman, S. T. (2003) 'State of the art electrical discharge machining (EDM)', *International Journal of Machine Tools and Manufacture*, 43(13), pp. 1287–1300. doi: 10.1016/S0890-6955(03)00162-7.

Hong, L., Vilar, R. M. and Youming, W. (1997) 'Laser beam processing of a SiC particulate reinforced 6061 aluminium metal matrix composite', *Journal of Materials Science*, 32(20), pp. 5545–5550. doi: 10.1023/A:1018668322943.

Hua J and Shivpuri, R. (2002) 'Influence of crack mechanics on the chip segmentation in the machining of Ti-6Al-4', in *Proceedings of the 9th ISPE international conference on concurrent engineering*. Cranfield, UK, pp. 357–365.

Huang, S. T. *et al.* (2012) 'Drilling of SiCp/Al Metal Matrix Composites with Polycrystalline Diamond (PCD) Tools', *Materials and Manufacturing Processes*, 27(10), pp. 1090–1094. doi: 10.1080/10426914.2011.654152.

Hung, N. P. *et al.* (1995) 'Machinability of cast and powder-formed aluminum alloys reinforced with SiC particles', *Journal of Materials Processing Tech.*, 48(1–4), pp. 291–297. doi: 10.1016/0924-0136(94)01661-J.

Hung, N. P. *et al.* (1996) 'Machinability of aluminum alloys reinforced with silicon carbide particulates', *Journal of Materials Processing Technology*, 56(1–4), pp. 966–977. doi: 10.1016/0924-0136(95)01908-1.

Hung, N. P., Yeo, H. and Oon, B. E. (1997) 'Effect of cutting fluid on the machinability of metal matrix composites', *Journal of Materials Processing Technology*, 67(ii), pp. 151–161.

Hwa Yan, B. *et al.* (2005) 'Examination of wire electrical discharge machining of

Al₂O₃p/6061Al composites’, *International Journal of Machine Tools and Manufacture*, 45(3), pp. 251–259. doi: 10.1016/j.ijmachtools.2004.08.015.

Imran, M. *et al.* (2014) ‘Comparison of tool wear mechanisms and surface integrity for dry and wet micro-drilling of nickel-base superalloys’, *International Journal of Machine Tools and Manufacture*, 76, pp. 49–60. doi: 10.1016/j.ijmachtools.2013.10.002.

Johnson, G. . and Cook, W. . (1983) ‘A constitutive model and data for metals subjected to large strains, high strain rates and high temperatures’, in *Proceedings of the 7th International Symposium on Ballistic*. The Netherlands, pp. 541–547.

Kadirgama, K. *et al.* (2011) ‘Tool life and wear mechanism when machining Hastelloy C-22HS’, *Wear*, 270(3–4), pp. 258–268. doi: 10.1016/j.wear.2010.10.067.

Kang, Y. C. and Chan, S. L. I. (2004) ‘Tensile properties of nanometric Al₂O₃particulate-reinforced aluminum matrix composites’, *Materials Chemistry and Physics*, 85(2–3), pp. 438–443. doi: 10.1016/j.matchemphys.2004.02.002.

Kannan, S., Kishawy, H. a. and Balazinski, M. (2006) ‘Flank Wear Progression During Machining Metal Matrix Composites’, *Journal of Manufacturing Science and Engineering*, 128(3), p. 787. doi: 10.1115/1.2164508.

Kannan, S., Kishawy, H. A. and Deiab, I. (2009) ‘Cutting forces and TEM analysis of the generated surface during machining metal matrix composites’, *Journal of Materials Processing Technology*, 209(5), pp. 2260–2269. doi: 10.1016/j.jmatprotec.2008.05.025.

Kiliçkap, E. *et al.* (2005) ‘Study of tool wear and surface roughness in machining of homogenised SiC-p reinforced aluminium metal matrix composite’, *Journal of Materials Processing Technology*, 164–165, pp. 862–867. doi: 10.1016/j.jmatprotec.2005.02.109.

Kim, C. S. *et al.* (2017) ‘Mechanical performance of particulate-reinforced Al metal-matrix composites (MMCs) and Al metal-matrix nano-composites (MMNCs)’, *Journal of Materials Science*. Springer US, 52(23), pp. 13319–13349. doi: 10.1007/s10853-017-1378-x.

Kovacevic, R. *et al.* (1997) ‘State of the art of research and development in abrasive waterjet machining’, *Journal of Manufacturing Science and Engineering-Transactions of the Asme*, 119(4B), pp. 776–785. doi: Doi 10.1115/1.2836824.

Kremer, A. *et al.* (2008) ‘Machinability of Al/SiC particulate metal-matrix composites under dry conditions with CVD diamond-coated carbide tools’, *Machining Science and Technology*, 12(2), pp. 214–233. doi: 10.1080/10910340802067494.

- Kumar, A., Mahapatra, M. M. and Jha, P. K. (2014) 'Effect of machining parameters on cutting force and surface roughness of in situ Al-4.5%Cu/TiC metal matrix composites', *Measurement: Journal of the International Measurement Confederation*. Elsevier Ltd, 48(1), pp. 325–332. doi: 10.1016/j.measurement.2013.11.026.
- Lai, X. *et al.* (2008) 'Modelling and analysis of micro scale milling considering size effect, micro cutter edge radius and minimum chip thickness', *International Journal of Machine Tools and Manufacture*, 48(1), pp. 1–14. doi: 10.1016/j.ijmachtools.2007.08.011.
- Lau, W. S., Lee, W. B. and Pang, S. Q. (1990) 'Pulsed Nd: YAG Laser Cutting of Carbon Fibre Composite Materials', *CIRP Annals*, 39(1), pp. 179–182. doi: [https://doi.org/10.1016/S0007-8506\(07\)61030-0](https://doi.org/10.1016/S0007-8506(07)61030-0).
- Lee, S. W., Mayor, R. and Ni, J. (2006) 'Dynamic Analysis of a Mesoscale Machine Tool', *Journal of Manufacturing Science and Engineering*, 128(1), p. 194. doi: 10.1115/1.2123007.
- Li, N. and Zheng, Y. (2013) 'Novel Magnesium Alloys Developed for Biomedical Application: A Review', *Journal of Materials Science and Technology*. Elsevier Ltd, 29(6), pp. 489–502. doi: 10.1016/j.jmst.2013.02.005.
- Li, P. *et al.* (2011) 'Design of micro square endmills for hard milling applications', *International Journal of Advanced Manufacturing Technology*, 57(9–12), pp. 859–870. doi: 10.1007/s00170-011-3330-6.
- Li, X. and Seah, W. K. H. (2001) 'Tool wear acceleration in relation to workpiece reinforcement percentage in cutting of metal matrix composites', *Wear*, 247(2), pp. 161–171. doi: 10.1016/S0043-1648(00)00524-X.
- Lin, J. T., Bhattacharyya, D. and Lane, C. (1995) 'Machinability of a silicon carbide reinforced matrix composite aluminium metal', *Matrix*, 183, pp. 883–888.
- Liu, J. and China, B. S. (2011) *Experimental Study and Modeling of Mechanical Micro-Machining of Particle Reinforced Heterogeneous Materials*. University of Central Florida.
- Liu, J., Li, J. and Xu, C. (2013) 'Cutting Force Prediction on Micromilling Magnesium Metal Matrix Composites With Nanoreinforcements', *Journal of Micro and Nano-Manufacturing*. American Society of Mechanical Engineers, 1(1), p. 11010. doi: 10.1115/1.4023286.
- Liu, J., Li, J. and Xu, C. (2014) 'Interaction of the cutting tools and the ceramic-reinforced metal matrix composites during micro-machining: A review', *CIRP Journal of Manufacturing Science and Technology*. CIRP, 7(2), pp. 55–70. doi: 10.1016/j.cirpj.2014.01.003.

- Liu, K. and Melkote, S. N. (2007) 'Finite element analysis of the influence of tool edge radius on size effect in orthogonal micro-cutting process', *International Journal of Mechanical Sciences*, 49(5), pp. 650–660. doi: 10.1016/j.ijmecsci.2006.09.012.
- Liu, X. *et al.* (2004) 'Cutting Mechanisms and Their Influence on Dynamic Forces, Vibrations and Stability in Micro-Endmilling', *Manufacturing Engineering and Materials Handling Engineering*, 2004, pp. 583–592. doi: 10.1115/IMECE2004-62416.
- Liu, X., DeVor, R. E., *et al.* (2004) 'The Mechanics of Machining at the Microscale: Assessment of the Current State of the Science', *Journal of Manufacturing Science and Engineering*, 126(4), p. 666. doi: 10.1115/1.1813469.
- Liu, X., Devor, R. E., *et al.* (2004) 'The Mechanics of Machining at the Microscale: Assessment of the Current State of the Science', *Journal of Manufacturing Science and Engineering*. American Society of Mechanical Engineers, 126(4), pp. 666–678. doi: 10.1115/1.1813469.
- Liu, X., DeVor, R. E. and Kapoor, S. G. (2006) 'An Analytical Model for the Prediction of Minimum Chip Thickness in Micromachining', *Journal of Manufacturing Science and Engineering*, 128(2), p. 474. doi: 10.1115/1.2162905.
- Ma, Z. Y. *et al.* (1996) 'Nanometric Si₃N₄ particulate-reinforced aluminum composite', *Materials Science and Engineering A*, 219(1–2), pp. 229–231. doi: 10.1016/S0921-5093(96)10444-5.
- Maekawa, K. *et al.* (2000) *Metal Machining: Theory and Applications*. New York: John Wiley & Sons.
- Mahdavinejad, R. A. and Mahdavinejad, A. (2005) 'ED machining of WC-Co', *Journal of Materials Processing Technology*, 162–163(SPEC. ISS.), pp. 637–643. doi: 10.1016/j.jmatprotec.2005.02.211.
- Manna, A. and Bhattacharayya, B. (2003) 'A study on machinability of Al/SiC-MMC', *Journal of Materials Processing Technology*, 140(1–3 SPEC.), pp. 711–716. doi: 10.1016/S0924-0136(03)00905-1.
- Manna, A. and Bhattacharayya, B. (2005) 'Influence of machining parameters on the machinability of particulate reinforced Al/SiC-MMC', *International Journal of Advanced Manufacturing Technology*, 25(9–10), pp. 850–856. doi: 10.1007/s00170-003-1917-2.
- Manna, A. and Bhattacharyya, B. (2004) 'Investigation for optimal parametric combination

for achieving better surface finish during turning of Al/SiC-MMC', *International Journal of Advanced Manufacturing Technology*, 23(9–10), pp. 658–665. doi: 10.1007/s00170-003-1624-z.

Mardi, K. B. *et al.* (2017) 'Surface integrity of Mg-based nanocomposite produced by Abrasive Water Jet Machining (AWJM)', *Materials and Manufacturing Processes*. Taylor & Francis, 32(15), pp. 1707–1714. doi: 10.1080/10426914.2017.1279306.

Markopoulos, A. P. (2013) *Finite Element Method in Machining Processes*. Edited by A. P. Markopoulos. New York: Springer. doi: 10.1007/978-3-319-02459-2.

Mazahery, A., Abdizadeh, H. and Baharvandi, H. R. (2009) 'Development of high-performance A356/nano-Al₂O₃ composites', *Materials Science and Engineering: A*, 518(1), pp. 61–64. doi: <https://doi.org/10.1016/j.msea.2009.04.014>.

Meenashisundaram, G. K. and Gupta, M. (2014) 'Low volume fraction nano-titanium particulates for improving the mechanical response of pure magnesium', *Journal of Alloys and Compounds*, 593, pp. 176–183. doi: 10.1016/j.jallcom.2013.12.157.

Mian, A. J., Driver, N. and Mativenga, P. T. (2009) 'Micromachining of coarse-grained multi-phase material', *Proceedings of the Institution of Mechanical Engineers, Part B: Journal of Engineering Manufacture*, 223(4), pp. 377–385. doi: 10.1243/09544054JEM1185.

Miller, W. . and Humphreys, F. . (1991) 'Strengthening mechanisms in particulate metal matrix composites', *Scripta Metallurgica et Materialia*, 25(1), pp. 33–38. doi: 10.1016/0956-716X(91)90349-6.

Mohammad Sharifi, E., Karimzadeh, F. and Enayati, M. H. (2011) 'Fabrication and evaluation of mechanical and tribological properties of boron carbide reinforced aluminum matrix nanocomposites', *Materials and Design*. Elsevier Ltd, 32(6), pp. 3263–3271. doi: 10.1016/j.matdes.2011.02.033.

Monaghan, J. and Brazil, D. (1997) 'Modeling the sub-surface damage associated with the machining of a particle reinforced MMC', *Computational Materials Science*, 9(1–2), pp. 99–107. doi: 10.1016/S0927-0256(97)00063-3.

Monaghan, J. and Brazil, D. (1998) 'Modelling the flow processes of a particle reinforced metal matrix composite during machining', *Composites Part A: Applied Science and Manufacturing*, 29(1–2), pp. 87–99. doi: 10.1016/S1359-835X(97)00047-X.

Movahhedy, M. R., Altintas, Y. and Gadala, M. S. (2002) 'Numerical Analysis of Metal

- Cutting With Chamfered and Blunt Tools', *Journal of Manufacturing Science and Engineering*. American Society of Mechanical Engineers, 124(2), p. 178. doi: 10.1115/1.1445147.
- Muguthu, J. N., Dong, G. and Ikua, B. (2013) 'Optimization of machining parameters influencing machinability of Al₂124SiCp (45%wt) metal matrix composite', *Journal of Composite Materials*, 49(2), pp. 217–229. doi: 10.1177/0021998313516141.
- Müller, F. and Monaghan, J. (1997) 'Electro Discharge Machining of Particle Reinforced Metal Matrix Composites', in Kochhar, A. K. et al. (eds) *Proceedings of the Thirty-Second International Matador Conference*. London: Macmillan Education UK, pp. 425–430. doi: 10.1007/978-1-349-14620-8_67.
- Müller, F. and Monaghan, J. (2000) 'Non-conventional machining of particle reinforced metal matrix composite-1', *International Journal of Machine Tools & Manufacture*, 40, pp. 1351–1366. doi: 10.1016/S0924-0136(01)00941-4.
- Muthukrishnan, N. and Davim, J. P. (2009) 'Optimization of machining parameters of Al/SiC-MMC with ANOVA and ANN analysis', *Journal of Materials Processing Technology*, 209(1), pp. 225–232. doi: 10.1016/j.jmatprotec.2008.01.041.
- Muthukrishnan, N., Murugan, M. and Prahlada Rao, K. (2008) 'Machinability issues in turning of Al-SiC (10p) metal matrix composites', *International Journal of Advanced Manufacturing Technology*, 39(3–4), pp. 211–218. doi: 10.1007/s00170-007-1220-8.
- Narahari, P., Pai, B. C. and Pillai, R. M. (1999) 'Some aspects of machining cast Al-SiCp composites with conventional high speed steel and tungsten carbide tools', *Journal of Materials Engineering and Performance*, 8(5), pp. 538–542. doi: 10.1007/s11665-999-0006-6.
- Nemat-Nasser, S. et al. (2001) 'Dynamic response of conventional and hot isostatically pressed Ti–6Al–4V alloys: experiments and modeling', *Mechanics of Materials*, 33(8), pp. 425–439. doi: 10.1016/S0167-6636(01)00063-1.
- Nicholls, C. J. et al. (2017) 'Review of machining metal matrix composites', *International Journal of Advanced Manufacturing Technology*, 90(9–12), pp. 2429–2441. doi: 10.1007/s00170-016-9558-4.
- O. Quigley, J. Monaghan, P. O. (1994) 'Factors affecting the machinability of an Al / SiC metal-matrix composite', *Journal of Materials Processing Tech.*, 43, pp. 21–36.

- Ozben, T., Kilickap, E. and Çakir, O. (2008) 'Investigation of mechanical and machinability properties of SiC particle reinforced Al-MMC', *Journal of Materials Processing Technology*, 198(1–3), pp. 220–225. doi: 10.1016/j.jmatprotec.2007.06.082.
- Ozcatalbas, Y. (2003) 'Investigation of the machinability behavior of Al₄C₃ reinforced Al-based composite produced by mechanical alloying technique', *Composites Science and Technology*, 63, pp. 53–61.
- Palanikumar, K., Muthukrishnan, N. and Hariprasad, K. S. (2008) 'Surface roughness parameters optimization in machining A356/SiC/20p metal matrix composites by PCD tool using response surface methodology and desirability function', *Machining Science and Technology*, 12(4), pp. 529–545. doi: 10.1080/10910340802518850.
- Paulo Davim, J. and Monteiro Baptista, A. (2000) 'Relationship between cutting force and PCD cutting tool wear in machining silicon carbide reinforced aluminum', *Journal of Materials Processing Technology*, 103(3), pp. 417–423. doi: 10.1016/S0924-0136(00)00495-7.
- Pedersen, W. and Ramulu, M. (2006) 'Facing SiCp/Mg metal matrix composites with carbide tools', *Journal of Materials Processing Technology*, 172(3), pp. 417–423. doi: 10.1016/j.jmatprotec.2005.07.016.
- Pham, D. T. *et al.* (2009) 'Micromilling of coarse-grained and ultrafine-grained Cu99.9E: Effects of material microstructure on machining conditions and surface quality', *International Conferences on Micro Manufacturing, ICOMM*, pp. 241–244. doi: 10.1243/17547164C0012009047.
- Poddar, P., Mukherjee, S. and Sahoo, K. L. (2009) 'The microstructure and mechanical properties of Sic reinforced magnesium based composites by rheocasting process', *Journal of Materials Engineering and Performance*, 18(7), pp. 849–855. doi: 10.1007/s11665-008-9334-1.
- Ponappa, K. *et al.* (2010) 'The effect of process parameters on machining of magnesium nano alumina composites through EDM', *International Journal of Advanced Manufacturing Technology*, 46(9–12), pp. 1035–1042. doi: 10.1007/s00170-009-2158-9.
- Popov, K. B. *et al.* (2006) 'Micromilling: material microstructure effects', *Proceedings of the Institution of Mechanical Engineers, Part B: Journal of Engineering Manufacture*, 220(11), pp. 1807–1813. doi: 10.1243/09544054JEM683.

- Pramanik, A. (2014) 'Developments in the non-traditional machining of particle reinforced metal matrix composites', *International Journal of Machine Tools and Manufacture*, 86, pp. 44–61. doi: 10.1016/j.ijmachtools.2014.07.003.
- Pramanik, A., Zhang, L. C. and Arsecularatne, J. a. (2007) 'An FEM investigation into the behavior of metal matrix composites: Tool-particle interaction during orthogonal cutting', *International Journal of Machine Tools and Manufacture*, 47(10), pp. 1497–1506. doi: 10.1016/j.ijmachtools.2006.12.004.
- Priyadarshi, D. and Sharma, R. K. (2016) 'Optimization for Turning of Al-6061-SiC-Gr Hybrid Nanocomposites Using Response Surface Methodologies', *Materials and Manufacturing Processes*. 2016, 31(10), pp. 1342–1350. doi: 10.1080/10426914.2015.1070427.
- Rahman, M., Senthil Kumar, a. and Prakash, J. R. S. (2001) 'Micro milling of pure copper', *Journal of Materials Processing Technology*, 116(1), pp. 39–43. doi: 10.1016/S0924-0136(01)00848-2.
- Ramaswami, R. (1971) 'The effect of the built-up-edge(BUE) on the wear of cutting tools', *Wear*, 18(1), pp. 1–10. doi: 10.1016/0043-1648(71)90059-7.
- Ramesh, M. V. *et al.* (2001) 'Finite-element analysis of diamond turning of aluminium matrix composites', *Composites Science and Technology*, 61(10), pp. 1449–1456. doi: 10.1016/S0266-3538(01)00047-1.
- Rawal, S. P. (2001) 'Metal-matrix composites for space applications', *Journal of the Minerals, metals, and Materials Society*. Springer-Verlag, 53(4), pp. 14–17. doi: 10.1007/s11837-001-0139-z.
- Rozenek, M., Kozak, J. and Da, L. (2001) 'Electrical discharge machining characteristics of metal matrix composites', *Journal of Materials Processing Technology*, 109, pp. 367–370.
- Sahin, Y. (2005) 'The effects of various multilayer ceramic coatings on the wear of carbide cutting tools when machining metal matrix composites', *Surface and Coatings Technology*, 199(1), pp. 112–117. doi: 10.1016/j.surfcoat.2005.01.048.
- Sankaranarayanan, S., Sabat, R., *et al.* (2014) 'Mg/BN nanocomposites: nano-BN addition for enhanced room temperature tensile and compressive response', *Journal of Composite Materials*. doi: 10.1177/0021998314559278.
- Sankaranarayanan, S., Pranav Nayak, U., *et al.* (2014) 'Nano-ZnO particle addition to

monolithic magnesium for enhanced tensile and compressive response', *Journal of Alloys and Compounds*. Elsevier B.V., 615, pp. 211–219. doi: 10.1016/j.jallcom.2014.06.163.

Sasimurugan, T. and Palanikumar, K. (2011) 'Experimental studies on machining characteristics of hybrid aluminium metal matrix composite and carbon nano tubes added hybrid aluminium metal matrix composite', *International Conference on Nanoscience Engineering and Technology ICONSET 2011*, pp. 159–162. doi: 10.1109/ICONSET.2011.6167944.

Satyanarayana, K. G. (1989) *Handbook of ceramics and composites*. New York, USA: Marcel Dekker, INC.

Seetharaman, S. *et al.* (2013) 'Synthesis and characterization of nano boron nitride reinforced magnesium composites produced by the microwave sintering method', *Materials*, 6(5), pp. 1940–1955. doi: 10.3390/ma6051940.

Seo, Y. W., Kim, D. and Ramulu, M. (2006) 'Electrical Discharge Machining of Functionally Graded 15–35 Vol% SiC_p/Al Composites', *Materials and Manufacturing Processes*, 21(5), pp. 479–487. doi: 10.1080/10426910500471482.

Sharma, V. and Kumar, V. (2016) 'Multi-objective optimization of laser curve cutting of aluminium metal matrix composites using desirability function approach', *Journal of the Brazilian Society of Mechanical Sciences and Engineering*. Springer Berlin Heidelberg, 38(4), pp. 1221–1238. doi: 10.1007/s40430-016-0487-9.

Sharma, V. and Kumar, V. (2018a) 'Comparison of machining characteristics of metal matrix composites using CO₂ laser curve cutting process', 232(3), pp. 349–368. doi: 10.1177/0954408917710145.

Sharma, V. and Kumar, V. (2018b) 'Investigating the quality characteristics of Al5052/SiC metal matrix composites machined by CO₂ laser curve cutting', *Proceedings of the Institution of Mechanical Engineers, Part L: Journal of Materials: Design and Applications*, 232(1), pp. 3–19. doi: 10.1177/1464420715608890.

Shehata, F. *et al.* (2009) 'Preparation and properties of Al₂O₃ nanoparticle reinforced copper matrix composites by in situ processing', *Materials and Design*, 30(7), pp. 2756–2762. doi: 10.1016/j.matdes.2008.10.005.

Shi, J. and Liu, C. R. (2006) 'On predicting chip morphology and phase transformation in hard machining', *The International Journal of Advanced Manufacturing Technology*, 27(7–8),

pp. 645–654. doi: 10.1007/s00170-004-2242-0.

Shukla, M. *et al.* (2018) ‘Characteristic behaviour of aluminium metal matrix composites: A review’, *Materials Today: Proceedings*, 5(2), pp. 5830–5836. doi: 10.1016/j.matpr.2017.12.180.

Simoneau, A., Ng, E. and Elbestawi, M. A. (2006) ‘Chip formation during microscale cutting of a medium carbon steel’, *International Journal of Machine Tools and Manufacture*, 46(5), pp. 467–481. doi: 10.1016/j.ijmachtools.2005.07.019.

Simoneau, A., Ng, E. and Elbestawi, M. A. (2006a) ‘Surface defects during microcutting’, *International Journal of Machine Tools and Manufacture*, 46(12–13), pp. 1378–1387. doi: 10.1016/j.ijmachtools.2005.10.001.

Simoneau, A., Ng, E. and Elbestawi, M. A. (2006b) ‘The effect of microstructure on chip formation and surface defects in microscale, mesoscale, and macroscale cutting of steel’, *CIRP Annals - Manufacturing Technology*, 55(1), pp. 97–102. doi: 10.1016/S0007-8506(07)60375-8.

Simoneau, A., Ng, E. and Elbestawi, M. A. (2007) ‘Grain size and orientation effects when microcutting AISI 1045 steel’, *CIRP Annals - Manufacturing Technology*, 56(1), pp. 57–60. doi: 10.1016/j.cirp.2007.05.016.

Slipenyuk, A. *et al.* (2006) ‘Properties of P/M processed particle reinforced metal matrix composites specified by reinforcement concentration and matrix-to-reinforcement particle size ratio’, *Acta Materialia*, 54(1), pp. 157–166. doi: 10.1016/j.actamat.2005.08.036.

Songmene, V. and Balazinski, M. (1999) ‘Machinability of Graphitic Metal Matrix Composites as a Function of Reinforcing Particles’, *CIRP Annals - Manufacturing Technology*, 48(1), pp. 77–80. doi: 10.1016/S0007-8506(07)63135-7.

Srinivas, S. and Babu, N. R. (2012) ‘Penetration ability of abrasive waterjets in cutting of aluminum-silicon carbide particulate metal matrix composites’, *Machining Science and Technology*, 16(3), pp. 337–354. doi: 10.1080/10910344.2012.698935.

Srivastava, A. K. *et al.* (2017) ‘Surface integrity in tangential turning of hybrid MMC A359/B4C/Al₂O₃ by abrasive waterjet’, *Journal of Manufacturing Processes*. The Society of Manufacturing Engineers, 28, pp. 11–20. doi: 10.1016/j.jmapro.2017.05.017.

Staiger, M. P. *et al.* (2006) ‘Magnesium and its alloys as orthopedic biomaterials: A review’, *Biomaterials*, 27(9), pp. 1728–1734. doi: 10.1016/j.biomaterials.2005.10.003.

- Su, H. *et al.* (2012) 'Processing, microstructure and tensile properties of nano-sized Al₂O₃ particle reinforced aluminum matrix composites', *Materials and Design*, 36, pp. 590–596. doi: 10.1016/j.matdes.2011.11.064.
- Sun, F. *et al.* (2004) 'High speed milling of SiC particle reinforced aluminum-based MMC with coated carbide inserts', *Key Engineering Materials*, 274–276(I), pp. 457–462. doi: 10.4028/www.scientific.net/KEM.274-276.457.
- Suresh Kumar Reddy, N., Kwang-Sup, S. and Yang, M. (2008) 'Experimental study of surface integrity during end milling of Al/SiC particulate metal-matrix composites', *Journal of Materials Processing Technology*, 201(1–3), pp. 574–579. doi: 10.1016/j.jmatprotec.2007.11.280.
- Takács, M., Verő, B. and Mészáros, I. (2003) 'Micromilling of metallic materials', *Journal of Materials Processing Technology*, 138(1–3), pp. 152–155. Available at: <http://www.sciencedirect.com/science/article/pii/S0924013603000645> (Accessed: 23 July 2015).
- Tansel, I. *et al.* (1998) 'Micro-end-milling—I. Wear and breakage', *International Journal of Machine Tools and Manufacture*, 38(12), pp. 1419–1436. doi: 10.1016/S0890-6955(98)00015-7.
- Tansel, I. *et al.* (2000) 'Tool wear estimation in micro-machining.', *International Journal of Machine Tools and Manufacture*, 40(4), pp. 599–608. doi: 10.1016/S0890-6955(99)00073-5.
- Taya, M. (1991) 'Strengthening mechanisms of metal matrix composites', *Material Transactions, JIM*, pp. 1–19.
- Teng, X. *et al.* (2016) 'Micro-machinability of nanoparticle-reinforced Mg-based MMCs: an experimental investigation', *International Journal of Advanced Manufacturing Technology*, pp. 1–14. doi: 10.1007/s00170-016-8611-7.
- Teng, X. *et al.* (2018) 'Finite element modelling on cutting mechanism of nano Mg/SiC metal matrix composites considering cutting edge radius', *Journal of Manufacturing Processes*, 32. doi: 10.1016/j.jmapro.2018.02.006.
- Teti, R. (2002) 'Machining of Composite Materials', *CIRP Annals - Manufacturing Technology*, 51(2), pp. 611–634. doi: 10.1016/S0007-8506(07)61703-X.
- Tjong, S. (2000) 'Microstructural and mechanical characteristics of in situ metal matrix composites', *Materials Science and Engineering: R: Reports*, 29(3–4), pp. 49–113. doi:

10.1016/S0927-796X(00)00024-3.

Tjong, S. C. (2007) 'Novel Nanoparticle-Reinforced Metal Matrix Composites with Enhanced Mechanical Properties', *Advanced Engineering Materials*, 9(8), pp. 639–652. doi: 10.1002/adem.200700106.

To, S., Lee, W. B. and Chan, C. Y. (1997) 'Ultraprecision diamond turning of aluminium single crystals', *Journal of Materials Processing Technology*, 63(1–3), pp. 157–162. doi: 10.1016/S0924-0136(96)02617-9.

Tomac, N., Tannessen, K. and Rasch, F. O. (1992) 'Machinability of Particulate Aluminium Matrix Composites', *CIRP Annals - Manufacturing Technology*, 41(1), pp. 55–58. doi: 10.1016/S0007-8506(07)61151-2.

Ucun, I., Aslantas, K. and Bedir, F. (2013) 'An experimental investigation of the effect of coating material on tool wear in micro milling of Inconel 718 super alloy', *Wear*, 300(1–2), pp. 8–19. doi: 10.1016/j.wear.2013.01.103.

Ulacia, I. *et al.* (2011) 'Tensile characterization and constitutive modeling of AZ31B magnesium alloy sheet over wide range of strain rates and temperatures', *Journal of Materials Processing Technology*. Elsevier B.V., 211(5), pp. 830–839. doi: 10.1016/j.jmatprotec.2010.09.010.

Umer, U. *et al.* (2015) 'Modeling machining of particle-reinforced aluminum-based metal matrix composites using cohesive zone elements', *International Journal of Advanced Manufacturing Technology*, 78(5–8), pp. 1171–1179. doi: 10.1007/s00170-014-6715-5.

Viala, J. C., Fortier, P. and Bouix, J. (1990) 'Stable and metastable phase equilibria in the chemical interaction between aluminium and silicon carbide', *Journal of Materials Science*, 25(3), pp. 1842–1850. doi: 10.1007/BF01045395.

Vogler, M. P., DeVor, R. E. and Kapoor, S. G. (2003) 'Microstructure-Level Force Prediction Model for Micro-milling of Multi-Phase Materials', *Journal of Manufacturing Science and Engineering*, 125(2), p. 202. doi: 10.1115/1.1556402.

Vogler, M. P., Kapoor, S. G. and DeVor, R. E. (2004) 'On the Modeling and Analysis of Machining Performance in Micro-Endmilling, Part II: Cutting Force Prediction', *Journal of Manufacturing Science and Engineering*, 126(4), p. 695. doi: 10.1115/1.1813471.

Wang, B. *et al.* (2016) 'The milling simulation and experimental research on high volume fraction of SiCp/Al', *International Journal of Advanced Manufacturing Technology*, 82(5–8),

pp. 809–816. doi: 10.1007/s00170-015-7399-1.

Wang, T., Xie, L. and Wang, X. (2015) ‘Simulation study on defect formation mechanism of the machined surface in milling of high volume fraction SiCp/Al composite’, *International Journal of Advanced Manufacturing Technology*, 79(5–8), pp. 1185–1194. doi: 10.1007/s00170-015-6876-x.

Wang, Z., Chen, T.-K. and Lloyd, D. J. (1993) ‘Stress distribution in particulate-reinforced metal-matrix composites subjected to external load’, *Metallurgical Transactions A*, 24(1), pp. 197–207. doi: 10.1007/BF02669616.

Weinert, K. and Lange, M. (2001) ‘Machining of magnesium matrix composites’, *Advanced Engineering Materials*, 3(12), pp. 975–979. doi: 10.1002/1527-2648(200112)3:12<975::AID-ADEM975>3.0.CO;2-L.

Weule, H., Hüntrup, V. and Tritschler, H. (2001) ‘Micro-Cutting of Steel to Meet New Requirements in Miniaturization’, *CIRP Annals - Manufacturing Technology*, 50(1), pp. 61–64. doi: 10.1016/S0007-8506(07)62071-X.

Y. El-Kady, E. (2015) ‘The Effect of Machining Parameters on the Cutting Forces, Tool Wear, and Machined Surface Roughness of Metal Matrix Nano Composite Material’, *Advances in Materials*, 4(3), p. 43. doi: 10.11648/j.am.20150403.11.

Yanming, Q. and Zehua, Z. (2000) ‘Tool wear and its mechanism for cutting SiC particle-reinforced aluminium matrix composites’, *Journal of Materials Processing Technology*, 100(1–3), pp. 194–199.

Yar, A. A. *et al.* (2009) ‘Microstructure and mechanical properties of aluminum alloy matrix composite reinforced with nano-particle MgO’, *Journal of Alloys and Compounds*, 484(1–2), pp. 400–404. doi: 10.1016/j.jallcom.2009.04.117.

Ye, H. Z. and Liu, X. Y. (2004) ‘Review of recent studies in magnesium matrix composites’, *Journal of Materials Science*, 9, pp. 6153–6171. doi: 10.1023/B:JMSC.0000043583.47148.31.

Yuan, Z. J., Zhou, M. and Dong, S. (1996) ‘Effect of diamond tool sharpness on minimum cutting thickness and cutting surface integrity in ultraprecision machining’, *Journal of Materials Processing Technology*, 62(4), pp. 327–330. doi: 10.1016/S0924-0136(96)02429-6.

Zerilli, F. J. and Armstrong, R. W. (1987) ‘Dislocation-mechanics-based constitutive relations for material dynamics calculations’, *Journal of Applied Physics*, 61(5), p. 1816. doi:

10.1063/1.338024.

Zhou, L. *et al.* (2011) 'Finite element and experimental studies of the cutting process of SiCp/Al composites with PCD tools', *International Journal of Advanced Manufacturing Technology*, 52(5–8), pp. 619–626. doi: 10.1007/s00170-010-2776-2.

Zhou, L. *et al.* (2014) 'Finite element and experimental studies of the formation mechanism of edge defects during machining of SiCp/Al composites', *International Journal of Machine Tools and Manufacture*, 84, pp. 9–16. doi: 10.1016/j.ijmachtools.2014.03.003.

Zhu, Y. and Kishawy, H. A. (2005) 'Influence of alumina particles on the mechanics of machining metal matrix composites (tie constrains)', *International Journal of Machine Tools and Manufacture*, 45(4–5), pp. 389–398. doi: 10.1016/j.ijmachtools.2004.09.013.

Zong, B. Y. *et al.* (2007) 'Strengthening mechanism of load sharing of particulate reinforcements in a metal matrix composite', *Journal of Materials Science*, 42(12), pp. 4215–4226. doi: 10.1007/s10853-006-0674-7.

Appendix

Fabrication process of Mg based MMCs specimen

- **Mg/Ti MMCs & Mg/TiB₂ MMCs:**

DMD process involved superheating the magnesium turnings and the powder reinforcement that are arranged in a multi-layered arrangement to 750°C in a graphite crucible under an inert argon atmosphere followed by stirring the molten melt at a speed of 465 rpm for 6 minutes using a twin blade (pitch 45°) mild steel impeller coated with Zirtex-25. The melt is then released from the base of the crucible, disintegrated by two jets of argon orientated normal to the melt stream and deposited onto a metallic substrate. The preforms are machined to remove the outer layer and cut into small billets. The billets are soaked in a constant temperature furnace at 400°C for 1 hour before being hot extruded at 350°C using an extrusion ratio of 20.25:1 on a 150 tonne hydraulic press to obtain 8mm diameter rods which are used for characterization studies. Further details of the DMD processing technique have been described elsewhere (Meenashisundaram and Gupta, 2014; Gupta and Wong, 2015).

- **Mg/BN MMCs & Mg/ZnO MMCs:**

Mg turnings and the reinforcement powder are placed in a graphite crucible and heated to 800°C using an electrical resistance furnace under inert argon atmosphere. Upon reaching the superheat temperature, the molten slurry is stirred at ~450rpm for 5-10 mins. The stirred melt is bottom poured and disintegrated by two jets of argon gas as it enters a steel mold located below. The deposited ingots is machined and hot extruded to obtain rods with diameter of 8 mm. More specific details regarding the fabrication process of Mg MMCs can be found in the earlier publication (Sankaranarayanan, Sabat, *et al.*, 2014).